INDIRA GANDHI CENTRE FOR ATOMIC RESEARCH

2009

ANNUAL REPORT

सत्यमेव जयते

IGCAR

2009
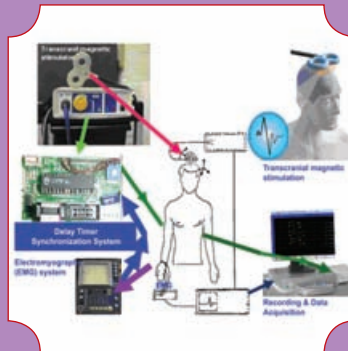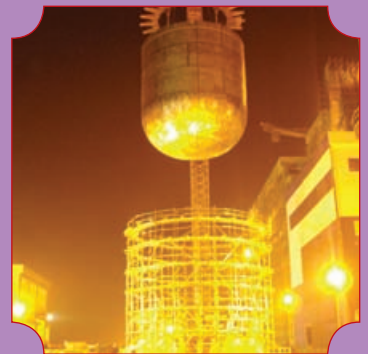
Indira Gandhi Centre for Atomic Research

ANNUAL REPORT

Government of India
Department of Atomic Energy
Indira Gandhi Centre for
Atomic Research
Kalpakkam 603 102

"Actions today mould our tomorrows"

- Indira Gandhi

BHABHA CENTENARY YEAR

OCTOBER 30, 2008 – OCTOBER 30, 2009

".... The relative role of indigenous science & technology and foreign collaboration can be highlighted through an analogy. Indigenous science & technology plays the part of an engine in an aircraft, while foreign collaboration can play the part of a booster. A booster in the form of foreign collaboration can give a plane an assisted take-off, but it will be incapable of independent flight unless it is powered by engines of its own. If Indian industry is to take-off and be capable of independent flight, it must be powered by science & technology based in the country ..."

- Homi Jehangir Bhabha

"There is a totality about modernisation, and in order to gain confidence, we must experiment with our resources even at the risk of failure. There is a need for a constant interplay between basic sciences, technology, industrial practice and management, if economic progress is to result from the activity undertaken."

- Vikram Sarabhai

Editorial Committee

Chairman
Dr. P.R. Vasudeva Rao

Members :
Dr. G. Amarendra
Dr. C. Anand Babu
Dr. K. Ananthasivan
Shri C. Jayakumar
Dr. M. Sai Baba
Dr. Saroja Saibaba
Dr. K.K. Satpathy
Shri Shekhar Kumar
Shri R.V. Subba Rao
Shri S. Varadarajan
Dr. Vidya Sundararajan

Address for Correspondence
Dr. P.R. Vasudeva Rao
Chairman, Editorial Committee
Director, Chemistry Group
Indira Gandhi Centre for Atomic Research
Kalpakkam - 603 102

Phone   : +91-44-2748 0229 / 0222
Fax   : +91-44-27480222 / 0065

Email   : vasu@igcar.gov.in
                    dcg@igcar.gov.in

Website   : www.igcar.gov.in

Published by:
Scientific Information Resource Division
Indira Gandhi Centre for Atomic Research
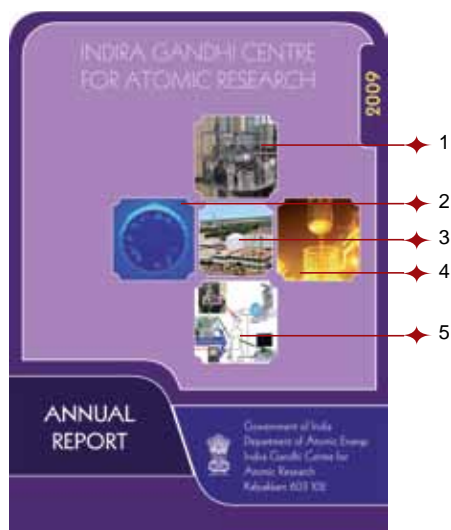Kalpakkam - 603 102

CONTENTS

FRONT COVER

1. Transducer holder with Subassembly heads

2. Simulated flux density along the periphery of pole piece during an analysis of ferro fluid seal

3. Fast Breeder Test Reactor

4. Erection of Prototype Fast Breeder Reactor Main Vessel

5. Transcranial Magnetic Stimulator and Electromyography System interfaced with the embedded design for synchronisation in event recording, for research and therapeutics in movement disorders

BACK COVER
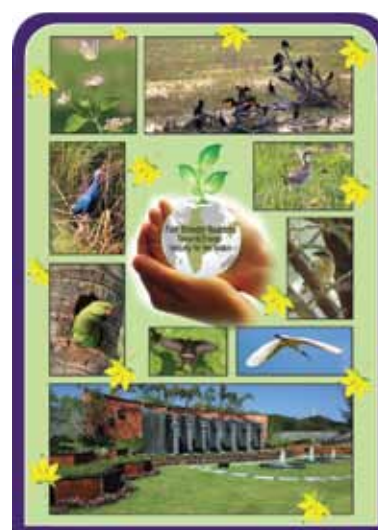
Flora & Fauna and Horticulture at IGCAR

Foreword

I am very happy to write the Foreword for the Annual Report of 2009 of IGCAR. The Annual Report of 2009 presents important achievements of the Centre covering diverse and intertwined domains with components of physical, chemical, biological and engineering sciences.

The Centre is engaged in developing robust science and technology of fast reactors with closed fuel cycle to provide energy security to the nation in a scaled manner. We are on a clear path to become a torch bearer and an eminent country in the fast reactor community of the world. The fruitful and successful experience gained in operating the sodium cooled Fast Breeder Test Reactor over the last twenty five years has generated rich and varied experience that has enabled us to achieve many international milestones in our journey. This confidence of research, development and experiences has resulted in the robust design, engineering development and successful installation of critical and mammoth components for the 500 MWe Prototype Fast Breeder Reactor such as safety vessel, main vessel, inner vessel, grid plate etc. The development and deployment of this high-end technology has enabled the Indian industries to master state of art technologies in terms of the critical fabrication of these components well within the engineering tolerances. This synergy with industries and their capacity development will

have promising spinoffs for other strategic sectors of our country including ultra super critical power plants of fossil fuels as well as for the development of fusion technology. Similarly, the manufacture of 1.8 meter long, 9Cr-oxide dispersion strengthened steel tubes and Reduced Activation Ferritic/Martensitic steels for future FBRs in close collaboration with Nuclear Fuel Complex, Mishra Dhatu Nigam Limited (MIDHANI) and International Centre for Powder Metallurgy (ARCI) in a record time is a testimony to our synergy in indigenous capabilities. This important development has clear applications for structural materials of the fusion programme. Our faith in science based technologies is further reinforced as we are emerging as pioneers in technology. Our philosophy of breakthroughs in science to deliver innovative technologies has resulted in the development of a variety of chemical and physical sensors that would find several applications in reactor and fuel cycle facilities. Another such example is the development of SQUID based ultrasensitive systems for detecting signals from the human heart and brain that would have several societal applications.

The road ahead is clear and visible. We have to strive hard to sustain the momentum to achieve the world leadership in sodium cooled fast reactors with closed fuel cycle based on innovative and robust design features and enhanced safety and cost-competitiveness.

This has to be demonstrated by ensuring the robust, safe and economic operation of PFBR as well as the fuel cycle facility. Thus, IGCAR needs to play a major role in the successful commissioning and operation of the PFBR as well as timely completion and robust operation of fast reactor fuel cycle facility. We need also to take urgent steps to complete all R&D that would be necessary for launching the next generation series of six fast breeder reactors. With the goal of establishing the metal fuelled FBRs in most expeditious manner, it is also important for us to accomplish all the necessary developmental activities that would enable the Department to launch the construction of Metal Fuelled 1000 MWe FBRs. This is indeed a mega challenge and we have a well defined R&D programme that has clearly identified necessary schedules and phases, but given the time frame and the complexity of the technology, there is no room for complacency. In addition to the FBR programme, we make pivotal contributions to selected areas of national security, energy and futuristic programmes of the nation. All these imply that in the year 2010 and the coming years, we will find IGCAR

engaged in intense R&D in a variety of front line areas. We have realised that the key to success of this programme lies in high quality human resources, fruitful collaborations with eminent national & international laboratories and synergistic linkages with industries. On each of this front we have taken decisive, clear and deliverable initiatives over the last few years, which is paying rich dividends. We have to improve the pace with more vigor, enthusiasm, hard work, ethics and team work so as to realise our dream.

I would like to quote **"I never think of the future. It comes soon enough… "**

- Albert Einstein.

I would like to compliment the editorial committee steered by Dr. P.R. Vasudeva Rao, Director, Chemistry Group for bringing out the report in a comprehensive way with established traditions of quality and aesthetic style.

(Baldev Raj)
Director, IGCAR

Mission of IGCAR

- To conduct a broad based multidisciplinary programme of scientific research and advanced engineering development, directed towards the establishment of the technology of Sodium Cooled Fast Breeder Reactors (FBR) and associated fuel cycle facilities in the Country

- The development and applications of new and improved materials, techniques, equipment and systems for FBRs and

- To pursue basic research to achieve breakthroughs in fast reactor technology

Vision

To be a Global Leader in Sodium cooled Fast Breeder Reactor and associated Fuel Cycle Technologies by 2020

Editorial

It is a great pleasure to place at the hands of the readers, the Annual Report of IGCAR for the year 2009. The excellent progress achieved by IGCAR in various fronts during the year, has made it a very enjoyable experience for the Editorial committee to bring out the Annual Report.

The articles on FBTR clearly indicate the fact that the operation of FBTR continues to be robust and experiments at FBTR are on the increase. The extension of life of operation of FBTR will thus be a most welcome development, since it will ensure continued availability of the necessary facilities for the development of innovative equipments and components for future reactor systems. With the initiation of the production of ^{89}Sr, we also have an immense possibility of reaching out to the society, by producing unique radioisotopes that could have application in therapy. In the next year and years to come, FBTR will also be a tool for the development of the metallic fuel which will play a crucial role in the fast reactor programme beyond 2020.

The articles on PFBR highlight the crucial contributions that have been made by IGCAR to this important project. It is obvious that we have met all the R&D commitments towards the PFBR in a timely manner. The large number of articles under research and development for fast breeder reactors show the strength of the department to realize innovative design of reactor systems, indigenous development of components and equipments and development of testing facilities, which would provide a firm base for the future of fast reactor programme. Similar is the case of the fuel cycle, where a number of challenging issues with fast reactor fuels at high burn-up are being addressed.

Basic research in physics and chemistry has also flourished in the Centre, and in many cases its direct applications in fast reactor programme has been realized. The centre has also continued to invest in the addition and maintenance of the infrastructure facilities in tune with R&D programme. The annual report clearly brings out the fact that while delivering all necessary data, materials, design and equipments for the mission programme, the blend of applied and basic research in the centre, will continue to provide breakthroughs that would enable our country to remain at the fore front of the fast reactor science and technology and ultimately reach a position of world leadership.

On behalf of the editorial committee, it is a pleasure to thank all the authors who have contributed to this issue. As in the previous years, we had to go through the challenging task of pruning the articles to make the issue compact and comprehensive. We have at the same time retained the over all structure of the report and appearance as in the previous years, to expedite the publication as well as to provide some continuity. We did receive a number of inputs from the readers for the last issue and we have tried to take them into account while designing the current one. It is our fervent hope that this issue will be equally readable and it will be cherished for the value of the articles.

I personally thank the members of the editorial committee and in particular Dr. M. Sai Baba, Dr. G. Amarendra, Shri R.V. Subba Rao and the SIRD team for the intense efforts to bring out a quality product in a reasonable time. Particularly I would like to acknowledge the hard work put in by Shri G. Pentaiah and Shri A. Rangarajan of SIRD in bringing out the report. We would be most happy to receive feedback from the readers on this issue.

On behalf of the editorial committee, I thank Dr. Baldev Raj, Director, IGCAR, for providing us the guidance for maintaining the high standard of the publication and at the same time reflecting the breadth and depth of the various activities.

Wishing all the readers a Happy and Prosperous New Year.

(P.R. Vasudeva Rao)
Chairman, Editorial Committee
Director, Chemistry Group
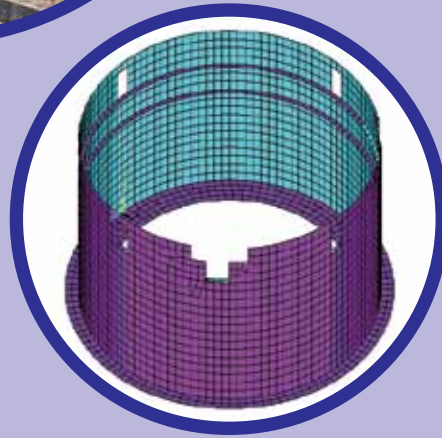
CHAPTER I

Fast Breeder Test Reactor

I.1 The 15th Irradiation Campaign – A New Milestone for FBTR

The primary goals for the 15th irradiation campaign were to operate the reactor at the maximum power attainable with the present core and achieve the sodium and steam temperatures close to the design values (corresponding to 40 MWt) and also to continue the irradiation of the high burn-up lead Mark-I fuel subassembly to establish its endurance limit.

The 15th irradiation campaign was started on 6th December 2008 and completed on 27th May 2009 when the high burn-up Mark-I fuel subassembly reached 165 GWd/t and the six subassemblies in the second outer ring reached the stipulated target burn-up of 155 GWD/t. The reactor was operated at a maximum power of 18.6 MWt with fifty fuel subassemblies (Figure 1) for 1732 hours. High sodium temperature was achieved by operating the steam generator with four of the seven water tubes in service in each of the four steam generator modules and the rest cut and blanked. The reactor inlet sodium temperature was 654.4 K. The maximum outlet temperature of sodium from the reactor was 755 K and the corresponding steam temperature was 703 K, thus setting up a new milestone in the operating history of FBTR. Performance of the reactor, heat transport systems and auxiliary systems was satisfactory. Central subassembly outlet temperature was 813 K, feed water temperature was 465 K and steam pressure was 122 kg/cm^2. During this campaign the PFBR test fuel subassembly attained a burn-up of 92.21 GWd/t, target being 100 GWd/t. The other experiments in progress were the

irradiation of structural materials (D9 & SS) and yttria capsule. Efficacy of clad rupture detection by monitoring the delayed neutrons was verified for two core locations using the experimental delayed neutron detection subassembly. There were two forced outages during the campaign. The cumulative thermal energy developed was ~30 GWh.

All the important modifications carried out in view of the high temperature operation were effective in yielding the desired improvements.

Provision of chilled water cooled heat exchangers and blowers of higher head in the sodium outlet pipe appendix cooling system were fruitful in limiting the temperatures at the appendices and the structural concrete within acceptable limits thus allowing the continuous reactor operation at high temperature.

The surge tank level maintenance circuit was modified to convert the hot sodium line between the surge tank and the expansion tank into a hot argon line based on the experience of PHENIX reactor to avoid possibility of thermal striping in the expansion tank. Performance of the level maintenance circuit during the campaign was satisfactory.

Blanking of three water tubes in each steam generator module facilitated achieving high temperature although the bulk steam temperature achieved was marginally lower than expected and also large difference in the steam temperature among the tubes. Investigation revealed that the spring loaded tube orifice assemblies with bayonet arrangement provided at the inlet of water header had got dislodged
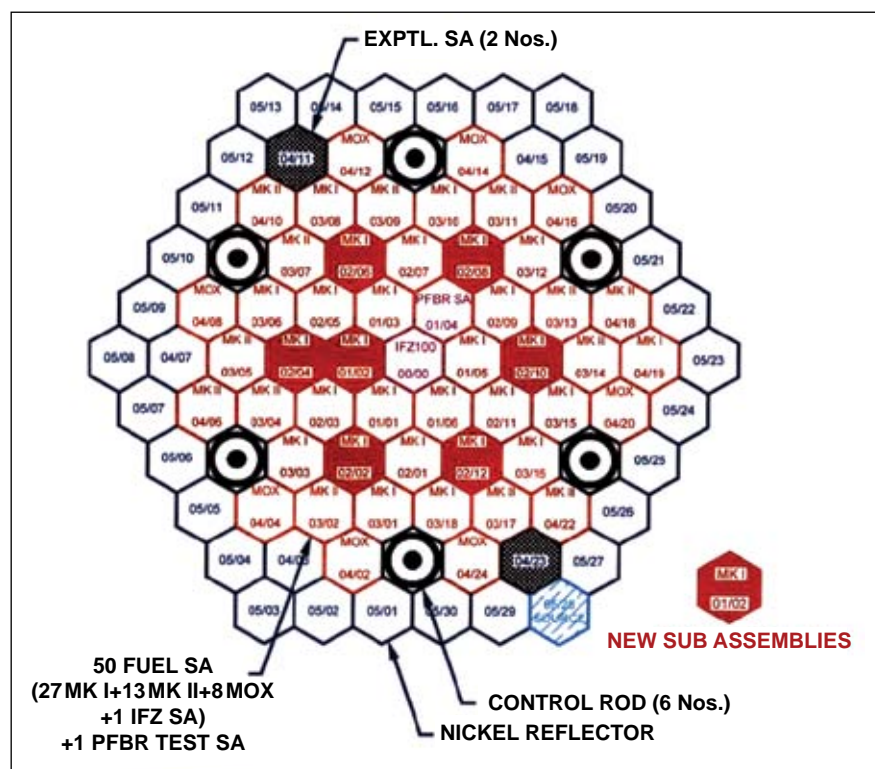

Fig. 1   Core configuration for the 15th irradiation campaign

Fig. 2 *Metallic shroud (cocoon) over the block pile*

from their locations in most of the tubes. These orifice assemblies are being replaced by modified welded type of orifice assemblies before commencing the next campaign.

Visual inspection of the internals of the reactor vessel and thermal shields indicated that the deposits of sodium/sodium oxide in some pockets observed during the previous inspection had dissolved exposing a shiny and clean stainless steel surface due to high temperature operation.

The metallic shroud (cocoon) with an exhaust blower (Figure 2) provided over the block pile was very effective in maintaining the background activity level in Reactor Containment Building within acceptable limits.

The reactor operation time during the campaign was 1732 hours at high power. Turbo generator synchronised to the grid generated about 3.5 million units of electricity.

With the encouraging experience of 15th irradiation campaign, the 16th irradiation campaign is expected to commence in December 2009 with the estimated power of 18.6 MWt with fortynine fuel subassemblies and heat transport system parameters being the same as 15th campaign. The experiments currently underway will be continued to complete the irradiation of PFBR test fuel up to the target of 100 GWd/t. It is also planned to test the PFBR neutron detector in the core at experimental canal location.

I.2   Seismic Re-evaluation of FBTR Civil Engineering Structures

The assessment of safety of an existing Nuclear Power Plant is undertaken to determine the seismic risk of the plant with respect to current seismic design specification. The seismic re-evaluation of an existing plant is prompted by the evidence of seismic hazard and revisions of standards in reinforced concrete and seismic design. FBTR is 40 MWt sodium cooled loop type reactor that was constructed twenty five years ago and it is required to seismically qualify the plant as per current standards to extend its operating plant life. Seismic re-evaluation of FBTR is carried out jointly by IGCAR, AERB and SRI. Seismic re-evaluation of FBTR civil engineering structures viz., cooling tower, concrete tunnel, reactor core and reactor containment building isolation wall carried out by IGCAR are presented here.

FBTR cooling tower is the ultimate heat sink of the reactor. It removes the heat carried by all the condenser cooling and service cooling heat exchangers and releases to the atmosphere. The cooling tower is an induced draft type tower through which, hot condenser cooling and service water pipe enters at the top and due to induced air draft gets cooled and goes back to the cooling water pit. The return from cooling tower passes through a 75 meter long, 1.8 meter inscribed diameter octagonal concrete channel to a 4500 × 3000 × 3000 mm concrete pit which acts as intermediate sump. From
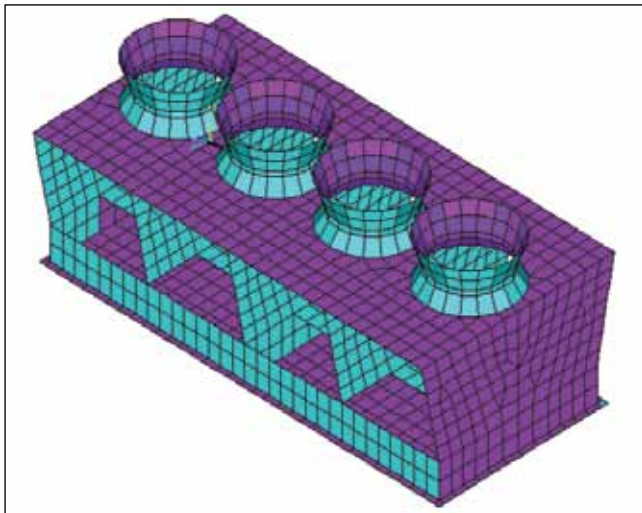
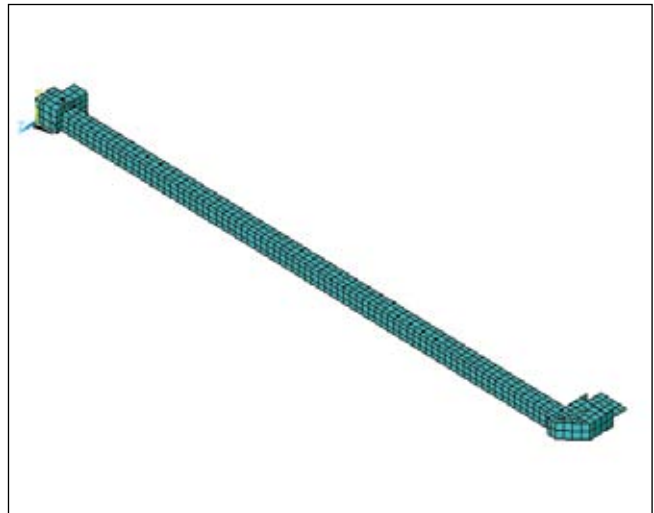***Fig. 1*** *Finite element model of cooling tower*

Fig. 2 *Finite element model of concrete channel*

this sump, water goes through a 800 mm diameter steel pipe, six meter long into a cooling water pit.

The Reactor Containment Building isolation wall of FBTR is a concrete retaining wall encompassing the reactor containment building descending up to an elevation of -17.4 meter from zero meter level and is constructed with an inside radius of 17 meter from the central line. The function of the isolation wall is to protect the inner frame during construction of the foundation mat and containment wall. It is also to form a first barrier of leak tightness, creating a space for drainage around reactor containment building. This wall forms an annulus of 3.6 meter with the reactor containment building wall.

Detailed finite element models of the cooling tower, concrete channel and reactor containment building isolation wall were developed using standard software (Figures 1, 2 and 3). The walls of the cooling tower, isolation wall and all surfaces of concrete tunnel were modeled using eight noded shell elements with transverse shear deformation capability. Seismic response analyses of the structures were carried out by response spectrum method for Review Level Earthquake which are shown in Figure 4. The capacity assessments of the structures were made by conservative deterministic failure margin method. In this method the high confidence low probability of failure value for a particular mode of failure is computed as a product of safety factor and peak ground acceleration, which is corresponding to review level earthquake at the site. The safety factor is obtained as the ratio of difference between capacity of the member and the demand due to non-seismic forces to the demand due to seismic forces. Members having high confidence low probability of failure values less than peak ground acceleration have inadequate capacity.
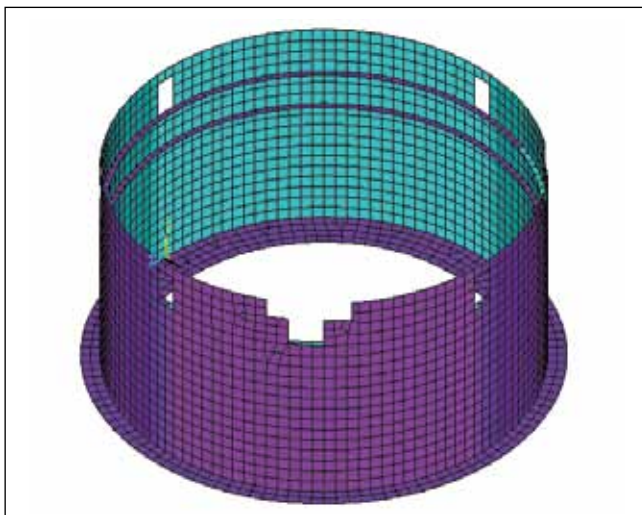

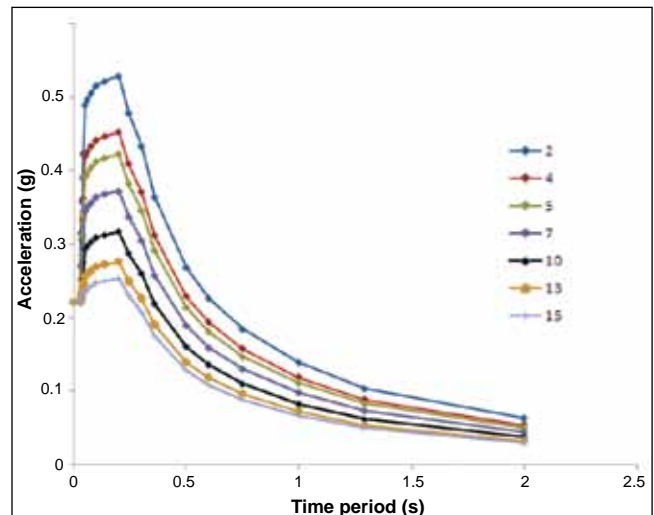***Fig. 3*** *Finite element model of RCB isolation wall*

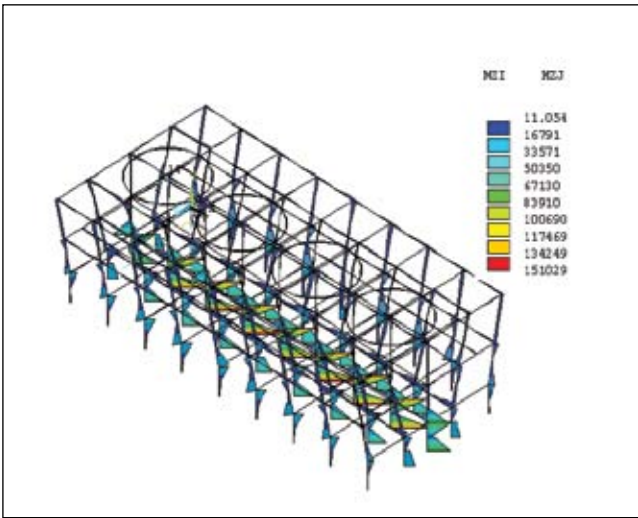***Fig. 4*** *Review level spectrum at different % of damping spectra*

Fig. 5 *Cooling tower-bending moment diagram for earthquake along longitudinal direction*
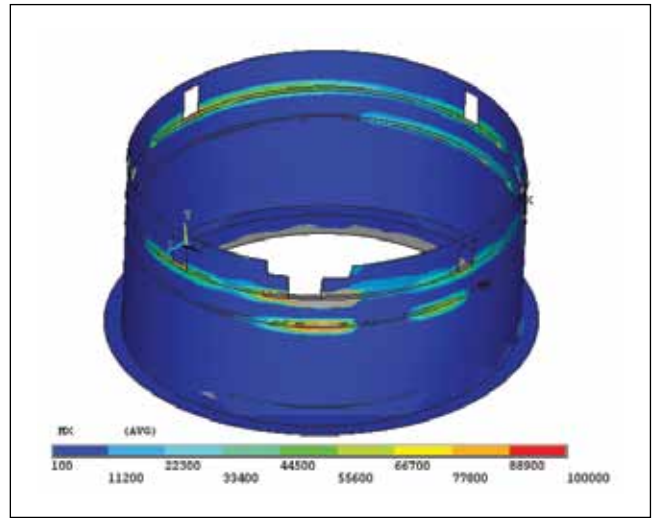

Fig. 6 *Isolation wall-bending stress resultants along circumferencial direction due to earthquake in horizontal direction*

Figures 5 and 6 show the bending moment diagram in the cooling tower frame due to earthquake in longitudinal direction and the circumferential bending stress resultants in reactor containment building isolation wall due to earthquake in horizontal direction respectively. Based on the capacity assessment, it is found that barring a few locations in the cooling tower and the reactor containment building isolation wall, the elements have adequate factor of safety against review level earthquake with peak ground acceleration of 0.2 g.

I.3 Calculation and Experimental Verification of Displacements per Atom Rate on the Grid Plate of FBTR

FBTR has operated for more than twenty four years so far. In order to assess the residual life of the grid plate, which limits the life of the fast reactors, it was decided to experimentally verify the calculated displacements per atom rate. The measurement was performed in the 14th irradiation campaign. The core has forty nine fuel subassemblies consisting of 27 Mark-I, 13 Mark-II and 8 MOX subassemblies. The core layout is given in Figure 1.

Historically, life of any nuclear component which is limited by the irradiation damage is given in terms of fluence seen by the component
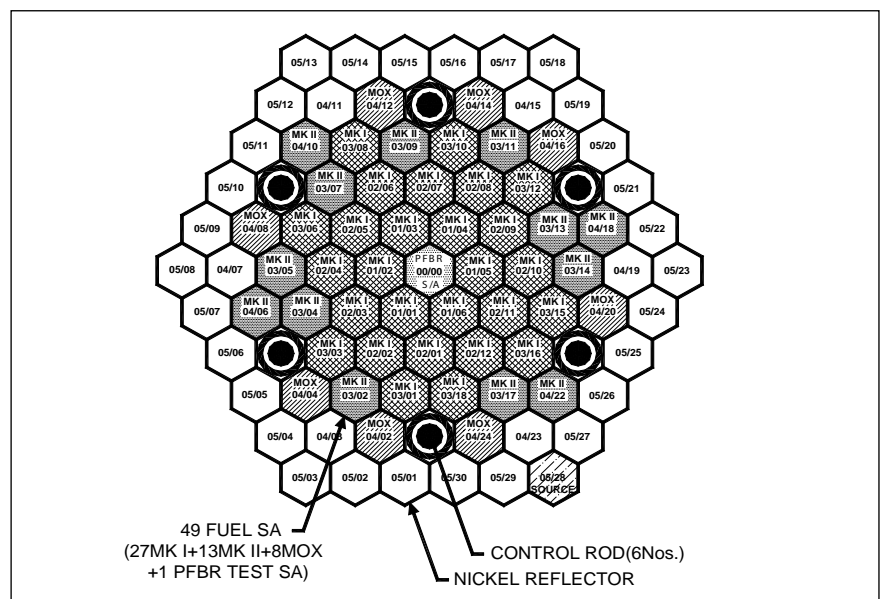

Fig. 1 *Core loading for 14th irradiation campaign*

during its life. Later the life is given in terms of fluence above 0.1 MeV. Subsequently displacements per atom is being used to express the life. There are various models to calculate the displacements per atom and Norgett-Robinson Torrens model is used widely.

For the purpose of calculating neutronic flux, Monte Carlo code MCNP was used. Reactor has been modelled representing all the axial regions of Mark-I and MOX subassemblies. Each of the axial regions of the subassembly is homogenised. Continuous energy cross sections generated using latest version of ENDF/BVI employing NJOY code was used. Twenty five energy group displacements per atom cross sections were generated using the code RECOIL, which uses Norgett-Robinson Torrens model. These displacements per atom cross sections along with the flux calculated were used to calculate the rate of displacements per atom. Displacements per atom

Table 1 : Displacements per atom rates per year of EFPD of operation		
Location	DPA PER YEAR - SS AXIAL REFLECTOR	
	Hybrid core	Mark-I core
Support plate	9.74791×10^2	3.80968×10^2
Guide plate	6.31441×10^1	2.84458×10^1
Cover plate	1.63884×10^1	5.76380×10^2

are calculated in the following regions: Radial distribution for each 5 cm from the centre at 1 cm from top of the support plate and guide plate of grid plate, Radial distribution for each 5 cm from the centre averaged over the thickness of the support plate and guide plate of grid plate.

The calculated displacements per atom rates for Mark-I core of twenty seven fuel subassemblies and Hybrid core (for peak linear heat rate of 400 W/cm) for guide plate, support plate and cover plate are given in Table 1.

Displacements per atom rate at any location can be estimated if

we know the flux. Alternatively if we measure reaction rates of any material whose reaction rates as a function of neutron energy looks similar to that of displacements per atom cross section. The fission cross section of ^{237}Np resembles that of displacements per atom cross sections. Hence, validation of calculated rates by measuring the fission reaction rate in ^{237}Np validates displacements per atom rate calculations.

In order to measure fission reaction rates at grid plate location a special subassembly (Figures 2 & 3) with a capsule loaded with foils is designed and fabricated and used for irradiating the ^{237}Np. Neptunium
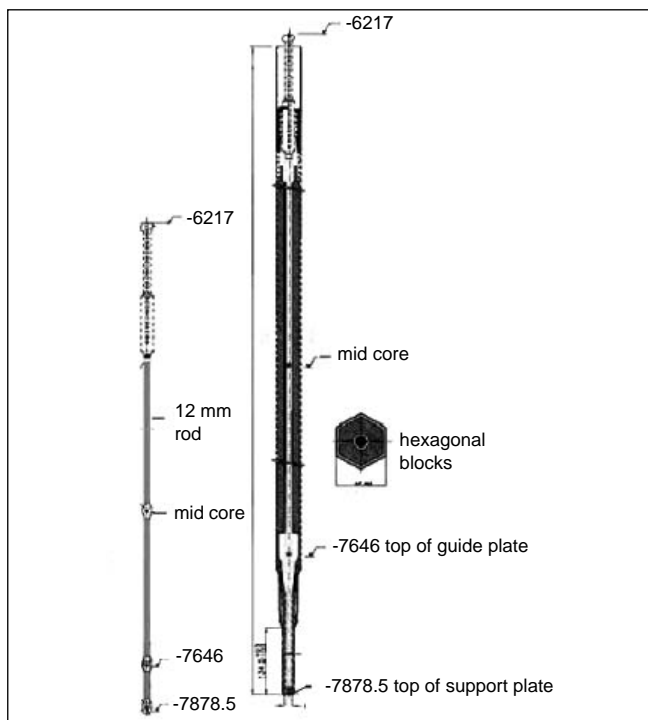

Fig. 2 *Special subassembly used for flux measurement experiment*
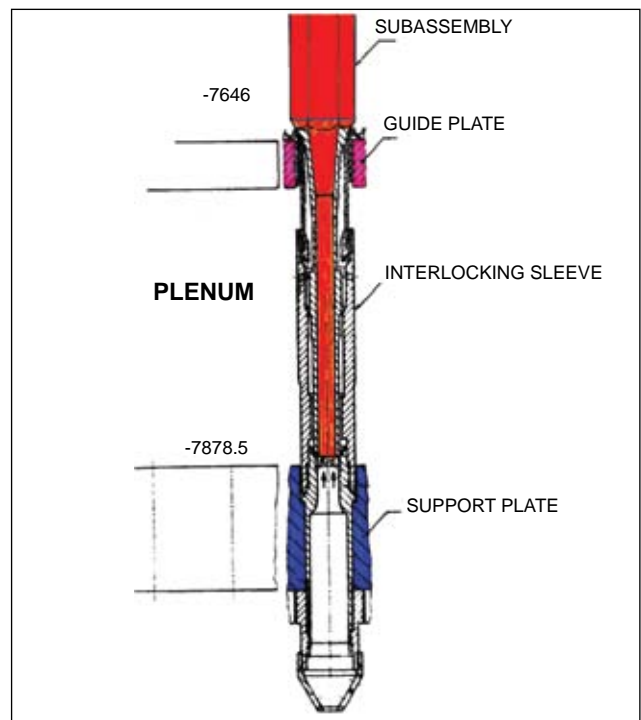

Fig. 3 *Foil locations in the grid plate and support plate*

oxide is fixed in titanium holders for irradiation. Along with these titanium holders, depleted and natural uranium, thorium and nickel are irradiated. The details of the foils are given in Table 2.

After the foils are irradiated, the special subassembly is discharged and foils recovered in the hot cells and the activity of the foils are measured. Based on the activity measured reaction rates are obtained. Table 3 gives the ratio of calculated to the experimental reaction rates.

It can be seen from the above table that the calculated ^{237}Np reaction rates agree very well with calculations. This gives the confidence in our displacements per atom rate calculation at critical components of the reactor.

Table 2 : Details of the foils irradiated				
Foil	**Masses of foils in g**			**Details of foils**
	Core mid plane	**Support plate**	**Guide plate**	
^{237}NpO$_2$	0.002905	0.002905	0.002905	All these foils are loaded in a Titanium Capsule holder
Natural U	0.026650	0.040010	0.047020	
Depleted U	0.026470	0.034650	0.029180	
Th	0.015000	0.015190	0.012730	
Ni	0.115400	0.111750	0.111980	Bare foil
Ti	0.137440	0.131300	0.138390	Planchet of around 0.5 mm thick

Table 3 : Ratio of calculated to experimental reaction rates at various locations			
Foils	**Location**		
	Core mid plane	**Guide plate**	**Support plate**
^{237}Np		1.139953	0.953482
Natural Uranium		0.618800	1.320300
Depleted Uranium	0.5945	0.594100	1.295900
Thorium	0.5046	0.663600	1.008600

I.4 Acoustic Drop Time Measurement System

A prototype online drop time system for the measurement of fall time of Diverse Safety Rods (DSR) in PFBR was developed using acoustic technique. In order to evaluate the performance of the system, experiments were carried out in FBTR to find out the drop time of Control Rod Drive Mechanism (CRDM), at sodium temperature of 443 K with both primary pumps running at 510 RPM and with a core flow of 340 m^3/h.

Acoustic Drop Time Measurement System (ADTMS) employs piezoelectric accelerometer as the primary sensing element, to detect shock signals produced at the end of control rods travel. By measuring the time delay between the switching off electromagnet and the receipt of acoustic shock signal, fall time can be found out. Accelerometers were placed on the top of the Control Rod Drive Mechanism (CRDM-E) and Control Rod Drive Mechanism (CRDM-F) in FBTR as in Figure 1.

The measurement system is a stand alone system, without interfering with other instrumentation of the reactor. It consists of a signal conditioner for amplifying the accelerometer signal, a high speed analog to digital converter module and a personal computer. Accelerometer from the field and a relay contact indicating the
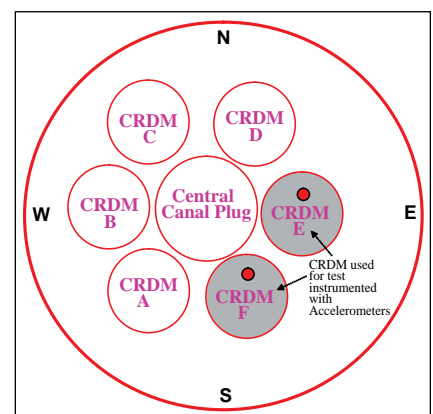

Fig. 1 *Position of sensors in FBTR*

initiation of Safety Control Rod Accelerator Moment (SCRAM) were connected to the acoustic drop time measurement system. The accelerometer signal and the relay are continuously monitored

and the data is sent to the personal computer through LAN. The relay contact input is used as trigger signal for logging. One second pre-trigger and three seconds post-trigger data are stored in the file. LabVIEW software running in personal computer is used for data analysis, from which the drop time is measured as in Figure 2.

Experiments were conducted with Control Rod Drive Mechanism (E & F) in FBTR, with both the control rods dropped from a height of 400 mm and 300 mm separately and simultaneously. The drop times were measured in all the cases
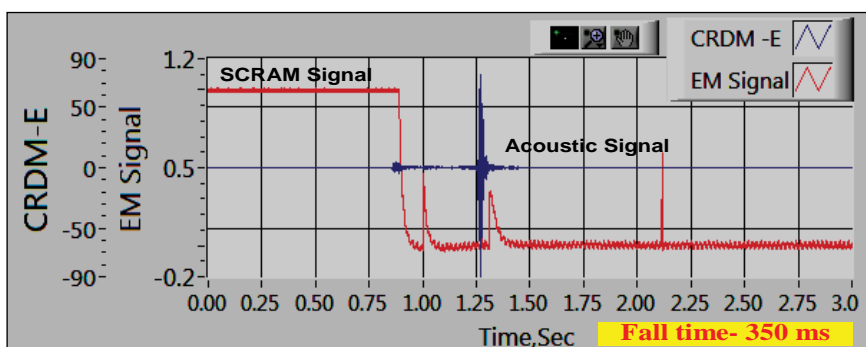

Fig. 2 *Drop time of control and safety rod of* control rod drive mechanism-*E in FBTR*

and found to be of the order of 350 milli seconds. From the results, it was concluded that acoustic technique can be implemented reliably for online measurement of

drop time of diverse safety rods in PFBR. Further, the requirement of Acoustic Drop Time Measurement System electronics was worked out.

I.5 Thermal Ionisation Mass Spectrometric Analysis of the Dissolver Solutions of FBTR Fuel

At various stages of fuel reprocessing, information on isotopic compositions and concentrations of uranium and plutonium is required for 'accountability' purposes. We have conducted thermal Ionisation mass spectrometric studies on many samples of the dissolver solutions of several batches of FBTR fuel pins (discharged after their burn-up of 25, 50, 100, and 154 GWd/t) as well as on some solutions representing the final purified product of PuO_2. The measurements were performed by using the thermal Ionisation mass spectrometer.

Prior to mass spectrometric analysis, appropriate amount of aliquots were drawn from the samples (diluted dissolver solutions) and subjected to an anion exchange separation for obtaining uranium and plutonium fractions. For concentration

measurements by Isotope Dilution Mass Spectrometry (IDMS), the samples were spiked with ^{233}U and ^{242}Pu prior to chemical separation. A small portion of the plutonium fraction was subjected to an alpha spectrometric analysis to deduce ^{238}Pu abundance. For isotopic analysis, about 1 or 2 μg of uranium and plutonium, drawn from the respective pure fractions, were loaded onto rhenium filaments in duplicate.

From the plutonium isotopic compositions, at different values of burn-up, one could infer that as the fuel burn-up increased from 25 to 154 GWd/t, the relative abundance of ^{239}Pu decreased by ~2.2 at.% while that of ^{240}Pu increased by ~ 2.1 at.%. There was a marginal increase in the relative abundances of ^{241}Pu and ^{238}Pu by ~ 0.1 and ~ 0.01 at.%, respectively. In general, the changes in relative

abundances with burn-up were small, as expected of a fast neutron irradiation.

From the results of uranium isotopic compositions, it is observed that the only noticeable trend in the relative isotopic abundance with burn-up was for ^{235}U it decreased from 0.82 at.% (at 25 GWd/t) to 0.74 at.% (at 154 GWd/t). The dissolver solution samples had the uranium/plutonium ratio ranging from 0.46 to 0.67. Some inexplicable trend in the values of relative abundances of uranium isotopes in the finished PuO_2 samples which had the uranium/plutonium ratios ranging from 0.002 to 0.02 were observed. The values for M = 234, 235 and 236 showed nearly a linear increase (and consequently the value for M = 238 showed a linear decrease) with the decrease in the uranium/plutonium ratio.

I.6 Post Irradiation Examination of Control Rod Assembly

Out of the six control rod assemblies used in FBTR, one was discharged after being subjected to a fluence level of 7.0×10^{22} n/cm^2 to assess its irradiation behaviour and to investigate the cause of excessive load encountered during raising of the control rod beyond a particular axial position. The control rod is of vented type design having nine sintered boron carbide pellets (90% enriched in ^{10}B) stacked to a length of 430 mm inside SS316 cladding. It moves axially inside an outer hexagonal sheath made of SS316 during raising and lowering and the interfaces have stellite coating/tracks. The design fluence limit of FBTR control rod is 1.14×10^{23} n/cm^2.

Examinations carried out on the control rod assembly include precise dimensional measurements to investigate the possibility of interference between the control rod and the outer sheath which can result in excessive load, neutron radiography and X-radiography to assess the integrity of the boron carbide pellets and other internals of the control rod, density measurements to assess the swelling behaviour of boron carbide pellets and metallographic examinations to study the cracking behaviour and microstructural changes in the pellet and the clad. Laser mass spectrometry was done to estimate the depletion of ^{10}B in the pellets.

Dimensional measurements did not indicate any significant changes in the outside diameters of the control rod or the inner diameters of the stellite tracks of outer sheath. Minor misalignment of the order of 1.01 mm and 0.83 mm was observed in the axes of the control rod and the outer sheath. This could have led to the interference between them during raising of power when the shoulder region of control rod begins to enter the top stellite track of the outer sheath.

Neutron radiography revealed that control rod internals are intact without any blockages which can restrict coolant flow. No gross depletion of ^{10}B was observed. Extensive cracking and fragmentation were observed in the X-radiographs particularly in the bottom pellets which has been exposed to higher neutron fluence. Figure 1 shows the X-radiographs of the boron carbide pellets inside the control rod. X-radiographs did not indicate any significant change in dimensions of the pellets.

The control rod was cut using laser beam on a dismantling bench to retrieve the pellets from the clad. Infiltration of sodium was observed

Fig. 1 *X-radiographs of the top and bottom B$_4$C pellet regions in the control rod (a) Top region and (b) Bottom region*
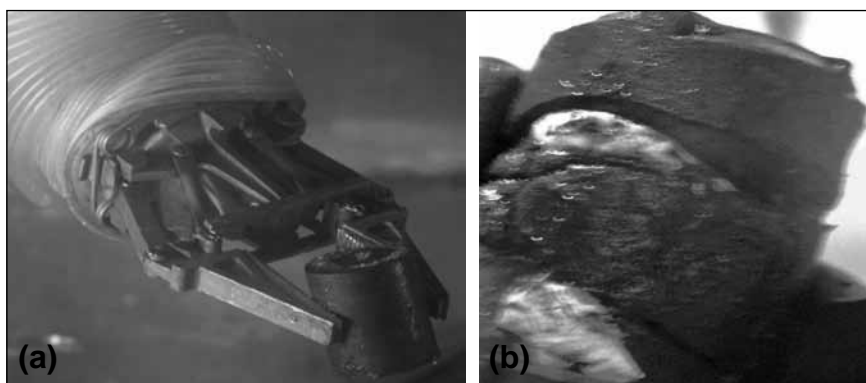
Fig. 2 *Photographs of (a) The pellet in the top region and (b) The bottom pellet showing the infiltration of sodium*

within the fragmented pellets in the bottom region. Extraction of bottom pellets was difficult due to the expansion of the pellet due to the presence of frozen sodium within the fragments. Figure 2 shows the photographs of one pellet located in the top region and one of the bottom pellets showing the pellet infiltrated with sodium.

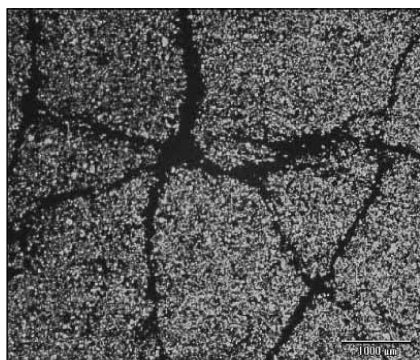Maximum volumetric swelling of 2% was estimated during density

Fig. 3 *Photomicrograph of the* B_4C *pellet cross section showing multiple cracks*

measurements of the pellets in the bottom region. Ceramographic examination of three pellets each from the top, middle and bottom regions of pellet column showed extensive cracking of the bottom pellet. The cross-section of the pellet is shown in Figure 3. No significant change in the microstructure was observed in the three pellets examined. Microstructural examination of the clad did not indicate any chemical interaction between the B_4C pellet and the clad. Laser mass spectrometric measurements on the pellets indicated that the depletion of ^{10}B is less than 1%.

Post Irradiation Examination of control rod assembly has provided valuable information regarding the dimensional changes in the control rod, pellet integrity, swelling behaviour and ^{10}B depletion in B_4C pellets. It has been concluded that the excessive load encountered during raising of the control rod could be due to the marginal interference between control rod and outer sheath. Pellet integrity assessment indicated that due to extensive cracking and fragmentation it may not be possible to reuse most of the pellets. The post Irradiation Examination has clearly indicated that the boron carbide pellets and the structural materials have not reached life limiting conditions.

I.7   Production of ^{89}Sr

The nuclide ^{89}Sr is used in the form of strontium chloride in order to alleviate the pain that is caused by certain forms of cancer. This treatment involves the administration of this isotope to the subject. Since strontium metabolism likens that of calcium it gets accumulated near the cancer afflicted area and irradiates the bone resulting in pain relief. ^{89}Sr is a pure beta emitter ($t_{1/2}$ = 50.53 d) and is produced by the neutron irradiation of a strontium target (enriched in ^{88}Sr > 99.9%, n, γ reaction). Enriched targets are necessary in order to avoid the formation of ^{85}Sr as well as to increase the specific activity. The usual adult dose of ^{89}Sr is around 148 MBq and this depends on the size, age and other clinical aspects of the patient. The compound is currently marketed under the brand name "METASTRON" in USA and Canada and costs about USD 3000 per dose.

Fast reactors have been used for the production of a large number of isotopes utilising either the (n, p) reaction or the (n, α) reaction. ^{89}Sr could be produced by the neutron irradiation of ^{89}Y in a fast reactor using (n, p) reaction. Subsequently strontium is recovered from the irradiated target through chemical separation with a desirable chemical purity (and specific activity). Pure ^{89}Sr samples possessing a specific activity of about 19 kCi/g have been derived through irradiation of targets in fast reactors vis-'a'-vis about 10 Ci/g strontium in thermal reactors. The major disadvantage of this route is the co-production of ^{88}Y ($t_{1/2}$ = 106.65 d, intense high energy gammas) by the (n, 2n) reaction necessitating shielded cell operations. Figure 1 gives
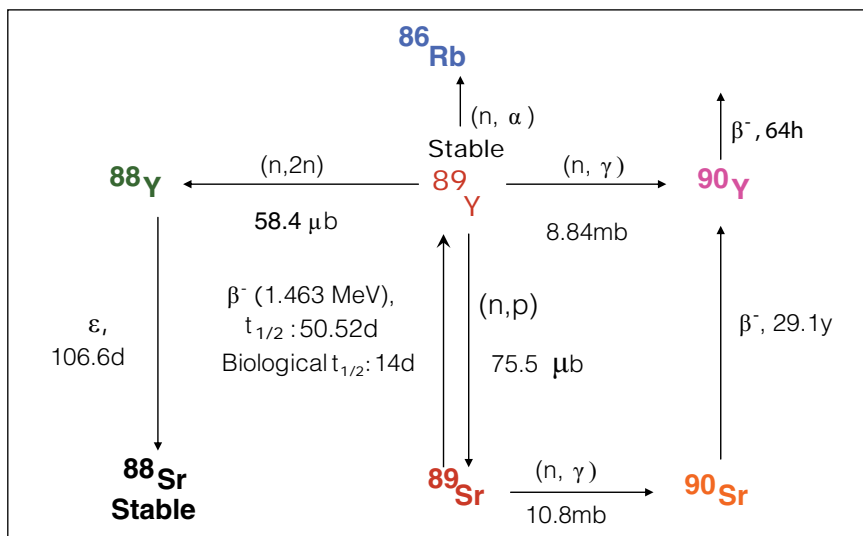

Fig. 1   *Schematic of production of ^{89}Sr*

the production route for various nuclides due to the irradiation of ^{89}Y.

Recently we produced this radionuclide through irradiation of targets in FBTR. This procedure involved the preparation and irradiation of yttria targets followed by its dissolution, chemical separation of ^{89}Sr, and finally purification and assay of the product.

A typical irradiation experiment involved the preparation of high density yttria (IRE, 99.9% purity) pellets by cold pressing with zinc oxide as binder and sintered at 1873 K. The pellets were then introduced into the stainless steel irradiation capsule and inserted into the IFZ 100 special subassembly. The IFZ 100 subassembly is a special subassembly where the inner seven pins have been removed for accommodating for irradiation experiments. This subassembly was loaded at the centre of the core and irradiated for seventy three days in two sessions, the first of which lasted for a period of thirty five days, while the second spanned over thirty eight days. These two irradiations were separated by a period of thirty eight days. Subsequently, the irradiation capsule and the pellets contained within were recovered from the subassembly in the hot cells located in the radio

	Isotope	**Route**	**Source of Origin**
		Table 1 : Isotopes produced **by the irradiation of ^{89}Y**	
1	^{86}Rb	^{89}Y(n,α)	From Target material
2	^{88}Y	^{89}Y(n, 2n)	
3	^{65}Zn	^{64}Zn(n,γ)	From the trace level remains of binder
4	^{58}Co	^{58}Ni(n, p)	Activation products of Stainless Steel
5	^{54}Mn	^{55}Fe(n,p)	
6	^{160}Tb	^{159}Tb(n,γ)	Rare Earth impurities from target material
7	^{141}Ce	^{140}Ce(n,γ)	

metallurgy laboratory. These pellets were then transferred to the Radio Chemistry Laboratory in a shielded cask. Preliminary experiments were carried out with one of these pellets (radiation dose 2Rh^{-1}). This pellet dissolved in concentrated nitric acid when refluxed. Even though the dissolution was rapid in the first eight hours, it took forty four hours for completion of the same. The results obtained in the gamma spectrometry of an aliquot of this solution are given Table 1.

While yttrium present in this solution ^{160}Tb (impurity) could be completely extracted into the organic phase using 100% TBP, strontium remained in the aqueous phase along with other radioactive isotopes viz., ^{86}Rb, ^{65}Zn, ^{58}Co, ^{54}Mn and traces of ^{88}Y.

Further purification of strontium fraction was carried out using the cation exchange resin Dowex 50×8, (100-200 mesh size). The sample

was loaded onto the column using 0.1 M nitric acid and eluted using 1 M nitric acid at a flow rate of 0.5 ml / min. The elution profile obtained is shown in Figure 2 reveals that ^{86}Rb, ^{65}Zn, ^{58}Co and ^{54}Mn get eluted first.

Quantitative assay of the amount of ^{89}Sr produced was carried out using radiometric techniques by using both beta counting and Cerenkov counting. The amount of ^{90}Sr produced by the (n,γ) of ^{89}Sr was estimated by extraction paper chromatography coupled with both beta and Cerenkov counting. PC88A and NaCl solution were used as the complexing agents for yttrium with aged samples in order to estimate the amount of ^{90}Sr by estimating the amount of ^{90}Y which has a beta maximum of 2.2 MeV and would be seen using both methods.

Irradiation of yttria pellets were carried out in FBTR in order to determine the amount of ^{89}Sr produced as well as to establish the chemical purification steps. It was seen that about 19 mCi of ^{89}Sr was produced in an yttria pellet (wt=1 g) against the computed value of 12 mCi. Dissolution of the irradiated pellet and chemical separation steps were standardised. Separation of ^{89}Sr using crown ethers (strontium separating reagent) is in progress. The adaptation of the dissolution and separation procedures for remote use in shielded facility is also in progress.
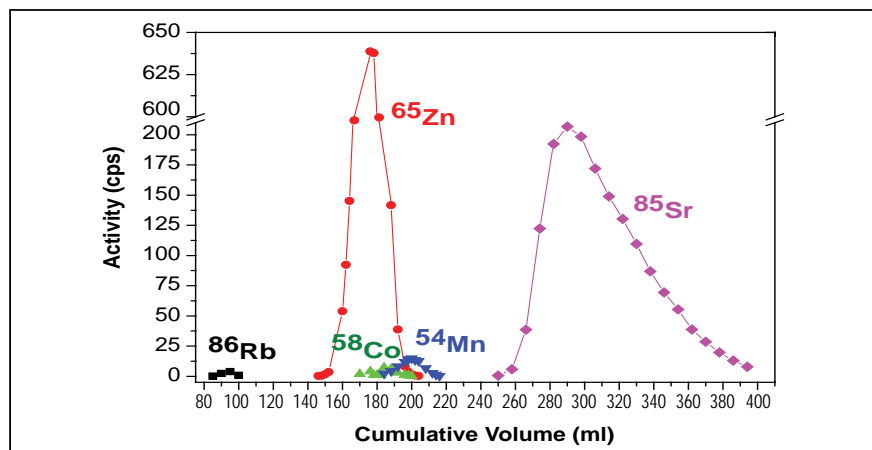

Fig. 2 *Elution profile of various isotopes using 1M HNO$_3$*

I.8 Investigation of High Water Activity in KAMINI

The ^{233}U fuelled KAMINI (Kalpakkam Mini) reactor is being utilized extensively for neutron radiography and activation analysis. In June, 2008, activity of reactor water sample was showing increasing trend and approaching the technical specification limit of 50 Bq/ml (sample counted after one hour delay) during continuous operation of KAMINI reactor at power levels more than 15 kW. Initial investigation revealed that this is due to gaseous fission products. The reactor tank (RT) water and mixed bed resins were completely replaced to rule out the possibility of high activity due to the leaching of activated corrosion products from the resins. Spectral analysis of the reactor tank water sample taken during operation and used resin was also carried out. Based on the results, clad beach was not suspected. The breach of the clad due to the corrosion is ruled out since the water chemistry was always maintained within the technical specification limits and increase in the Be, Al level in the reactor tank water was also not observed.

To find the cause for the high water activity, an experimental set up for sipping the water sample from each fuel subassembly was devised. The setup consists of a pump , with suction line reaching up to the fuel subassembly top and aluminum foot valve (Figure 1).

The discharge line of the pump branches into two, one back to reactor tank as recirculation with a charcoal filter (for trapping any solid fission products such as Iodine and cesium) and the other to DM plant for taking sipping samples with proper isolation valves.
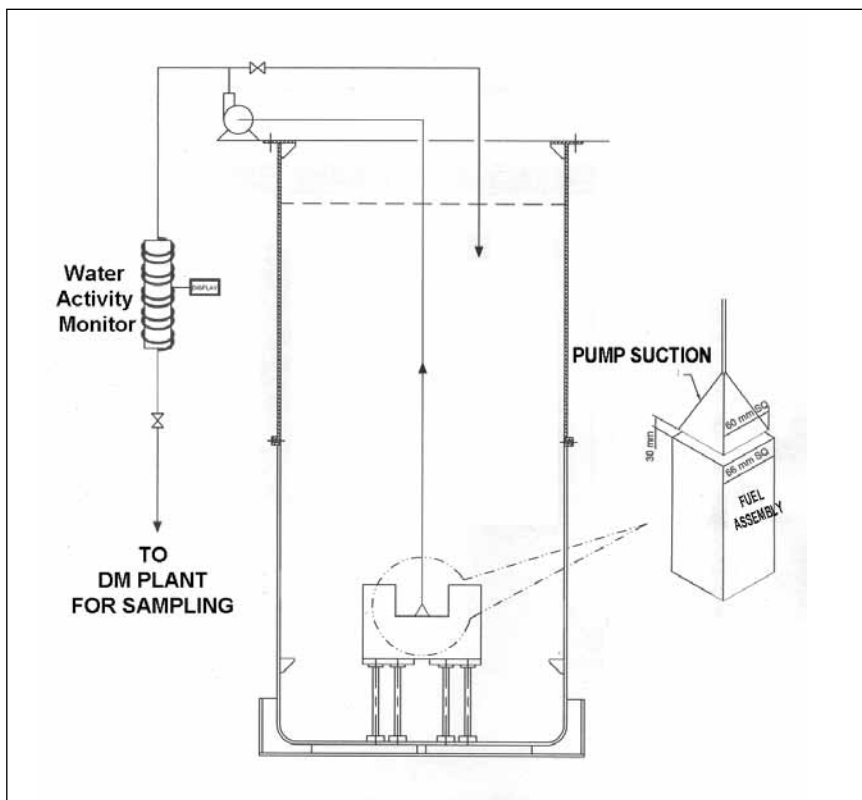

Fig. 1 Set up for taking water sample from fuel subassembly outlet by sniffing

One water activity monitor was installed just before the sampling point to get an immediate activity level of the sip sample taken. After getting approval from safety bodies for operating the reactor for investigations with a higher water activity limit of 200 Bq/ml instead of 50 Bq/ml, sipping experiments were conducted at 20 kW power, taking samples from the outlet of fuel subassemblies. No solid fission products were seen in the analysis. The investigations done in the reactor tank water samples confirmed that the fission products observed in the reactor tank water originate from the fission of ^{233}U and not due to Pu from the Pu-Be source, which is still in the reactor.

The activities of the fission gases in B1 position are higher by a factor more than 10 to 20 times relative to the activities seen in A3 and A1

(Figures 2, 3 & 4). Subassemblies B2, C2 and C3 appear to show activity levels few times higher than A3 or A1. The water activity of one-hour delay sample from reactor tank water reached a maximum of 131 Bq/ml after four hours reactor operation at 20 kW.

The contribution of effluent gas activity from KAMINI to the FBTR stack was found to be negligible during 20 kW operations, with the higher water activity levels. The

East		
SCP1		SCP2
C 3	B 3	A 3
C 2	B 2	A 2
C 1	B 1	A 1
West		

Fig. 2 Core configuration of KAMINI

effluent gases from the reactor directly go to the stack and hence the radiological impact in accessible areas in KAMINI is very less.

Fuel subassembly designers and fabricators have confirmed that all quality checks such as glycol leak testing, radiography and decontamination process were adopted for all fuel subassemblies including the spare Pu-Al fuel subassemblies. It is quite likely that the plates for this fuel subassembly which were rolled first would have got higher sub-surface contamination than the others. It is suspected that the increase in the fission gas activity is due to the

burn-up seen by the ^{233}U lodged in the sub-surface of the clad while rolling the clad during fabrication.

The activity of the water in case of a clad rupture will be very high and should also increase with operating time. It is seen from the results that the global activity remains stable after one and half to two hours of operation. It is confirmed from the spectral analysis results on water samples, resin and charcoal that the high water activity is only due to fission product noble gases. There are no solid precursors (^{135}I) in the samples. The spectral analysis of gas sampled from the top of the reactor during 20 kW operation

showed only negligible amount of fission product noble gases as seen earlier and the radiation levels measured in all accessible areas in KAMINI were well with in the safe limits.

Similar phenomenon has been reported from SLOPOK reactors. Reactor is now being operated with the limit on water activity increased, with additional precautions like periodic monitoring of water sample for solid precursors. There has been no increase in fission product noble gas activity, nor have any solid precursors been detected after 164 cycles of operation during the year.
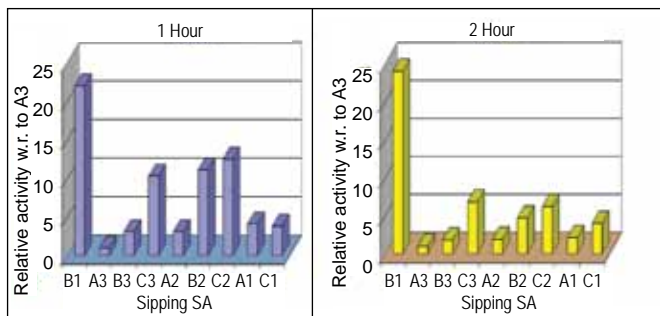

Fig. 3 *Comparison of sip sample activity (^{135}Xe) for different* fuel subassemblies *at 20 kW*
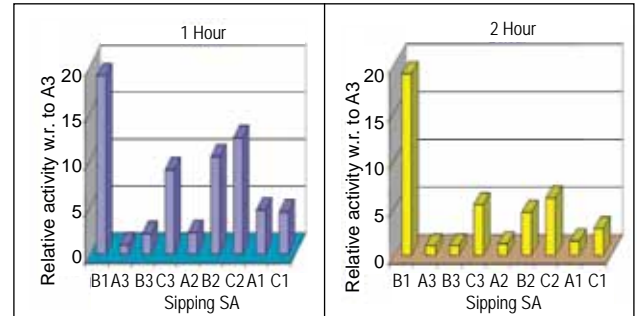
Fig. 4 *Comparison of sip sample activity (^{87}Kr) for different* fuel subassemblies *at 20 kW*

I.9 Modification of Orifice Assemblies of Steam Generator

FBTR steam generator (SG) generates superheated steam at 125 bar, 753 K and has four once through type modules made of niobium stabilised ferritic steel. The modules, two each, are connected to the east and west loop of secondary sodium system. Hot sodium flows in the shell side transferring heat to the water flowing through the tubes. Each module has seven tubes out of which three tubes were blanked recently for

raising the system temperatures near design temperatures even at less reactor power level. The modules are interconnected at water and steam sides. All the four modules are located in an insulated leak tight metallic casing.

The steam generator modules being shell and tube type are vulnerable for instability in case there is two phase flow through it. The two types of instabilities

experienced by these heat exchangers are static instability and dynamic instability. Static instability arises when the steam generator can sustain more than one flow for the same pressure drop. The dynamic instability is caused due to multiple regenerative feed backs between heat transfer and pressure drop. In order to mitigate these two instabilities, pressure reducing orifice assemblies are introduced at the inlet of the tubes in the

Fig. 1 *Gamma radiograph of dislocated orifice assemblies*

Fig. 2 *Flared ends of water tubes*

feed water header of each steam generator module. For stability of steam generator at all powers of reactor, the minimum pressure drop required in the orifice is 15 bar at 74 l/h flow rate. The orifice assemblies are made of austenitic stainless steel and are kept locked to the steam generator tubes by means of a spring and bayonet type locking arrangement.

During the 15th irradiation campaign at 18.6 MWt (in February 2009), large variation was observed among the steam temperatures of the four steam generator modules. Temperature was found varying from 663 to 741 K. For investigation, surface thermocouples were installed at the outlet of the sixteen tubes which are presently in service and on the outlet header of all the four steam generator modules. In the subsequent operation of the reactor, the individual tube outlet temperatures showed large variations among the modules and among the tubes in the same module. In the east loop modules SGna700 and SGna500B, the steam temperatures were 643 and 721 K, whereas in the other loop, the temperature was 697 K. Feed water flow through SGna700 was found to be 44% more than the other three modules.

For further investigation, gamma radiograph of the orifice assemblies at the water inlet of all the tubes was taken during plant shutdown. It was observed that the orifice assemblies from twenty two tubes out of total twenty eight tubes got dropped from their position (Figure 1). Out of the twenty two fallen orifice assemblies, thirteen assemblies were in the tubes which were in service and nine were in the blanked tubes (Figure 2) indicating that the orifice assemblies have fallen before the blanking of tubes.

Subsequently, all the water inlets were cut and orifice assemblies were retrieved. Flaring of the bayonet holders and deformation of the springs were noticed in most of the tubes. No erosion was noticed on the orifices or flow breakers. Wall thickness of the tubes upstream of the orifice assemblies was measured and no thinning was noticed.

A safety assessment of this deficiency in the steam generator assembly was carried out. As per the configuration, the orifice assemblies supported by the spring experience an upward thrust. Due to this, its top end gets seated in a step in the water tube making a leak tight seating. The entire quantity of water flows through the orifice creating the required pressure drop. Even in the dropped condition of the orifice assemblies, there will be a flow through the orifice. In addition to this flow, there will be a bypass flow through the assembly clearances to the extent of an additional flow of 35%. Hence, there will not be any reduction or blockage of flow due to this deficiency. The stability test conducted at the end of 14th irradiation campaign also did not indicate any instability in steam generator. Even though the readings obtained showed some difference in the module to module steam temperature, the values
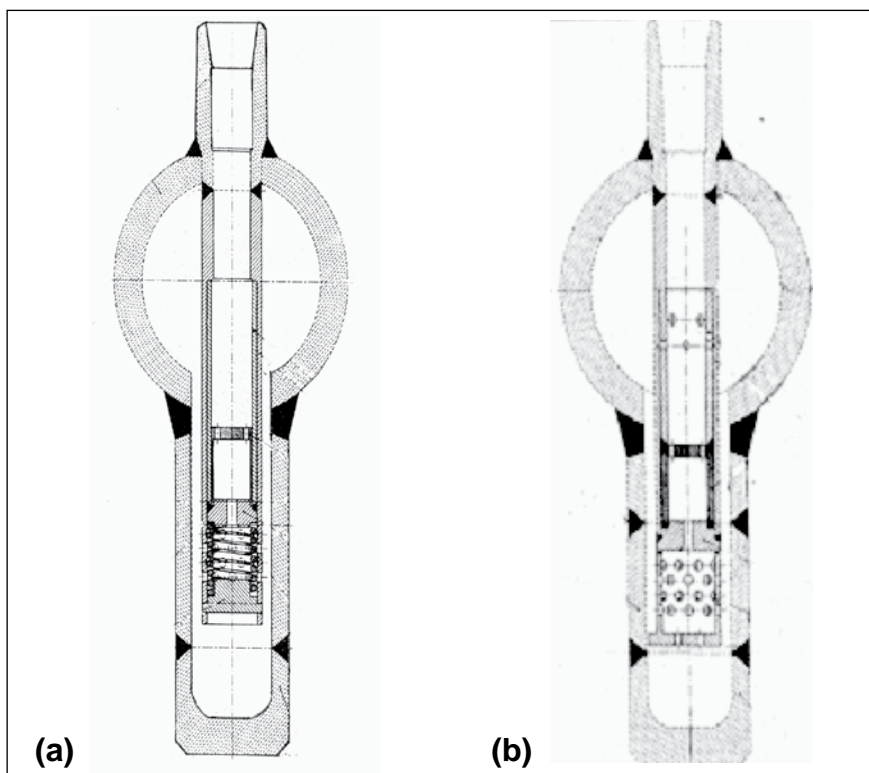

Fig. 3 *Orifice assembly (a) Existing and (b) Modified*

obtained were marginal as the earlier operating temperature was less. The difference became highly predominant when the operating temperature was raised in the 15th irradiation campaign.

The reason for dislocation of the orifice assembly has been analysed. The design of FBTR orifice assembly envisages periodical replacement of orifice plates in case of any erosion. Hence, a removable assembly with a bayonet type locking was provided. During normal operation, in addition to the spring force, there will be an upward thrust on the assembly keeping it in position. However, during steam generator depressurisation, there will be downward force acting on the orifice assembly because of the large pressure gradient across it. This exerts a large force on the orifice holder resulting in flaring of the bayonet holder and dislocation of orifice assemblies.

As the existing holding arrangement alone has failed and the orifice dimensions were found to be intact, it was decided to modify the design by welding the orifice assembly directly to the water tube end eliminating the need for spring and bayonet locking arrangement. Design group has come up with the new design (Figure 3). It is estimated that the weld joints can withstand 30,000 cycles taking into consideration of all pressure and thermal loadings. New orifice assemblies were machined and these assemblies are being welded to the steam generator modules. Necessary regulatory clearance at various levels has been obtained for the modification. All quality assurance requirements will be met as per FBTR specification ASME section VIII Division 1 standard.

I.10 Laboratory Scale Facility for Sodium Bonded Metallic Fuel Fabrication

Metallic alloy of uranium and plutonium are the fuel envisaged for the future FBRs in India. Since this is an advanced fuel, on which this country has little experience, it is imperative to generate fabrication and irradiation experience before launching commercial FBRs with metallic alloy fuel. Towards this, a sodium bonded metallic test fuel pin fabrication facility is being setup. Subsequently the pins fabricated would be irradiated in FBTR, in order to assess their irradiation behaviour. The qualified fuel slug will be received from BARC and the same will be used for fabrication of this test fuel pins. A facility comprising the equipment necessary for carrying out i) bottom end cap welding ii) sodium wire extrusion iii) sodium loading into the one end closed clad tube iv) blanket and fuel slug loading v) top end cap welding and vi) sodium bonding of the fuel pin is being constructed and commissioned along with the facility for qualifying the pin for the irradiation tests. This facility would comprise a train of inert atmosphere glove boxes.

These glove boxes would provide a high purity argon ambience in which oxygen and moisture are controlled to 10 and 50 ppm respectively. This is achieved by way of careful design that ensures a high degree of leak tightness and by incorporating a special purpose purification system. Interconnections between the members of the train are facilitated through transfer ports. The equipment for sodium extrusion and sodium filling are housed in inert atmosphere glove boxes that are maintained at a pressure more positive with respect to the ambient, while the boxes in which the fuel slug loading, end cap welding and sodium bonding operations are carried out are maintained at a pressure lesser than (negative pressure) that of the ambient. Figure 1 shows the facility for sodium handling and inert
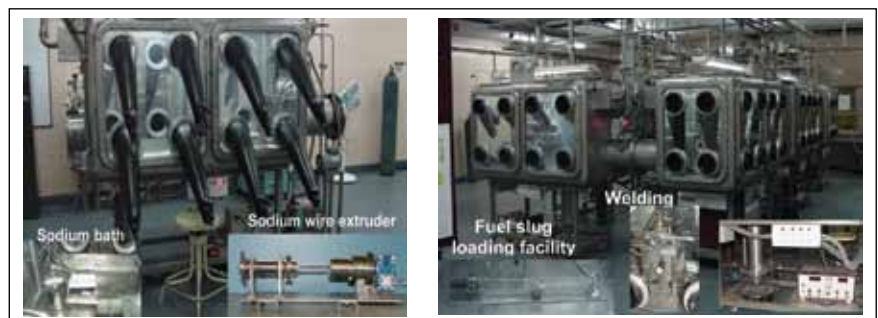

Fig. 1   *Inert atmosphere glove box for sodium handling*

atmosphere glove box train facility. The inset shows the components housed in this facility.

Sodium filling and slug loading facility

A sodium wire measuring about 3 mm in diameter is extruded into a PVC sleeve using a sodium extruder set up. The technique for transferring this sodium wire from the PVC sleeve into a one end closed clad tube was standardised. These operations were carried out in inert atmosphere glove boxes. After qualifying the bottom end plug weld by using non-destructive testing techniques, the tube is taken inside the sodium handling facility. Required quantity of sodium is added inside the fuel pin by extrusion method and heated to 423 K. After cooling to room temperature, the clad tube is closed with a suitable veeco coupling in order to ensure leak tightness. It is then encapsulated in a polyethylene sleeve and transferred to the fuel slug loading facility.

Blanket and fuel slug loading facility

The clad tube along with the sodium wire contained within is encapsulated in a PVC sleeve. This along with the steel blanket and U-Zr slug are taken into the glove box through the bag-in procedure. The clad tube is then positioned horizontally in the slug loading setup. Subsequently the blanket and the U-Zr slug are loaded into the clad tube by levitation. Finally the clad tube positioned inside the slug-loading furnace housed inside the glove box is heated to 423 K and vibrated at 20 Hz with vibrating amplitude of 5 mm. This process allows the slow settling of blanket and U-Zr slug at the bottom of the clad tube with sodium filling in the annular gap between slug and clad tube. Later, the furnace is cooled from bottom to top in order to avoid shrinkage of the sodium fill during cooling. The top end is closed with a veeco coupling and then transferred to the end cap-welding facility.

End cap welding facility

The top end plug is welded with the sodium bonded fuel tube by using pulse TIG Welding process, in a special welding chamber which is filled with helium. Several trial welds were made in order to optimise the weld parameters. These welds were qualified by the non-destructive testing techniques viz., helium leak test and X-radiography. A U-Zr slug fuel pin containing sodium has been welded and was subjected to helium leak test and X-radiography.

Sodium bonding facility

The fuel pin containing the U-Zr alloy slug would serve as simulate for the actual fuel pin. For this purpose, a prototype sodium bonding furnace with vibrating facility has been fabricated. The furnace is attached with the glove box floor to facilitate loading of the metallic fuel test pin from inside the box. The vibrator assembly is kept outside the glove box and coupled to the furnace through metal / neoprene bellows in order to ensure proper containment. Cooling fins were provided both at the top and the bottom of the furnace in order to prevent the floor of the glove box from getting heated up. In addition, a provision has also been made in order to cool the furnace from bottom to top after completion of heating and vibrating cycle of sodium bonding procedure. The heater assembly was made out of a nichrome heating element with ceramic beads. The heater assembly was tested for satisfactory performance and the temperature profile of this furnace was monitored using a data logger connected to a personal computer. The flow of current through the heaters in the furnace assembly was optimised in order to achieve a constant temperature zone having a length of 300 mm at 723 K in the sodium-bonding region of the fuel pin. The electrical connections to the heater and the thermocouple were taken out through vacuum tight feed-throughs provided at the top flange of this furnace assembly.

After qualifying the top end plug it was subjected to the sodium bonding procedure in sodium bonding setup. The portion of fuel pin containing sodium and U-Zr slug was heated to 723 K and vibrated using a vibrator for sixty minutes at a frequency of 20 Hz and suitable amplitude such that this slug would vibrate with an amplitude of 10 mm. After heating and vibration, the fuel pin was cooled from bottom to top using argon gas to avoid shrinkage voids in sodium-bonded region. After completion of sodium bonding procedure, it was subjected to X-radiography for sodium level measurement.

Procedures for standardizing various operations like sodium extrusion, sodium loading, slug loading, end plug welding and sodium bonding with U-Zr alloy are carried out before taking up active runs with U-Pu-Zr fuel slug.
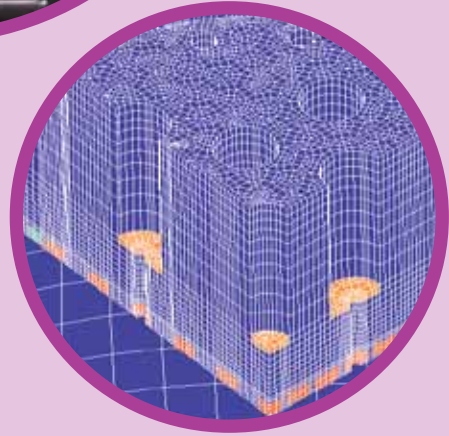
CHAPTER II

Prototype Fast Breeder Reactor

II.1 Construction Status of PFBR

The construction of PFBR has made significant progress during the year 2009. The main vessel of 12.9 meter diameter, which was manufactured at site (Figure 1) in austenitic stainless steel 316LN grade to stringent fabrication tolerances has been lowered to its position (Figure 2) along with core support structure and core catcher. Manufacturing of the inner vessel, intermediate heat exchanger (Figure 3), sodium to sodium decay heat removal heat exchanger, integration of grid plate with primary sodium piping (Figure 4), Horton spheres for gas storage and all the shutdown mechanisms have been completed.

Manufacturing of steam generators, sodium pumps, top shields, rotatable plugs, control plug are in advanced stage of completion at Indian industries. All the diesel generator sets have been received at site.

Construction of nuclear island connected buildings, diesel generator buildings and sea water intake structure are in advanced stage of completion. Sea water outfall structure has been completed. 230 kV switchyard package and 6.6 kV switchgear package, MCC, HCC and PCC packages are in advanced stage of completion. About one thousand tons of sodium has been filled into the reactor tanks. The project has achieved 52.5% overall physical progress as of December 2009.

Fig. 1   Overall view of nuclear building

Fig. 2   Erection of main vessel of PFBR

Fig. 3   Intermediate heat exchanger

Fig. 4   Integration of grid plate with primary piping

II.2   Establishment of Reactor Start-up Scheme

One of the important plant operations that requires detailed investigation on its execution strategy is the reactor start-up as it is expected to be about one thousand times in the life time of the plant. The plant dynamics studies carried out have demonstrated the feasibility of having a simple manual operating scheme for the start-up of PFBR by satisfying various constraints imposed by the design of the components and thermomechanical loading on various structures within permissible levels. The plant start-up operation, which is planned to be totally manual, comprises of three major activities viz. (i) termination of decay heat removal system and establishment of the regular heat sink (ii) approach to criticality in the reactor core and (iii) power raising in the reactor core by the lifting of control and safety rods.

Prior to reactor start-up, feed water in the deaerator is preheated to 423 K using steam from the auxiliary boilers. Decay heat removal system is taken out of service and feed water flow from the deaerator is injected through steam generators. In order to prevent the cool down of sodium systems (473 K) due to the injection of relatively cold water (423 K) through steam generator, the water flow rate through steam generators at this phase is limited to about 3%. Primary and secondary sodium pumps are operated at full speed such that the heating of the sodium systems due to the operation of pumps and heat losses through various systems balance each other. Now, criticality can be achieved at isothermal conditions in the core. Final activity of power raising through control rod movement is the longest

operation in the start-up. During this operation, it is necessary to keep the heating rate of hot pool below 20 K/h to avoid thermal shocks to various components. The reactivity additions during the start-up procedure should be such that the total reactivity is not more than 5 pcm (alarm threshold of reactivity trip parameter). A simplified procedure with a minimum time delay between two control rod raise operations and with control rod raise by a definite

distance (less than a limiting distance) every time has been worked out for the raising of reactor power using the plant dynamics code, DYANA-P. This wait and raise mode of start-up procedure is elaborated in Figure 1. Feed water flow adjustment is devised in such a manner to avoid flow instability problems in steam generators The control rods are moved every time by 2.5 mm with a minimum time interval of 3.5 minutes between two rod movement steps. The
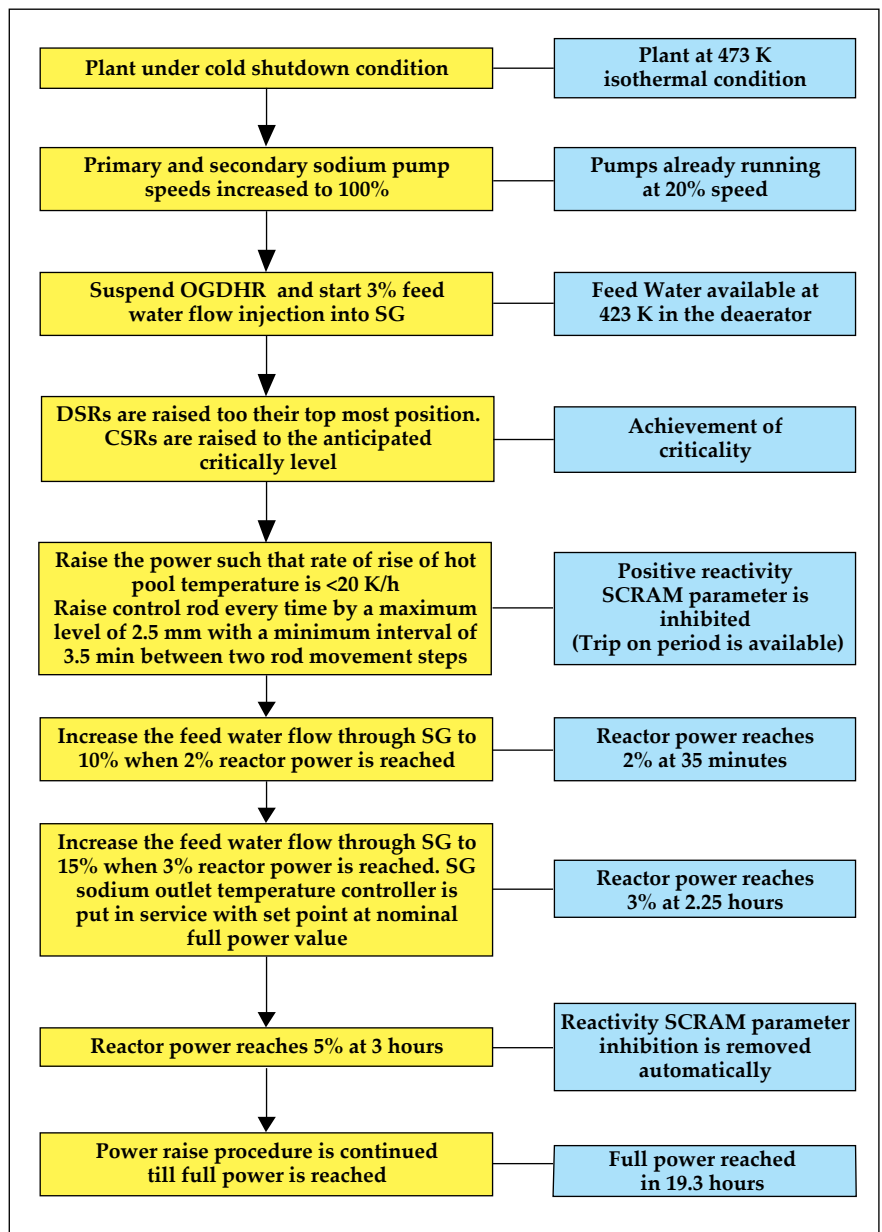

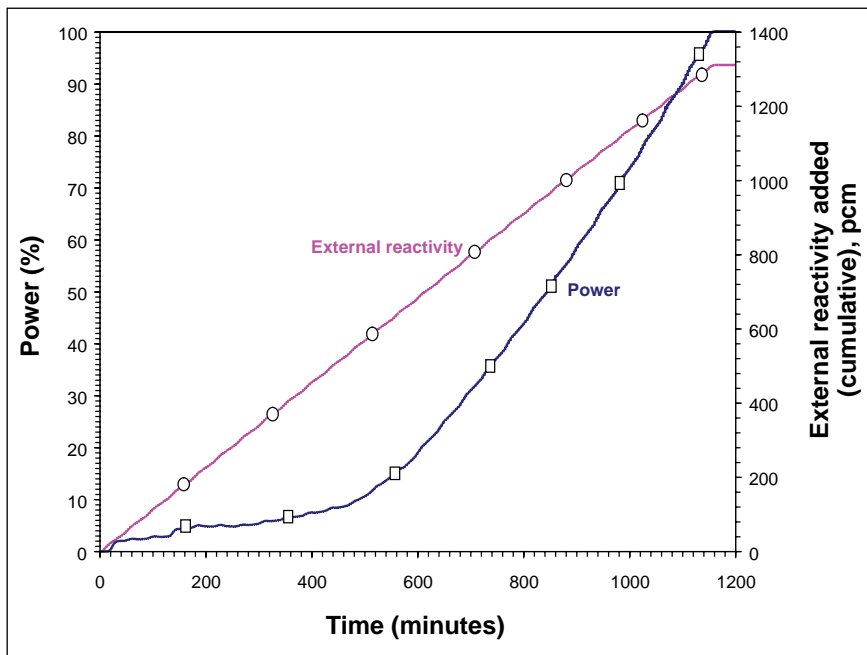**Fig. 1**   *Start-up procedure for PFBR*

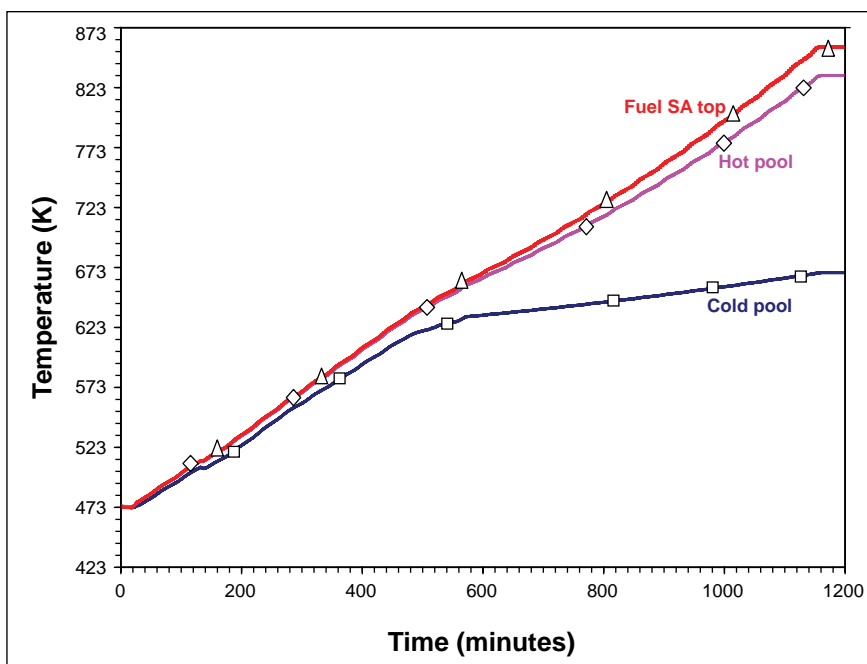**Fig. 2** *Evolution of reactor power and external reactivity added*

Fig. 3 *Evolution of primary circuit temperatures*

scheme respects the constraints of thermomechanical loading on the structure and simple/minimum operator actions. Various possible enveloping design basis events during the start-up procedure have also been investigated and availability of sufficient plant protection has been ensured.

During the initial period of start-up, since the feed back reactivity does not respond quickly with the external reactivity, total reactivity increases up to 22 pcm. However, this will not interfere with the start-up procedure as reactivity trip parameter is inhibited up to 5% power. The reactor period at this time decreases to a minimum of 138 seconds only which is away from the alarm threshold of twenty seconds. Total external reactivity added during power raising to full power is 1310 pcm. The maximum value of total reactivity reached after the initial peak is 3.5 pcm only. Evolutions of reactor power and temperatures of primary circuit are shown in Figures 2 and 3 respectively. The overall rate of rise of hot pool temperatures achieved is 18 K/h. Turbine rolling will be possible when the reactor power reaches 31%. Temperature gradients on various components are also acceptable from structural integrity point of view.

II.3   Fuel Handling Start-up System

In PFBR, before starting the fuel handling operations, certain plant system conditions are to be checked. VME based fault tolerant fuel handling startup (FSU) system checks these conditions and gives authorisation outputs to control logics of Small Rotating Plug/Large Rotating Plug (SRP/LRP), Inclined Fuel Transfer Machine (IFTM) and Transfer Arm to start fuel handling operations. FSU system is classified as safety class 2 (SC2) system and this system has been configured using dual redundant

Real Time Computer (RTC) system with Switch Over Logic System (SOLS). Architecture of FSU system is shown in Figure 1.

Hardware configuration

Each Real Time Computer system consists of VME bus based 68020 CPU card, Digital Input (DI) cards and Relay output cards. SOLS consists of Switch Over Logic Card (SOLC) and ORing logic cards. Various plant system conditions and inhibition inputs (for each condition) are connected to both the Real Time Computer systems. Both the Real Time Computer systems scan the physical inputs, receive soft inputs from Process Computer (PC) of Distributed Digital Control System (DDCS) using TCP/IP protocol, check the conditions and generate authorisation outputs and soft outputs. Real Time Computer system does all these functions in one second interval. Physical outputs from Real Time Computer systems are connected to ORing logic card of SOLS. Both the Real Time Computer systems check the healthiness of all the cards present in the system and generate healthiness output to SOLC. If both the Real Time Computer systems are healthy, then SOLC routes RTC1 outputs to plant. If RTC1 fails, then RTC2 outputs are routed to the plant. If both the Real Time Computer system fail then fail safe outputs are routed to the plant.

Software development & testing

Fuel handling startup software was developed using well defined software development methodology. Waterfall model was selected for software development, because of its simplicity, ease of Verification & Validation (V&V) and tracking & control on deliverables across life cycle. AERB safety guide SG/D-25 was followed in all phases of software development.
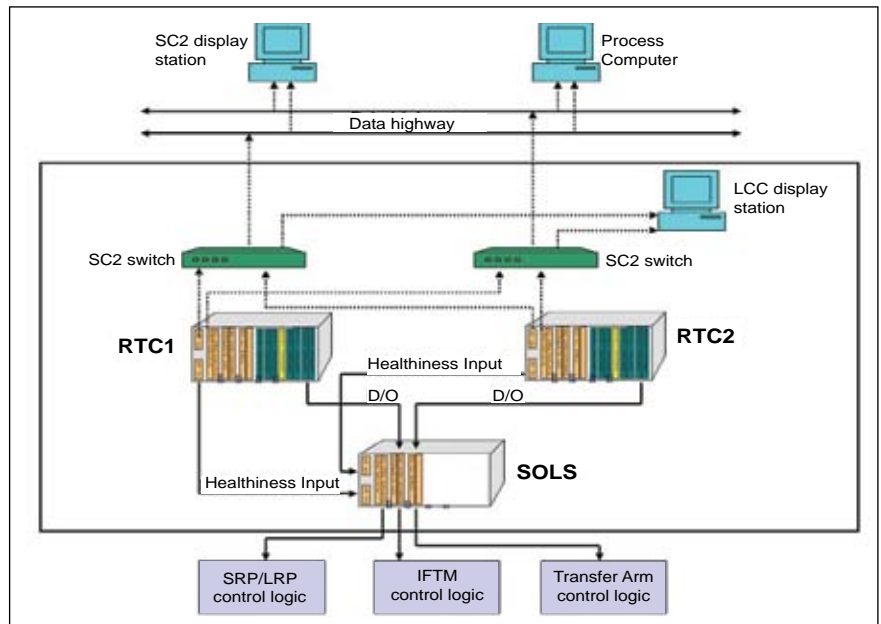

Fig. 1 *Architecture of fuel handling start-up system*

Computer Aided Software Engineering (CASE) tools were extensively used at various phases.

Software was developed in C language using tasking C cross compiler for 68K family of processors and fused into EPROM of both the CPU cards. 'C' Programming guidelines given by NPCIL were strictly followed. Developed code was checked for Motor Industries Software Reliability Association (MISRA) 'C' compliance using LDRA tool. This tool was also used to generate various software metrics (cyclomatic complexity, Halstead metrics etc. shown in Figure 2) and software quality aspects like maintainability, testability and analysability. Startup system software was thoroughly tested by simulating field inputs. Hard wired inputs were connected to DI cards of both the Real Time Computer systems and soft inputs were received from Personal Computer. Complete functionality of the system was successfully tested at laboratory.
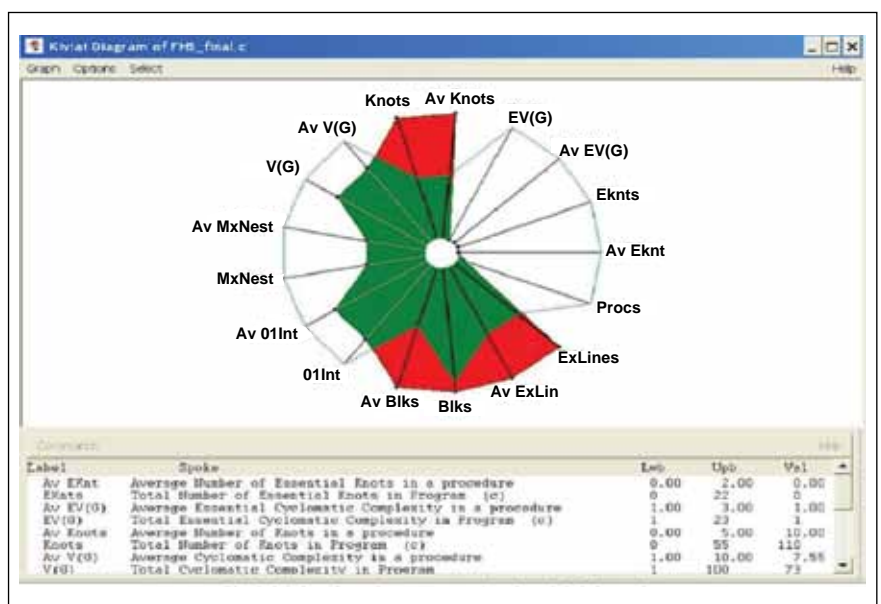

Fig. 2 *Kiviat graph generated using LDRA tool*

II.4   PFBR Operator Training Simulator

A Full Scope Replica Type Training Simulator is being developed at Computer Division, in collaboration with the Reactor Engineering Group. The main objective is to provide comprehensive training on all reactor subsystems under various plant conditions and enhance the capability of the plant operators. The PFBR operator training simulator is a training tool designed to replicate the steady state and dynamic response of the plant to operator actions and incidents. It incorporates all the features that allow the operator to be trained for normal and abnormal plant conditions covering the full spectrum of reactor operation, including plant transient conditions and design basis events under various categories. One of the most important developments in Nuclear Power Plant training methodology is the inclusion of Full Scope Replica Simulators in the training programme. It is an AERB guideline that the operators shall be trained and qualified before operating the main plant.

Development of PFBR Operator Training Simulator follows the ANSI standard ANSI-3.5-1998 for operator training and examination, IAEA – TECDOC – 995 and IAEA – TECDOC – 1411. These standards establish criteria for the degree of simulation, performance, and functional capability of the instrumentation and controls of the simulated control room. It consists of mathematical models representing various subsystems that are executed in real time and in right sequence. The simulator is designed to replicate the steady state and dynamic responses of the plant. The operator carries out plant operations on the simulator and looks for responses as they would occur in the real plant.

The physical components of the Hardware include Simulation Computers, Control Panels, Operator Information Consoles, I/O systems, Instructor Station, Simulation Network, and Power Supply Distribution System as shown in Figure 1. Simulator software consists of three basic development tools for process, logic and virtual panel modeling. Further, the development of simulator models are classified into two broad categories i.e. Internal Model (Steam Water System and Electrical system) and External Model (indigenous development of code using FORTRAN/C language). The in-built simulator tool provides a template which integrates internal and external models using shared memory concept.

Development of PFBR Simulator includes modeling of various reactor subsystems like Neutronics, Primary and Secondary Sodium, Decay Heat Removal, Steam and Water, Electrical, Fuel Handling and Instrumentation & Control system in collaboration with various divisions of Reactor Engineering Group. The plant conditions that are essential for training the operators are included in the simulator development. The various plant operating conditions that are envisaged for modeling of the Simulator include, shut down of reactor, preparation for start up, reactor start up operation, Reactor Criticality (Hot, Cold and first Criticality), Power Rise Operation, Full / Partial Power Operation, Preparation for Fuel Handling Operation, Fuel Handling Operation, Reactor Trip under various conditions, Reactor Setback and Reactor Trip and subsequent start up. Simulation of Plant Dynamics including the transients, incidents and malfunctions such as failure/ tripping of components like pumps, valves, control systems etc are also being modeled.

Transient identification in nuclear power plant is often a very difficult task and may involve a great amount of perception, learning and reasoning by operators. During an abnormal event, the operator needs to monitor large amount of
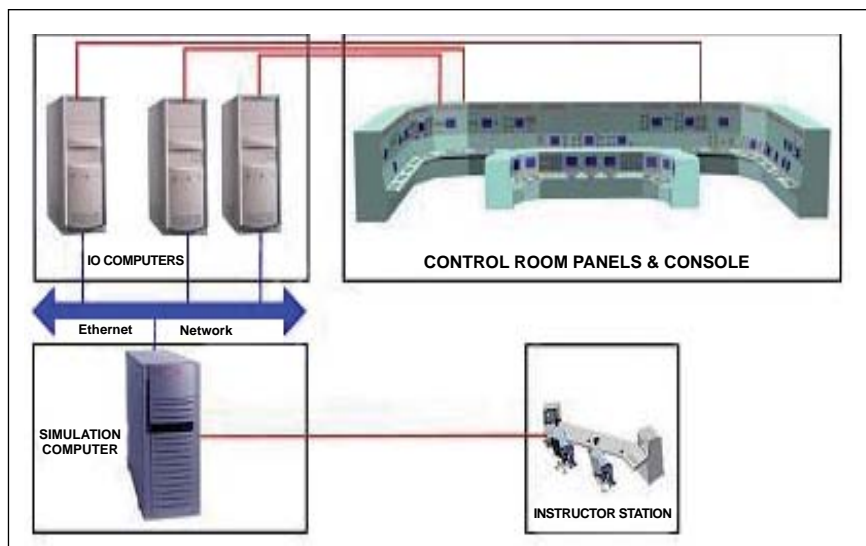

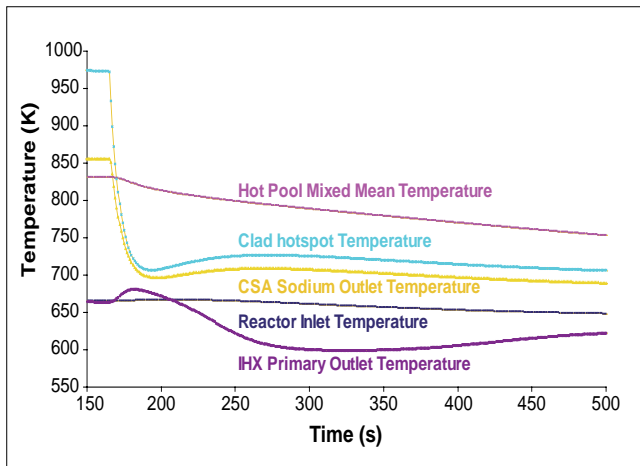*Fig. 1*   *Hardware architecture of PFBR operating training simulator*

Fig. 2 *Core temperature profile (one PSP trip at core and IHX primary outlet temperature)*
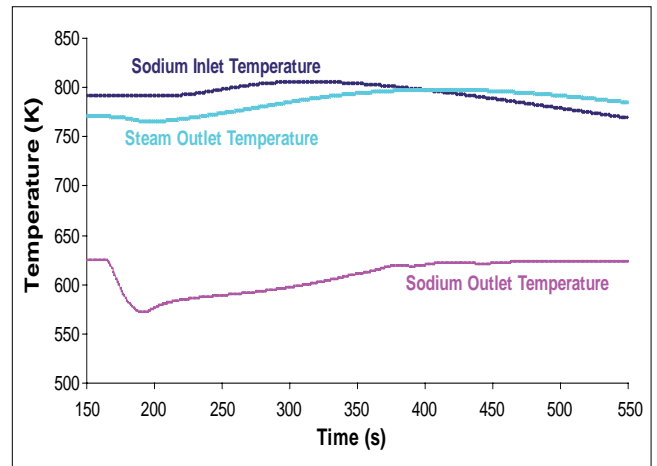

Fig. 3 *Temperature profile of steam generator (one PSP trip at SG - temperature)*

information connected to various reactor processes. The operator can diagnose malfunctions by observing and analysing the behavior of process variables such as pressure, temperature, level, flow etc. in the reactor subsystems. Training on plant dynamics during transient conditions provides better understanding and enhances the decision making capability of the operators.

The Benchmark Transients representing Design Basis Events of four categories (Cat-1, Cat-2, Cat-3 and Cat-4) starting from more frequently occurring incidents to less frequently occurring incidents are also being modeled under each subsystem. Incidents and events connected to each process are simulated and the plant operators are trained to handle any situation to safeguard the plant. The list of transients that are considered for

qualifying the simulator for training purpose include Continuous withdrawal of one control safety rod, One primary sodium pump trip, One primary sodium pump seizure, Primary pipe rupture, One secondary sodium pump trip, One boiler feed pump trip, Feed water flow increase events etc. The dynamic behaviour for one primary sodium pump trip event is depicted in Figures 2 and 3.

II.5 Fabrication and Erection of PFBR Top Shield Layout Model

PFBR, being a pool type reactor, the top shield supports all the components through respective support flanges. The major components include primary sodium pump (two numbers), intermediate heat exchangers (IHX – four numbers), decay heat exchangers (DHX- four numbers), cold pool and hot pool level detectors (two numbers), delayed neutron detectors (DND – eight numbers), control plug, in-vessel transfer machine (IFTM) and inclined fuel

transfer machine, periscope and under sodium ultrasonic scanner. Also, top shield is criss-crossed with cooling pipelines, number of other argon and sodium lines, complementary shields, power/control/instrumentation cables and associated trailing cable system.

The number of equipment and other pipelines makes the layout of components over the top shield very complex. Hence, an efficient and operable/maintainable layout

of equipment over top shield is very much essential for the successful and economical construction/commissioning/operation of the reactor. Towards this, a 1:1 scale layout model shown in Figure 1 was fabricated and erected.

The layout model was fabricated and erected on a common steel base structure (which represents reference elevation of 30000 mm in PFBR) at a height of two meter from the ground level. All the

components were fabricated with 3/5 mm thick sheets for shells and 10 mm thick plate for flanges with enough stiffeners within the model to maintain the integrity of the structures. The overall diameter of the model is twenty meter and the maximum height is twelve meter. All the components which are projecting above top shield (i.e., above reference elevation 30000 mm) were fabricated.

To facilitate rotation of the small rotatable plug and large rotatable plug (SRP & LRP) models, the same are innovatively supported at bottom over specially manufactured large diameter bearings (ϕ 2 & ϕ 3.5 m).

In order to manufacture this heavy structural Top Shield Layout Model assembly weighing 110 tons to optimise the utilisation of resources and to meet the targeted schedule, a micro level process planning was evolved and each stage was meticulously tracked to accomplish the targeted schedule. Components which need similar process and non succession manufacturing activities were grouped in four different stages to facilitate the fabrication activities namely, fabrication of structural supports for roof slab, reactor vault, fabrication of equipments, fabrication of cooling systems and fabrication of platforms for reactor vault and roof slab. The components were fabricated in accordance with IS 7215 Group-C standard/Drawing requirements, integrated, transported, erected and tested at Top Shield Layout Model site.

Layout marking on the concrete industrial floor base (ϕ 20 m) to position columns (135 numbers) for Reactor Shield and Reactor Vault with respect to reactor center axis was critically carried out in-situ and achieved the tolerance within

Fig. 1   *PFBR top shield layout model (scale 1:1)*

±1.0 mm. Forty two tonnes of structural support members like beams and columns were fabricated to the drawing dimensions with suitable end configuration to connect interconnecting beams (387 numbers). Fabrication of thin walled slender 1:1 scale models to design requirement was a highly challenging task, the models of intermediate heat exchanger, decay heat exchanger, in-vessel transfer machine, transfer arm, sodium pump, delayed neutron detector, valve station, argon storage tank, large rotatable plug and small rotatable plug measuring unit were successfully manufactured adopting innovative fabrication techniques.

Top Shield Layout Model assembly comprises thirty two numbers of pipe spools with multiple plane pipe bends. A unique layout was drawn for each pipe spool and fabricated in line with the design requirements. During welding of pipe spool, segment welding, controlled heat input and subsequent cooling techniques were adopted to control distortion in pipe spools.

Due to non-availability of standard size single piece raw material plates to machine large rotatable plug bearing ring of O.D 3.6 m x ID 3.4 m x 40 mm height and SRP

bearing ring 10 of OD 2.1 m x ID 1.9m x 40 mm height, the rings were fabricated from the circular plate segments and welded together. Further, fabricated rings were subjected to post weld stress reliving heat treatment. It was a challenging task to machine two critical areas in the bearing rings. Machining two rectangular cross section grooves of width 12.5 mm and 4.5 mm depth with 20 micron tolerance in circumference on the tapered bearing ring surface, the other was machining the hardened bearing strips of 45 HRC with 0.8 μm surface finish. It demanded the expertise in turning operation and was successfully machined using heavy duty vertical turret lathe and optimum machining parameters. Eight numbers of spur gears of varying pitch circle diameter from 90 to 540 mm using IS 1570 C40 material were precisely machined for small rotatable plug and large rotatable plug drive using gear hobbing process as per quality class BIS 3681. Gears were hardened and tempered to 45 HRC.

The prefabricated columns, inter connecting beams, equipments and platforms were transported and erected at Top Shield Layout Model site accurately at various levels from ground to 34500 mm height

using 10T and 40T capacity cranes. The height and verticality of each column and level of platforms were checked using optical instruments to ensure the uniform distribution of equipments load to structural supports. Large rotatable plug and small rotatable plug bearings were positioned accurately and tested to ensure the smooth rotation and designed RPM. The reactor centre axis was transferred from the base to 30000 mm platform level and layout marking was done accurately within ±1.0 mm to position the various Top Shield Layout Model equipments. Transporting the slender and heavy Top Shield Layout Model equipments from CWD to Top Shield Layout Model site and erecting the equipments at various high elevations was a challenging task and demands meticulous planning and safety precautions to be followed and it was successfully completed. All the slender and heavy Top Shield Layout Model equipments, pipe spools, trailing cable systems, electronic signal processing modules were erected, aligned and checked with respect to reactor centre axis and found the systems working satisfactorily.

II.6 Development of Cryogenic Cover Gas Purification System for PFBR

In the rare event of fuel pin failure in PFBR, fission gases released will get mixed with argon cover gas, above the sodium surface. This may lead to radioactivity leakage into reactor containment building (RCB) and through the stack. In accordance with the principle of ALATA (as low as technically achievable), it is necessary to remove radioactive fission gases from the cover gas.

Activated charcoal is used for adsorbing the fission gases. Dynamic adsorption coefficient (DAC) of activated charcoal is higher at cryogenic temperature than at ambient temperature. A pilot Cover Gas Purification System (CGPS) was set up (Figure 1) to study the different operating parameters.

Experiments at various temperatures from ambient (303 K) to cryogenic (130 K) were conducted in CGPS pilot plant. The system consists of gaseous argon tank, diaphragm compressor (DC), exchanger-economiser, liquid nitrogen bath, adsorption column with activated charcoal, sample injection facility and online gas chromatograph (OLGC). The liquid nitrogen refrigerant is used to cool the recirculating argon, which in turn cools the adsorber bed.

The required temperature in adsorber bed was achieved by maintaining the pressure level in liquid nitrogen bath and the required flow rate by throttling a DC by-pass valve. Then argon containing 1% xenon was injected into the main flow of argon. Online gas chromatograph was used to monitor the xenon concentration at the outlet of the adsorption column bed. Once xenon was detected at the outlet, the re-circulation mode was changed to once through mode to remove xenon from the system. To conserve the argon carrier gas, remnant xenon was flushed out by

Fig. 1 *Cover gas purification system pilot plant*

nitrogen gas, after the temperature of the bed was raised to ambient by removing the liquid nitrogen. The bed and other systems were then purged using argon to ensure that all the nitrogen was replaced and the plant was kept ready for the next experiment.

Experiments were carried out from ambient temperature to 130 K to determine the dynamic adsorption coefficient of indigenous activated charcoal. This data was used to compute the amount of charcoal required to obtain a decontamination factor of 10^4 (Figure 2). This Figure also shows the charcoal amounts required as computed by extrapolating the laboratory scale experiments between 258 K and 313 K conducted earlier. The dynamic adsorption coefficient values obtained in both experiments, at near ambient temperatures, agree within experimental error. However, predicted dynamic adsorption coefficient values in the temperature range from 258 K to 110 K, using limited laboratory data, was significantly higher than the experimental values obtained in the pilot plant. Operation of the
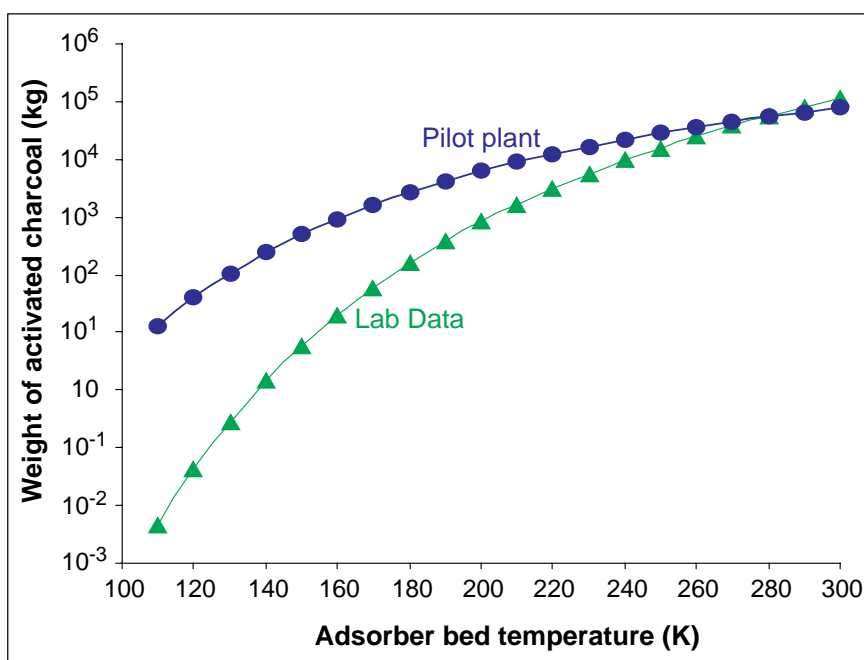

Fig. 2 *Weight of activated charcoal required for PFBR as a function of temperature*

cryogenic pilot plant generated the requisite experience with respect to the following :

a) Maintaining the adsorber at constant cryogenic temperature.

b) Mitigating the effects of unusual occurrences in a cryo-system.

c) Improved method of cryogenic temperature measurement.

d) Avoidance of icing over cold lines and equipments.

e) Confidence in safe handling and transfer of bulk cryogenic fluid in plant conditions and at higher pressures.

f) Trouble shooting and maintaining a diaphragm compressor in continuous operation.

Based on the above data, design of the PFBR adsorber bed was carried out. With the pilot plant experience gained specifications of the PFBR CGPS was improved.

II.7 Thermal Hydraulic Investigation of Deviations in Core Temperature Monitoring due to Flow Dilution Effects

During the operation of Liquid metal cooled Fast breeder reactors subassembly outlet temperatures serve as important indicators of reactor health levels. By ensuring safe reactor operation they contribute towards preservation of adequate safety levels. Control plug (CP) of the PFBR holds a system of core monitoring thermocouples. This system plays the role of measurement of outlet temperatures of individual subassemblies. Thus it is imperative for these thermocouples to detect and return accurate temperature readings of subassembly outlet temperatures. As this system is playing such a crucial part in the day to day decision making process during reactor operation, estimation of system capabilities becomes

important. This is important not only from the perspective of safety but also for prevention of spurious shut down and in turn ensuring smooth reactor operation.

A total of two hundred and ten subassemblies (180 fuel subassemblies and 30 blanket subassemblies) have monitoring thermocouples (enclosed in thermowells). After a vertical exit from the subassembly top positioned directly beneath the Control Plug, hot sodium faces its first obstacle in that direction. In the form of a horizontal porous plate placed 475 mm above subassembly top, the lattice plate, has a porosity of 60%. Subsequently, it enters a cylindrical cavity enclosed at the top and bottom by the core cover plate (CCP) and lattice plate respectively. The core cover plate which is a solid plate is located at a distance of 1260 mm from the subassembly top. Another cylindrical shell, the porous skirt with a porosity of 10%, completes the cavity by forming its lateral walls. The thermowells holding the thermocouples are supported on core cover plate and guided by lattice plate. The flow which is vertical when coming out of the subassembly develops a strong horizontal component after it exits the cylindrical cavity, either below or through the porous skirt, with the former mode dominating. These directional changes in velocity of hot sodium emanating from various subassemblies are non uniform and depend on the relative positions of the subassembly themselves. Thus, this whole setup leads to a phenomenon called flow flowering. This occurrence in turn gives birth to the problem investigated i.e. spatial dilution of subassembly outlet flow leading to temperature masking at thermocouples positions. Thus
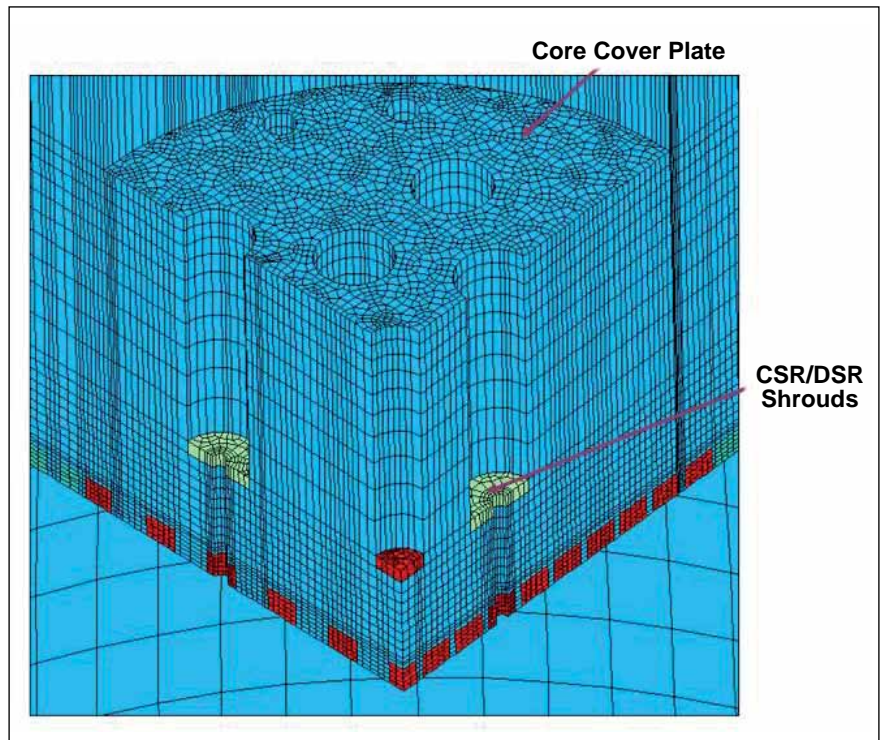

Fig. 1 *Figure showing the meshed model used for CFD studies (below control plug region)*

the temperature registered by a thermocouples will deviate from actual subassembly outlet temperatures.

For accurate temperature measurement, the tips of thermocouples should be as close to the subassembly top as possible. From previous 2-D Computational Fluid Dynamics studies, to ensure accuracy a radial shift of 20 mm from subassembly centerline positions was recommended for thermocouples positions. However, this configuration could only be partially realised owing to certain positional constraints viz. under-sodium inspection system for refueling (all subassemblies), interference from CSR/DSR shrouds and in core neutron detectors (36 subassemblies).
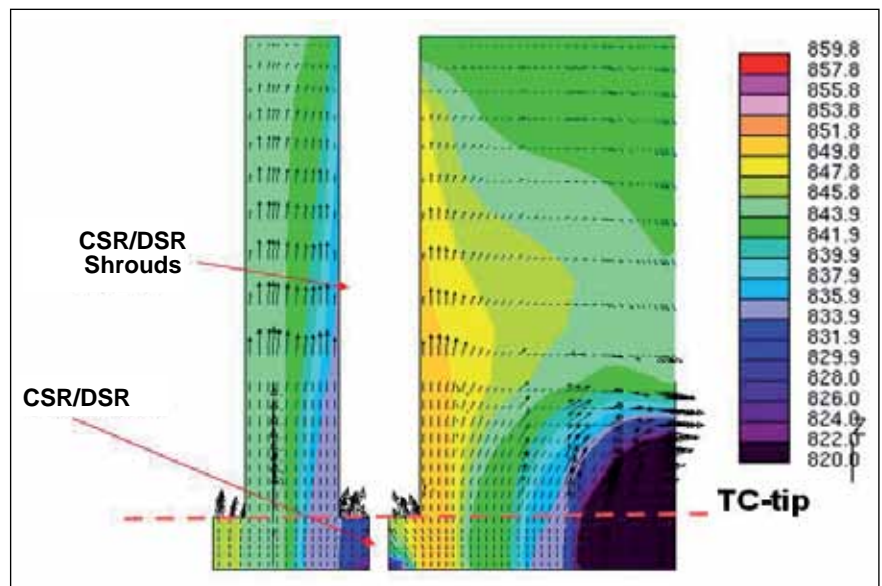

Fig. 2 *Temperature (K) distribution below the control plug at θ = 0°*

As a part of this investigation 3-D flow and temperature distributions below the core cover plate have been predicted for full power conditions of the reactor. The focus of the study is to investigate flow dilution and resulting deviations in the core monitoring thermocouple readings. The study considers positional variations of the thermocouples with respect to the subassembly due to erection tolerances and subassembly bowing. Studies have been carried out for fresh as well as irradiated core (100 MWd/kg). Monitored subassembly and absorber rod shrouds have been physically modeled to understand the effect of shrouds and control subassembly sodium flow on the thermocouple readings. The model used is shown in Figure 1. All studies are carried out using commercial CFD codes. These codes are based on control volume formulations, employed to obtain discretised conservation equations of mass, momentum and energy. For simulation of effects of turbulence K-ε high Reynolds number model is used with standard coefficients. Whole domain is discretised using hexahedral elements and relevant formulation is used. Buoyancy effects are simulated by means of Boussinesq approximation. Temperature and
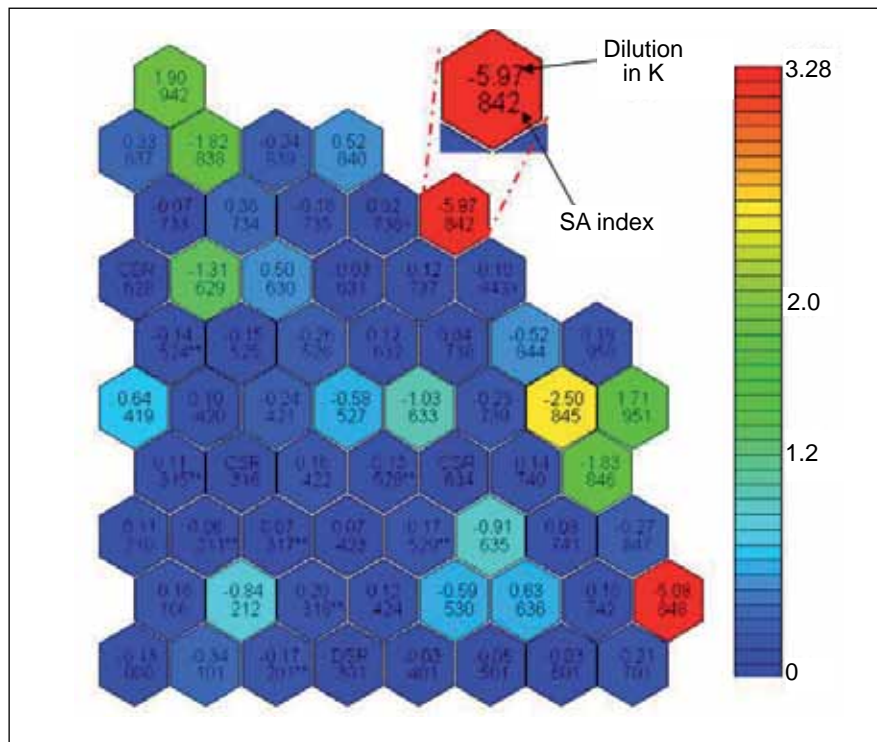

Fig. 3 *Temperature dilution levels of subassemblies*

velocity distribution below the control plug is shown in Figure 2. Figure 3 shows temperature dilution values of monitored subassemblies. From the studies it is found that the cold sodium from CSR/DSR subassembly does not influence the thermocouple readings of the neighboring subassembly. The readings of the thermocouples which are not shifted due to their proximity to CSR/DSR shrouds would be diluted to a maximum of approx. two degree at the end of irradiation campaign, while the dilution in the fresh core is much less (0.5 K). Also the maximum dilution in the thermocouples readings of fuel subassembly is 2.5 K. Due to the initial radial shift of 20 mm in thermocouples position, dilution generally reduces with burnup. Thermocouple corresponding to blanket subassembly are able to read their temperature with a maximum dilution of eight degree.

II.8   Investigation on the Effect of Interwrapper Flow on Safety Grade Decay Heat Removal in SAMRAT Model

Safety grade decay heat removal (SGDHR) system is provided to remove the decay heat from the core, when normal heat transport paths are not available, to limit the core temperatures within the acceptable limits. During SGDHR operation, the cold sodium from the outlet of decay heat exchangers (DHX) penetrates into the inter wrapper space (IWS) of subassemblies,

which enhances heat removal. An accurate evaluation of core thermal hydraulics is important to enhance passive safety features of PFBR by safety grade decay heat removal. An assessment of the effect of the inter wrapper space on decay heat removal was carried out by conducting thermal studies using water as a simulant.

Studies were conducted in the 1:4 scale SAMRAT model of PFBR to demonstrate the core coolability by natural circulation in the primary pool and the inter wrapper space. Mainly the temperature and flow pattern in hot pool was studied under different operating conditions to validate numerical code. Richardson number (Ri), which is the ratio of buoyancy and inertial forces was simulated for these experiments. Decay heat generation during the safety grade decay heat removal condition is taken as 2% of the full power. Accordingly, the corresponding decay heat for the experimental studies was estimated as 60 kW based on Ri number simulation. Decay heat generated in the core is simulated with the help of heaters provided inside the model. Heat removal by decay heat exchangers was achieved by forced circulation in the secondary side of the decay heat exchangers.

Temperatures were measured in hot pool, core outlet and inter wrapper spaces using thermocouples. Four experiments were carried out with different configuration (Case 1 to 4) to understand core cooling. In Case 1, IHX flow path (Path–A in Figure 1) was made unavailable by blocking IHX inlet window. The storage and blanket subassembly outlets were also blocked to avoid reverse flow circulation from hot pool (Path-B). In Case 2, storage and blanket subassembly outlet blockings were removed to make
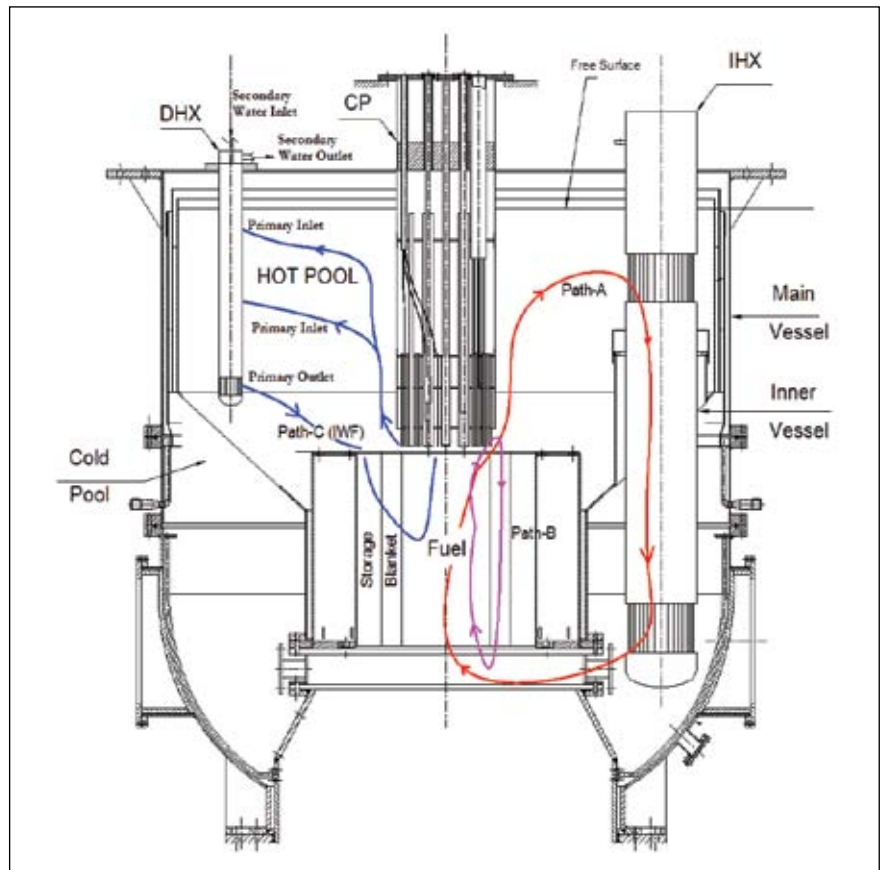
Fig. 1 *Natural convection flow paths during decay heat removal in the pool*

reverse flow through blanket subassembly Path-B was available for heat removal. In Case 3, all the flow paths were available to simulate the normal condition. In Case 4, only blanket and storage

subassembly outlets were blocked, to avoid reverse flow through these subassemblies from hot pool.

Steady state hot pool temperatures, across the hot pool, when all DHX

Fig. 2 *Temperature profile of the hot pool*

are operating are shown in the Figure 2. Steady state temperature is lowest in Case 3 and highest in Case 1. Steady state temperature was higher in Case 4 than in Case 2, which shows that heat removal by reverse flow through blanket and storage is more dominant than heat removal by primary flow path. Similar observations were made during transient studies. Spatial distribution of steady state temperature gradients varies acr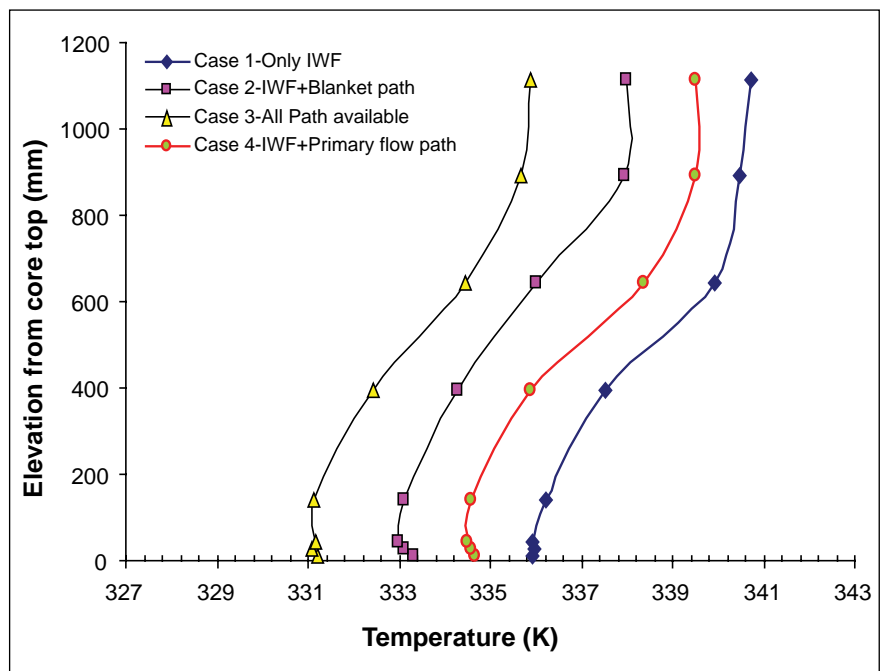oss IWS inside the core. The increase in IWS temperature gradient with the availability of only inter wrapper space path (Case 1) suggests that the heat transfer by inter wrapper space is comparable with normal heat removal paths. Comparative studies of different configuration have revealed that inter wrapper space is effective as heat transport path and reverse flow though blanket and storage subassembly also contributes towards core cooling.

II.9 Commissioning of Safety Grade Decay Heat Removal System in SADHANA Loop

To study the thermal hydraulic behaviour of Safety Grade Decay Heat Removal (SGDHR) system of PFBR, a 1:22 scaled down model called SADHANA loop (Figure 1) was set-up. The capacity of SADHANA loop is 355 kW. Height difference between the thermal centers of decay heat exchanger and sodium to air heat exchanger is 19.5 meters. Sodium in test vessel 4 (TV 4), which simulates the hot pool of PFBR is heated by electrical heaters. This heat is transferred to the secondary sodium through decay heat exchanger. The secondary sodium gets circulated in the secondary loop by the buoyancy head developed in the loop due to the temperature difference in hot and cold legs. The heat from secondary sodium circuit is rejected to the atmosphere through the air heat exchanger. A twenty meter high chimney develops the air flow required to transfer the heat from secondary sodium to the atmosphere. The scaling down of PFBR – SGDHR secondary sodium loop to SADHANA secondary sodium loop was done by Richardson number similitude. SADHANA loop consists of a vertically mounted vessel TV-4, which houses the model decay heat exchanger, electrical heaters of 600 kW capacity and sodium instrumentation. Different sodium pool temperatures can be achieved by controlling the heat input to the sodium pool.

Sodium to sodium decay heat exchange in SADHANA is similar to the type-A decay heat exchanger of PFBR SGDHR system. Air heat exchanger is a four pass heat exchanger of capacity 355 kW (Figure 2). The scaling down of this equipment is in terms of number and length of tubes in the sodium to air heat exchanger. This will simulate the air side heat transfer characteristics of air heat exchanger.
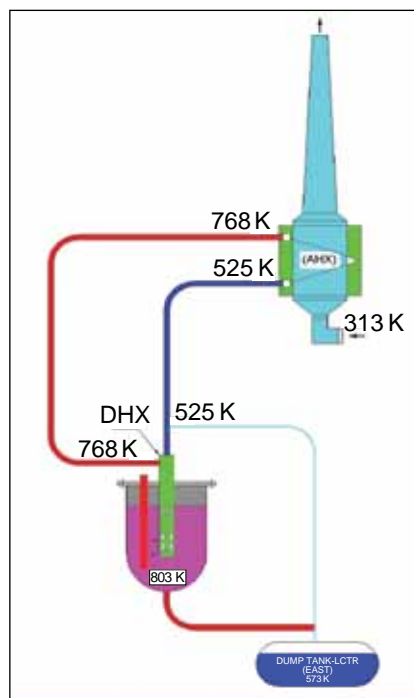

Fig. 1 *Schematic of SADHANA*

Fig. 2 *Air heat exchanger in the side plate opened condition*

SADHANA was commissioned by filling sodium in the primary and secondary circuits and circulated by means of an EM pump at isothermal condition of 573 K. Both air heat exchanger inlet and outlet dampers were functioning as desired. During the commissioning campaign the sodium pool temperature raised gradually to 743 K. A sodium flow of 6.31 m³/h was established in the secondary system with hot and cold leg temperatures of 708 and 518 K respectively. Air flow of 9150 m³/h was established in the chimney with outlet temperature of 561 K. The thermal power transferred was 378 kW. Detailed thermal hydraulic experiments are underway using this system.

II.10   Sodium Freezing Studies in 400 NB Horizontal Pipe

Butterfly type isolation valves are provided at the inlet and outlet of steam generator modules in order to isolate the faulty one in PFBR. This isolation allows uninterrupted reactor operation with the other steam generator modules. In order to attain perfect leak tightness of the valve it is necessary to freeze sodium upstream / downstream of the valve. An experiment was conducted to demonstrate the feasibility of formation of sodium plugs inside a butterfly valve body with provision of forced cooling arrangement around the valve body. Computational analysis was also carried out and validated with the experimental results. Finally, the validated computational technique will be used to evaluate the sodium freezing phenomena in the pipeline of PFBR steam generator inlet.

The experimental study of steam generator isolation valve was carried out in SILVERINA sodium loop. A cylindrical duct with 15 mm annular gap was provided over the valve body for cooling of sodium by air. Sodium was filled in the test setup and temperature was raised to 633 K. Surface heaters over the valve body were switched off and air was circulated and maintained at 35 m/s by a centrifugal blower. The air circulation was stopped once the temperatures of sodium at different locations in the valve were well below the freezing point of the sodium. After forty minutes, surface temperature reached the freezing point of sodium of 371 K. The forced cooling was continued up to 100 minutes to ensure temperature of the sodium in the valve to reach much below the freezing point. When the air flow was stopped it was observed that temperature rose, because of the heat transfer from sodium to the pipe. However, it reached a steady state temperature, which was below the freezing point.

Transient computational analysis was carried out using a 2-D axi-symmetric model in r-z co-ordinates simulating the vertical section of the upper half of the
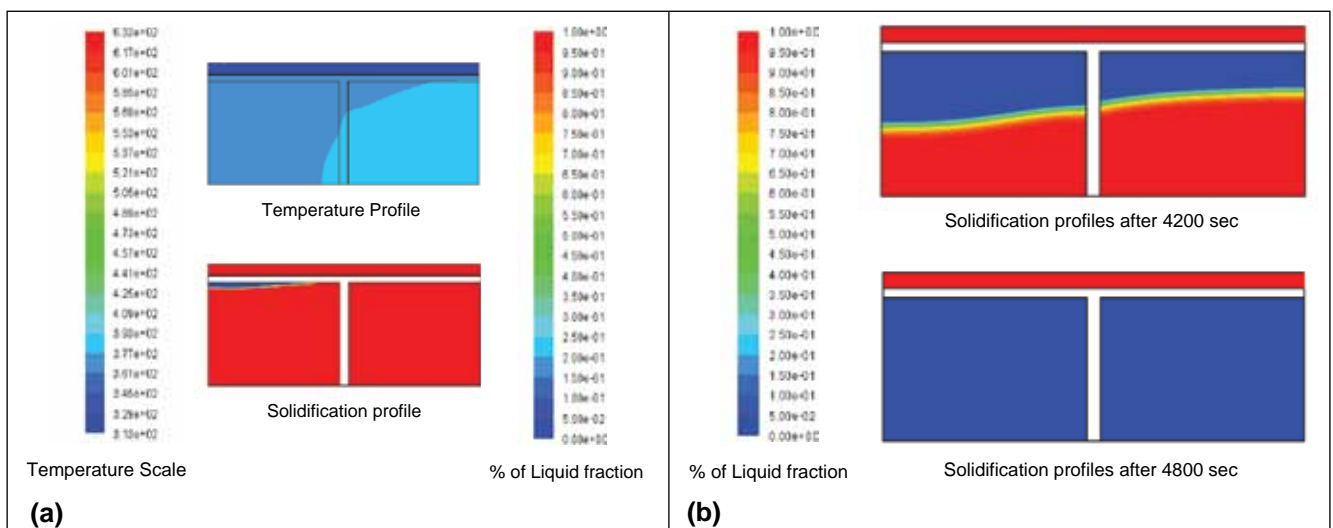

Fig. 1 *(a) Temperature and solidification profiles (when freezing just started) and (b) Intermediate solidification profiles*

pipeline with the valve body. A horizontal pipe and an air duct with 15 mm annular gap between them were modeled. Constant mass flow rate of air was set as the inlet boundary condition. The other boundary conditions considered for the air duct were pressure at the duct outlet and adiabatic wall. The initial temperatures for sodium and air were set as 633 and 313 K respectively. To simulate the freezing phenomena, the solidification model was chosen. The analysis was first carried out for 100 minutes with a time step of 0.5 seconds. To simulate the blower switched off condition, further transient studies were carried out by setting the air inlet mass flow rate to zero. The result obtained at the end of the 100 minutes was considered as the initial boundary condition for the second phase of the study.
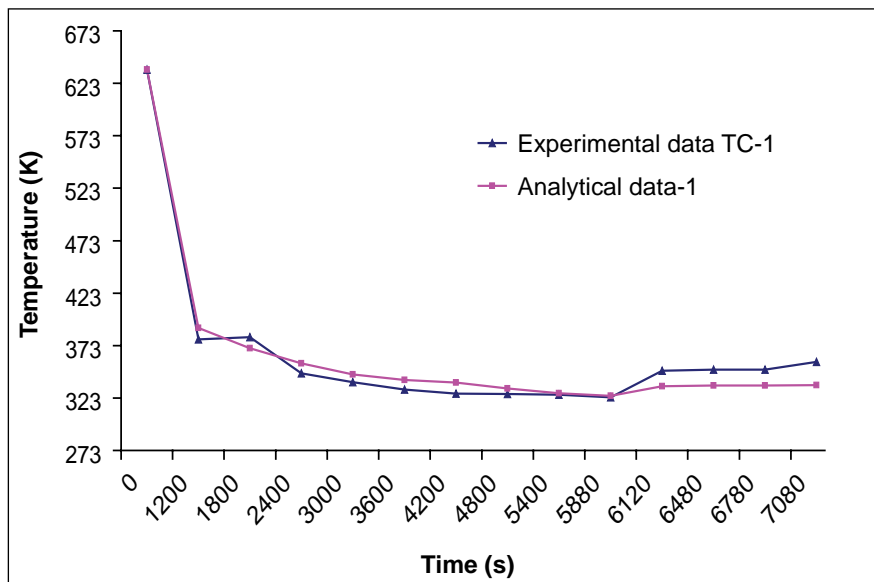
Figure 1 shows the temperature and solidification profiles at different intermediate states. Comparison of the analytical results with the experiment is the shown in Figure 2. It can be seen from figure that the trend and magnitude of temperature obtained are in fair agreement. It has been found from the analysis that total sodium can be frozen in 4800 sec (80 min) which is fairly in line with the experimental freezing time of 100 minutes.

Fig. 2 *Temperature profile of analytical data along with experimental data*
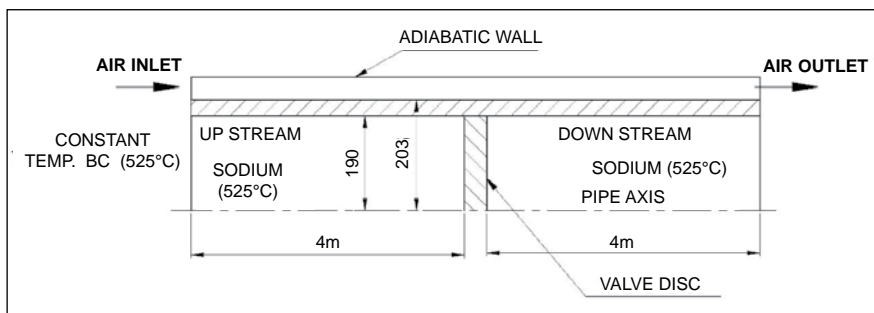
Fig. 3 *Model for simulation of PFBR condition*

To simulate the PFBR condition, analysis of un-insulated pipe along with the valve body was carried out using a 2D model. Whole pipe was assumed to be full of sodium with an initial temperature of 798 K. The geometry of the model along with the boundary condition is shown in Figure 3. In order to model continuous heat input, constant temperature boundary condition was applied at the end of upstream pipe. Transient study was carried out with a time step of 0.5 sec, keeping all other parameter same as in the previous case. Therefore, it can be concluded that with the provision of air cooling of un-insulated pipe, it is possible to form sodium plug at the downstream of the steam generator isolation valve.

II.11 Testing of Ultrasonic Under Sodium Scanner for PFBR in Simulated Conditions

Opacity of liquid sodium, used as coolant in Fast Breeder Reactors, restricts visual inspection of components immersed in it by optical means. Viewing of components under sodium is achieved by ultrasonic technique. An ultrasonic under sodium scanner (USUSS) was developed
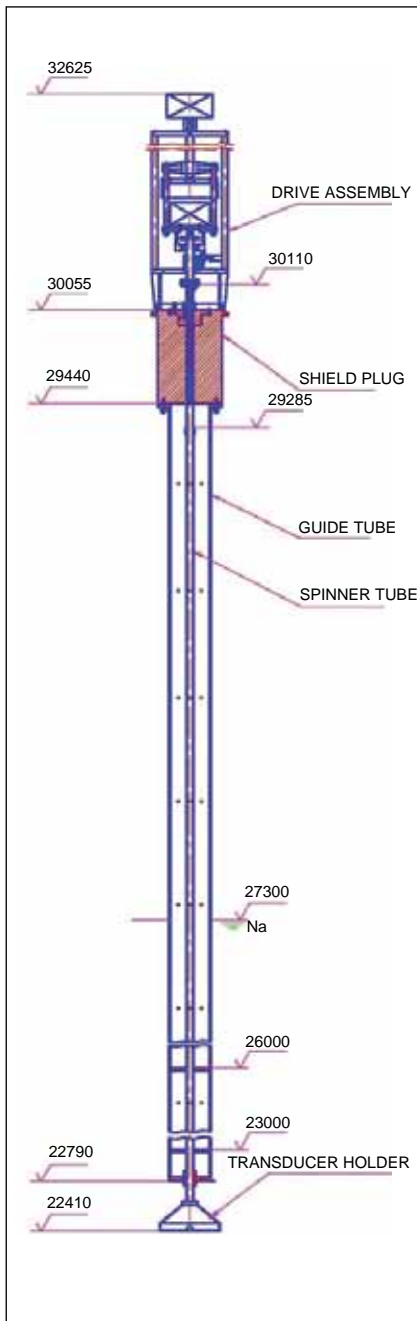
Fig. 1 *Ultrasonic under sodium scanner (USUSS)*

for PFBR to detect any fuel subassembly projecting from its original location, which may hinder the fuel handling operation and to locate the top head of some of the core assemblies to estimate bowing or growth.

The USUSS (Figure 1) consists of a stainless steel spinner tube having a conical transducer holder at its bottom. Four numbers of Downward Viewing Transducers (DVT) operating at a frequency of 5 MHz and four numbers of Side Viewing Transducers (SVT) operating at a frequency of 1 MHz are fixed to the transducer holder. These transducers are developed in-house and are capable of operating in liquid sodium upto 453 K. The spinner tube can be rotated 360° about its axis (θ motion) and can also move vertically (Z motion) over a distance of 150 mm. Separate AC Servo motors are provided for θ and Z motion.

The test facility for the scanner consists twenty seven numbers of subassembly heads (Figure 2). 19 numbers of subassembly Head simulate central subassembly, first and second rings of PFBR core subassemblies for down viewing. One of them is taller by 5 mm to simulate growth of subassembly.

Fig. 2 *Transducer holder with subassembly heads*

Remaining eight subassembly heads are located in the periphery with varying heights from 200 to 250 mm for side viewing. The scanner and test setup were erected in a test vessel for sodium testing at 443 K and the cover gas pressure of 0.1 kg/cm^2 to simulate reactor shutdown condition.

Core mapping experiments using DVTs were carried out by parking the scanner at various heights above the subassembly heads top viz. 100, 50 and 25 mm. The 3 mm flat surfaces at the top of the subassembly heads are used as the reflecting surfaces for ultrasound. The angle θ was also varied from
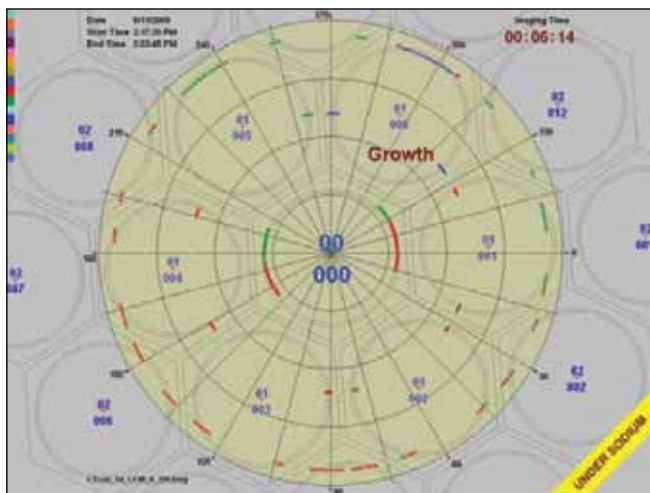
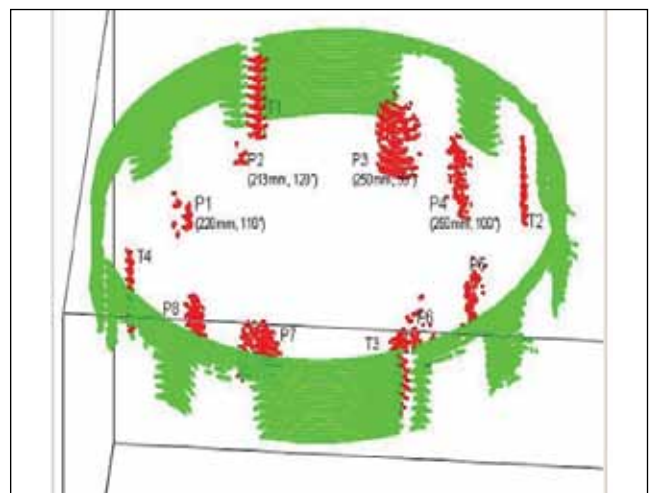

Fig. 3 *Depth based mapping using DVT*

Fig. 4 *Image of protruded subassemblies using SVT*

33

0° to 360 degrees in steps of 1°. The result of depth based mapping using DVTs is shown in Figure 3. Side scanning experiments to detect protrusion using SVTs were carried out by positioning the transducer holder initially at 10 mm above the top of subassembly heads. The scanning of the protruding subassembly Heads was carried out by moving the transducer holder 360° in steps of 1° in the theta axis and 100 mm in the Z-axis in steps of 5 mm. The 3D view of the image of the protruded subassembly heads and the tie rods are shown in Figure 4.

From the experiments it was concluded that, USUSS is able to detect the growth of 5 mm of subassembly heads in down viewing mode. In the side viewing mode, it is able to detect protruding subassembly heads, if they are favorably oriented Work is in progress to detect protruding subassembly heads, even if they are not favorably oriented from ultrasonic point of view. The integrated testing of mechanism, transducer, electronics, motor drives and automation using PC was successfully done in sodium to collect ultrasonic images. Further improvements will be carried out to make the Scanner reactor worthy.

II.12 Seismic, Drop and Topple Test Qualifications of Real Time Computer Systems

VME bus based Real Time Computer (RTC) systems have been developed for Instrumentation and Control of Safety Class 1 (IA), Safety Class 2 (IB) and Non-nuclear Safety (NNS) systems of PFBR. SC1 systems are configured with three identical RTC systems. The SC2 systems are configured with two identical RTC systems with Switch Over Logic System (SOLS). NNS systems are configured with stand alone RTC system. Performance of RTC systems were evaluated by Seismic, drop and topple tests as per IS 9000 standard. These tests are regarded as type tests.

The VME bus based RTC systems were subjected to seismic test for Operating Basis Earthquake (OBE) and Safe Shutdown Earthquake (SSE) as per the test procedure "PFBR/60000/SP/4020". The tests were carried out at Structural Mechanics laboratory in IGCAR. The seismic test setup is shown in Figure 1 and the context diagram of the seismic test system is shown in Figure 2. Test system comprises of two identical RTC systems, Switch Over Logic System (SOLS), associated power supplies and exhaust/cooling fan modules was mounted in a 48 U height cabinet. Each RTC system consists of VME
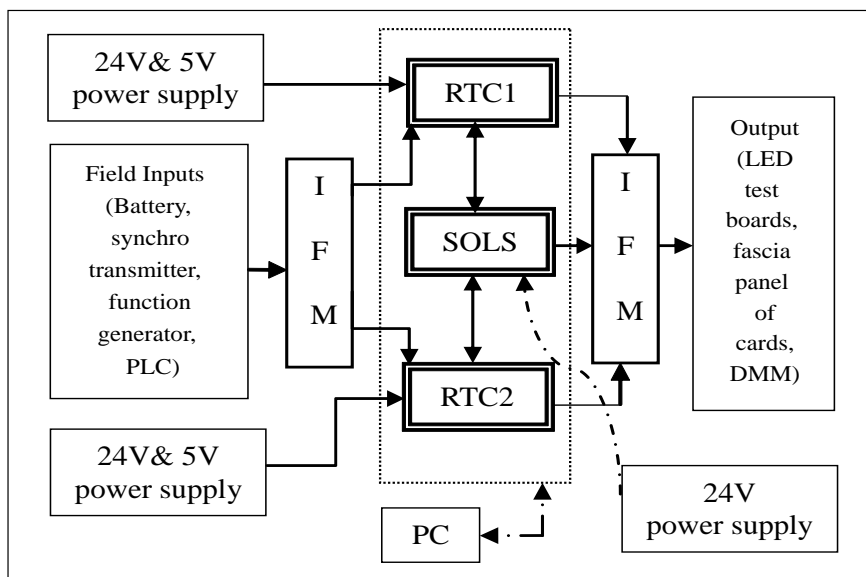

Fig. 1 *Seismic test setup*

Fig. 2 *Context diagram of seismic test system*

bus based CPU card and I/O cards (digital I/O, analog I/O, relay output, synchro to digital converter and counter timer) along with VME bus backplane and I/O backplane was mounted in a 19", 6U card frame. SOLS consists of Switch Over Logic Circuit card and ORing logic cards was mounted in a 19", 6U card frame. This test system is a representative configuration of the system which will be used in PFBR for safety class 2 applications.

The required field inputs were simulated using Programmable Logic Controller, synchro unit, set of batteries, function generator. Inputs from simulator were connected to respective input cards via interface modules (IFM), and outputs from cards were routed through ORing logic cards. The outputs were monitored using LED test boards, fascia panel of the I/O cards & digital multimeter. Software to check the functionalities of each card was written in 'C' language using Tasking 'C' cross compiler, fused into EPROM of CPU card. The test system was subjected to OBE & SSE tests under power-on condition. During each test, the system performance was monitored and logged. A post data analysis was carried out to find the performance of the system. It was found that the test system was performing within the design limits during the OBE and SSE tests.

Drop and topple test

The object of this drop and topple test is to assess the effects of knocks and jolts likely to occur during repair work or rough handling of the system in the field. The drop and topple test setup is shown in Figure 3 and the context diagram of the test system is shown in Figure 4. Test system consists of VME bus based CPU card, analog I/O card, digital I/O card, relay output card, Synchro to Digital converter (SDC) card and Counter Timer Card (CTC) card along with VME bus backplane and I/O backplane was mounted in a 19", 6U card frame.

This test included three distinct procedures

a. Dropping on to a face.

b. Dropping on to a corner.

c. Toppling (or push over).

The test platform consists of a steel plate of 6.5mm thick which has been wet floated on and bolted down to a fully set concrete block of 500 mm thick. The height of drop was selected as 100mm. Similar to seismic test, inputs were simulated and connected to respective input cards via interface modules, and outputs were monitored using
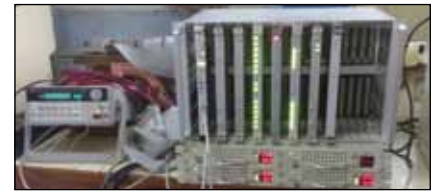
Fig. 3 *Drop and topple test setup*
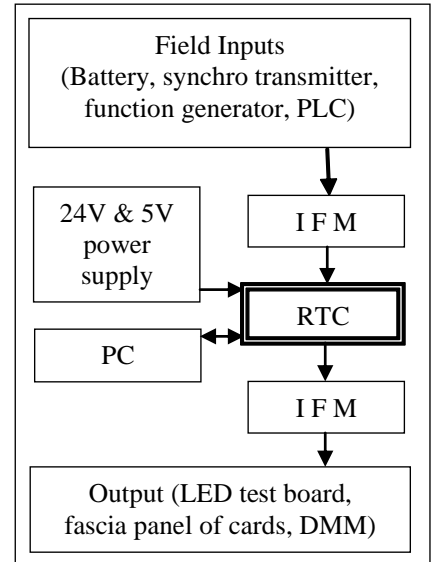
Fig. 4 *Context diagram of drop and topple test system*

LED test board, fascia panel of the I/O cards & digital multimeter. The software used is similar to the seismic test, but modified for the drop and topple test configuration. As per the test procedure "PFBR / 60000 / SP / 1013-IS 9000 part VII, Sec 3" the test system was dropped and toppled on the test platform under power off condition. The performance of the system was observed prior and after the test and the system was found working properly.

II.13 Central Sub-Assembly Temperature Monitoring System for PFBR

Core temperature monitoring is provided for detection of core anomalies like plugging of fuel sub-assemblies (FSA) in PFBR It is achieved by means of a computer based core temperature monitoring system. But, the power density of central subassembly (CSA) is 0.3 MWt, which is much larger than other fuel subassemblies (FSAs). So, it is essential to monitor the temperature of central subassembly at a faster rate, in order to detect transient over power and to prevent the clad hot spot and
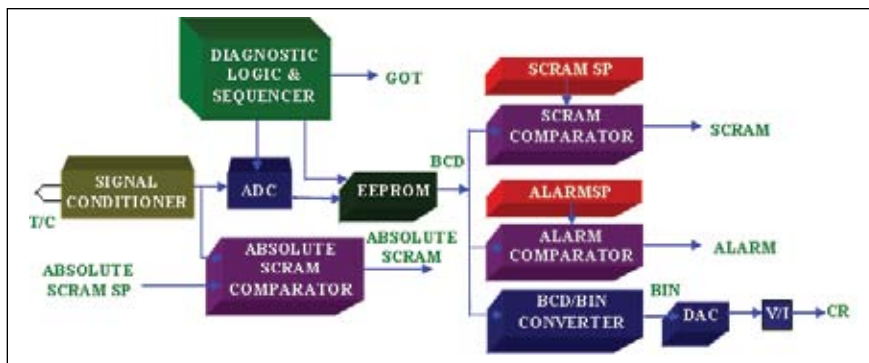
Fig. 1 *Block diagram of CSATM system*

fuel temperature from reaching the limits. Hence, central subassembly is provided with fast response K-Type thermocouples, which are in direct contact with sodium. A scaled, Central Subassembly Temperature Monitoring (CSATM) system, to monitor the temperature of central subassembly provided to generate, when the temperature exceeds the SCRAM limit. SCRAM output is connected to Shutdown System II. In order to achieve, a hardwired system developed with no microprocessor, thus avoiding software verification and validation. For triple modular redundancy, three CSATM systems are provided for three thermocouples with provision of connecting a spare thermocouple to any one of the systems. The measurement range is 273 - 1273 K with an accuracy of one degree kelvin and response time of 30 ms. Alarm and SCRAM set points are 278 K and 283 K above the nominal value respectively.

The block diagram of CSATM system is shown in Figure 1. It consists of a Signal Conditioner Module (SCM) located in the reactor containment building, Local Control Centre (LCC) and a System Module (SM) located in the control building LCC. SCM consists of pre-amplifier, isolation amplifier, second order filter, test circuit and cold junction compensation circuit. SM consists of ADC, look-up table for linearization, digital comparators, sequencing logic, diagnostics logic, DDCS connectivity and DAC for analog output for indication in control room. The system is provided with extensive testability.

II.14 Design and Development of Switch Over Logic System (SOLS)

The Switch Over Logic System plays a vital role in all Safety Class - 2 (SC-2) I&C systems like Reactor Start-up, Online Supervision of Reactor Shut Down, Fuel Handling Start-Up, Discordance Supervision & Alarm Generation System and Fault Tolerant Non-Nuclear Safety (FT-NNS) I&C systems like Primary Sodium, Secondary Sodium, Chilled Water and AC and Ventilation Systems of PFBR. The SC-2 & FT-NNS system architecture of PFBR as shown in Figure 1(a), consists of twin VME bus based Real Time Computer (RTC) systems that takes sensor signals from plant for its processing and generates control output signals for final control elements that is routed
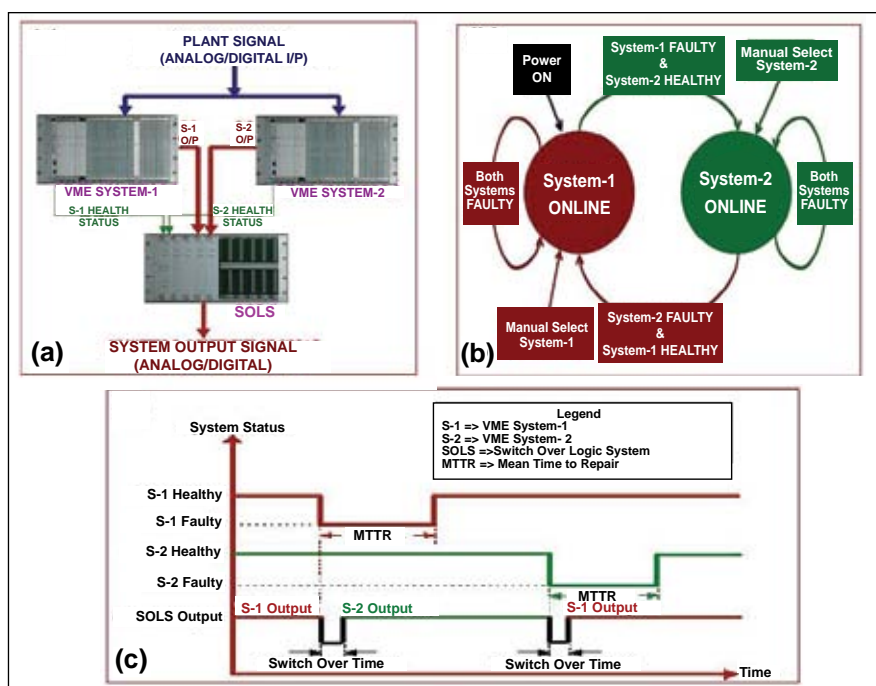

Fig. 1 *(a) SC-2 & FT-NNS I&C system architecture, (b) State transition and (c) Timing diagrams of SOLS*

through an independent monitoring system called Switch Over Logic System. The Switch Over Logic System checks the healthiness of both Real Time Computer systems and depending on Real Time Computer system's healthiness it permits to route healthy system's output to the plant.

SOLS overview

The Switch Over Logic System consists of one Switch Over Logic Circuit (SOLC) board with maximum of nine ORing Logic Circuit (OLC) boards depending on the system requirements, housed in 19" high 6U card frame sitting on both P1-Backplane and P2-Backplane as shown in Figure 2 meant for receiving output control signals from twin Real Time Computer systems and sending ORed output signal to the plant.

Salient features of SOLS

Switch over logic is implemented using highly reliable hermetically sealed latch and non-latch mechanical relays.

Switch Over Logic System receives health status from both Real Time Computer systems either in the form of potential free contact or Logic Level.

Switch over takes place in the event of online Real Time Computer system becomes faulty and standby Real Time Computer system remains healthy.

Fig. 2 *SOLC board, OLC board, P1 & P2-backplane*

When both Real Time Computer systems are faulty, the fail-safe output from last failed Real Time Computer system is routed to the plant.

On power ON, when both the Real Time Computer systems are healthy RTC-1 output is routed to the plant.

In the presence of both healthy Real Time Computer systems, provision is made for manual selection of any of the Real Time Computer system's output to be routed to the plant.

Provisions are made for local and remote indication of Online Status and Health Status of Real Time Computer systems and Power Supply Status of SOLS.

Each OLC card can route maximum of 15 channels output from RTC system.

Each channel can route either signals of Analog, Digital or Potential Free Contact.

Each contact is rated as 500mA @ 24Vdc (max) & 30µA @ 30mVdc (min).

Output switch over time is 22 mSec.

Switch over logic function

The switch over logic system can be represented by two different states as System-1 ONLINE and System-2 ONLINE enclosed in circles as shown in Figure 1(b). The online state of switch over logic system indicates the healthy Real Time Computer system's output being routed to the plant. The failure of online Real Time Computer system triggers the state of switch over logic system to transit from current online state to next online state provided the other Real Time Computer systems is in hot standby mode.

When both the Real Time Computer systems become faulty, the switch over logic system does not change its state and routes the fail safe output from the last online Real Time Computer system to the plant. Apart from that in the presence of both healthy Real Time Computer systems, manual selection of online status of switch over logic system can be done using local push button switches provided on the fascia panel of switch over logic card board. The associated timing diagram is shown in Figure 1 c.

Analysis of SOLS

The Switch Over Logic System is thoroughly analysed for its Reliability (as per MIL-HDBK-217F) FMECA (as per MIL-HDBK-338) De-rating, Switch Over Time and Power Consumption. It is estimated that one failure of Switch Over Logic System may occur in nearly thirty nine years of continuous operation in reactor environment.

Qualification test of SOLS

Switch Over Logic System has successfully qualified for the following tests:

Environmental Test conducted using in-house test facility

EMI/EMC Test conducted at SAMEER, Chennai

Seismic Test conducted at Structural Mechanics Laboratory, IGCAR

Transfer of technology

The design technology of Switch Over Logic System along with PCB fabrication details and supporting documents have been transferred to ECIL, Hyderabad for bulk production towards building various Safety Class-2 and FT-NNS systems for PFBR.

II.15 Design and Development of Remote Terminal Unit

Remote terminal units (RTU) are industrial grade microcontroller based single board computers distributed geographically across various reactor buildings of PFBR to acquire analog/digital signals (like 4-20 mA current signal/voltage signal, signal inputs from surface thermocouple (K-type) present over sodium pipelines, leak detector of SPLD type distributed over sodium pipelines and limit switches) and send digitized data packets over ethernet to the nearest local control centre (LCC) and also generate control outputs in the form of potential free contacts to control various process parameters during reactor operation. Remote terminal units are categorised as non-nuclear safety (NNS) systems and are designed to operate in the extreme field conditions present inside the reactor building which in turn helps in reducing the cabling from sensors to control room. To cater the data acquisition and control requirements for PFBR, seven different types of remote terminal units namely 16 Channel Leak Detector Input, 16 Channel Thermocouple Input, 16 Channel Analog Input, 30 Channel Digital Input, 16 Channel Relay Output, Combination of 16 Channel Digital Input and 16 Channel Relay Output and Combination of 16 Channel Digital Input, 8 Channel Analog Input and 8 Channel Relay Output have been designed and developed in IGCAR.

Salient features of remote terminal unit

* Each remote terminal unit has common features like CMOS Flash based 8 bit Microcontroller with the In-System Programming (ISP) capability and 64 Kbytes of on-chip flash program memory, external nonvolatile SRAM of 32 Kbytes with Real-Time Clock (RTC), Power-fail control circuit and lithium energy source to retain data for ten years, Century byte register, Programmable watchdog timer (1-30 sec), Remote terminal unit alarm, Power-on and manual reset, Board fail indication on fascia panel and through potential free contact, Serial Port for both ISP and serial communication and two Ethernet Ports (10/100 Base TX, full duplex operation, embedded TCP/IP and MAC protocol) for Ethernet communication.

* The I/O section of seven different types of remote terminal units varies with the type of input and output signals handled by that particular remote terminal units, like - 16 Channel Leak Detector Input accepts variable resistance through SPLD type leak detector, 16 Channel Thermocouple Input accepts signals from K-type surface thermocouple, 16 Channel Analog Input accepts high level voltage signals of ±10 V / ±5 V, 16 Channel Digital Input accepts discrete signals of 0/24V, 16 Channel Relay Output generates potential free contact outputs, Combination of 16 Channel Digital Input & 16 Channel Relay Output and Combination of 16 Channel Digital Input, 8 Channel Analog Input & 8 Channel Relay Output.

Remote terminal units were analysed for its Reliability (as per MIL-HDBK-217F), FMECA (as per MIL-HDBK-338), De-rating, and Power Consumption. Remote terminal units were subjected to Round-the-Clock operation in laboratory environment and further qualification for Environmental; EMI/EMC and Seismic requirements is in progress. The design of all seven types of remote terminal units along with PCB fabrication details (Gerber files) and supporting documents have been transferred to ECIL, Hyderabad for bulk production towards building various Non-Nuclear Safety systems for PFBR.

II.16 Optimisation of Thermal Design of Electronics Panel

The majority of electronics required for PFBR I&C systems are housed in a 2400 mm high, 600 mm wide & 1000 mm depth electronics panels (EP) kept in local control centre (LCC). These LCCs are

maintained at 298 K normally and in case of air conditioning failure, the ambient temperature can go up to 318 K. The power dissipation in the EP of PFBR exceeds 1 kW, which is the maximum power dissipation of NPCIL panels. Hence, it is imperative to carry out the thermal analysis of these panels and optimise the thermal design, in order to assure proper functionality, the reliability and availability of the I&C systems, without compromising Electro-Magnetic Compatibility (EMC).

In PFBR Real Time Computer (RTC) based systems, consisting of VME bus based Motorola MC68020 CPU card, Analog input and output cards, Digital input and output cards, Synchro to Digital Converter card and Counter Timer card as well as 89C51 microcontroller based Real Time Units (RTU) and switch over logic card (SOLC) are used safety critical, safety related and non nuclear safety I&C systems. Since, large number of systems are there, it is not possible to analyse all the different configurations. Hence, thermal analysis was carried out for Alarm Generation panel only, which is having a maximum power dissipation of 1,578 watts.

This Alarm Generation panel contains two numbers of VME sub-racks, two switch over logic card sub-racks, 5 V and 24 V fault tolerant power supplies and fan modules between the sub-racks. These are mounted with 100 mm recess from the front door. Further,

louvers are provided in the front door, in addition to louvers in the back door of NPCIL panels. The single ETRI features exhaust fan on the top is replaced with six numbers of electro magnetic compatible EEBM Nadi exhaust fans, with more total air flow. In addition, heat diverters were used in between the sub-racks, so that the heat from the lower sub-rack does not heat the upper sub-rack.

Thermal analysis was carried out for this configuration, with the help of ECIL, using Flowtherm software at SAMEER, Chennai, at the maximum expected ambient temperature of 318 K, due to failure of air conditioning. It was found that the temperature at the power supply location was quite high. Because of the heat diverters, there was a swirling effect of air from front louvers going through sub-racks & diverters and the air from back door louvers. Further, the fan modules did not function efficiently, because of availability of only a small free space of 9 mm below and above the fan modules. Providing louvers in the top of back door or moving the exhaust fans to the top of the back door did not help. Then, air filters were moved 20 mm away from the louvers. VME sub-racks were kept below the corresponding SOLC sub-racks. Finally, the heat diverters occupying 44.5 mm height were removed, the fan modules were kept in the centre of a 89 mm high box, covered in the back and sides, opened in the front & bottom
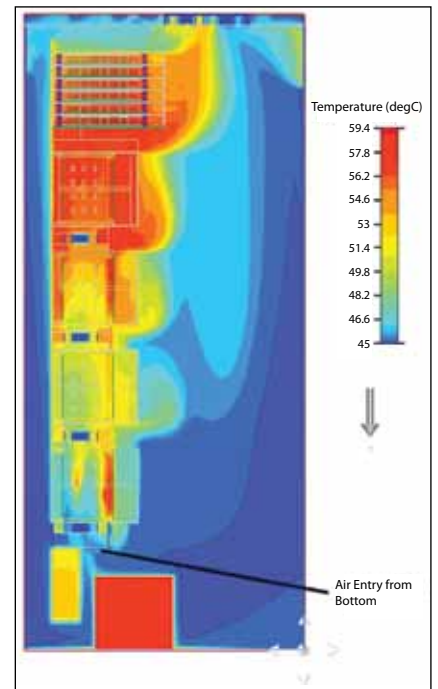
Fig. 1 *Temperature in the region of sub-racks*

and the cable manager was moved to the top below the power supply, without affecting functionality. With this arrangement, the fan modules get ample free space of 32 mm below. Thus, the air flow was found proper, moving from front to the sub-racks, thrown up by the fan modules, going to the exhaust fans. The temperatures in the regions of VME sub-racks, switch over logic card sub-racks as well as the power supplies were under control as shown in the Figure 1.

Thus with thermal analysis, proper thermal design was arrived at for the electronics panel with the maximum power dissipation, thus ensuring proper functioning of electronics.

II.17 Long-Term Creep Properties of Grade T91 Steel for PFBR Steam Generator Application

Modified 9Cr-1Mo ferritic steel has been chosen for all the steam generator (SG) components like shell, tubes and tube plates of the prototype fast breeder reactor (PFBR) in view of its superior

creep-rupture properties compared to 9Cr-1Mo steel. The steel billets were produced at M/s. MIDHANI Ltd., Hyderabad and subsequently processed at Nuclear Fuel Complex, Hyderabad into steam generator tubes of dimension 17.2 mm outer diameter and 2.3 mm wall thickness. The steam generator tubes were normalised and tempered. Creep deformation and fracture behaviour of indigenously developed modified 9Cr-1Mo steel steam generator tubes has been studied at 823, 848 and 873 K. Creep tests were performed on flat creep specimens machined from steam generator tubes at stresses ranging from 100 to 275 MPa.

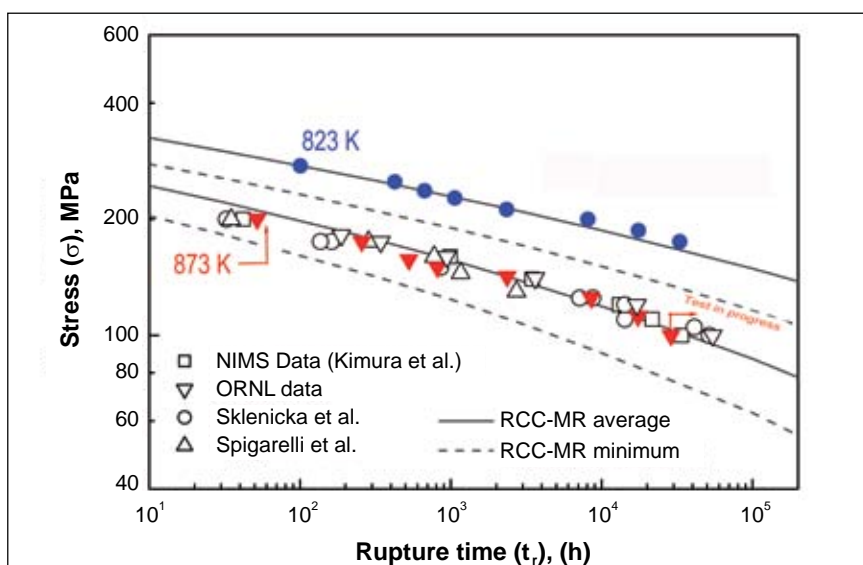*Fig. 1 Comparison of creep-rupture strength of modified 9Cr-1Mo steam generator tube steel with that reported in the literature as well as specified in the design code RCC-MR*

The modified 9Cr-1Mo steel exhibited a negligible instantaneous loading strain, a small transient creep strain and a secondary creep characterised by a minimum creep rate followed by a prolonged tertiary creep regime. The stress dependence of minimum creep rate obeyed Norton's power law. Similarly, the rupture life dependence on stress obeyed a power law. The steel exhibited good creep ductility and transgranular fracture at all test conditions examined. The analysis of creep data in terms of creep rate-rupture life relations indicated that the steel obeys Monkman-Grant and modified Monkman-Grant relationships. Further, a high creep damage tolerance factor obtained for the steel indicates resistance to

localised cracking as confirmed by the fracture behaviour. The tertiary creep was examined in terms of the variations of time to onset of tertiary creep with rupture life, and a recently proposed concept of time to attain Monkman-Grant ductility, and its relationship with rupture life that depends only on damage tolerance factor. The extensive tertiary creep in modified 9Cr-1Mo steel appears to be generic to most of the 9%Cr ferritic steels and is ascribed to the effects associated with microstructural degradation such as coarsening of precipitates and dislocation substructure.

The creep-rupture strength of steam generator tube steel at 823 and 873 K has been compared with the data available in the literature

as well as specified in the French nuclear design code RCC-MR for modified 9Cr-1Mo steel (Figure 1). At all temperatures, steam generator tube steel exhibited creep-rupture strength comparable to that reported in literature. It is evident that the long-term creep strength (for rupture lives of more than 10000 h) of indigenous steam generator tube steel is comparable with the strength values reported for the steel. Also, the creep strength of the steam generator tube steel is close to the average strength values given in the design code RCC-MR followed for the construction of PFBR components. This suggests that the indigenous steam generator tube steel satisfies the design code requirement in terms of its long-term creep strength.

II.18 Screening of Antifouling Paints for Biofouling Control in PFBR Cooling Water Tunnel

Materials exposed to the marine environment get colonized by a variety of sedentary organisms.

This colonization, a natural process, assumes economic importance, when the biological

debris thus formed, affects the functioning of the facility using sea water. These sedentary organisms

are identified as "Biofouling organisms" or "Biofoulers". PFBR would use seawater at the rate of ~30 m^{3}s^{-1} for cooling the condenser and process (pump, biological shield, etc.) water. Thus, biofouling control in the seawater cooling system has become a priority. In order to devise an effective biofouling control measure for PFBR cooling water system, it is essential that the present biofouling potential at Kalpakkam coastal water is evaluated considering a big hiatus has lapsed between the last study (almost 20 years old) and the present need. Thus, a study was carried out with the objective to find out the present seasonal settlement pattern of biofoulers, the dominant species and their breeding period.

Teak wood panels of size 9×12 cm were suspended in the coastal waters and retrieved periodically for analysing the fouling pattern. The results revealed a wide variation in the colonization of the biofoulers on the weekly panels. A visible shift in the peak settlement period of green mussel (September - October), the dominant as well as climax species, was observed as compared to earlier reports (April – August). In view of this, a modified chlorination regime needs to be applied during September to October. Appearance of oysters in sizable number on the panels (~7%) was observed, unlike their negligible presence in previous studies. Biomass values observed (648 g/ 100 sq. cm) were different from that of the earlier reports (135 g / 100 sq. cm). In view of the above, it is suggested that i) a long-term investigation on biofouling be continued to confirm the observed trends and ii) laboratory toxicity studies are needed to obtain effective biofouling controlling strategies.

Screening of antifouling paints

Settlement of fouling organisms in the seawater intake tunnel is generally controlled by chlorination (~0.5 ppm residual). However, when the tunnel is ready and waiting for the chlorination plant to become operational, there is a need to keep the tunnel free from fouling during this period. Antifouling coating could be the only plausible method to combat fouling inside the tunnel during this gestation period. In view of this, a study was carried out to screen three different antifouling paints (Nukote, Paint-2 and Sigma Glide), supplied by BHAVINI for their biofouling control potential with the objective of assessing temporal variations in settlement pattern, growth rate, biomass and area coverage by fouling organisms. Panels were exposed to coastal waters by suspending them from MAPS jetty and were retrieved after a specified time. During each retrieval total biomass, type of organisms settled and area coverage were assessed (Table 1).

Important observations

- The Nukote paint was found more prone to biofouling and the attachment of organisms was found to be with strong adhesiveness as compared to other two paints. The area

Day	Biomass (g/100 cm^2)			Area coverage (%)		
	Nukote	Paint-2	Sigma Glide	Nukote	Paint-2	Sigma Glide
7				25	15	25
15	11.1	8.0	8.8	90	60	50
31	18.7	18.4	45.4	100	80	90
37	19.7	16.7	54.6	100	95	90
45	19.0	15.8		100	40	
52	18.7	9.8		100	60	
66	41.0	41.0		100	100	
80	26.3	34.3		100	70	
108	27.3	36.0		100	90	
122	33.2	45.0		100	40	
150	68.2	76.6		100	70	

Table 1 : Temporal variations in biomass and area coverage of biofouling organisms on panels coated with different antifouling paints
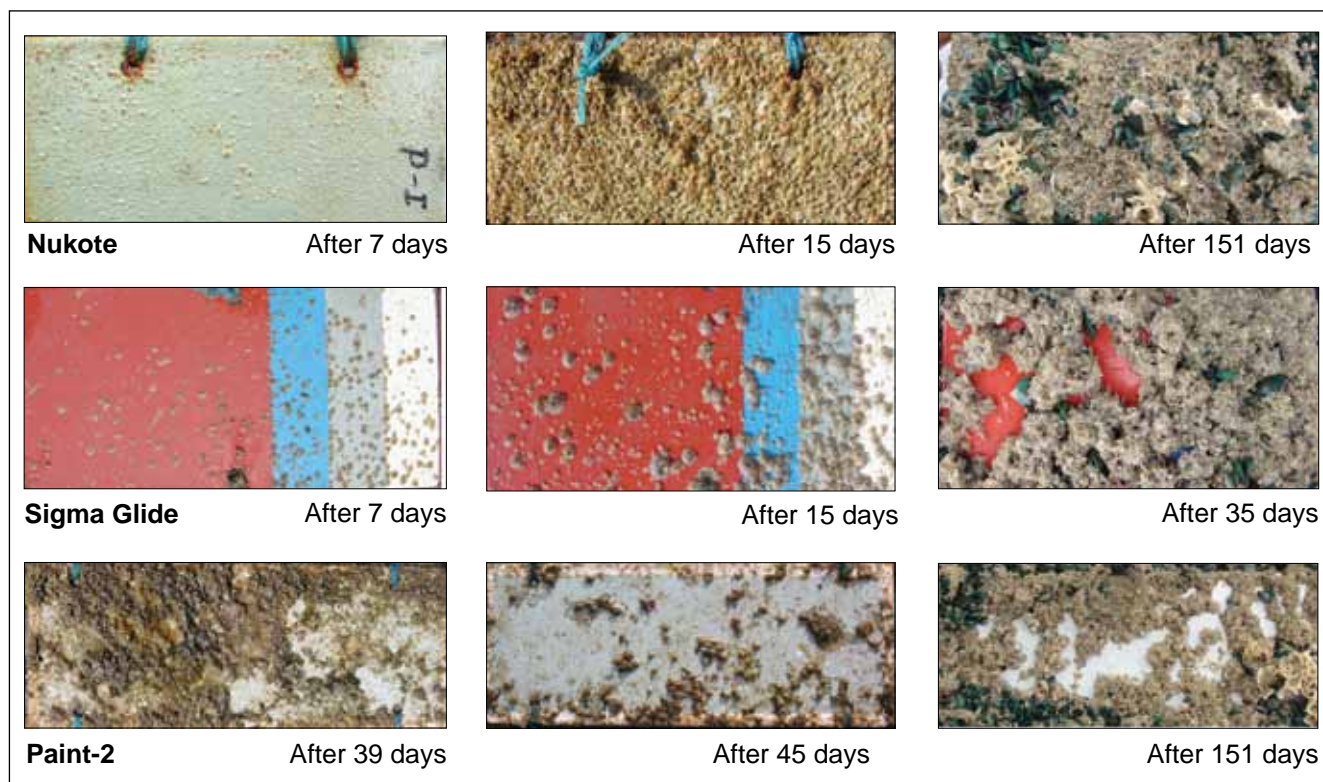
Fig. 1 *Growth of fouling organisms on panels coated with antifouling paints with different exposure periods*

Fig. 2 *Penetration of barnacle (a) Through the paint coating (Paint-2), (b) After removal of bio-growth (Nukote-151 days old) and (c) After removal of bio-growth (Sigma Glide-35 days old)*

coverage attained 100% just after a period of seventeen days of exposure and the panel remained fully covered throughout the five months study period (Figure 1).

• Bio-growth on Paint-2 was found to be relatively less as compared to that of the Nukote paint and 100% area coverage was observed only after sixty six days of exposure. Biomass was found to be relatively low in almost all the observations as compared to that of the Nukote paint. The area coverage reduced significantly from about 95%

on 37th day to about 40% on 45th day (Figure 1). This was due to the easy peeling off of the organisms from the panel surface. One of the most important observations was that barnacles grew on the base metal of the panel by penetrating the paint coating (Figure 2) and thus adversely affected the panel integrity.

• Rate of bio-growth on Sigma Glide was the highest as compared to the other two paints. However, it showed a unique behaviour of detachment of organisms very easily as

compared to the other two paints (Figure 2). The area coverage did not attain 100% during the thirty five days of study. This indicated that, the adhesiveness of organisms attached to the panels coated with paint-2 and Sigma Glide was relatively weak. Thus it would get peeled off in a dynamic cooling water system (during flow) and as well as in presence of chlorine.

From the above observations it was concluded that Sigma Glide showed promising results for its use against biofouling and thus recommended for PFBR.
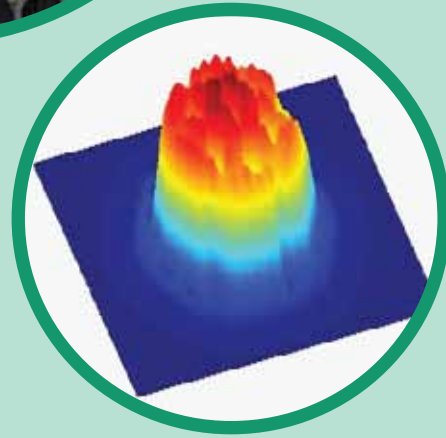
CHAPTER III

Research & Development for FBRs

III.1 Design, Simulation, Testing and Calibration of Eddy Current Flow Meter for Sodium Flow Measurements in FBRs

Eddy Current Flow Meter (ECFM) is used for flow measurement of liquid metal flows. A probe fitted with ECFM sensor developed at IGCAR was used for in-core flow measurement in FBTR. CEA, France requested a similar sensor for core flow measurement in PHENIX, which is undergoing end of life tests, before it is decommissioned. As the subassembly design and elevations are different for PHENIX, IGCAR developed and supplied only ECFM sensor (Figure 1) along with associated electronic unit. A probe suitable for PHENIX was designed and fabricated by CEA and fitted with IGCAR sensor. In PHENIX, the probe was used to measure flow rate variation in the blanket subassembly (SA), during an experiment planned for analysing power fluctuations encountered.

PHENIX required a flow sensor for sodium flow measurement in a pipeline of 22 mm ID. The flow sensor with 14 mm OD when inserted into this pipeline leaves an annular radial gap of 4 mm for sodium velocity of 0 to 5 m/s. The temperature variation of sodium is
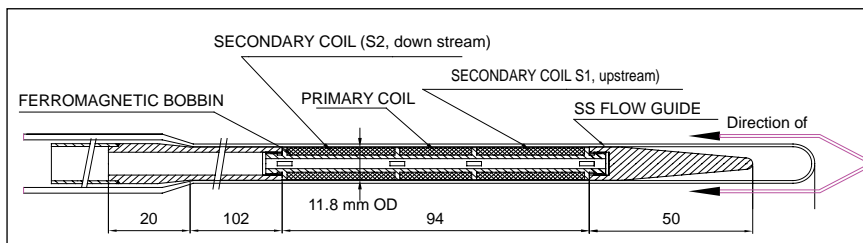

Fig. 1 *Eddy current flow meter sensor developed at IGCAR*

523 to 823 K. Since the radial gap is very less, CEA was suggested to use SS410 for the sodium pipeline, so that it will act as magnetic shield. Signal output of the ECFM is a function of annular gap, exciter frequency and temperature of sodium. For each annular gap there exists an optimum frequency at which variation of signal output due to temperature is minimum. Eddy Current Flow Meter was modeled using finite element based software COMSOL 3.4. Earlier the predictions of this software were validated based on the sodium tests done for the ECFM used in FBTR. The optimum exciter frequency was found to be 1400 to 1500 Hz, compared to 400 Hz for FBTR sensor and the sensitivity was determined for

different sodium velocities and temperatures.

The calibration of ECFM was carried out in PHENIX at different operating temperatures under shut down condition with the participation of an engineer from IGCAR. The ECFM was used to measure the flow for blanket subassembly, when PHENIX was in shutdown state and three primary pumps were running at 290 rpm (maximum 540 rpm). Flow rate in blanket subassembly for different rpm established earlier was used for calibration of ECFM. The sensor was calibrated for frequency response and variation in the pump speed (Figures 2, 3). A constant exciter current of 200 mA was passed through the primary coil of the sensor, at different exciter frequencies.
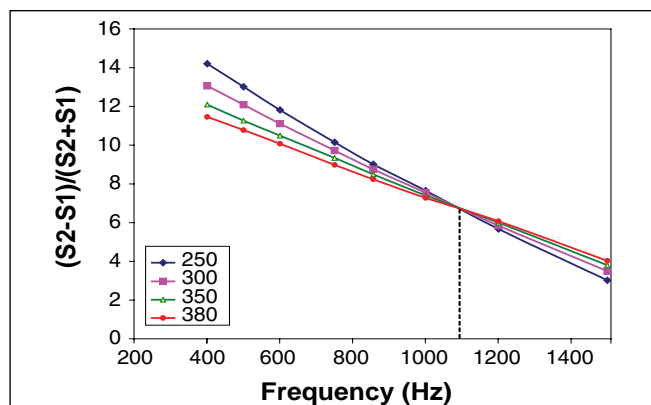

Fig. 2 *PHENIX experimental results: Frequency response*
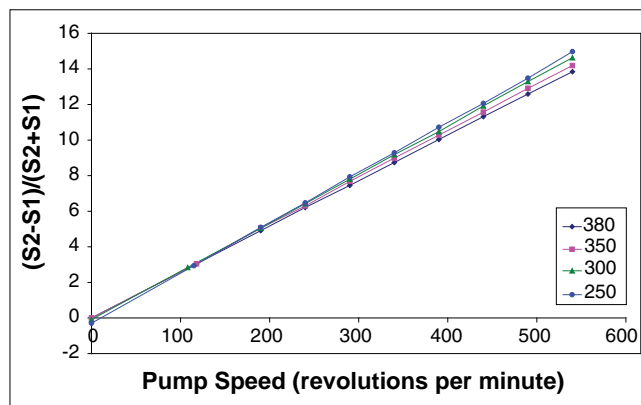

Fig. 3 *PHENIX experimental results: Pump speed vs signal output*

Frequency response of signal output was found out at reactor operating temperatures of 523, 573, 623 and 653 K at a constant pump speed of 290 rpm. The optimum exciter frequency was found to be 1100 Hz. The sensor was then calibrated at pump speeds varying from 0 to 540 rpm, in steps of 50 rpm, at temperatures between 523 to 653 K and 1000 Hz exciter frequency. The error due to temperature was found to be ±4%. It was concluded from the experiments that:

(i) Signal output of the sensor was 14% at the maximum pump speed of 540 rpm.

(ii) The sensor output varies linearly with pump speed, similar to FBTR core flow measurement.

(iii) Optimum exciter frequency was found to be 1100 Hz.

(iv) The signal output ratio matches very well with FEM analysis results.

(v) No core saturation was found upto 653 K for 200 mA excitation.

III.2 Development of an Electrochemical Sensor for Monitoring Sodium Aerosol

Liquid sodium is used as the heat transfer fluid in fast breeder reactors (FBR). In the event of an accidental leak, high temperature sodium reacts with oxygen and moisture (in air) leading to sodium fires. Such fires produce sodium aerosol containing oxides of sodium (Na_2O and Na_2O_2) and NaOH. In order to detect these sodium fires early, a sensor system based on a sodium ionisation detector (SID) had already been developed and is being used in FBTR as well as in those facilities of this Centre that handle large quantities of sodium. The present study deals with the development of an electrochemical sensor for sodium aerosol using Na-β-Al_2O_3, a sodium ion conductor.

The schematic of this sensor assembly is shown in Figure 1. Polycrystalline alumina wafers of 0.5 mm thickness were used as the substrate. A serpentine platinum heater pattern printed on one side of the alumina substrate is used to maintain the sensor at a desired temperature and on the other side of the substrate, a circular gold film was screen printed at its center, which is used as the reference electrode. Sintered Na-β-Al_2O_3 pellet was placed on the circular gold film and sides of the pellet in contact with the substrate were sealed using a high temperature ceramic cement. The reference electrode, Au_2Na / Au was made in-situ by pumping sodium ions through beta alumina membrane. Electrode for the sample side was made by depositing platinum on Na-β-Al_2O_3 by using pulsed laser deposition. The electrochemical sensor was housed in a compact stainless steel test chamber with provisions for streaming of synthetic air, sodium aerosol inlet and outlet facility. The baseline electro-magnetic field (emf) of this sensor was first measured in the stream of dynamic synthetic air in the absence of sodium aerosol. The electro magnetic field (emf) was measured at 423 K while the sensor was continuously being swept with air containing sodium aerosol.

Under the experimental conditions, the sodium activity at the reference electrode is fixed by the equilibrium:

$$Au_2\, Na \Leftrightarrow 2Au\ +\ Na$$
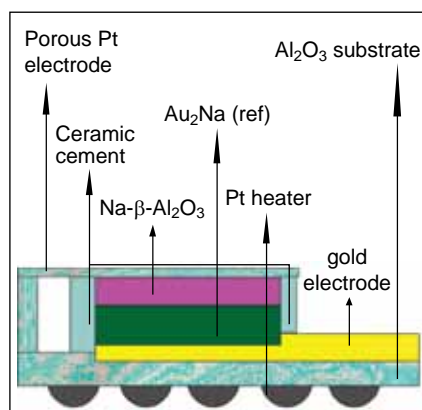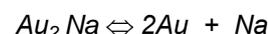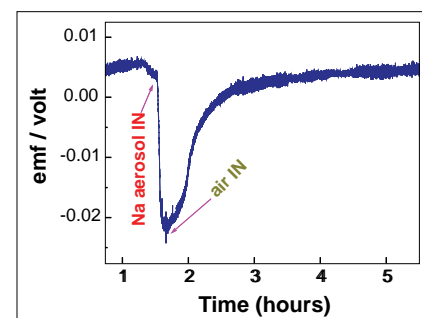

Fig. 1 *Schematic of side view of sensor assembly*

Fig. 2 *Typical response of Na-β-Al_2O_3 based sensor at 623 K on exposure to sodium aerosol (response time : 4 minutes and recovery time : 120 minutes (100%))*

By using the thermodynamic data available in the literature for Au_2Na at 623 K, the sodium activity was evaluated as: $a_{Na}^{ref} = 0.051$.

In clean air, the sodium activity at the sample side would be fixed by the equilibrium involving Na_2O in Na-β-Al_2O_3 atmospheric oxygen as shown below:

$$2\,[Na] + 1/2O_2 \Leftrightarrow [Na_2O]\beta\text{-}Al_2O_3$$

Figure 2 shows the typical response behaviour at 623 K for Na-β-Al_2O_3 sensor on exposure to sodium aerosol. The sensor responded reproducibly to sodium aerosol bearing air. One such sensor was tested in aerosol test facility (ATF) of Safety Group (Figure 3). About five gram of sodium was burnt and the performance of the sensor along with aerosol dust collector was tested. These studies showed that the aerosol sensor responded instantaneously to sodium aerosol and the response
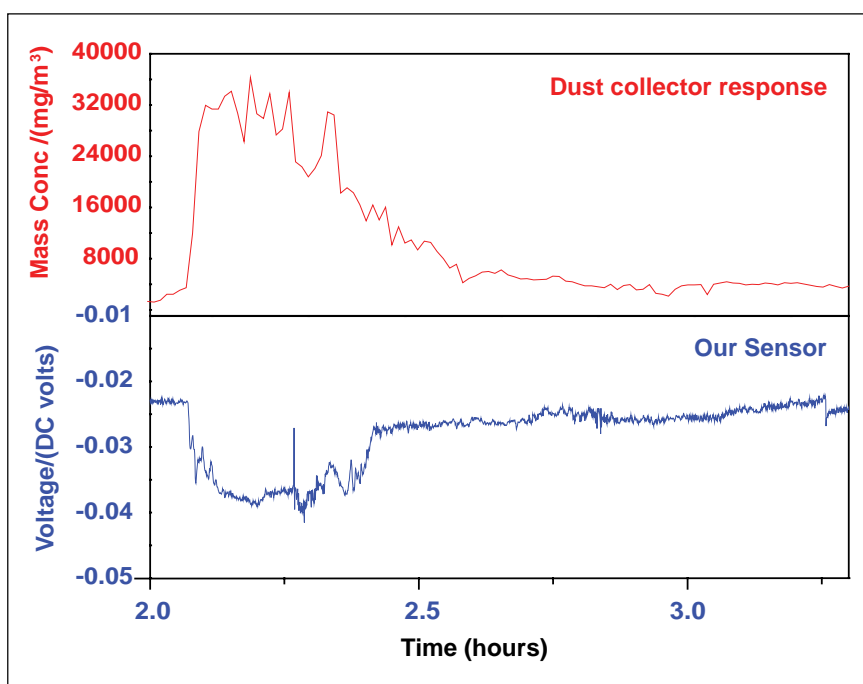
Fig. 3 *Comparison of the performance of Na-β-Al_2O_3 sensor with dust collector tested in aerosol test facility (ATF)*

corroborated with aerosol dust collector.

The $\beta-$alumina based sensor developed for sensing sodium aerosols produced in the event of a sodium fire shows promise for its deployment in large sodium facilities to monitor sodium aerosol.

III.3   Test on Fast Breeder Reactor Steam Generator

Steam Generator Test Facility (SGTF) is set up to test a scaled down sodium heated 5.5 MWt Once Through Steam Generator (OTSG) having nineteen tubes similar to PFBR Steam Generator (SG). The plant attained full power in April 2007. Instability test was carried out at lower power of steam generator and it was observed that outlet steam temperature were oscillating with a frequency of 0.3 to 0.6 Hz due to flow instability at steam outlet pressure less than 120 bar. At higher power, fluctuations were observed in the steam temperature up to 160 bar

pressure, when the feed water flow was kept at 20% of the rated value (Figure 1). Flow instability was not observed for higher steam temperatures and higher degree of super heat. Endurance test of steam generator was started in December 2008 at rated steam temperature and pressure (172 K and 766 bars) and 3600 hours of operation was completed.

Flow instability test at startup conditions was carried out at six different steam pressures. At each pressure, onset and vanishing of instabilities were

recorded. It is observed that stable steam generator operation could be achieved at pressure of 45 kg/cm^2, temperature of 689 K and with a degree of superheat of 431 K, which is quite adequate
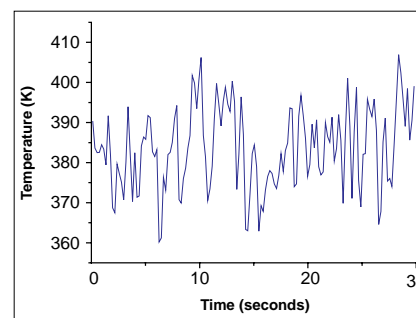
Fig. 1 *Temperature fluctuation at tube outlet*

Fig. 2 *Unstable region in low pressure operation*

for turbine preheating (Figure 2). Steam generator was operated with rated sodium flow of 104.5 m³/h and inlet temperature of 798 K. It was found that steam generator could transfer 5.95 MWt at rated conditions. Actual heat transfer area margin was calculated as 12.25%, which may reduce to 8.3%, considering the scale resistance for an operating life of forty years.

Following steam generator transient tests were conducted at 3.3 MWt to assess the performance of steam generator thermal baffle assembly:
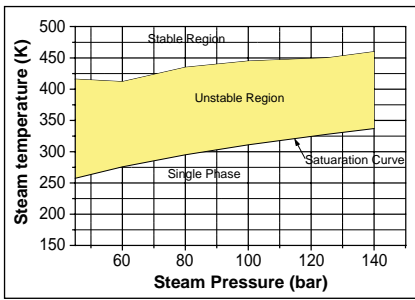
1. Loss of heat sink flow was simulated by tripping the boiler feed pump. Temperature of the bottom thermal baffle increased at a rate of 37 K/min. Temperature of the bottom tube sheet increased at a rate of 18 K/min.

2. Loss of heat transport system was simulated by tripping the sodium pump. Steam generator bottom thermal baffle temperature reduced by 96 K but only 42 K drop in the bottom tube sheet temperature within hundred and fifty seconds.

3. Loss of heat source was initiated by tripping oil fired heater

while running boiler feed pump. Temperature of thermal baffles and tube sheets were reducing gradually without causing any thermal shocks.

In the rare event of a tube failure in the steam generator, steam/water leaks into sodium resulting in sodium-water reaction. Small leak in the range of 50 mg/s to 10 g/s results in damage of single adjacent tube. Sodium-water reaction jet consists of steam/water in its core, reaction zone in the periphery and high temperature corrosive reaction products in the outer zone (Figure 3). Jet impingement on adjacent tube causes impingement wastage due to combined action of corrosion and erosion. Once a through-hole is formed on the adjacent tube, it will start leaking with a much higher leak rate. In Sodium Water Reaction Test (SOWART) facility, small leak is simulated to study impingement wastage on Mod9Cr-1Mo tube.

A tube of Mod9Cr-1Mo having a calibrated pinhole, is used for injecting steam into sodium. This tube is inserted into impingement wastage test section from bottom. Its one end is dummied and the other end is connected to the steam system. The target tube assembly, which is having a tube of Mod9Cr-1Mo is fixed into the test section. The reaction jet from the leaking tube produces wastage on the surface of the target tube. hydrogen meters in sodium and argon and acoustic detectors are used as reaction detectors. Electrochemical hydrogen meter is used for on-line monitoring of leak rate. Both sodium and steam systems are equipped with rupture discs for safety against over pressurisation.

$$Na + H_2O \rightarrow NaOH + \frac{1}{2}H_2 + 185 \text{ kJ/mol}$$

Fig. 3 *Sodium water reaction flame*

Experiment was carried out in the impingement wastage test section of sodium water reaction Test loop. Super heated steam at 723 K and 172 bar was injected for 10.75 minutes for the study. Sodium flow meter signal was fluctuating, indicating presence of hydrogen bubbles. No appreciable self-wastage was observed in the leaking tube. But there was a slight enlargement of the hole. Impingement wastage on target tube was noticed at the location
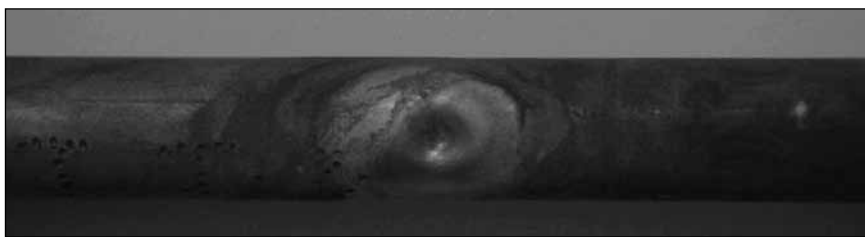
Fig. 4 *Target tube after experiment*

where leaking jet hit the tube (Figure 4). The maximum depth of wastage was measured as 2.02 mm. The wastage rate was evaluated to be 0.0032 mm/s.

The leak rate estimated from electrochemical hydrogen meter was 500 mg/s. From the profile, it was concluded that wastage is of 'pitting type'.

III.4 Development of an Electrochemical Brush for the Decontamination of Hot Spots in the Primary Components of a Fast Reactor

Decontamination is a cleaning method by which the radioactive contaminants are removed from the contaminated surfaces. This is often necessary in order to reduce the radiation dose to the personnel involved in the maintenance of these components. Often the complete removal of radioactivity from such contaminated reactor components requires repeated cleaning or decontamination. The removal of residual radioactivity from the surface of these components is highly challenging, but with the choice of the right decontamination method one can achieve a high decontamination factor. At the operating temperatures, the deposited radionuclide diffuses through a distance of a few microns into the structural material of the fast reactors. Hence, in order to achieve complete decontamination, it is required to remove the surface layer of the base metal that is a few microns thick. The need for

decontamination of the reusable primary components is the main objective behind the development of efficient electrochemical techniques for this purpose. The first step in such decontamination is the clean up of sodium with which a large portion of the radioactive contaminant gets removed. Subsequently, chemical decontamination is carried out with a mineral acid. Yet, some regions on the component could still be found contaminated. These zones termed as hot spots, pose problems in handling during the maintenance of these components. Earlier a chemical cleaning procedure was developed in order to get rid of such hot spots that used a mixture of sulphuric and phosphoric acid. As a refinement to this procedure an electrochemical method based on the conventional electropolishing principle was developed. These studies focused on the development of an electrochemical brush that is a portable device for selective decontamination, has been taken

up in collaboration with CECRI, Karaikudi.

As part of the trials in the development of this methodology studies were carried out on the electrochemical decontamination of SS316LN. The component to be decontaminated is made as the anode while a graphite block covered with a polymer gauze serves as the cathode. A mixture of sulphuric and

Fig. 1 *Photograph of electro-chemical brush developed*

Table 1 : Layer thickness of metal removed obtained from weight loss data with bath parameters			
Sl. No	Voltage (V)	Time (min)	Thickness removed (μm)
1.	6	9	5.3
2.	7	15	4
3.	8	15	4.7

Fig. 2 *SEM micrograph of 20% CW AISI type SS 316 LN. (a) Exposed to sodium at 873 K for 1000 hours and (b) Exposed to sodium and immersed in a mixture of 5g/L of H_2SO_4 and 30g/L H_3PO_4 at 6V for 3 minutes*

phosphoric acid is used as the electrolyte. Initially, experiments were carried out on rectangular test coupons made out of inactive SS316LN in order to optimise the experimental parameters viz., composition of the electrolyte, voltage and time of exposure. Experiments were carried out with manual swiping for the following SS316LN specimens; (i) 20% cold worked (ii) vacuum annealed (iii) 20% cold worked specimens exposed to sodium at 873 K for 1000 hours and iv) vacuum annealed specimens exposed to sodium at 873 K for 1000 hours. The thickness of the layer of the metal removed was calculated from the weight loss measurements and is shown in Table 1. The structural integrity of the metal was examined with a scanning electron microscope (SEM) (Figures 2(a) and 2(b)). It is evident that the electrochemical polishing leaves the surface most unaffected while it removes the contaminant effectively. In order render this technique suitable for handling highly radioactive samples, the manual swiping has to be replaced by an automated swiping system with the continuous flow of electrolyte. Such a system is being developed.

III.5 Effect of Sodium Environment on the Creep-Fatigue Interaction Properties of Reactor Structural Materials

Sodium being the coolant in fast reactors, it is important to characterise the mechanical properties of structural materials in sodium environment. A detailed study has been undertaken to assess the effects of dynamic sodium on the creep, low cycle fatigue and creep-fatigue interaction (CFI) of reactor structural materials. As part of this study, the creep-fatigue interaction properties of 316LN stainless steel and modified 9Cr-1Mo ferritic steel in dynamic sodium environment have been evaluated. A unique test chamber with all safety features for carrying out the tests in dynamic sodium was developed in-house. CFI tests were conducted at 873 K at a strain range of ±0.6% with hold times in tension of one and ten minutes. The sodium test temperature was controlled within ±2 K, the sodium velocity was maintained at 2 m/s in the test chamber and the oxygen level was maintained at less than 2 ppm. As compared to fatigue life in air, both the materials showed enhanced fatigue life in sodium environment. Figure 1 gives the results of CFI tests conducted on

Fig. 1 *Influence of flowing sodium on creep-fatigue interaction properties of Mod9Cr-1Mo Steel*

mod9Cr-1Mo steel. The fatigue life in sodium environment was found

to be higher by a factor of five under one minute hold time tests and by a factor of two under ten minutes hold time. This suggests that while the lack of oxidation in sodium environ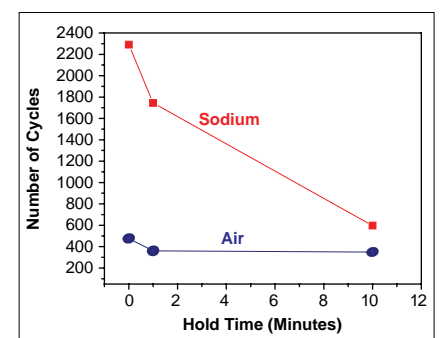ment contributes to delayed crack initiation and consequent increase in Low Cycle Fatigue life, the bulk creep damage is only marginally influenced by the sodium environment. Therefore, the design rules for creep-fatigue interaction, based on data in air environment is valid for components operating in sodium environment, and no design advantage can be taken for the sodium environment.

III.6 Development of Ferro Fluid Seal for 25 mm Diameter Shaft

In centrifugal sodium pumps, the argon cover gas is sealed from the atmosphere using mechanical seals. Oil is used for cooling the mechanical seals as well as top thrust and radial bearings. The oil leaking past the bottom mechanical seal is collected in a catchpot. The catchpot is designed to contain the entire oil in the cooling circuit and its level is periodically monitored to prevent any overflow into sodium. A Ferrofluid Seal (FFS) used in combination with a magnetic bearing can eliminate the oil circuit, thereby preventing any possibility of oil ingress into sodium as a result of leak in the catchpot.

The Ferrofluid developed in-house is used for Ferrofluid Seal. Burst

Fig. 1 Photograph of 25 mm diameter shaft seal setup
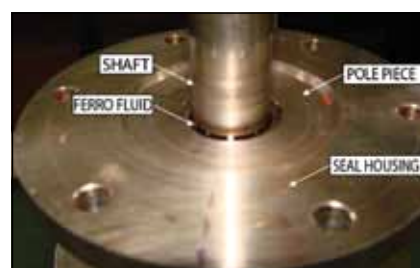
Fig. 2 Photograph of sealing region

pressure tests of Ferrofluid Seal with 25 mm diameter shaft (Figure 1) were carried out in a test setup, which consists of shaft, bearing housing, ferrofluid seal housing, motor with speed control system, vessel and argon gas header with pressure regulating and monitoring devices (Figure 2). Three test campaigns were carried

Test Campaign	Max. RPM	Magnet material & geometry	Ferro Fluid Sample (developed by IGCAR)	No. of teeth	Seal Radial Gap (mm)	Burst pressure achieved, mbar (g)
1	700	Alnico-V magnets, annular ring type	No. K25S (Kerosene base)	2	0.1	135/29
2	520	12 numbers of cylindrical NdFeB magnets, each of 10 mm dia. & 10 mm length, arranged circumferentially around the shaft in a non-magnetic cage	No. MSV03K (Kerosene base)	1/2	0.15	For single tooth: 68/64 For two teeth (one test only): 128
3	1000		No. K30	1	0.15	For K30 FF : 180/165
			MSV03(30K) (both kerosene based)	1	0.15	FF : 176/74

Table 1 : Summary of burst pressure test results and important parameters

out to study burst pressure. From the experimental results, it can be seen that burst pressure of 165 mbar is obtained for single stage Ferro Fluid Seal (Table 1). The requirement for higher burst pressures can be achieved by having multiple stages.

Simulation was carried out using COMSOL software, to analyse the effect of variation of radial gap between the pole piece tooth and the shaft. It was found that for an average radial gap of 0.1 mm and a radial eccentricity of the shaft by 0.09 mm, the burst pressure of the seal was reduced to 2/3rd of original value (Figure 3).
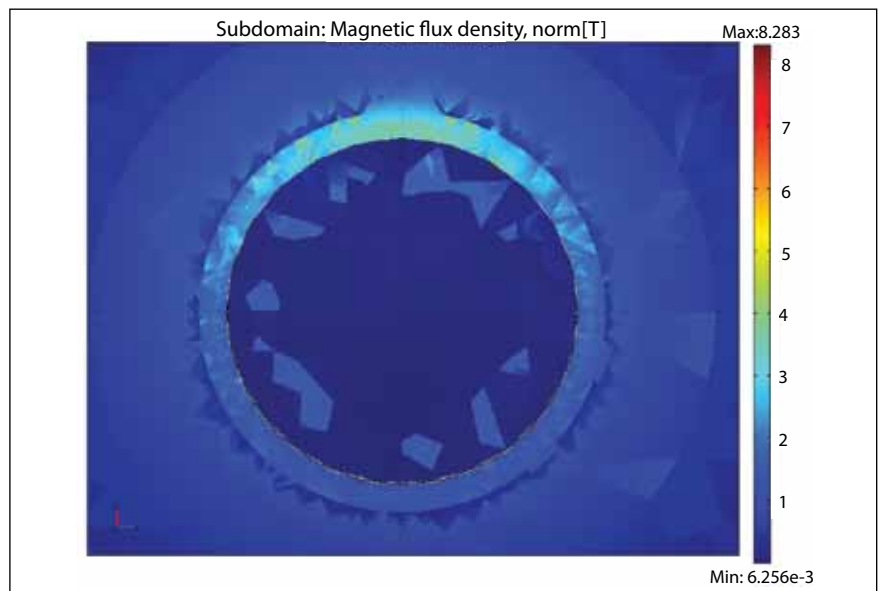
Fig. 3 *Flux Density along the periphery of the pole piece when the shaft is displaced by 0.09 mm on one side*

III.7 Feasibility of using Ferro-Boron as Cost Effective Radial Shields in FBRs

Shields around core and blankets form major part of reactor assembly in fast reactors. The incident neutron spectrum is hard with negligible thermal component and has anisotropic angular distribution. Boron carbide and stainless steel have been the main choice shield materials for shields in fast reactors. In future FBRs, there is a desire to achieve a more economic design. Shield optimisation is complicated by the fact that combination of several shield materials are involved with varying thickness. A neutron undergoes many elastic and inelastic scatterings before it gets absorbed in shields. A relative study has been made on the use of ferro-boron as a radial shield material in pool type of fast reactors with reference to the shield design in PFBR. Another change with respect to the reference design is

replacement of the axial stainless steel shield in blanket by boron carbide pellets. The study has brought out, through 2D transport calculations, that the new design even with eight radial shield rows is capable of satisfying the radiological safety criteria.

PFBR core is surrounded by 120 radial blanket subassemblies in two rows with depleted uranium oxide. There are two SS reflector rows followed by one row of B$_4$C pellet shielding subassemblies and two rows of internal storage locations for fuel. Then there are 1058 shield subassemblies in nine rows. The outermost three rows are B$_4$C powder assemblies and the rest are SS subassemblies.

The geometry of the proposed case is the same as the reference case. All the nine shield rows are now replaced by eight rows of

cheaper ferro-boron assemblies. Commercially available ferro-boron has about 15-18 of % boron. A boron percentage of 17 wt % is considered in the study taking the same volume fractions as the reference case. Here only eight rows of radial ferro-boron shield subassemblies are used instead of nine rows in the reference case. Also, 65.5 cm steel region in the axial blanket subassemblies are replaced with B$_4$C pellets.

Calculations are performed by the well validated two dimensional transport code DORT and IGC-S3 cross section set. For this bulk shield calculation, the angular quadrature approximation used is S$_8$ and the order of scattering cross section anisotropy is P$_3$. Totally 571 meshes are taken in the radial direction and 718 meshes are taken in the axial direction.
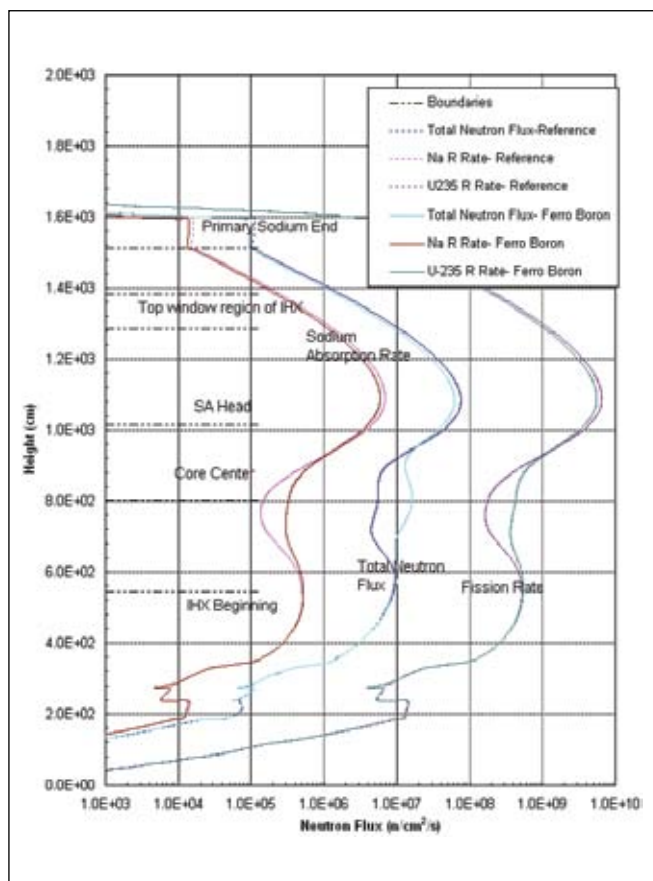
Fig. 1 *Comparison of total neutron flux, capture reaction rate and ^{235}U reaction rate for reference case and ferro-boron case*
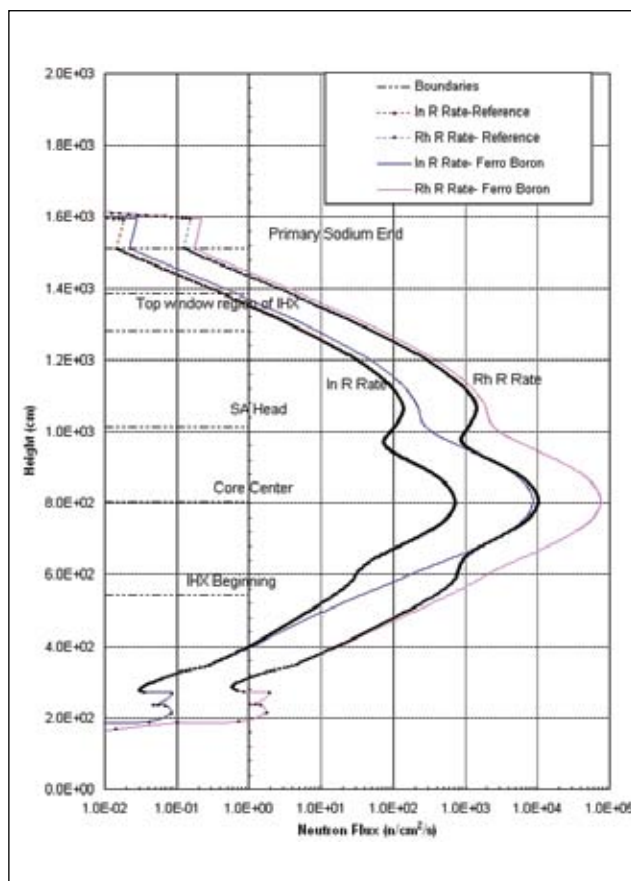
Fig. 2 *Comparison of indium and rhodium reaction rates for reference case and ferro-boron case*

The secondary sodium activity computed for the eight rows of ferro boron shield design is lower by 12% as compared to the nine rows of stainless and boron carbide assemblies in the reference case.

The reasons are clear from the Figures 1 and 2. In the case of ferro-boron shields, the sodium capture rates are about two times more than that of the reference case in intermediate heat exchanger region in the core mid plane. However, this is only a small fraction of the peak sodium capture rate. In the position in intermediate heat exchanger region showing maximum value of flux, sodium capture rate in the ferro-boron case is found to be less than that of the reference case. The reason is because of the B_4C region introduced in the blanket subassemblies and also that top parts of shield subassemblies in between core subassemblies and the intermediate heat exchanger peak position have significant boron atom densities. The reference case, the top portion of the first six SS rows does not have any boron and the neutrons are streaming above the last three rows of B_4C. Possibility of movement of intermediate heat exchanger towards core centre is also studied. Secondary sodium activity is still 4% less than the reference value by 5 cm movement of intermediate heat exchanger towards core centre. But 10 cm movement of intermediate heat exchanger towards core centre shows an increase in secondary sodium activity by 14%.

The present study has clearly shown that replacement of all the shield assemblies by only eight rows of ferro-boron is capable of satisfying all the radiological safety criteria as good as the reference case. Its effectiveness has stemmed from the fact that

a) boron is spread throughout the shield region, though in lower atom densities

b) iron present in shield regions also contribute significantly to slowing down

c) B_4C present in the upper axial blanket also contribute. Preliminary results of metallurgy and chemistry experiments in progress have shown promise in establishing the use of this much cheaper material in pool type fast reactors.

III.8 Development of Non-Instrumented Gas-Gap Type Irradiation Capsule for Irradiation of Specimens at Higher Temperatures in FBTR

Irradiation performance testing of present and newer fuel cladding and wrapper tube materials at temperatures above ambient sodium temperature can be carried out in FBTR using gas-gap type irradiation capsule. Non-instrumented gas-gap type irradiation capsule has been designed for irradiation of pressurised capsules, tensile and swelling specimens in FBTR at temperatures from 673-873 K. Pressurised capsule made of the material of interest is used to determine the irradiation creep performance of the material.

There are five sub-capsules coaxially located in the irradiation capsule and the specimens are kept in static sodium inside the sub-capsules with gas-gap between sub capsules and irradiation capsule (Figures 1(a) and 1(b)). The gap between each sub-capsule and irradiation capsule will be filled with a distinct composition of helium and argon gas mixture. During irradiation, the specimen temperature will depend on the neutron and gamma heating rate at the location of irradiation. The width of the gas-gap and the gas composition in the gas-gap will be adjusted to attain a desired temperature of irradiation in the specimens. The annular spaces around different sub-capsules are not inter-connected and due to this, the specimen irradiation temperatures of 673, 723, 773, 823 and 873 K (temperatures of interest to fast reactor programme) will be achieved in the five sub capsules.
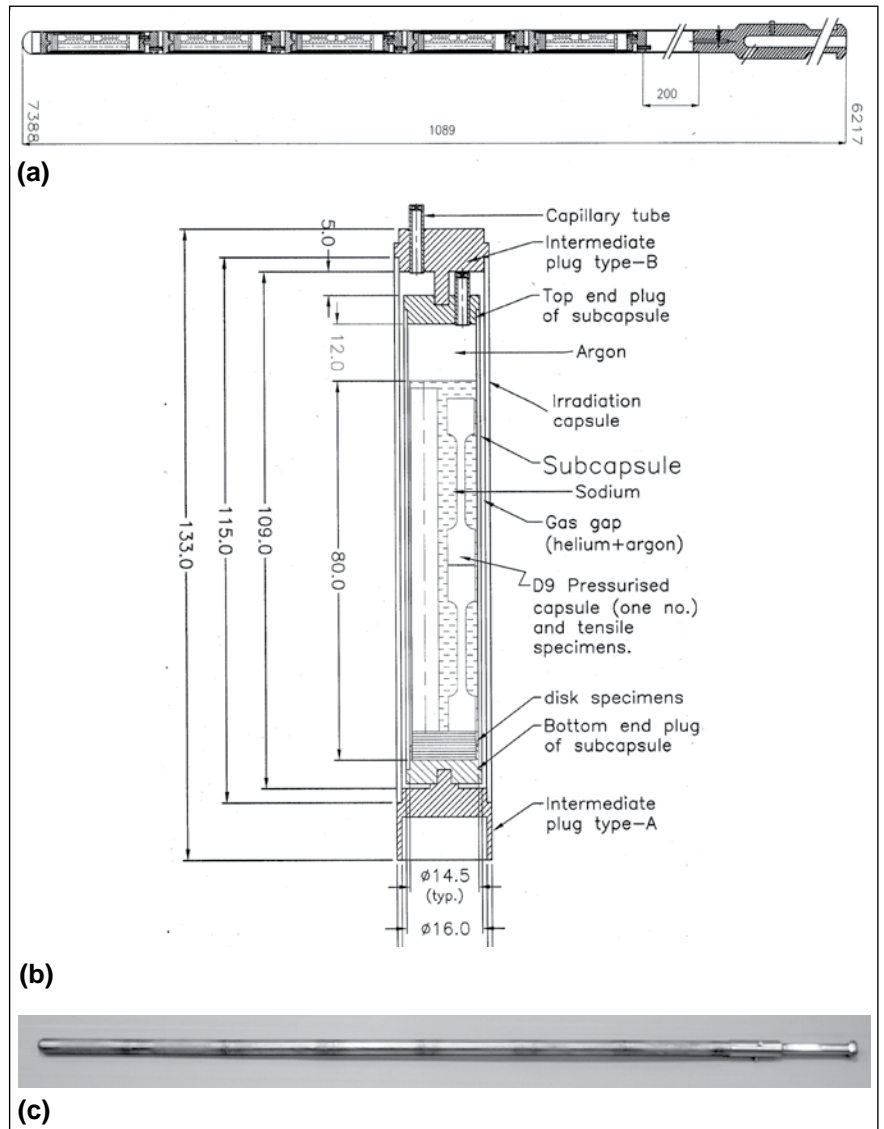
Fig. 1 *(a) Sketch of non-instrumented gas-gap capsule, (b) Details of a sub capsule and (c) Photograph of mock up gas-gap capsule*

A mock up irradiation capsule containing five sub capsules has been fabricated (Figure 1(c)). Sodium filling in the sub capsules was carried out at Radiochemistry Laboratory in an argon atmosphere glove box and an innovative sealing method was successfully developed to seal the sodium-filling path in a leak tight manner. The sub capsules were machined in such a way that they were located coaxially within irradiation capsule one over the other and have a separate uniform gas insulation layer around each of the sub capsules. X-radiography examination was carried out on the mock up irradiation capsule to verify the internal configuration of the capsule. This type of capsule will be used in FBTR for generation of irradiation performance data on fuel cladding and wrapper tube materials of interest at desired higher irradiation temperatures.

III.9 Constitutive Modeling and Hot Workability Studies of Modified 9Cr-1Mo Steel

To find out the optimum hot workability domain for the processing of modified 9Cr-1Mo steel and to find suitable constitutive equations to represent the elevated temperature flow behaviour of this material over a wide range of strain, strain rate and temperature, experimental data have been generated through isothermal hot compression testing. The compression tests have been carried out on the cylindrical specimens of 10 mm diameter and 15 mm height over a range of temperature (323–1373 K in steps of fifty degrees) and strain rate (10^{-3}–10^2 s^{-1}). Standard equations have been used to convert the load-stroke data to true stress-true strain data after removing the machine compliance. The elastic region has been subtracted from the true stress-strain curve to get true stress-true plastic strain data. The flow stress data obtained at different processing conditions were corrected for adiabatic temperature rise, if any, by linear interpolation between ln σ and $1/T$, where σ and T are the flow stress and absolute test temperature, respectively.

The experimental data has been employed to determine suitable constitutive equations. The Johnson Cook (JC) model has been employed to represent the flow behaviour as this model considers the major material behaviour like isotropic hardening, strain rate hardening and thermal softening. It is found that the JC model in its original form is inadequate to provide good description of high temperature flow behaviour of

the material over a wide range of temperature, strain and strain rate. This is attributed to the inadequacy of the Cook model to incorporate the coupled effects of strain and temperature and of strain rate and temperature. A new model based on the Zerilli-Armstrong (ZA) model has been proposed to represent high temperature flow behaviour of this material. This modified-ZA model considers the effect of isotropic hardening, strain rate hardening, thermal softening and the coupled effects of temperature, strain, strain rate and temperature on flow stress. This model involves seven material constants, whereas the JC model involves only five. The proposed modified-ZA model could predict the elevated temperature flow behaviour of modified 9Cr-1Mo steel over the specified range with good correlation and generalisation over a wide range

of temperatures (1123–1373 K in steps of fifty degrees), strain rates (0.001–0.1 s^{-1}) and strains (0.1–0.5). However, the modified-ZA model is not able to adequately track the trend of the flow curves for modified 9Cr-1Mo at few temperatures and strain rates. Finally, a strain-compensated Arrhenius-type equation has been formulated to suitably represent the flow behaviour of modified 9Cr-1Mo steel. The model could represent the elevated temperature flow behaviour of modified 9Cr-1Mo steel precisely over the specified hot working domain. Further, the strain compensated Arrhenius-type equation could track the deformation behaviour more accurately and precisely over the entire working domain. In comparison with other two models, this model is able to predict the flow behaviour of the material over a wider range of strain
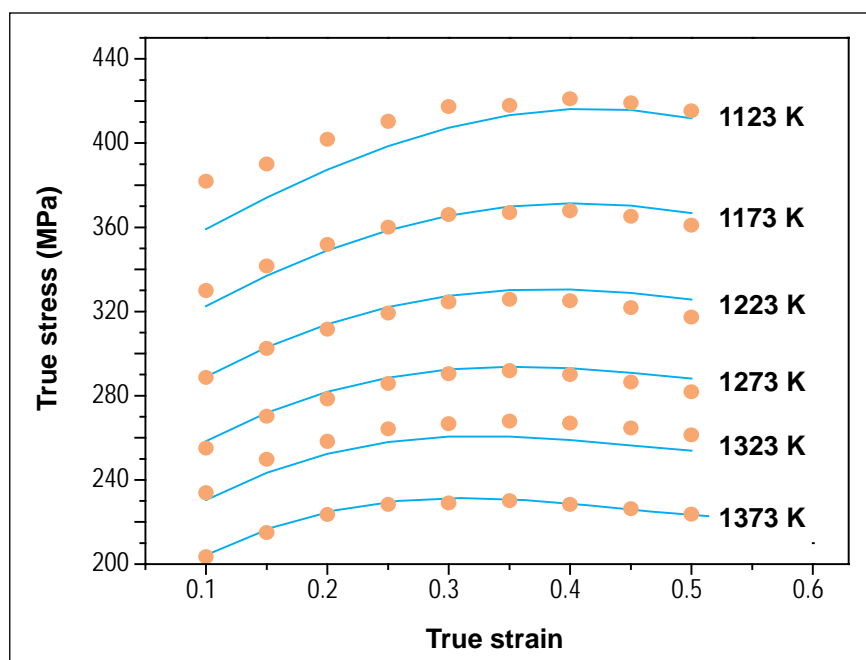

Fig. 1 *Comparison between the experimental and predicted flow stress by strain compensated Arrhenius-type equation at strain rate 100 s^{-1}. The lines give predicted values and the data points are experimental values*
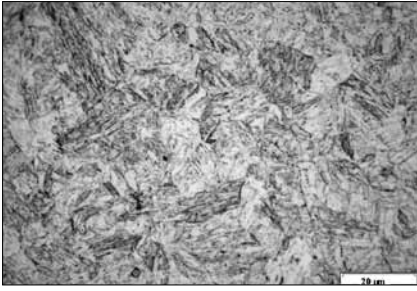
Fig. 2 *Microstructure at 1323 K at strain rate 0.1 s⁻¹*

rates (0.001–100 s⁻¹) for the same range of temperatures. However, it involves thirteen material constants and takes more computational time for the evaluation of these constants. The experimental flow curve and predicted flow curve at strain rate of 100 s⁻¹ and at various temperatures is given in Figure 1.

Hot deformation behaviour of modified 9Cr-1Mo steel has been characterised over a wide range of strain rate (0.001–100 s⁻¹) and temperature (1123–1373 K), at 0.5 true strains using processing map. Various domains of the map have been validated by studying the microstructure of specimens from that domain. The optimum hot working domain for modified 9Cr-1Mo steel is in the strain rate range of 0.01–0.1 s⁻¹ and temperature range of 1248–1348 K. The peak efficiency of this domain is 38%, whereas the minimum efficiency is 32%. In optimum hot workability domain, the material exhibits homogeneous, uniform and defect free microstructure without any sign of flow localisation (Figure 2).

III.10 On the Temperature Dependence of Fatigue Crack Growth of SS 316L (N) Weld near Threshold

For the damage tolerant design of the SS316L(N) components of PFBR, inter alia the fatigue crack growth properties of the weld are necessary. Therefore, fatigue crack growth (FCG) behaviour of the SS316(N) weld, prepared using the consumables developed for PFBR applications was examined in the reactor operating temperature range. Fatigue crack growth tests were carried out in the Paris and threshold regimes at 300, 573 and 823 K on compact tension (CT) samples following the guidelines of ASTM standard E647. The weld material contained about 5.5 FN δ−ferrite distributed uniformly in the γ austenite matrix. The notch was placed in the weld such that the crack growth is along the welding direction.

For intermediate crack growth rates, the relation is given by the well known Paris equation $da/dN = C\Delta K^n$ where the

Table 1 : The Paris constants and exponents for the three temperatures				
Temperature K	**Paris constant, logC**		**Paris exponent, *n***	
	ΔK	ΔK_{eff}	ΔK	ΔK_{eff}
300	-3.24	-1.48	3.0	1.53
573	-2.31	-1.26	2.65	1.83
823	-4.16	-0.85	4.98	2.13

coefficient, *C*, and the exponent, *n*, are material constants. As ΔK is gradually reduced, the crack growth rate drastically decreases, approaching a threshold value ΔK_{th} at which *da/dN* ostensibly equals zero. Typical fatigue crack growth curves, i.e., d*a*/d*N* vs ΔK in the Paris and threshold regime on SS 316(N) weld metal in the as-welded condition are presented in Figure 1(a). In the Paris regime, the crack growth rate increased with increasing temperature. However, in the threshold regime,

the crack growth rate at 823 K was lower than that at 573 K, indicating a higher ΔK_{th} for 823 K than 573 K. The ΔK_{th} values were 11.2, 7.5 and 9.3 MPa m^{1/2} respectively at 300, 573 and 823 K. The crack closure load (P_{cl}) was determined from the load (*P*) vs displacement (*v*) data collected immediately following a crack growth rate determination, and the ΔK_{eff} corresponding to $\Delta P_{eff} = P_{max} - P_{cl}$ was determined. The plots of d*a*/d*N* vs ΔK_{eff} for all the three temperatures are presented in Figure 1(b). The values of
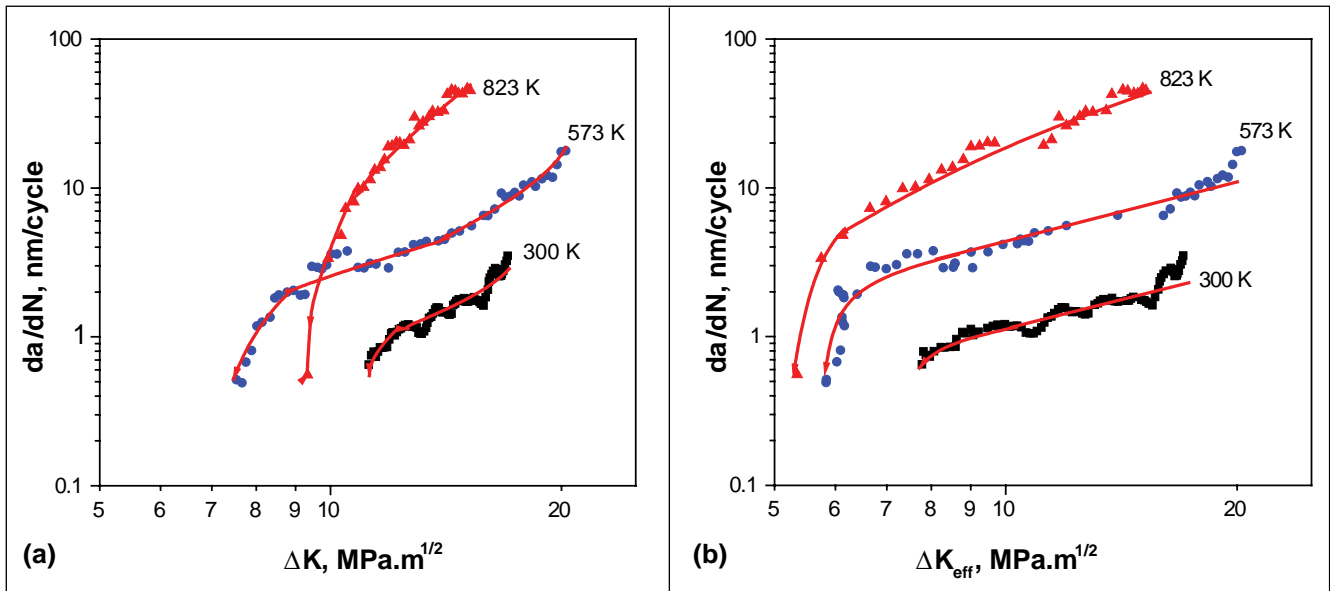
Fig. 1 *Fatigue crack growth curves for SS 316L (N) weld metal in Paris and threshold regimes (a) With out and (b) With crack closure correction*

$\Delta K_{eff, th}$ decreased with temperature; 7.7, 5.8 and 5.3 for 300, 573 and 823 K respectively. Both the Paris constants *C* and *n*, follow an increasing trend with temperature, though marginal when the closure correction is incorporated whereas without closure correction, no such trend was observed (Table 1).

These results clearly indicate that the magnitude of the closure contribution is the smallest at the intermediate temperature 573 K, with the ambient temperature and high temperature (823 K) being much more; 31, 22 and 43% of the applied ΔK for 300, 573 and 823 K respectively. Several mechanisms of crack closure have

been discussed in the literature depending on the material and test conditions. These are mainly in the following four categories; plasticity induced, roughness induced, oxide induced and transformation induced. Optical and scanning electron microscopic examination of the tested specimens was carried out to understand the relative importance of each of the mechanisms at different temperatures. In the specimen tested at 300 K, frequent changes in crack growth direction and crack branching at interfaces were observed in the optical micrographs which resulted in a highly rough fracture surface (Figures 2(a)

and 2(b)). At 573 and 823 K, the crack path was not as tortuous. A possible explanation can be based on the reduced reversibility of slip at high temperatures leading to easier crack initiation across the boundaries. Heavy oxidation of the crack surface was observed at 823 K, (Figure 2(c)) but not at 573 K (Figure 2(d)). Therefore, it is concluded that while crack closure at 300 K was roughness-induced, it was oxide-induced at 823 K, and both these mechanisms are insignificant at 573 K. Thus, the temperature-dependence of FCG could be rationalised taking into account the crack closure effects.
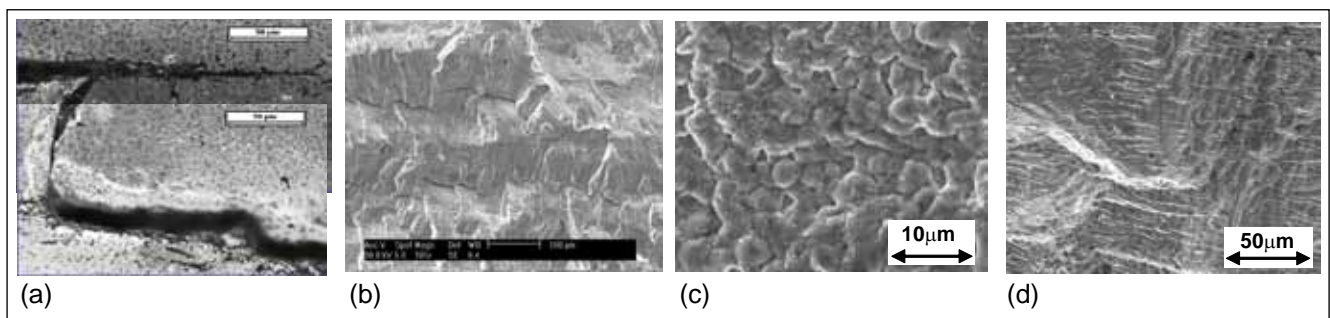
Fig. 2 *(a) The optical micrograph showing crack branching and crack path deflection in specimen tested at 300 K, (b) The rough fracture surface of the specimen in (a), (c) Heavy oxidation of the crack surface at 823 K and (d) Relatively smooth and oxidation-free fracture surface at 573 K*

III.11   Improvement of Type IV Cracking Resistance of P91 Steel

Modified 9Cr-1Mo steel (P91), is used extensively in the rationalised (1323 K/1hour) and tempered (1033 K/3hour) condition with grain size of 20-30µm in fossil power plants, steam generator of PFBR, petrochemical industries and many other heat transport systems due to its good mechanical properties up to 853 K and physical properties. However, the weldments of these steels are susceptible to Type IV cracking during service due to its low creep strength of the inter-critical and fine grained heat affected zone (ICHAZ and FGHAZ) and presence of strength gradient across the weld interface. These make strain localisation during creep and creep rupture life of weldment shorter than that of base metal. Addition of boron in modified 9Cr-1Mo steel (P91B) brings down the strength gradient across the weld interface and promotes uniform deformation behaviour. This was confirmed (Figure 1) from the tensile tests conducted on specimens with various heat affected zones simulated by heating them to peak temperatures in the range of 1073 -1273 K and cooling rapidly. In contrast to this, for simulated HAZ of P91, significant variation in the tensile properties was observed (Figure 2). As a result of reduction in the strength gradient the creep strength of the steel is improved significantly by boron addition. Creep test carried out at 873 K and 120 MPa showed that rupture life of P91 weldment is 1000 hours while creep test for P91B steel weld joint is still continuing even after
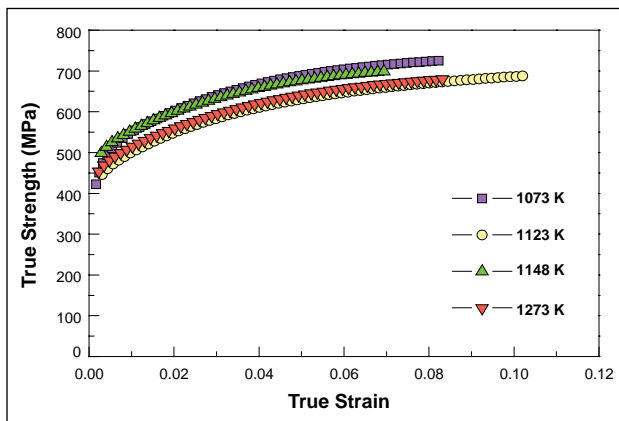
Fig. 1   *True stress-strain plot of P91B material subjected to different simulated heat treatment*
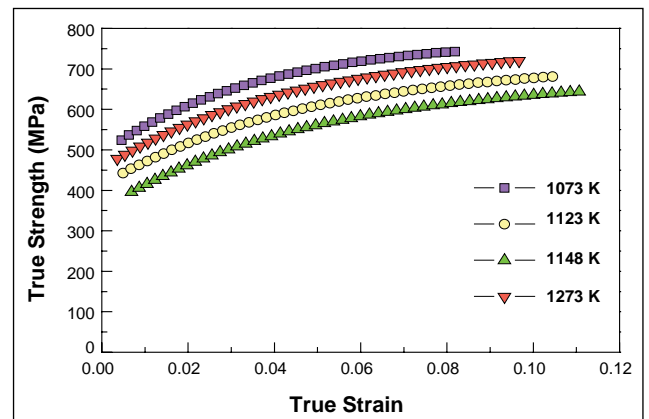
Fig. 2   *True stress-strain plot of P91 material subjected to different simulated heat treatment*
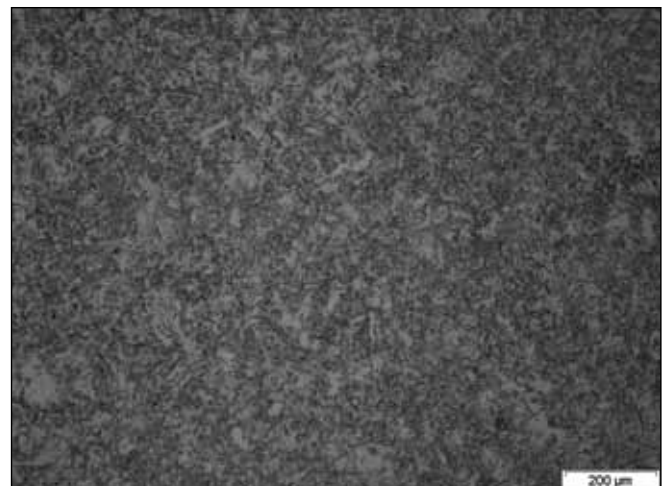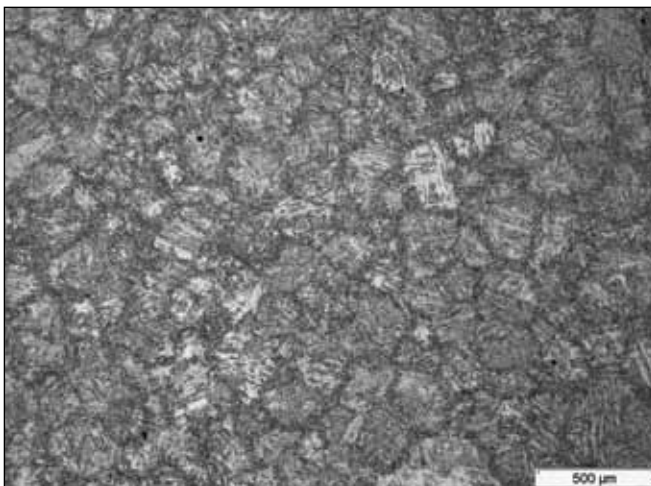
Fig. 3   *Microstructure ICHAZ simulated (1148 K/10min) Heat Affected Zone specimens after tempering (1033 K/3h) made from a) P91B and b) P91 steels*

completing 2000 hours of testing. Creep strain rate observed is much lower for P91B steel weldment than for the P91 steel weldment.

Heat affected zone microstructures of boron added modified 9Cr-1Mo steel show the prior austenite grain size in different parts of heat affected zone including ICHAZ,

does not vary much and is similar to that of the base metal. In contrast wide variation in the prior austenite grain size is observed in different parts of the heat affected zone of P91 steel without boron. Microstructures of simulated ICHAZs (1148 K/10 min) of both the steels are shown in Figure 3.

Retention of original prior austenite grain structure in the heat affected zone even after experiencing weld thermal cycle is the reason for improved creep properties of the heat affected zone of boron containing modified 9Cr-1Mo steel and its better resistance to Type IV cracking.

III.12 Experimental Investigations and Theoretical Modeling of Nitriding Behaviour of Inconel 600

Austenitic stainless steel is the preferred structural material for radiation detectors in fast breeder reactors due to its resistance to high radiation, sodium corrosion and high temperature strength. However, when stainless steel is exposed to nitrogen containing environments at high temperature (>723 K) in radiation detectors, there is a possibility of it getting nitrided which may affect the detector efficiency. Hence to avoid nitridation, nickel based Inconel 600 (75Ni-15Cr-8Fe) was chosen as an alternative structural material for radiation detectors since nickel is difficult to nitride. In this context, it is important to understand the nitriding kinetics of Inconel 600.

Inconel 600 was plasma nitrided in N_2-H_2 atmosphere using conventional DC plasma nitriding set up under 1 millibar pressure. Nitriding experiments were carried out at 723, 773, 823, 848 and 873 K for various time durations in the range of one to twenty four hours. The nitriding behaviour of Inconel 600 has been studied using both experimental techniques and theoretical calculations.

Figure 1 shows the optical microstructure and superimposed hardness profile of the cross section of the Inconel 600 surface plasma nitrided at 873 K for 24 hours. The nitride layer appears as a grayish featureless band on the surface having a sharp interface with the substrate. Very high hardness of ~1100 VHN was obtained in the nitride layer compared to that of Inconel substrate (~200 VHN). Even at the maximum temperature
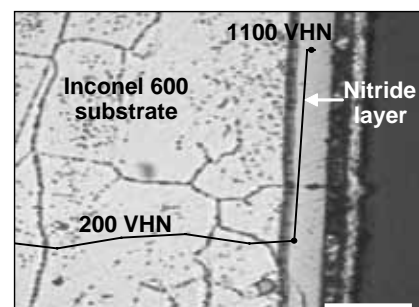
Fig. 1 *Optical microstructure and superimposed hardness profile across Inconel 600 plasma nitrided at 873 K for 24 hours*
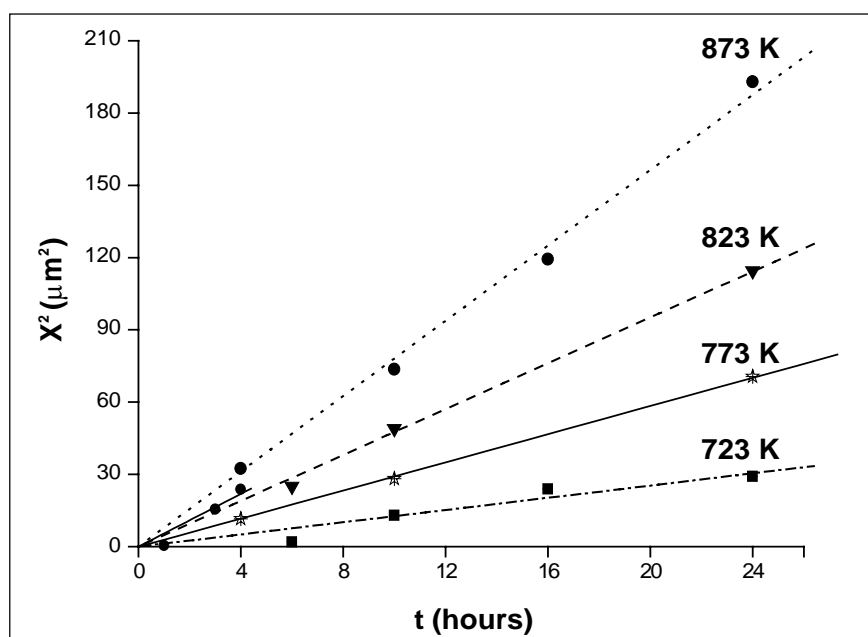
Fig. 2 *Plot of square of the nitride layer thickness versus time for various plasma nitriding temperatures*

of plasma nitriding i.e 873 K, only 14 μm thick nitride layer was obtained in Inconel 600. This value is much lower than the reported value for thickness of nitride layer in stainless steel (~200 μm) for the same temperature of exposure. Growth of the nitride layer in Inconel 600 was monitored as a function of temperature and time of plasma nitriding. The thickness of nitride layer was found to be proportional to the square root of time as shown in Figure 2 indicating that the process is diffusion controlled. Using the thickness of the nitride layer as the kinetic parameter, an Arrhenius type relationship was obtained between ln DN (where DN is the diffusion coefficient of nitrogen in Inconel) and reciprocal of temperature. Diffusion coefficient and activation energy values (Q) for diffusion of nitrogen in Inconel 600 obtained in this study was compared with the values reported in literature for similar systems, as shown in Table 1. Diffusion coefficient values agreed well with the values reported in literature. Quantitative elemental analysis carried out using the electron microprobe confirmed enrichment of nitrogen

Table 1 : Comparison of D_N and Q values obtained for nitrogen diffusion in various nickel based alloy systems			
Alloy	Temperature (K)	D_N (m^2/sec) x 10^{-16}	Q (eV)
Inconel 600 75Ni-15Cr-8Fe (present study)	873	5.43	0.63
	848	3.80	
	823	3.30	
	773	2.03	
	723	0.88	
Inconel 690 59Ni-29Cr-10Fe	673	1.00	1.1
Ni-20Cr-2Ti	923	8.00	0.43
Ni-5at%Cr	873	1.80	1.5

corresponding to the nitride layer. In-depth characterisation of the surface using X-ray diffraction, X-ray photo electron spectroscopy and transmission electron microscopy confirmed the presence of high volume fraction of fine CrN precipitates in the nitride layer.

Numerical computations using finite difference method, Dictra and Thermocalc were also used to predict the nitrogen diffusion profiles for various temperatures and durations of exposure. It has been reported that in Inconel matrix

CrN is the only stable phase for Chromium contents less than 22 at%. Hence, in the calculation, effect of the major alloying element (i.e.) Chromium has been taken into consideration for predicting the nitriding behaviour of Inconel 600. Figure 3(a) shows a comparison of the nitrogen concentration profiles obtained using Dictra and electron microprobe. Surface nitrogen concentration obtained using Dictra was found to be higher than the experimentally measured values. It is possible since the surface nitrogen concentration considered
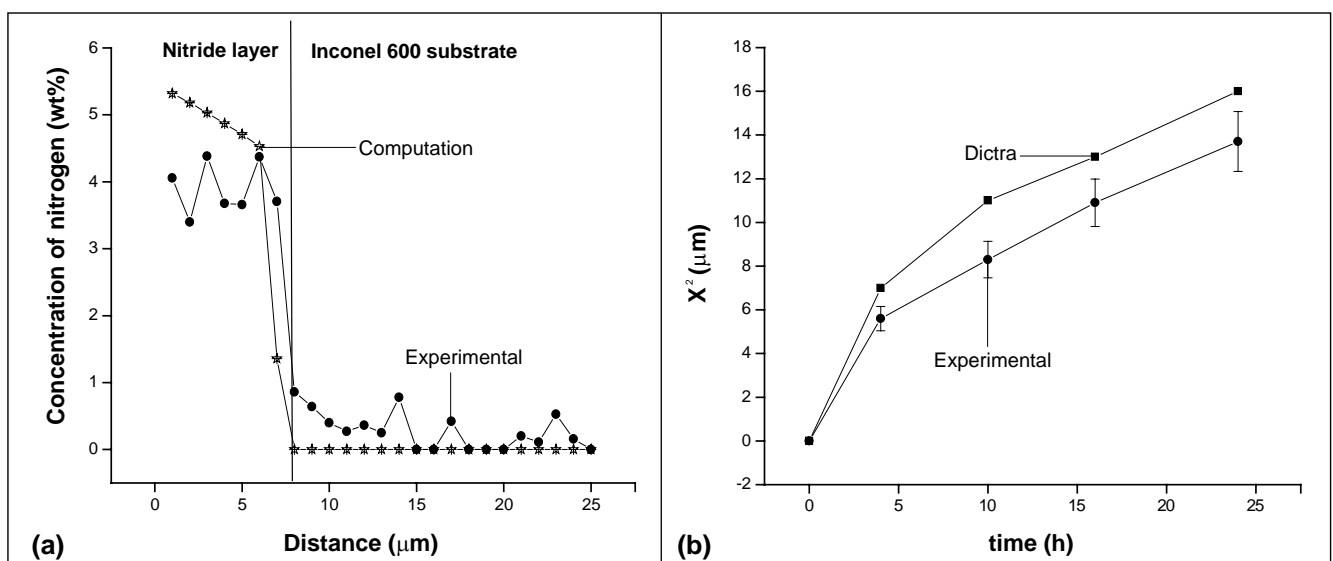
Fig. 3 *Comparison of (a) nitrogen concentration profiles and (b) nitride layer width obtained using experimental methods and numerical computation*

in the calculation is the equilibrium value corresponding to fcc/CrN phase boundary, whereas in the actual experiment sputtering effects also will decide the surface nitrogen content.

Other than the above mentioned disparity, reasonably good match was obtained for the predicted layer thickness as shown in Figure 3(b). Volume fraction of CrN precipitates in the nitride layer was also calculated as a function of distance from the surface for various temperatures and times of exposure. From the above studies, it was concluded that nitriding kinetics in Inconel 600 is slower than that in austenitic stainless steel and hence Inconel 600 is a better structural material for service in nitrogen containing atmospheres.

III.13 Laser Welding of Precision Engineering Components

Nd-YAG laser has been used extensively in the fabrication of small precision components at IDEAS, MMG. Some important laser welding works carried out in the recent past related to Eddy Current based Position Sensor (ECPS) and Sodium Leak Detector (SLD) in Diverse Safety Rod Drive Mechanism (DSRDM) of PFBR are briefly described here.

Laser welding of mineral insulated (MI) coil termination arrangement of ECPS for use in PFBR

In PFBR, there are three diverse safety rods (DSR) in the core, which during normal operation of the reactor, are held outside the active core region by the respective DSRDM. Whenever there is a SCRAM (reactor shutdown) signal, the electromagnet holding the rod gets de-energised and the DSR falls under gravity. At the end of free fall, the diverse safety rods is decelerated by a sodium dashpot and is brought to rest. The free fall time of DSR during SCRAM under normal operating condition is to be less than one second, including the response time of the electromagnet. ECPS is planned to be used for detecting the free fall of the diverse safety rods. Total length of the ECPS coil is around 100 meters and at both the ends, coil termination has to be carried out. This coil termination arrangement requires laser welding of small size precision components. Suitable design of termination was arrived at after conducting many trials. Figure 1 shows the general coil termination arrangement of ECPS and the welds to be carried out.

There are three welds to be carried out in the termination region. The first weld is between the MI cable sheath and 2 mm outer diameter portion of part no.1. The second weld is between 4.6 mm inner diameter portion of part no.1 and part no.2. The third weld is between part no.3 and part no.1. Before the start of weld 1, the dimensions of the MI cable were measured and found that the thickness of the stainless steel sheath used in the MI cable was 0.13 mm. From the MI cable, stainless steel sheath was removed carefully to a length of 5 mm to expose the copper lead and part no. 1 was inserted into the MI cable and pushed to a suitable length. Then, part no.2 was inserted into part no. 1 and the copper lead was passed through the sleeve portion (dimensions: 1.5 mm inner
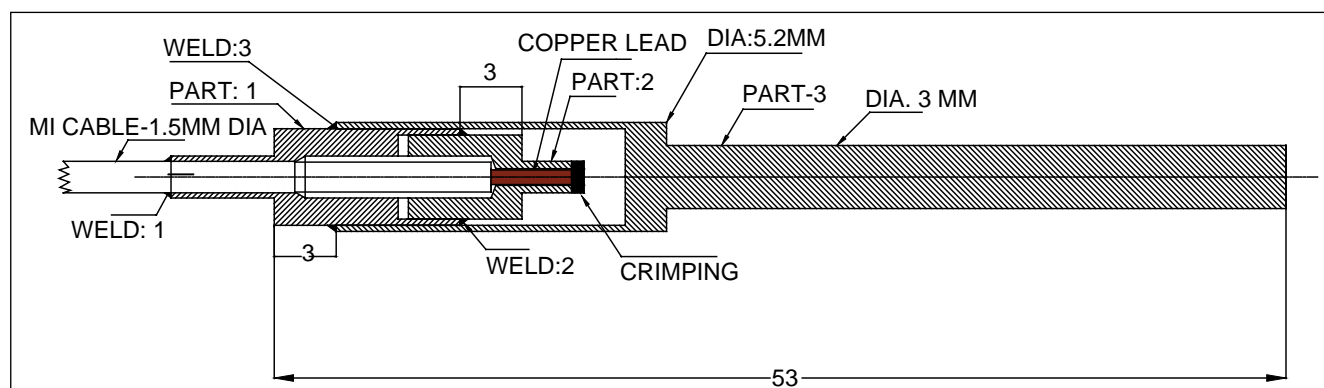
Fig. 1   *Sketch showing the general coil termination arrangement of eddy current based position sensor*
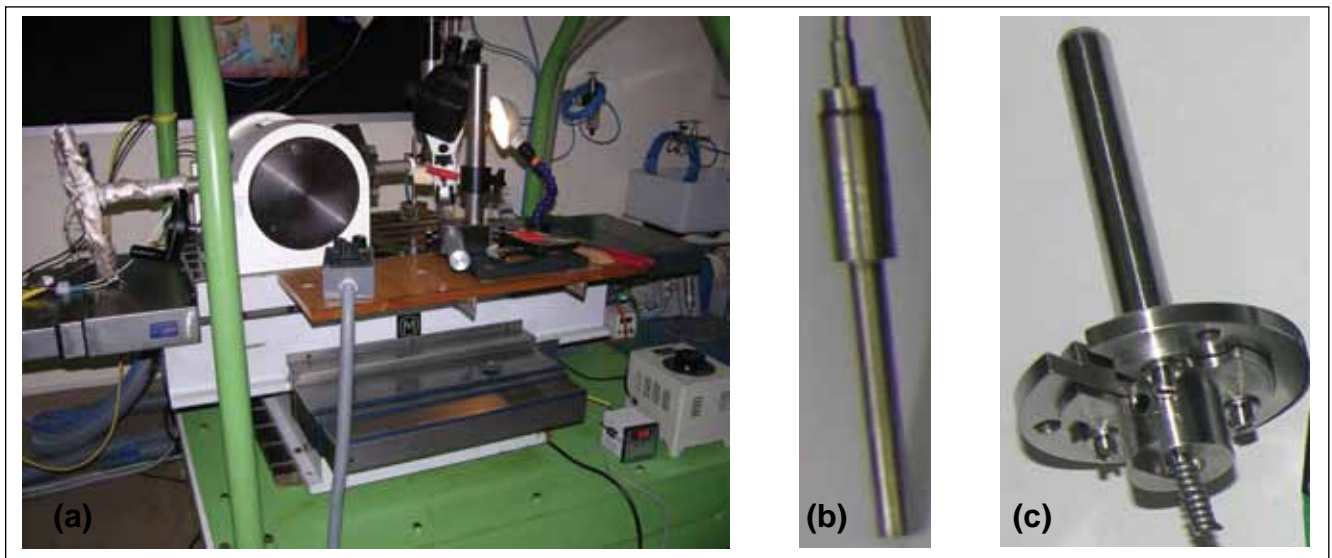
Fig. 2 *Photograph of (a) Laser welding set up for the ECPS coil termination, (b) Photograph of completed ECPS coil termination and (c) Photograph of completed sodium leak detector*

diameter and 3 mm length) of part no. 2. Copper and the sleeve of part no. 2 were crimped using a specially developed tool. Subsequently, weld no.1 was carried out between stainless steel sheath of MI cable and the part no. 1 followed by weld no. 2 between part no. 1 and 2 and weld no. 3 between part no. 1 and 3. During entire welding operation the MI cable was heated to 393 K to remove the moisture that would have entered inside the cable, using a specially made heating setup.

The completed welds were subjected to visual and radiographic inspection. The qualification welds which were carried out prior to the actual welds, were subjected to visual, radiographic inspection and helium leak testing to a level of less than 10^{-8} std cc/sec. Figure 2(a) shows the photograph of the laser welding set up and Figure 2(b) shows the photograph of the completed job.

Laser welding of components for the fabrication of sodium leak detector for use in PFBR

Sodium leak detector is housed inside the electromagnet assembly of DSRDM of PFBR to indicate if there is any leakage of sodium into the electromagnet. The fabrication of sodium leak detector required precision laser welding of few of its components. The laser-welding was carried out after standardisation of procedures involved. Sodium leak detectorconsisted of four components: pocket, sensor flange, support tube and bobbin. Figure 2 (c) shows the fabricated of sodium leak detector. The first weld was between the support tube and the sensor flange. Part of the support tube was inserted into the sensor flange and welded. This was a fillet weld by laser welding process. After winding 0.5 mm diameter MI cable on bobbin, the free leads of winding were inserted into support tube and the leads were taken out through the holes on the sensor flange of the above assembly. After taking out the free leads, bobbin was inserted into support tube of the above assembly and tack welded using laser. This was the second weld.

Following operations were carried out for each of the two welded joints: standardisation of laser welding parameters, metallographic sample preparation and examination of cut sections of welds as per prescribed procedure, actual welding of components as per welding procedure specification (WPS) prepared, followed by inspection by quality assurance group of PFBR. During weld qualification three consecutive welds were examined for depth of penetration by metallographic examinations in addition to dye penetrant test and visual examination. One pre and post weld samples were destructively tested before and after the actual welding.

Finally, sensor assembly was inserted into the pocket and was tack welded using laser at two places. Then a cap was kept in position, fastened to the pocket using the screws. The screws were then welded at two places by laser welding. These are third and fourth welds respectively. A total of four such sets of SLDs were fabricated.

III.14 Laser Raman Microscopic Studies of Passive Films Formed on 316LN Stainless Steels during Pitting in Chloride Solution

Austenitic stainless steels (SS) are prone to intergranular attack, which is caused by sensitisation. The problem of sensitisation is overcome by reducing the carbon content. Since low carbon grades have lower strength than normal grades, nitrogen is added to improve the strength to values comparable to those of the normal grades. High nitrogen stainless steel have become important structural materials for fast breeder reactors.

The role of nitrogen in the formation of passive films and providing the observed improvement in the resistance to pitting attacks is still not fully understood. Laser Raman Microscopy has been employed to carry out a systematic study. Electrochemical potentiodynamic polarisation tests were conducted on 316LN SS with different nitrogen contents at room temperature in deaerated 1M NaCl solution acidified to a pH of 1.6 by addition of 2 ml/l of HCl. Figure 1 shows the potentiodynamic polarisation curves of 316LN SS, which indicate that E_{pit} increases with increasing nitrogen content. After completion of the polarisation experiments in 1M NaCl, ex-situ Raman experiments were performed to characterise the surface film that caused improvement in the pitting corrosion resistance of 316LN SS with increasing nitrogen content.

The Raman spectra of 316LN SS with different nitrogen contents to assess the Raman shift range of 650-1150 cm^{-1} are shown in Figure 2. The spectra were recorded inside a pit. The laser
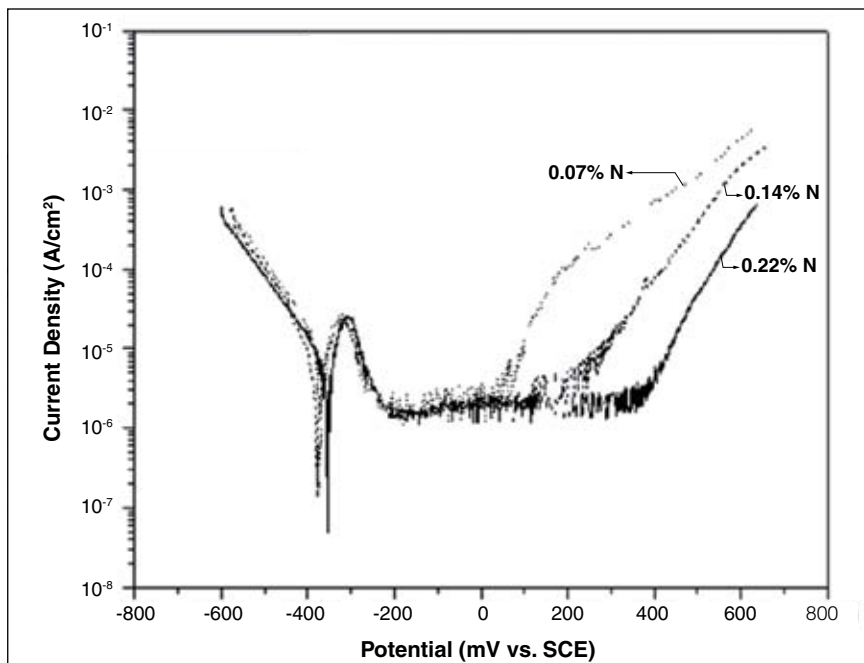
Fig. 1 *Electrochemical polarisation curves for type 316LN SS with different nitrogen contents in deaerated acidified 1M NaCl solution*
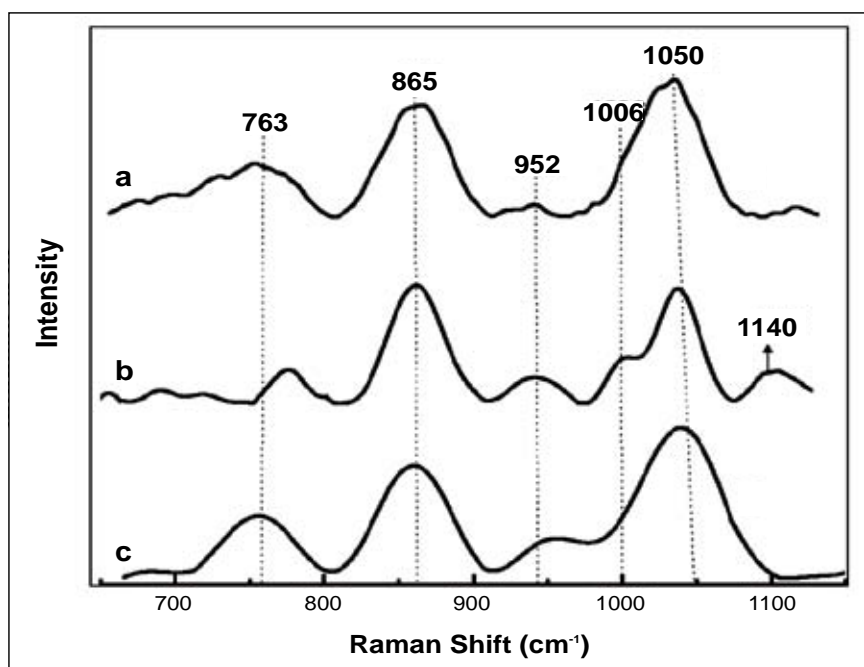
Fig. 2 *Raman spectra in the 650-1150 cm^{-1} range of 316LN SS with different nitrogen contents (a) 0.22 wt. % N, (b) 0.14 wt. % N and (c) 0.07 wt. % N*

excitation wavelength was 633 nm and the laser power was 8.6 mW. In addition to basic oxides of iron and chromium, the above Raman spectra showed a small peak at 1048-1050 cm^{-1} due to the
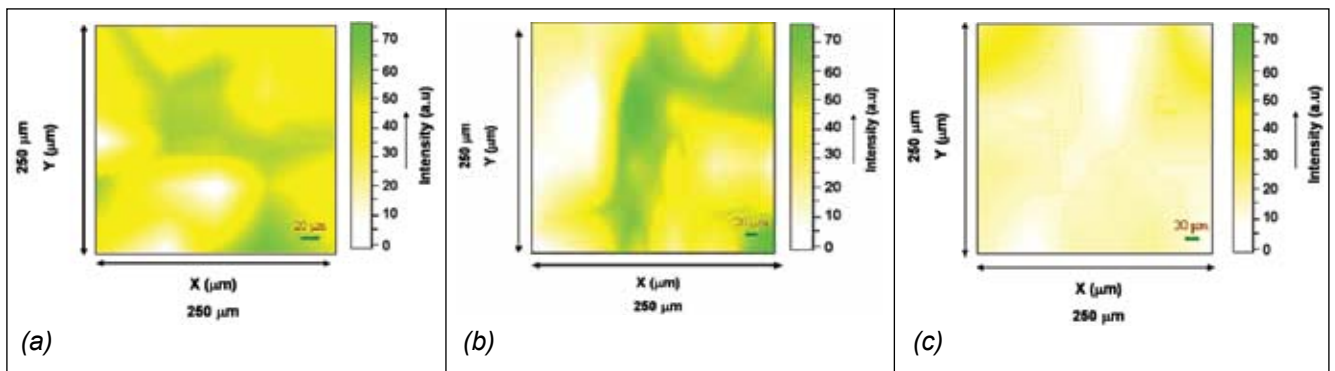
Fig. 3 *Distribution of nitrate ions in the surface films formed on type 316LN SS with different nitrogen contents*

presence of nitrates. Many reports suggested a synergistic effect between nitrogen and molybdenum, where molybdenum was believed to take part in the deprotonation of hydroxides. This created oxygen abundance in the inner regions of the passive film, thereby increasing the proton activity on the surface and assisted the formation of ammonium ions. The NH_4^+ ions may undergo feasible reactions to form the final stable compounds such as nitrates and nitrites, which are powerful corrosion inhibitors. The peak at 1140 cm^{-1} pertains to ammonium ions. Though the formation of nitrate

was evident from the present study, the identification of cation bonded to nitrate was rather difficult based on laser Raman spectroscopic experiments. However, the complexation of nitrogen with iron was expected over other elements, since nitrates form stable metal complex only with iron.

Figure 3 shows the Raman map of nitrate ions on the surface of the corroded 316 LN SS. It is seen that the distribution of nitrate ions on the surface increased with the increasing nitrogen content and was considerably higher in 316LN SS

with 0.14 and 0.22 wt% of nitrogen. Literature suggests that nitrogen and oxygen ions in the passive film combined to form nitrate ions which got incorporated into the passive film along with hydrated chloride ions, thereby increasing the pitting corrosion resistance. This study has further revealed that nitrate formation could be through the formation of ammonium ions (confirmed by the presence of Raman peak at 1140 cm^{-1}), followed by the complexation with iron chlorides and hydroxy chlorides to form a stable $[FeNO_3]^{2+}$ metal complex.

III.15 Non-destructive Measurement of Isotopic Ratio of Boron in Irradiated B$_4$C Pellets

The Fast Breeder Test Reactor (FBTR) employs a control rod that comprises a stack of nine B$_4$C pellets (39 mm dia and 40 mm length), 90% enriched in ^{10}B, contained in a stainless steel clad. These rods usually are replaced after a certain residence time. During reactor operation most part of these rods stay outside the core while only a small portion resides within the former. Thus at the time of their removal only a small fraction

of ^{10}B would have been consumed. Further, most of these pellets would retain their mechanical integrity expecting a few that would have undergone radiation damage. Production of B$_4$C containing enriched boron is an expensive and energy intensive process. Hence, it would be prudent to reuse the good B$_4$C pellets recovered from the spent control rods. Thus, an accurate evaluation of the isotopic fractions of ^{10}B and

^{11}B in the spent B$_4$C samples is necessary. If any technique that involves breaking of these pellets is used then the latter cannot be reused. Further such a method could also be tedious and could result in the chemical contamination of the sample for B$_4$C is one of the hardest materials known, next to diamond and cubic boron nitride. A non-destructive method would be most suited for the above application.

Such a method was developed in order to analyse the isotopic ratio of ^{10}B and ^{11}B present in the irradiated B_4C pellets with the help of a laser mass spectrometric (L-MS) facility that uses a home-built reflectron time-of-flight mass spectrometer (RTOFMS) housed inside a glove box. Compared to other mass spectrometry based methods, this is practically a non-destructive method.

In the laser mass spectrometric method only a few nanograms of the material is removed by vapourisation from the laser-irradiated spot of the surface, without any other physical damage to the pellet.

A schematic of this facility is shown in Figure 1 and a photograph of the same is presented in Figure 2. Initial experiments for standardising the method were done by using unirradiated B_4C samples. Subsequently, the isotopic ratio of ^{10}B to ^{11}B in five irradiated B_4C pellets, namely 1st, 3rd, 6th, 8th and 9th pellets (9th being the bottom most pellet) from a spent control rod removed from FBTR were measured. All other pellets excepting the 1st and 3rd were received as broken pieces with an irregular shape. In the 1st and 3rd pellets, measurements were carried out on both the faces of the cylinder and across its diameter. Results indicated that the ^{10}B content had decreased only marginally. In order to hold and analyse the other pellets that were received in the broken condition suitable sample holders were fabricated out of graphite. The isotopic ratio between ^{10}B and ^{11}B could be measured on only one face of these pellets. The fraction of ^{10}B in these specimens was deduced from the ratio of the intensity of the peaks corresponding to the isotopes of ^{10}B and ^{11}B for a given laser pulse
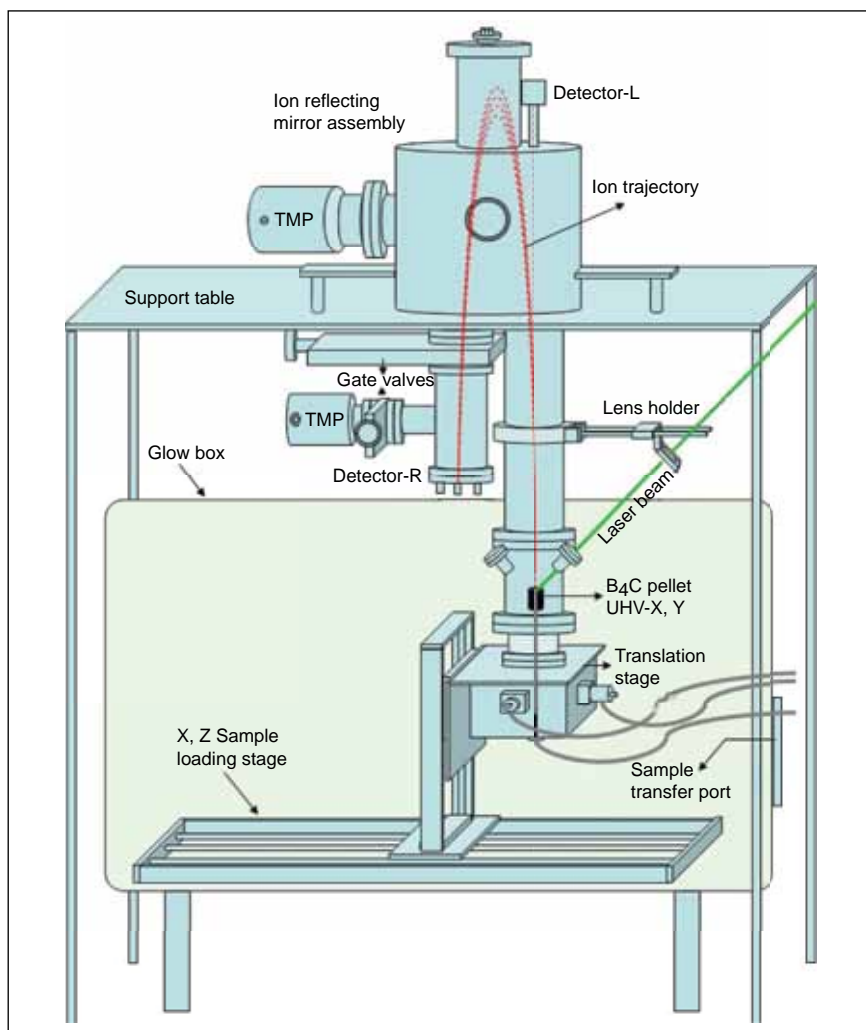
Fig. 1 *Schematic of the in-house developed laser mass spectrometry (L-MS) facility*

Fig. 2 *Photograph of the L-MS facility*

(vapourisation and ionisation in one single step). The results obtained with all the pellets analysed by us so far indicated no significant ($\leq$ 1%) reduction in the isotopic content of ^{10}B. The mass spectrum evidenced the presence of ^7Li and the absence of ^6Li. This results supports the fact that ^{10}B had undergone (n,α) reaction during irradiation. However, in the experiments carried out so far the amount of ^7Li could not be quantified. A typical mass spectrum is shown in Figure 3 and the variation of ^{10}B content as a function of distance across the face of a pellet is shown in Figure 4.
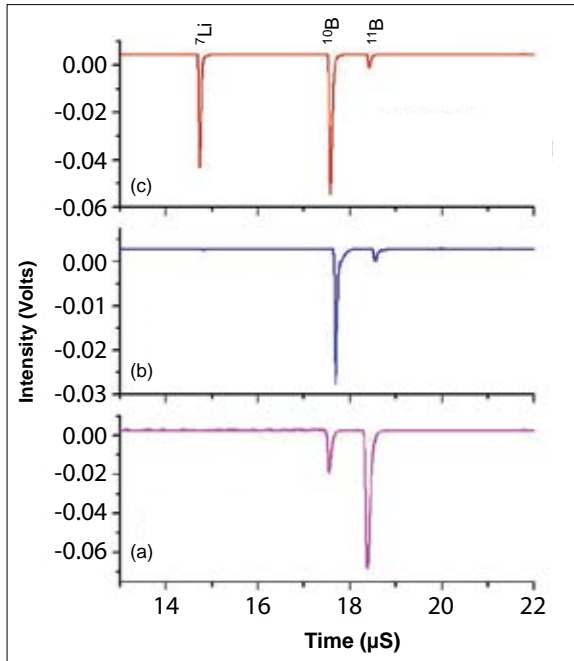
Fig. 3   Typical mass spectrum (a) Unirradiated Natural B_4C, (b) Unirradiated FBTR Control road B_4C pellet and (c) Irradiated FBTR Control rod B_4C pellet
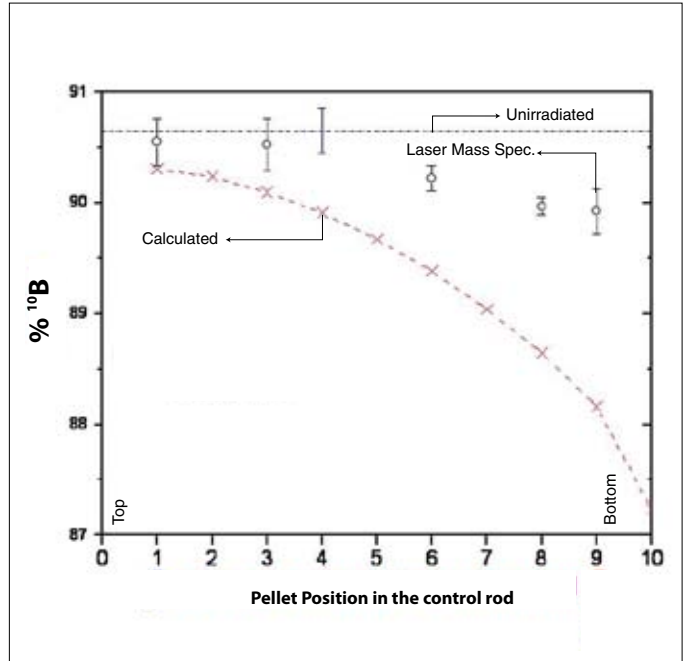
Fig. 4   Measured % ^{10}B in comparison with calculated value

III.16   Residual Stress Measurement in A-TIG Weld Joints using an Ultrasonic Technique

The critically refracted longitudinal (L_{CR}) ultrasonic waves have been used for the assessment of surface/ sub-surface longitudinal residual stresses in AISI type 316LN stainless steel welded joints made by TIG and A-TIG welding processes. Figure 1 shows the variation in the longitudinal residual stresses obtained across the weld joint of AISI type 316 LN stainless steel weld joints made by TIG and A-TIG welding processes. The maximum tensile stress of 225 MPa is observed at 6 mm away from the weld centre for the weld joint made with TIG welding process. As the distance is moved away from the weld centre, there is a changeover from tensile to compressive stress at about 20-25 mm away from weld centre on both sides of the weld. The maximum compressive stress obtained is about 20 MPa at 50 mm distance from the weld centre. The maximum tensile stress observed for the weld joint made with A-TIG welding process is 45 MPa at the weld centre and the maximum compressive stress observed is around 12 MPa at about 10 mm distance from the weld centre line. Maximum error bar is found to be $\pm$ 3MPa in both the above weld joints (TIG and A-TIG). It is clear from the residual stress profiles shown in Figure 1, that the weld regions exhibited maximum tensile stresses. Tensile residual stress present in A-TIG weld joint is significantly lower than that of the weld joint made by TIG welding. This has been attributed to the smaller weld metal volume in the case of A-TIG weld joint compared to that of the TIG weld joint. The A-TIG weld joint was made in single pass

without filler metal addition while the multipass TIG weld was made using six passes with filler metal addition. The benefit in terms of the reduction in the residual stresses in A-TIG weld joint is very significant. The compressive residual stresses are smaller and their profiles are comparable in both the weld joints. These measurements indicate that the L_{CR} wave based method is useful to assess surface/sub-surface residual stresses in the weld direction, with respect to their nature and magnitude in welded joints. The L_{CR} method offers advantages which are not possible with other acoustic methods, such as Rayleigh method, acoustic birefringence and the method based on longitudinal volume waves. L_{CR} wave method is less sensitive to texture, very sensitive to stress and capable of identifying the stress profiles more
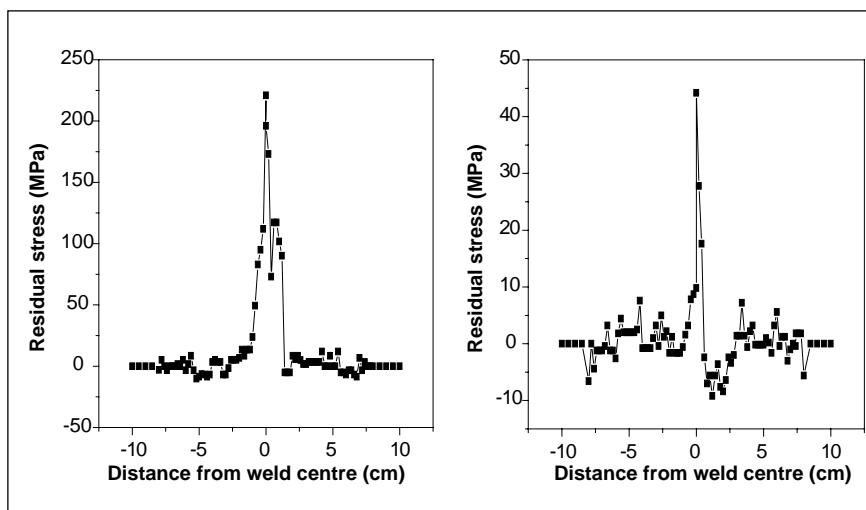
Fig. 1 *Residual stress profiles across the 316 LN stainless steel weld joint made by TIG and A-TIG welding processes*

accurately. Furthermore, L_{CR} wave method does not require opposite parallel surface as other acoustic methods and therefore, does not impose any geometric limitations on test specimens. This residual stress measurement method has several advantages including high spatial resolution for longitudinal residual stresses across the weld joints, easy and simple to use, cost effective and non-destructive.

III.17 Evolution of the Eddy Current Position Sensing Technique for Measurement of Free Fall Time of Diverse Safety Rod

In PFBR, there are three Diverse Safety Rods (DSR) which are held outside the active core by their respective Diverse Safety Rod Drive Mechanisms (DSRDMs). An Electromagnet (EM) at the lower end of the mobile assembly of DSRDM holds the head of Diverse Safety Rod. During normal operation, DSR is parked above the core and is always within its sheath. On receiving SCRAM signal, the electromagnet de-energises and drops the DSR, which falls under gravity in sodium. The free fall time of DSR plus the response time of the electromagnet should be within prescribed limits to ensure fast

shutdown of the reactor. The free fall time is required to be monitored during each SCRAM action. It is mandatory to measure its free fall time and ensure that the DSR has dropped within prescribed time limit. For measurement of free fall time an Eddy Current Position Sensor (ECPS) has been developed.

ECPS version 1

The sensor shall not have any wired connectivity from the DSR subassembly to be routed and brought out of the reactor. This single salient design specification has made the development a very challenging task. To circumvent

this problem, an indirect excitation through inductive coupling was
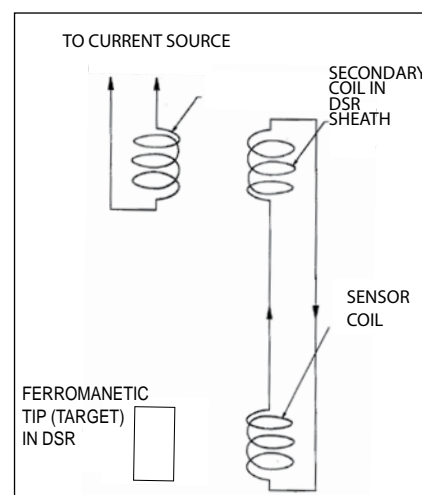
Fig. 1 *Schematic of ECPS version 1*

incorporated in the design, the schematic of which is shown in Figure 1. The primary coil was excited with a 200 mA constant current frequency driver. The induced voltage in secondary would drive a circulating current in sensor coil. The magnitude and phase of this current depends on the total impedance of the secondary and sensor coil. When the target, which represents diverse safety rods is inserted towards the sensor coil, the impedance of sensor coil changes and is measured as change in voltage across the primary coil. The change in the voltage of the primary coil indicates the presence of the target near the sensor coil. In the room temperature experiments itself, there was no appreciable response on the primary coil side for this configuration. The signal was lost in the noise, which was of the order of a fraction of mV at the primary coil.

ECPS version 2

A drawback in the earlier configuration was that the signal of the order of microvolt was buried in a measure of 3 to 6 volts on the primary side. Though there was measurable variation on the secondary coil side, variation on the primary coil side was below the measurable limit. In order to overcome this limitation, a signal transfer and a pickup coil were incorporated. The introduction of separate signal transfer and pick-up coil improved the signal to noise ratio many fold from 10^{-6} to 10^{-2}. With this lab scale results, coils suitable for sodium immersion and high temperature operation were manufactured and tested. The results were very encouraging and sensitivity of the order of minimum 5% was assured at various operating temperatures.

ECPS version 3

In the due course of development, it was realised that significant axial misalignment of the order of 45 mm would get introduced between the primary and secondary coils of position sensor during operation of the reactor. This again led to ECPS version 3 whose schematic is shown in Figure 3. In this configuration, on the DSRDM side, there are two pick up coils and one primary coil. On the sheath side, there is one secondary coil and one sensor coil. During the initial positioning, bottom pickup coil is under the influence of secondary coil and when 45 mm misalignment is introduced, the top pick up is under the influence
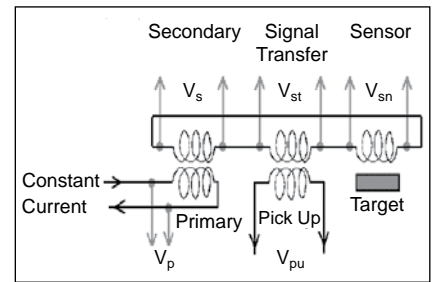
Fig. 2 *Schematic of ECPS version 2*

of secondary coil. Thus the axial misalignment was taken care. The sensitivity of the designed system, which is a measure of detection of the system was obtained through the experiments in sodium and is shown in Figure 4.

Thus, a novel technique to detect position of diverse safety rods based on eddy current and variation in inductance has been developed which overcomes constraints of no direct electrical connection, high temperature sodium atmosphere, space constraints and variation in axial position between primary and secondary side coils during reactor operation. Successful engineering model testing in sodium of eddy current position sensor to detect DSR position is a harbinger towards implementation of this system for measurement of free fall time of DSR in reactor.
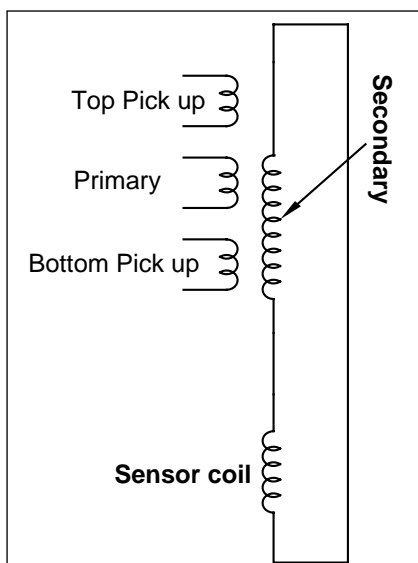
Fig. 3 *Schematic of ECPS version 3*
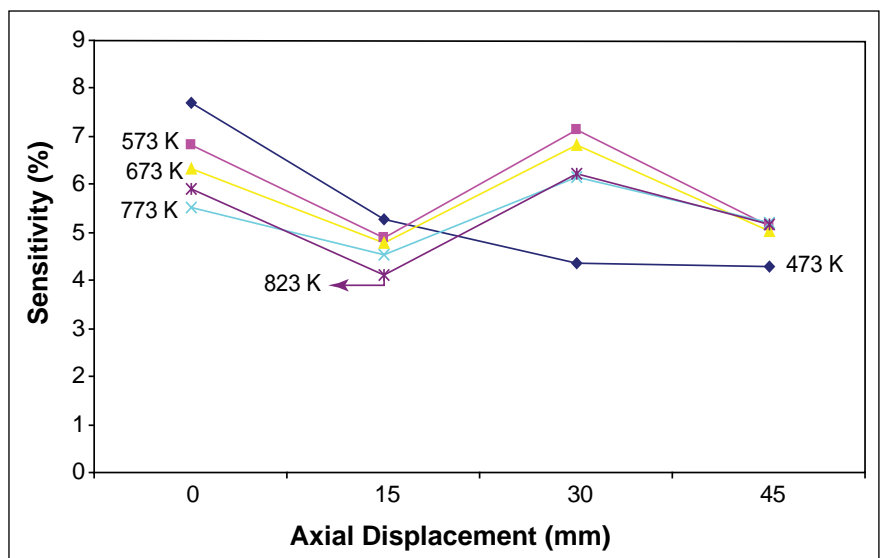
Fig. 4 *Sensitivity plot of ECPS version 3*

III.18 Modeling Studies of Small Specimen Tests and Experimental Validation

Small specimen mechanical test techniques are viable alternatives to conventional mechanical tests especially in situations when there is very little volume available for testing like in weld-joints, failure analysis, coatings, new materials, residual life assessment of plant components etc. These test techniques are based on the use of small disc type specimens of sizes ranging from 3-8 mm in diameters and thicknesses 0.3-1.0 mm which have no corresponding large specimen equivalent. The three most popular techniques are (i) shear punch, (ii) small punch and (iii) spherical indentation tests. These tests largely involve loading a clamped specimen with a disc shaped indenter and analysing the resulting load-displacement data obtained during the deformation process. In all these test techniques, evaluating the required tensile and fracture properties of the material (data inversion) becomes challenging due to the presence of inhomogeneous stress-strain states caused by complex loading conditions. Numerical simulation of the small specimen tests using finite element modeling (FEM) has been initiated to study the deformation behaviour of smaller specimens and for extracting practically useful information.

The shear punch test involving blanking of disc specimen (8 mm diameter & 0.5 mm thick) with a flat cylindrical punch has been analysed using FEM to study the specimen deformation up to yielding and validate the results with experimental data. The results indicated a large influence of the punch compliance on the elastic portion of load-displacement plot. This is shown in Figure 1 where simulated loading curve with (i) punch displacement (elastic punch condition) is markedly different from that of (ii) the specimen displacement (rigid punch condition). By shifting the point of displacement measurement from punch movement to the bottom surface of specimen in the experiments, the elastic loading lines of experimental curve matched well with the FEM generated curve (Figure 1). Based on the development of plasticity through the specimen thickness, the stress state was found to be primarily shear up to yielding. This was also reflected in the observation that the experimental yield stress values satisfied the von Mises relation $\sigma_{ys} = 1.73\tau_{ys}$. This study was used to rationalise the method of estimating shear yield strength using the 0.2% offset definition so as to enable reliable estimation of tensile yield strength of irradiated alloys from shear punch tests using the von Mises yield relation.

The finite element modeling of Ball-Indentation test carried out in collaboration with IIT Mumbai, has aided in identifying the compliances of the test fixtures and in visualising pile-up effects associated with indentation process. There is a good overlap of the FEM generated load-depth plot with the experimental data after including the ball holder in the model. The effects of pile-up were visualised through simulations and expressions for pile-up corrections verified. The model is presently used for generating a set of L-h (load-depth) curves for various combinations of YS (yield strength) and n (strain hardening exponent), and developing an inversion methodology based on an optimisation technique for a direct
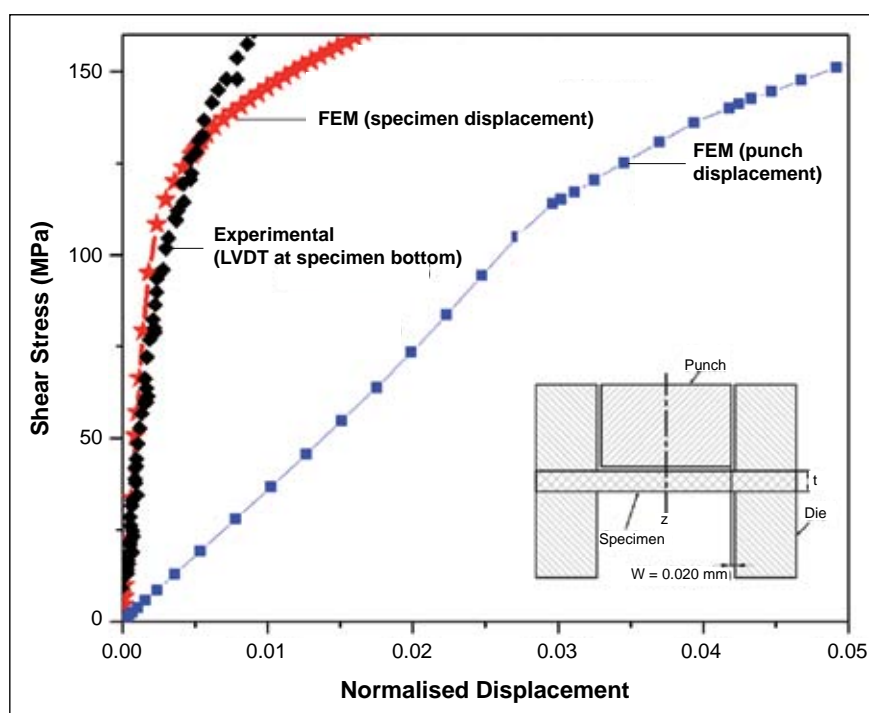
Fig. 1   *Comparison of the elastic portion of the load-displacements plots of shear punch experiments with that generated from the FEM (Inset shows the shear punch loading configuration)*
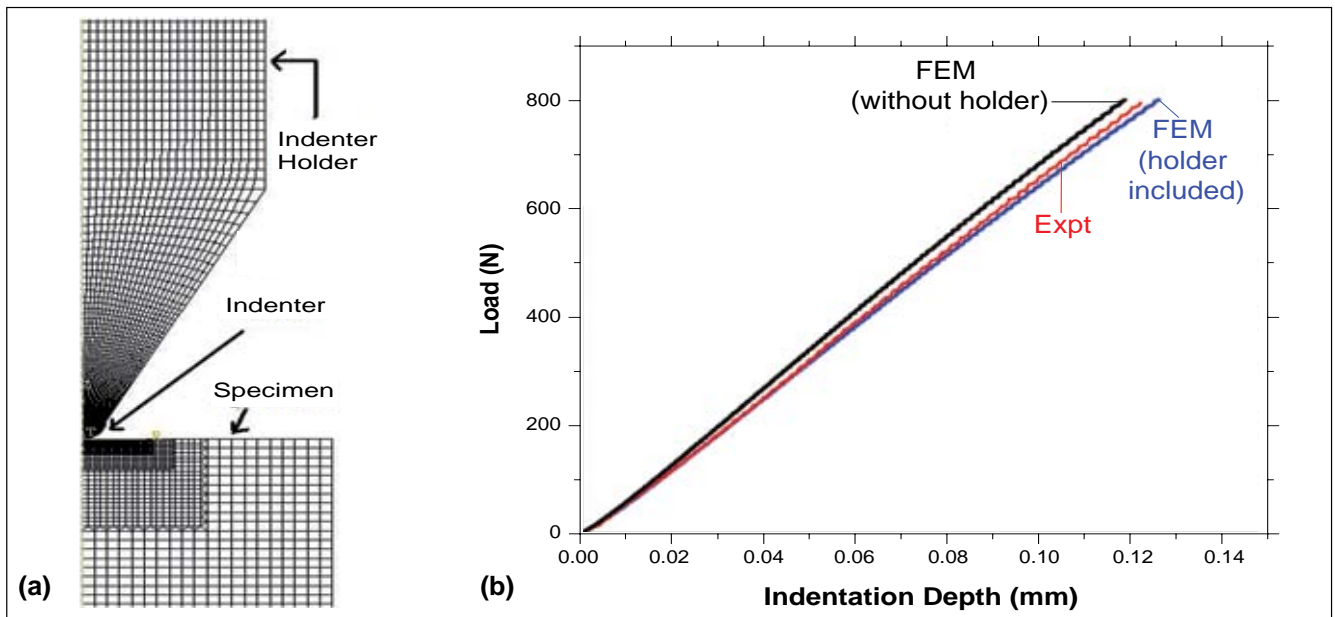
Fig. 2 *(a) FEM of the spherical indentation and (b) Comparison of the load–depth plot of experiments with that generated from FEM*

evaluation of σ-ε (stress-strain) curve from a given experimental L-h data (Figures 2 (a) and 2 (b)).

The small punch test involving the deformation of a clamped disc specimen (10 x 10 x 0.5 mm) under a spherical punch (2.5 mm diameter) has also been modeled using a general purpose finite element solver to understand deformation behaviour in the specimen. Figure 3(a) shows the comparison between the FEM and experimental load displacement curves for SS304. Figure 3(b) shows the plastic strain distribution in the specimen at peak load. Efforts are underway to develop an in-house finite element code to study the specimen deformation in small specimen test. The code
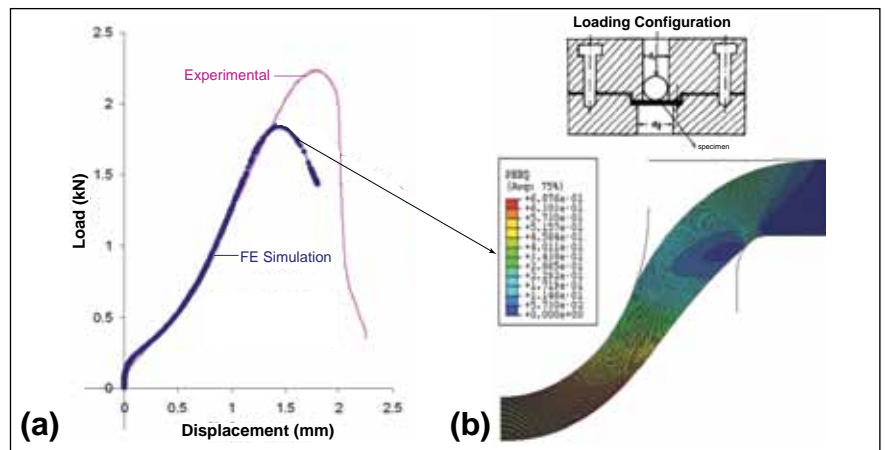
Fig. 3 *(a) Comparison of FEM simulated curve and experimental curve of small punch test and (b) Plastic strain distribution in the specimen at peak load*

development is based on the updated Lagrangian formulation to simulate the finite elasto-plastic deformation. An automatic triangular mesh generator is built in

to the code for generation of meshes of varying sizes. The code is capable of handling the contact nonlinearities that arise during the simulation of the small specimen test.

III.19 Development of Ultrasonic Guided Wave Based Methodology for Inspection of Hexcan Sheaths of Fuel Subassemblies of PFBR

Fuel subassemblies of Prototype Fast Breeder Reactor (PFBR)

consist of a hexagonal wrapper tube (Hexcan) that houses fuel pins.

The hexcans of PFBR are 3600 mm long and made up of 3.2 mm thick

20% cold worked alloy D9 (Ti-modified 316 austenitic stainless steel). Structural integrity of the hexcan sheath is important as any failure of this during service may result in separation of fuel pins from the subassembly, thus interfering with fuel subassembly unloading operation and/or failure of fuel pins leading to contamination of the coolant with fuel and radioactive fission products. Hence, stringent nondestructive quality control of hexcan sheath is essential. This demands that the nondestructive evaluation techniques employed to be sensitive to detect defects of the order of 10 mm length x 200 µm width x 100 µm diameter in hexcan sheaths.

Scanning of large area (~ 3600 x 75 mm^2 x 6 faces / subassembly) using conventional angle beam ultrasonic testing is highly time consuming. Hence, an alternate methodology based on guided waves is envisaged for rapid inspection of the hexcan sheath. In ultrasonic surface waves, the

energy is contained within about one wavelength depth and can travel along the surface of a component for a long distance with low attenuation. When the inspected component wall thickness is comparable to the wavelength of the ultrasonic surface waves, the wave propagates along the full thickness and is guided by the two surfaces of the component and is known as 'Guided Waves'. Main advantages of the guided waves are long distance inspection from single probe position and very good overall defect detection sensitivity. Based on these advantages of employing guided waves, inspection of hexcan sheath using guided waves has been attempted. In order to establish an inspection procedure, reference defects (EDM notches) of 200 µm width, two different lengths (6 and 12 mm) and three different depths (100, 150 and 300 µm) were made on various faces of a 3.2 mm thick and 500 mm long hexcan calibration tube. The experimental setup along with the hexcan calibration
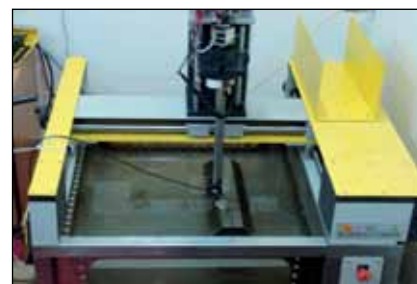
Fig. 1 *Photograph of the immersion guided wave experimental set up*

tube used for developing immersion guided wave methodology is shown in Figure 1. A typical collated B-scan image obtained on a face containing longitudinal ID defects of varying dimension is shown in Figure 2. From this, it is evident that even fine defects of the order of 6 mm length x 200 µm width x 100 µm diameter could be detected with reliability. Similar detection sensitivity could also be obtained for outer diameter as well as corner defects. Using the developed immersion guided wave based methodology; complete inspection of hexcan sheath could be established.
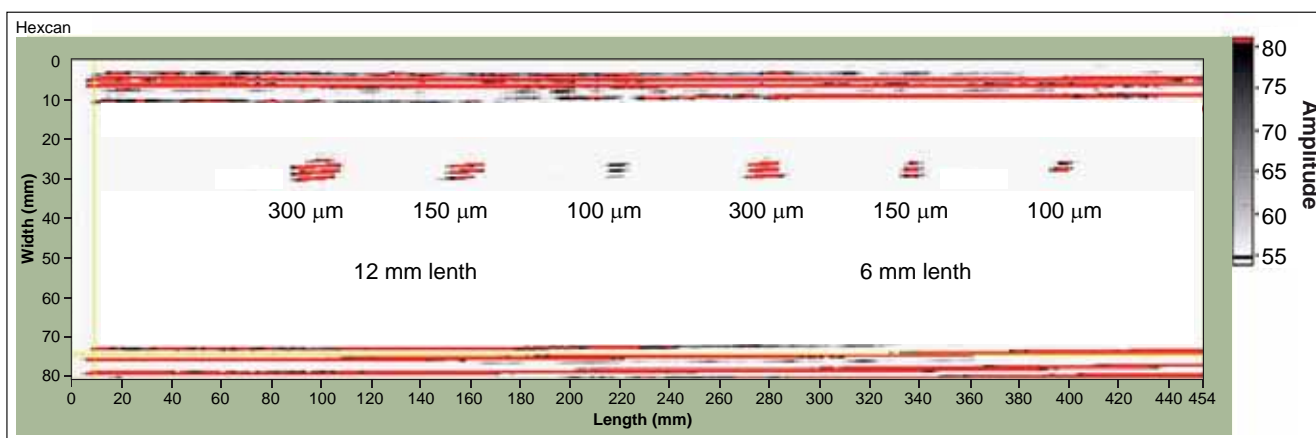
Fig. 2 *Collated B-scan image of longitudinal inner diameter defects in a face of the hexcan calibration tube*

III.20 Development of Intumescent Material for Extinguishing Sodium Fire

In fast breeder reactors, in the event of sodium leakage,

sodium fire is inevitable and is an exothermal oxidation of metal

by oxygen, moisture and carbon dioxide. It is necessary to

develop suitable and efficient fire extinguisher. In principle, sodium fire can be extinguished either by removing oxygen or by cooling the sodium. Self-extinguishment, dilution of oxygen with an inert gas, and covering the surface of the sodium with an extinguishant powder are popular means to extinguish sodium fire. Conventional 'D' class fire extinguisher like Dry Chemical Powder (DCP) effectively controls sodium fire whereas the quantity required is very large and possesses disadvantages in its removal and disposal after use.

Phosphorus containing non-halogenated intumescent material with excellent sodium extinguishing property has been developed in collaboration with Kamaraj College of Engineering and Technology, Virudhunagar. Intumescent material, on heating, forms a charred layer of cellular foam on the surface of the material, providing resistance
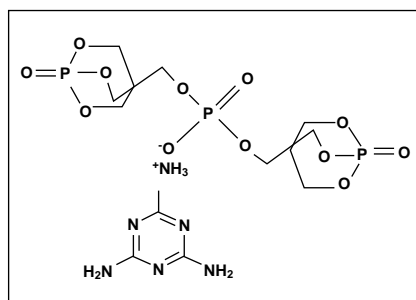
Fig. 1 *Melamine derivative of PEPA*

to heat and mass transfer. In-situ expansion of the intumescent material extinguishes sodium fire quickly, effectively and without much environmental pollution.

The intumescent behaviour of indigenously synthesised melamine derivative of pentaerythritol polyphosphate (Figure 1) and its suitability as sodium fire extinguisher has been studied on small scale sodium fire. When applied over sodium fire, the free flowing fine powder of this intumescent material expands about 200 times (Figure 2) and
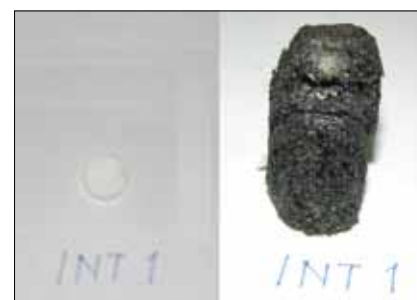
Fig. 2 *Intumescence on heating*

covers the sodium fire effectively and extinguishes the sodium fire by preventing the oxygen supply. The quantity required for extinguishing the sodium fire depends on the sodium pool area and it is measured to be 1 g/cm^2.

It was also observed that there was secondary fire due to the combustion of the intumescent material at 1200 K (temperature of sodium fire). Attempts are being made to improve the fire retardancy by incorporating additives such as nano silicates and functionalised carbon nanotubes.

III.21 Formal Equivalence Checking of Digital Designs

For Safety Systems of PFBR, a number of complex digital circuits using VLSI techniques have been designed and developed. These designs have been implemented using Very High Speed Integrated Circuit (VHSIC) Hardware Description Language (VHDL).

The design of any safety system – hardware or software - needs to be verified as to whether it meets the required specification. During the software development, concurrent to every stage of the life cycle, software verification and validation

is performed. Similarly for digital hardware, we have functional verification and formal verification. Functional verification involves exercising the given Design Under Test (DUT) by input test vectors as needed by a test plan and observing the outputs. For this purpose, hardware verification languages are used.

Formal verification attempts to prove the functional correctness of a system with respect to a certain formal specification. A formal specification is different from other design specifications like

the Register Transfer Level (RTL) etc., as the former describes *what* the system should do in contrast to the latter which describes *how* the system should do. There are several levels of abstraction for describing a design that includes, order of decreasing levels of abstraction: behavioural level, register transfer level, gate level, transistor level and layout level. A design description at a higher level of abstraction is more formal than a design description at a lower level. For example, a behavioural description of a design is more formal than a RTL description of

the same design. It should be noted that a design can never be stated as *correct* in isolation, but only *correct with respect to a given specification*. The formal equivalence checking involves comparing models at different levels of abstraction, for example, a Transaction Level Model (TLM) (a higher level of abstraction) – with the given RTL (lower level of abstraction).

After the successful completion of our earlier project "Functional verification of digital designs", one more collaboration project was undertaken with Indian Institute of Technology, Madras (IIT-M) for the "Formal equivalence checking of digital designs". In this project, six

VHDL designs from IGCAR and one VHDL design from BARC are subjected to formal equivalence checking. The design flow of the project is shown in Figure 1. In the first phase, specifications and RTL code of all the designs are handed over to the IIT-M team. In the second phase, from the given specification of each design, IIT-M has to develop very high level abstract models using a highly behavioural language like bluespec. The high level bluespec code is synthesised and a verilog code is resulted. Then formal equivalence checking of the developed model with the given RTL code from IGCAR and BARC is performed using FormalPro tool. Formal equivalence checking of
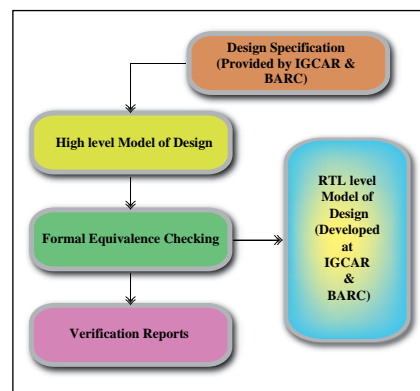
Fig. 1   Design Flow

VHDL code (Supplied by IGCAR and BARC) and verilog code (generated from Bluespec) is done both functionally and structurally. Formal equivalence checking of most of the designs is complete and reports are under progress.

III.22   Development of Sodium Flowmeters using Samarium Cobalt Rare Earth Magnet

Permanent Magnet Flow Meter (PMFM) made with ALNICO-5 is mainly used for measuring flow in sodium circuits. A new compact PMFM with Samarium and Cobalt (SmCo), which is having higher coercivity and energy product than ALNICO-5 has been developed. The magnetic flux density obtained at the centre of air gap was 60%

higher than the flux density of ALNICO-5.

The 20 NB SmCo PMFM was fabricated and installed in 500 kW loop to calibrate against a reference meter. Sensitivity of the reference permanent magnet flow meter was 0.27 mV/m^3/h. Calibration runs were conducted at different

Fig. 1   20 NB SmCo permanent magnet flow meter
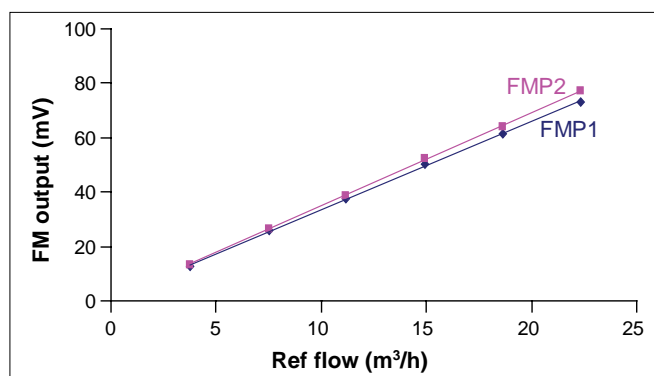
Fig. 2   Flow meter output versus reference flow
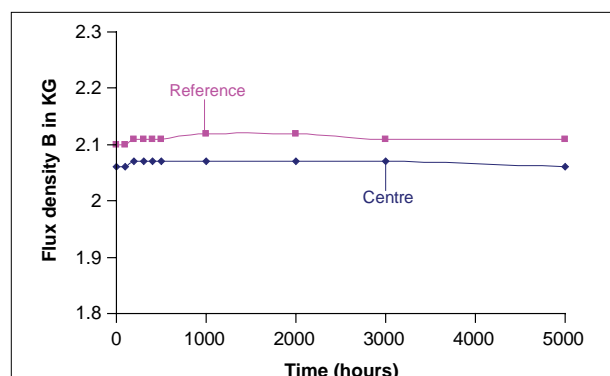
Fig. 3   Flux density versus time

temperatures of 573, 673 and 773 K and at different flow rates. Photograph of the 20 NB SmCo PMFM is given in Figure 1. Sensitivity of the SmCo PMFM was found to be 3.4 mV/m^3/h compared to 2.1 mV/m^3/h with ALNICO-5. Calibration curve of the flowmeter is given in Figure 2.

Two SmCo magnet assemblies from the same lot were used for stability testing. Flux density of the magnet assemblies were measured at the centre of air gap and also at a reference point. Both assemblies were electrically stabilised at 5% below the original flux density value by the process known as AC knock down. Magnet assembly-1 is used for the stability testing at operating temperature of 423K. The magnet assembly-1 was subjected to three rapid heating and cooling cycles at this temperature and flux density was noted after each cycle. Later it was subjected to three gradual heating and cooling cycles at the same temperature. No significant change in the flux density was observed. Long term stability of this stabilised magnet is tested by keeping the magnet in the furnace at 373K for five thousand hours. During the long term stability test magnet assembly was removed from furnace at intervals, cooled to room temperature and flux density at the air gap center and reference point was measured. Negligible change in flux density over a period of 5000 hours was observed as shown in Figure 3.

In order to accelerate the long term stability test, magnet assembly-2 was subjected to rapid and gradual heating cycles at 523K. It was found that the flux density remains steady.

SmCo magnet flow meter gives around 60 % high sensitivity for the same size and weight compared to ALNICO-5 magnet flow meter. Stability of the magnet with time and temperature is found to be good. These compact flow meters can be deployed in future reactors.

III.23   End of Life Tests in PHENIX

In order to achieve the desired levels of safety of public and operating personnel, integrity of all the systems and components have to be assured. This is achieved through rigorous analysis of various reactor systems and by taking care of all possible loadings through out the reactor life. Several design tools are employed for this purpose. Validation of these tools against benchmark data is very important. Availability of reactor data for this purpose is most warranted. The French fast reactor PHENIX, which was permanently shutdown in late 2009 after its 56th irradiation cycle, created a platform for this. The final shutdown of the plant was accompanied by a series of "End-of-Life" tests in support of the future development of sodium cooled fast reactors. The main experiments on which IGCAR scientists participated
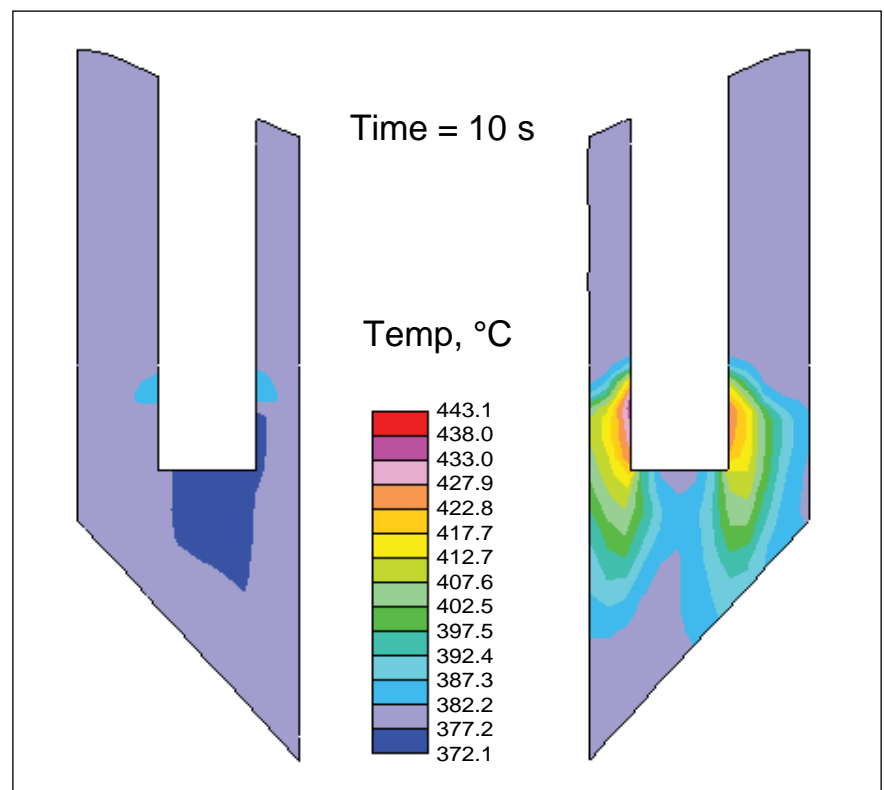
Fig. 1   *Temperature distribution in cold pool during asymmetric thermal conditions*

were (i) test on asymmetric thermal hydraulic conditions, (ii) natural convection test and (iii) control rod withdrawal test.

Asymmetric thermal hydraulic test involved development of thermal stratification in cold pool due to asymmetric conditions arising due to the coast down of sodium pump in one out of two secondary sodium circuits. Pre-calculation of the asymmetric thermal hydraulic conditions in the cold plenum of the reactor was carried out using a general purpose Computational Fluid Dynamics code. In view of one secondary sodium circuit not operating permanently, in the reactor and the test simulating asymmetric thermal hydraulic conditions between the other two loops, a complete three dimensional CFD model of cold plenum of the reactor was essential to be developed. The velocity distribution of primary sodium along the height of outlet window of IHX has been simulated through an equivalent porous body simulation of the heat exchanger. The predicted asymmetric thermal hydraulic conditions in the cold plenum at 10 s during the transient is shown in Figure 1, which demonstrates the capability of the code in simulating the test conditions.

The natural convection test involved simulation of natural convection heat transfer in the primary sodium circuit of the reactor. The test was carried out by tripping the reactor from normal operating conditions. Subsequently, all the sodium pumps were tripped under decay heat conditions of the core. Theoretical calculations were carried out using a detailed three dimensional CFD model which simulates thermal hydraulics in the whole primary sodium circuit. Important components of the primary sodium circuit viz. core, hot pool, cold pool,

primary side of IHX and pump are modeled in an integrated manner as shown in Figure 2. Establishment of natural convection in the primary sodium circuit was predicted using this model. The approach followed for this simulation is different from the system level modeling approach generally adopted for this kind of studies. The model developed is capable of predicting the development of stratification in sodium pools which system level models are not able to. A complete
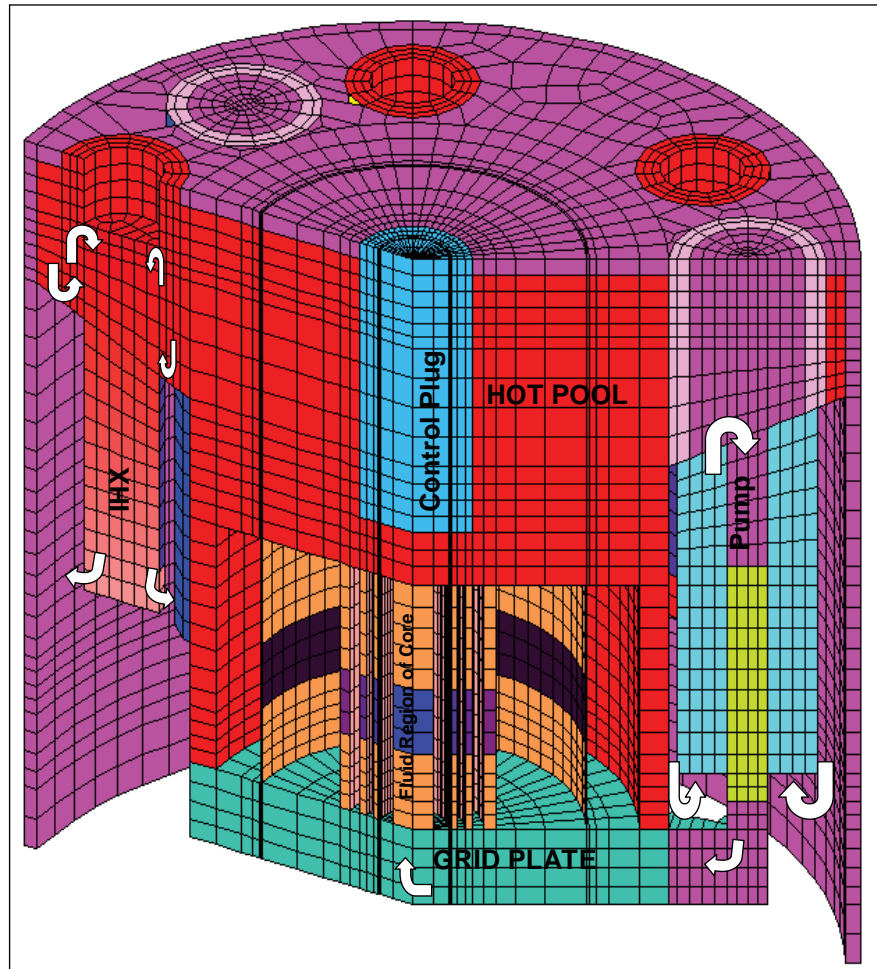
Fig. 2 *Computational fluid dynamics model of primary circuit developed for natural convection studies*
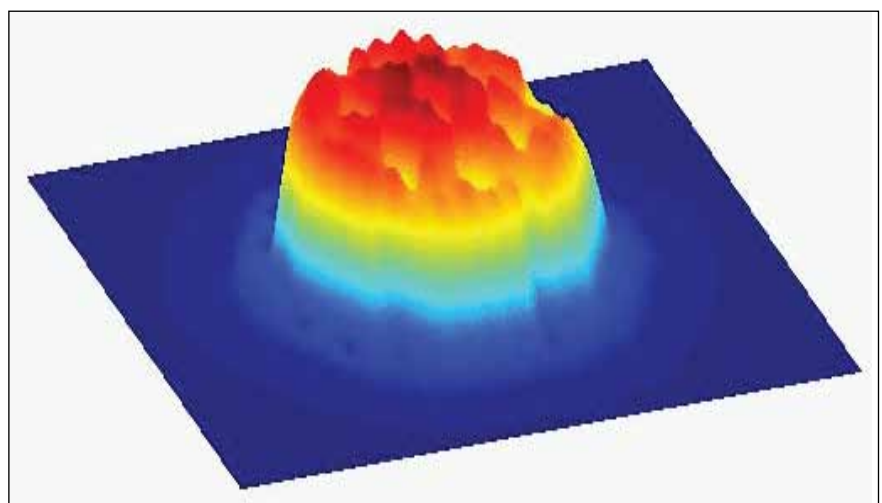
Fig. 3 *Three dimensional power profile predicted for control rod withdrawal test*

understanding and validation of multidimensional nature of sodium flow in the pools can also be obtained from this model.

The control rod test involved the simulation and measurement of power distribution in the core under four different critical states of relative positions of different control rods. This test will form a basis for the validation of multi-dimensional reactor physics codes. Pre-calculation of the test was carried out using the FARCOB and ERANOS codes. Comparison of the inter code predictions has shown that both the code predictions are very close except for the K-eff. FARCOB under predicts the K-eff by 0.85%. The predicted three dimensional power profile for one of the critical states is shown in Figure 3. Post test calculations of all the three tests are being carried out.

III.24 Application of Remote Sensing in Atmospheric Dispersion Modeling Studies

Characterisation of the terrain and land surface is an important issue in atmospheric dispersion models for realistic treatment of the dispersion and deposition patterns. The surface processes in the atmospheric model are dealt with a land surface physics module (LSM) to compute diurnally varying surface heat and moisture fluxes as surface boundary condition in atmospheric model. The land surface physics module involves the energy/moisture balance equations considering the detailed thermodynamics, hydrology, snow-sea ice processes in the surface-atmospheric medium. The parameters needed in the energy and moisture conservation equations are specified in terms of two primary variables i.e., vegetation (type and fraction) and soil type for each horizontal grid cell in the model. The vegetation cover provides information on albedo, roughness length, moisture availability, emissivity, canopy conductance, thermal inertia and the soil type provides details of its texture, bulk density, porosity, available water capacity, wilting point moisture and hydraulic conductivity.

Satellite remote sensing provides a number of crucial data on the earth surface which can be utilised to represent the surface characteristics in atmospheric models. A high resolution vegetation data (1 km) over the south Indian region is developed in collaboration with Indian Space Research Organisation.
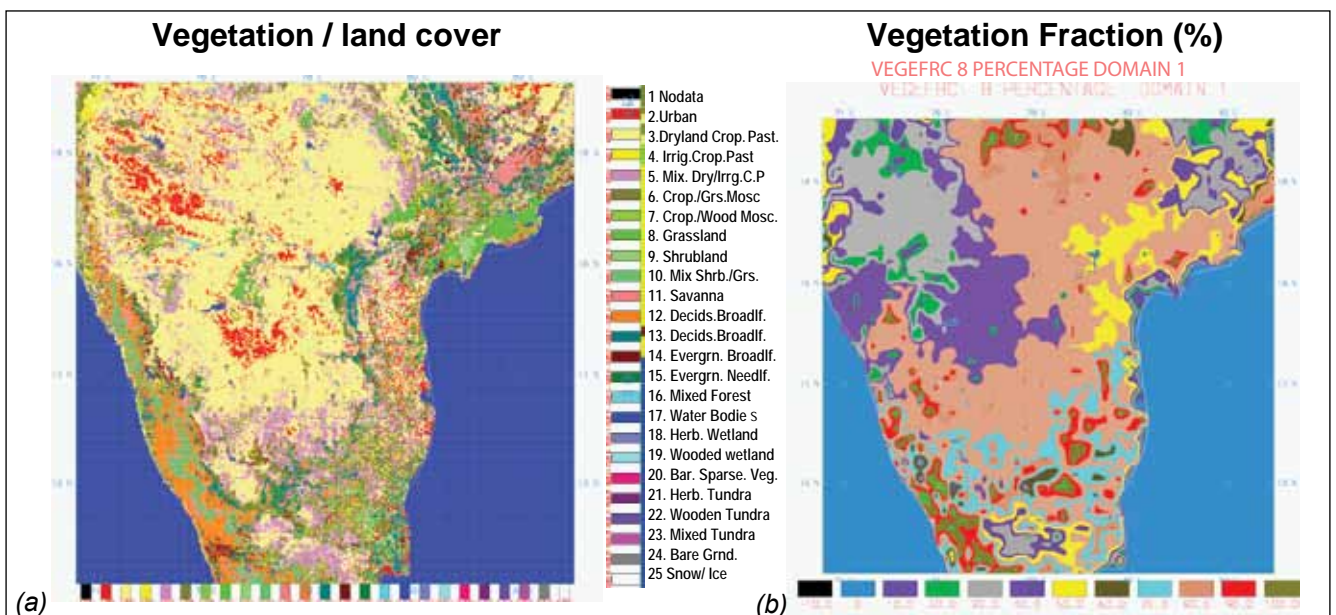
Fig. 1 *(a) Vegetation types and (b) Vegetation fraction data developed from satellite remote sensing techniques as input in operational atmospheric model*
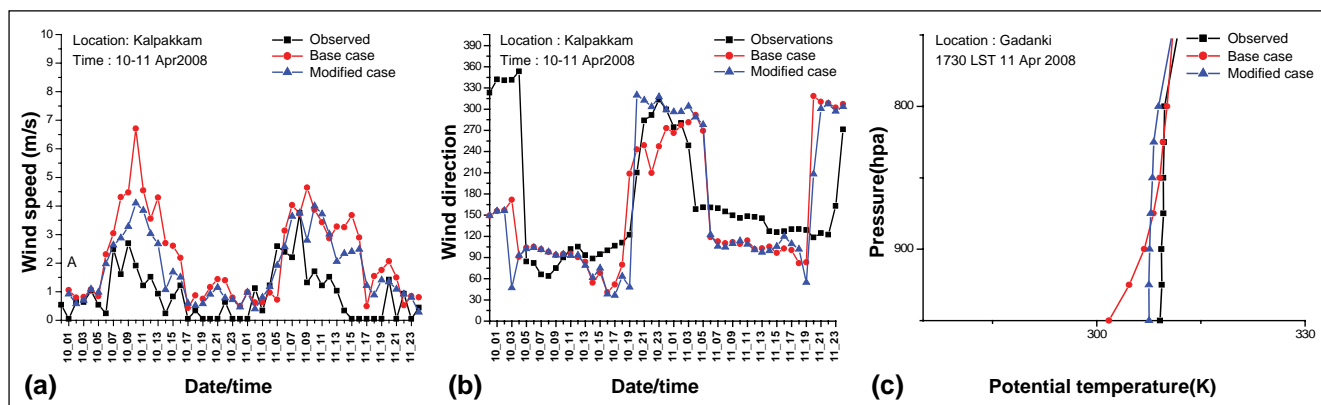
Fig. 2 *(a) Simulated wind speed, (b) Wind direction and (c) Potential temperature base data and modified terrain / vegetation data at Kalpakkam and Gadanki stations*

The data is generated from the multi-date 8-day composite of Moderate Resolution Imaging Spectroradiometer (MODIS) satellite seven band surface reflectance data for 2007, 2008 and 2009. The data is digitally classified using unsupervised classification technique into eleven land use categories. A seasonal vegetation fraction data for different months is also derived by computing vegetation index from blue, red and infrared bands of IRS-P4 Ocean colour monitor data. The soil types data are generated from digitisation of the field soil maps by application of spatial data analysis methods in GIS.

The modified data is used to improve the simulation of the wind field, turbulent fluxes, mixing height and other lower atmospheric parameters in operational mesoscale atmospheric model for dispersion prediction at Kalpakkam. Extensive simulations are conducted with model default terrain data (base case) and the data derived through remote sensing methods (modified case) for different seasonal cases and validated with available observations. Model statistics are derived with correlations, mean absolute error and RMSE to quantify model performance in runs with the modified surface data sets.

Model comparisons with observations for twenty six cases in different weather conditions have revealed that the modified surface data provides more realistic surface boundary condition than the default data available to the model from global sources. The results indicated that the alteration in vegetation fraction data has significant influence on the predicted atmospheric fields.

III.25 Physical Oceanographic Modeling Study for Location Specific Storm Surge, Extreme Wave and Dispersion Prediction Modeling for Radiological Environmental Safety

A comprehensive, location specific, numerical ocean modeling system is designed for Kalpakkam coast under a multi-institutional collaborative programme. The objective is to establish an operational ocean state simulation system for Kalpakkam comprising of on-line aquatic dispersion model, GIS integrated storm surge and inundation model and an extreme wave prediction model. Daily site specific and customised weather and ocean state/storm surge prediction, simulated aquatic dispersion pattern, extreme wave estimation etc are the deliverables of the system. These data serve as input to the radiological emergency decision support system already in place. The programme is divided into relatively independent modules with specific goals that have been undertaken by IIT Delhi and IIT Kharagpur.

A major feature of the research study is to dynamically couple the atmospheric model with the

ocean models which are hitherto used mutually independently. Another feature is to incorporate local data of bathymetry in high resolution, meteorology from site measurements and GIS data of the topography (coarse level) in the model. A third feature is to execute the models in multi-nested mode so that the large scale features are specified realistically in realtime at the model boundaries of the small scale domain around Kalpakkam coast.

Various components of the coupled modeling system are depicted in Figure 1. The large scale and mesoscale meteorological model already in operation provides forecasted data to the ocean current and wave models. The current and wave models are also mutually coupled so that the output of one model is taken as input by the other periodically so that the simulation is realistic. The storm surge model takes input of meteorological condition from the mesoscale meteorological model and ocean state parameters from the current and wave models. The ocean current model is used for dispersion simulation of the thermal and radioactive effluents discharged hypothetically from PFBR outlet.

In a scoping study, the dynamically coupled ocean model (Princeton Ocean Model- POM) is investigated for its applicability over Bay-of-Bengal and tested with meteorological model WRF operational for wind forecast. A transport-dispersion code was developed and coupled with POM and a case study of thermal pollutant dispersion from MAPS Jetty was carried out for four seasons for one full year using tower based local meteorological data. Two domains are considered for the current and wave models

D1 and D2 as shown in Figure 2. Simulated plume of the thermal effluent discharged from MAPS is shown in Figure 2 for a typical day in summer and winter.

For extreme wave prediction, a coastal SWAN model was adopted for Kalpakkam. While the numerical framework is common for all sites, physical parameterisation

connecting wave age with drag coefficient has been done to improve the physics in the model. The strength in this developed formulation is its close match with Janssen parameterisation both for young and mature waves. This is expected to fit into better air-sea interaction parameterisation in wind-over-wave models. Another important phenomena
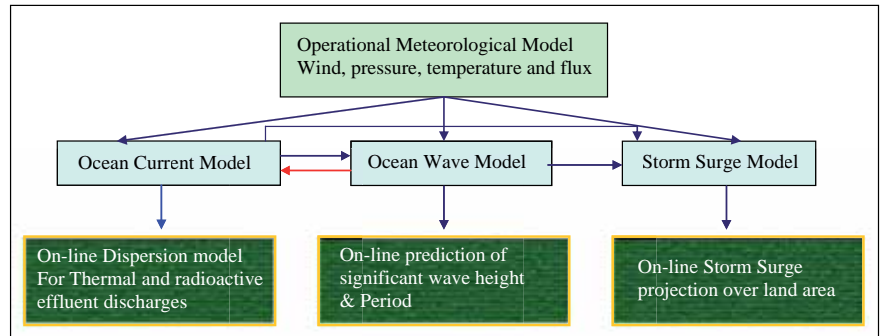
Fig. 1 *Various components of the integrated ocean modeling system*
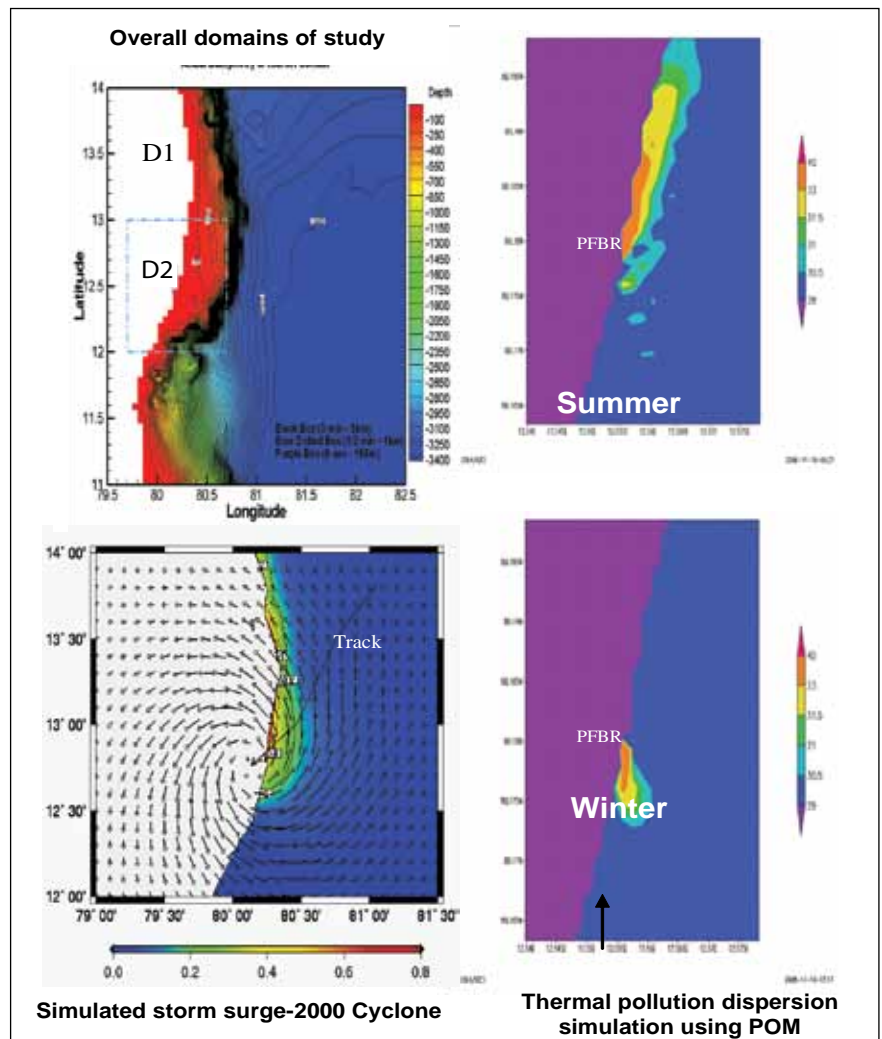
Fig. 2 *Model domain, dispersion pattern and storm surge prediction at Kalpakkam coast*

of swell generation and swell-wave interaction is also being incorporated in the wave model.

Kalpakkam specific analysis of cyclone tracks using past data has been studied. An advanced circulation model (ADCIRC), for inundation was implemented for Kalpakkam coast and a case study of year 2000 cyclone that crossed near Cuddalore was carried out to test the performance of the model in surge prediction. Figure 2 shows the surge height in coarse and fine resolution. Simulated surge height (1.4 meter) showed close agreement with actual observation.

Site specific data over the ocean needs to be collected for inter-comparison of the model results. A comprehensive experimental programme for measurement of currents is initiated in collaboration with National Institute of Ocean Technology (NIOT), Chennai. A high frequency radar has already been installed by NIOT at Kalpakkam coast for wave height and current monitoring.

III.26 Operation of Augmented Boron Enrichment Plant in Cascade Mode

The Augmented Boron Enrichment Plant (ABEP) has been commissioned with a mission to develop technology for the production of enriched boron of 91% in ^{10}B using Ion-Exchange Chromatographic process to meet the requirements of control rod material for Fast Breeder Test Reactor. Strong base macro porous type II fine resin of particle size ranging between 75 and 150 mm, which was developed in collaboration with one of the Indian resin manufacturing industry, was used in the process.

Augmented boron enrichment plant has two streams, Stream-I and Stream-II, each consisting of five process ion exchange columns loaded with this fine resin (Figure 1). Stream-I of augmented boron enrichment plant was charged with 50-60% enriched boric acid in ^{10}B obtained from boron enrichment plant, to operate in cascade mode. 1.5 kg of enriched boron with the target level of 91% was obtained after 18 months of operation. In Stream-II, initial borate band was developed with natural boric acid and is in continuous operation. Profile samples taken after 27 months of operation has shown an enrichment of 80% in ^{10}B. The profile samples were taken from both the streams at different intervals of time period and analysed for enrichment (Figure 2). It is evident from the Figure that the Stream-I, in which cascading operation was carried out, gives quicker enrichment. Hence, cascading operations was recommended for commercial production of enriched boron at Heavy Water Plant, Manuguru.

Fig. 1   A view of the plant
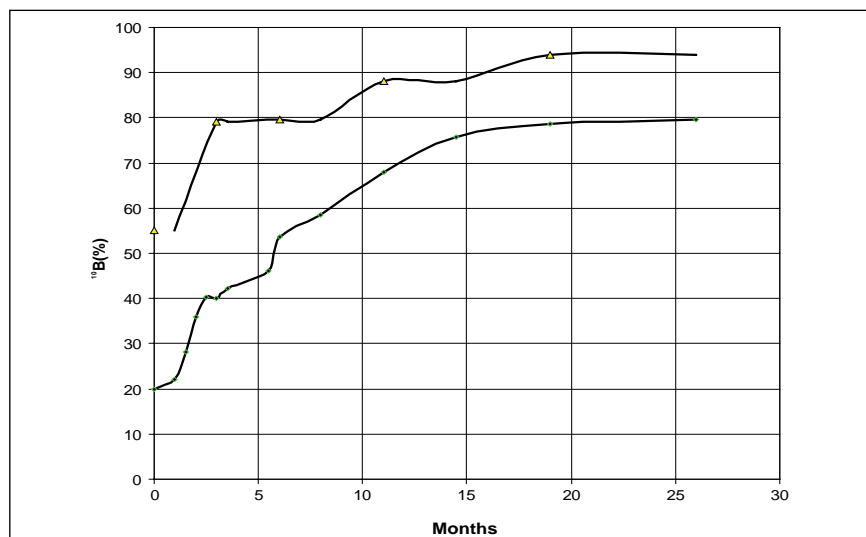
Fig. 2   Enrichment profiles for HP stream (cascade operation) and LP stream (conventional operation)

In-cell
Crane

Artic...
Manipu...

Viewing
Window

UJ T"

Operat...
Platfo...

Containment
Box
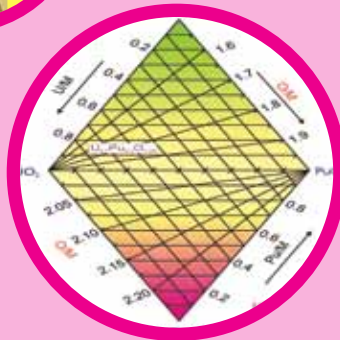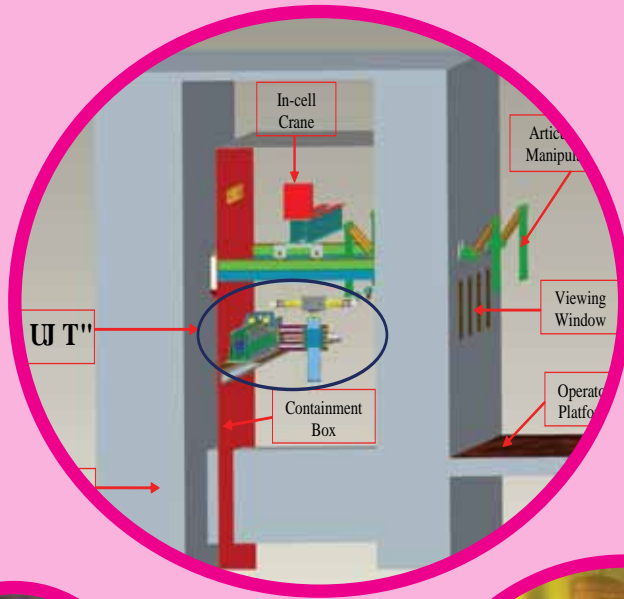
CHAPTER IV

Fuel Cycle

IV.1 Fast Reactor Fuel Cycle Successfully Closed

The plutonium produced from the reprocessing of spent fuel of FBTR in CORAL facility in the earlier campaigns was refabricated into pellets. The fuel pins with these pellets have been loaded into a fuel subassembly which was sent back to FBTR for reuse. The surface dose on the subassembly is well within the specifications. With this the closure of Indian fast reactor fuel was demonstrated successfully reaching an important milestone in the history of Indian nuclear power programme.

With the experience gained from the reprocessing of spent fuels with varying burn-ups, the process flowsheet and design of equipment was upgraded for the "Demonstration Fast Reactor Fuel Reprocessing Plant". The installation of equipment and systems are in progress. The safety assessment review by AERB is in the advanced stage of completion.

Extensive exercise of wash down inventory was completed successfully in CORAL for obtaining the safety clearance for the next campaign with 155 GWd/t burn-up mixed carbide fuel from FBTR. This provided invaluable experience in nuclear material accounting methods for the future plants. In this campaign, improved versions of the centrifugal extractor motor which is being developed concurrently, is used which will reduce the frequency of maintenance.

The proposal for temporary storage of α-bearing solid wastes in tile holes at CWMF has been cleared by safety authorities. The disposal will commence after demonstration of the transfer system. $\gamma-$spectrometry based plutonium assaying of hulls was successfully carried out using the hulls from fuels of 100 and 155 GWd/t burn-ups. This established the viability of this method for high burn-up and short cooled FBR fuels. Also neutron flux based plutonium assaying system for low $\beta-\gamma$ bearing α-solid waste has been fabricated which is under evaluation.

IV.2 Extractants for Actinide Separation

Tri-n-butyl phosphate (TBP) is the most important and widely used extractant for the recovery and purification of various actinides by solvent extraction in nuclear fuel reprocessing. Nevertheless this extractant has several limitations such as, significant solubility in water/nitric acid, tendency to form third phase during the extraction of tetravalent actinides at macro level from nitric acid medium. This necessitates the development of alternate extractants which are devoid of such limitations. Several trialkyl phosphates and phosphonates have been synthesised, characterised and compared with respect to their physico-chemical properties and extraction behaviour with TBP.

Trialkyl phosphates such as Tri-*iso*-butyl phosphate (T*i*BP), tri-*sec*-butyl phosphate (T*s*BP), tri-*n*-amyl phosphate (TAP), tri-2-methylbutyl phosphate (T2MBP), tri-*iso*-amyl phosphate (T*i*AP), tri-*sec*-amyl phosphate (T*s*AP), tri-*cyclo*-amyl phosphate (T*cy*AP) and tri-*cyclo*-hexyl phosphate (T*cy*HP) were synthesised, purified and characterised using FTIR, GC and NMR. Their physico-chemical properties such as, density, aqueous solubility, solubility of water etc. were measured. These measurements revealed the influence of the structure on these properties. For example the density was found to be decreasing with the elongation of the alkyl chain or by the introduction of branching on the first carbon atom of the alkyl groups. Studies indicated that third phase formation in the extraction of Th(IV) can be prevented by the elongation of the alkyl groups or by branching at the first carbon atom of the alkyl groups of trialkyl phosphate. Studies on the extraction of nitric acid by trialkyl phosphates indicated that the structure of the alkyl group does not significantly influence the nitric acid extraction. Also, the extraction of actinides such as Th(IV), U(VI) and Pu(IV) was not significantly affected by the elongation of the alkyl chain or by the introduction of branching away from P=O group. However, branching at the first carbon atom of the alkyl groups increases the extraction of U(VI) and decreases the extraction of Th(IV). The results are shown in

Figures 1 and 2. Feasibility of use of TAP on engineering scale has been validated by carrying out continuous counter-current runs using a 16-stage ejector mixer-settler, for the extraction of U(VI) by 1.1 M TAP/HNP followed by stripping.

A flow sheet for uranium/thorium separation with high separation factors has been developed with 0.183 M TsBP/HNP as solvent using the same equipment. Further studies indicate that isomers of TAP such as TiAP and T2MBP are also potential extractants for fast reactor fuel reprocessing, uranium/thorium separation etc.

Phosphonates which belong to the neutral organophosphor extractant family, are also very powerful extractants for actinides. Dibutylbutyl phosphonate (DBBP) and Diamylamyl phosphonate (DAAP) were synthesised by Michaelis Becker reaction, purified and characterised. The extraction of uranium and thorium were carried out by 1.1M DBBP and 1.1 M DAAP in n-dodecane as a function of nitric acid concentration and compared with their phosphate analogue, viz. TBP and the results are shown in Figure 2. The extraction is higher in the case of phosphonates because of the high basicity of the phosphoryl oxygen. The macro loading of thorium into the organic phase is also higher for phosphonates suggesting better loading capacity as compared to phosphate system. Better extraction of U(VI) and Th(IV) at higher nitric acid concentrations and identical stripping behaviour compared to TBP suggest that phosphonates have high potential in recovery of thorium and uranium by THOREX (THORium-uranium EXtraction) process.

High-level waste (HLW) obtained after nuclear fuel reprocessing
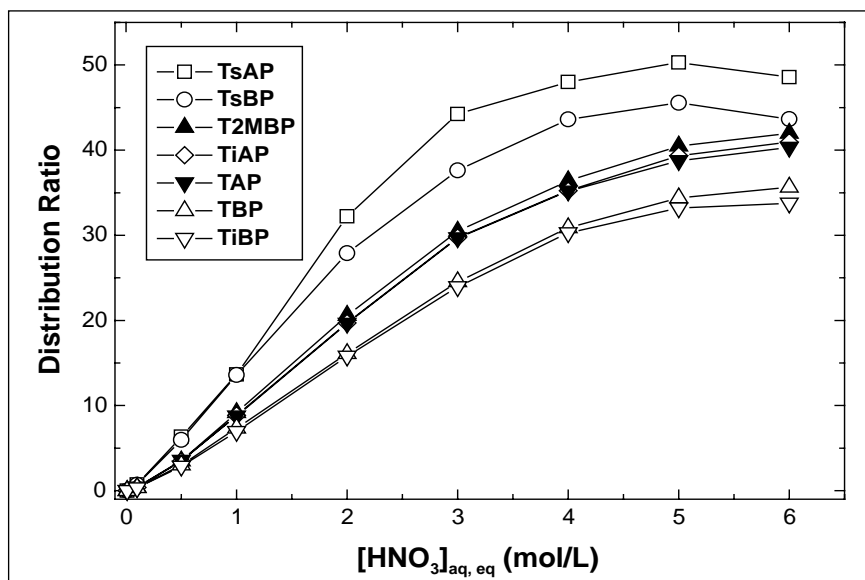
Fig. 1 *Variation of distribution ratio with equilibrium aqueous phase nitric acid concentration for the extraction of U(VI) by 1.1 M TiAP/ n-dodecane from nitric acid media at 303 K*
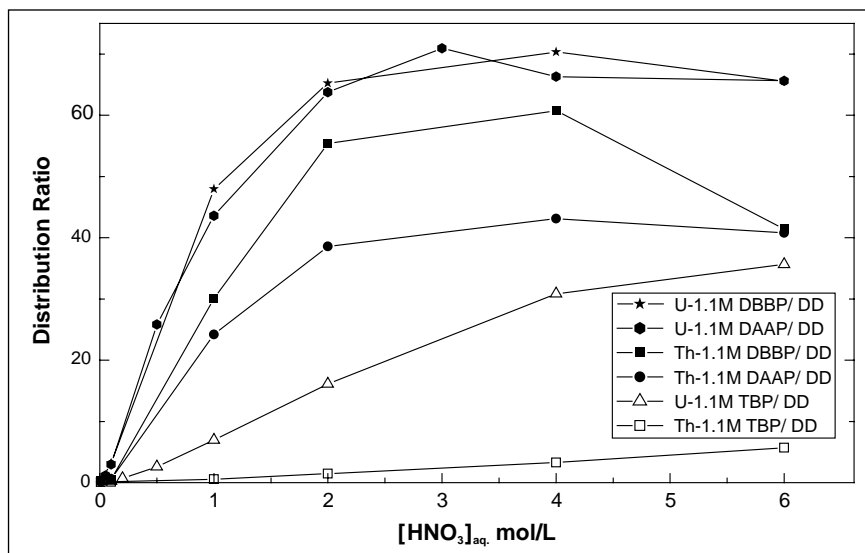
Fig. 2 *Variation of distribution ratio with equilibrium aqueous-phase nitric acid concentration for the extraction of U(VI) and Th(IV) by phosphonates and TBP in n-dodecane from nitric acid media at 303 K*

contains long-lived minor actinides such as Am and Cm. To reduce the repository cost and minimising the long-term radiological risk associated with HLW, isolation of the long-lived is desirable. The process involves initial separation of minor actinides and lanthanides and a subsequent actinide/lanthanides separation. An extractant 2,6-bis (5,6-dipropyl-1, 2,4-triazin-3-yl) pyridine (n-Pr-BTP) was synthesised and studied for the separation of americium

from the lanthanides. Extraction chromatograph method was used for the separation of actinides from lanthanides because of advantages such as lower solvent requirement, redundance of moderator, simplicity of equipment etc. nPr-BTP was impregnated on XAD-7 resin and the adsorption behaviour of Am (III) and some lanthanides such as, La(III), Ce(III), Nd(III), Eu(III) and Gd(III) from nitric acid solutions was studied in the presence of ammonium

nitrate. Figure 3 shows the effect of NH$_4$NO$_3$ concentrations on the uptake of Am(III), Eu(III) and Gd(III) from 0.1 M nitric acid medium at 303 K for three hours by n-Pr-BTP/XAD-7 resin. It can be seen that the uptake of Am(III) increases with increase in NH$_4$NO$_3$ concentration. However, for the lanthanides the uptake is insignificant at all NH$_4$NO$_3$ concentrations. Using nPr-BTP impregnated XAD-7, Am was separated from lanthanides with a separation factor of ~ 43.
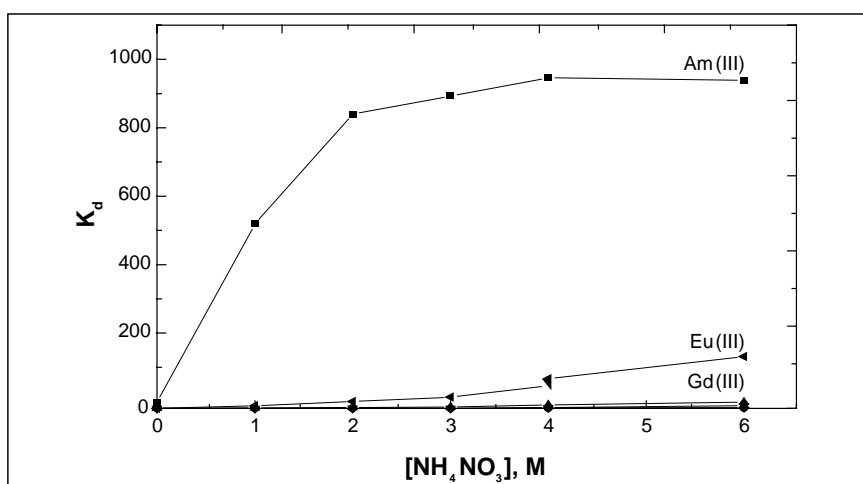
Fig. 3 *Effect of nitrate concentrations on the adsorption of Am(III) and Ln(III) onto nPr-BTP impregnated XAD-7 resin*

IV.3 Purification of Plutonium Oxide Recovered from the Lean Solvent

CORAL has reprocessed spent fuels from FBTR with burn-ups of 25, 50, 100 and 155 GWd/t. The reprocessing was carried out using the modified PUREX process. The solvent TBP undergoes extensive degradation during extraction cycles due to the radiation emitted by high concentrations of the Plutonium present as well as fission products, while processing short-cooled and high burn-up fuels. It was difficult to remove all the plutonium from the loaded solvent during stripping since it is retained by the degradation products DMP and MBP of the solvent. This residual plutonium has to be recovered from solvent before recycling, after removal of DBP and MBP or before discharge as waste.

A process based on treatment with carbonates has been developed and deployed in CORAL for the selective removal of plutonium as well as degradation products. The plutonium from this carbonate solution was precipitated as oxalate after destruction of plutonium carbonate complex by addition of nitric acid. The plutonium oxalate cake is decomposed to oxide by calcination.

Since, plutonium oxide obtained by the above process was found to have impurities, a purification method was developed. The treatment procedure involves washing of plutonium oxide with nitric acid, water, ammonium hydroxide and then again with water. The plutonium oxide after the above washing treatment is dissolved in nitric acid in the presence of hydrofluoric acid followed by precipitation in oxalic acid and then calcination.

IV.4 Development of Fast Separation Methods for Lanthanides and Actinides using HPLC

To study the measurement of burn-up of nuclear reactor fuel, lanthanides need to be separated from highly radioactive solutions. These measurements need to employ a fast and high performance separation method to ensure the exposure to the operator is kept to a minimum.

Lighter lanthanides (La, Ce, Pr, Nd, Sm and Eu) constitute about one fourth of the total fission products produced in the nuclear fission of uranium or plutonium. Hence, separation and accurate estimation of Nd (or La) in the dissolver solution of the spent fuel could be used to determine the burn-up. The separation of lanthanides from uranium, uranium from thorium, uranium from plutonium etc., in various studies related to the nuclear fuel cycle, also necessitates a rapid and high-resolution separation.

The major advantages of HPLC are its characteristic fast and high performance separations. In all the studies reported in literature, the separation of lanthanides was achieved in not less than eight minutes using supports of 5 µm sized particles. It is evident from the Van Deemter curve for particle size versus resolution that the packing materials with particle sizes less than 2 µm provide better resolution for high speed separations and in resolving complex mixtures compared to 5µm based supports.

In the present work, 1.8 µm based reverse phase support HPLC was investigated in order to obtain high column efficiencies for the development of a rapid separation procedure for isolating individual lanthanides as well as actinides. In these studies, the retention behaviour of lanthanides and actinides was studied under various experimental conditions with 3 cm and 5 cm long columns to achieve faster separation.

A camphor-10-sulfonic acid (CSA) solution of 0.023 M with hydroxy isobutyric acid (α-HIBA) (gradient, 0.05 to 0.25M) was employed with 3 cm support for achieving the separation of all 14 lanthanides,
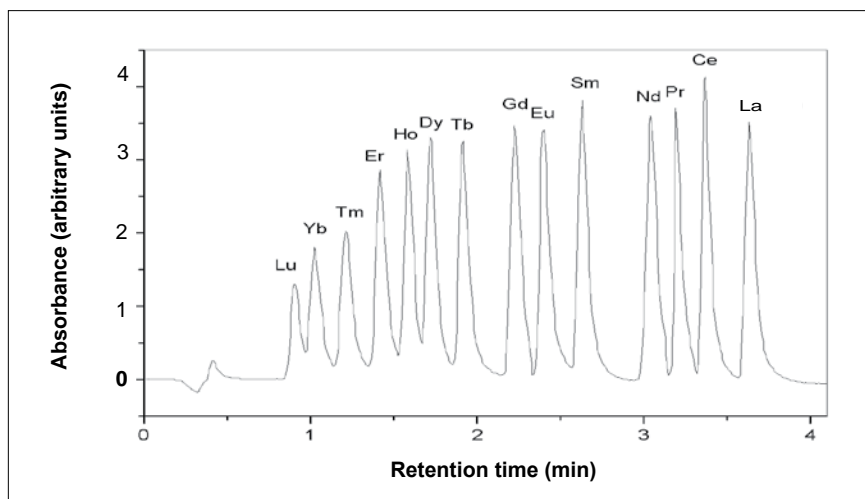
Fig. 1 *Fast separation of lanthanides on a reverse phase column (1.8 µm support)*
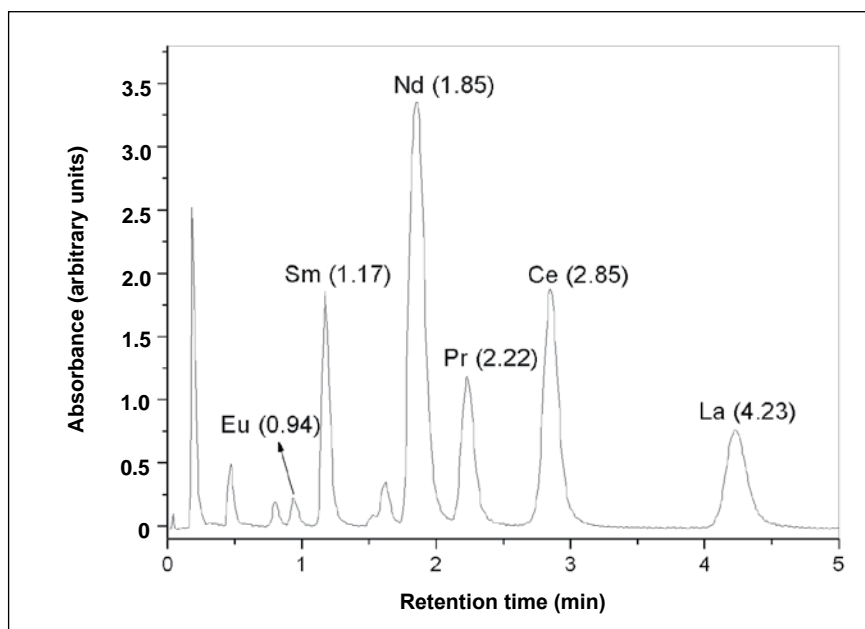
Fig. 2 *Separation of lanthanide fission products from dissolver solution of nuclear reactor fuel*

in a duration under 3.6 minutes (Figure 1). The separation time is much shorter compared to a total separation time of 7.8 minutes obtained with a 25 cm long column packed with 5 µm sized particles, and 4.9 minutes obtained with a 5 cm long column with 1.8 µm support. An isocratic elution procedure was also developed for the separation of lighter lanthanide fission products (La-Eu). They could be resolved from each other in about four minutes. Lanthanum could be very well separated from cerium and other lanthanides using

a mobile phase consisting of 0.02 M CSA and 0.1 M α-HIBA (Figure 2). Since the assay of lanthanum is essential in the experiments involving burn-up measurements, where it is employed as the fission product monitor, these experiments are useful for the determination of burn up. Detection limits (3 σ) for lanthanides were found to be in the range of three to six nanograms.

Rapid separation of U from Th as well as uranium from plutonium was achieved by reverse phase chromatography using a 3 cm

long column with 1.8 μm support. For example, when U and Th are present in similar quantities, an excellent base-line separation is obtained in less than a minute and these experimental conditions could be used for analysing solutions of uranium and thorium; similarly, uranium was separated from plutonium by using reverse phase chromatography (Figure 3).

These rapid separation by HPLC techniques, developed for the isolation of individual lanthanides from uranium, uranium from thorium and uranium from plutonium could be applied at various stages of nuclear fuel cycle.
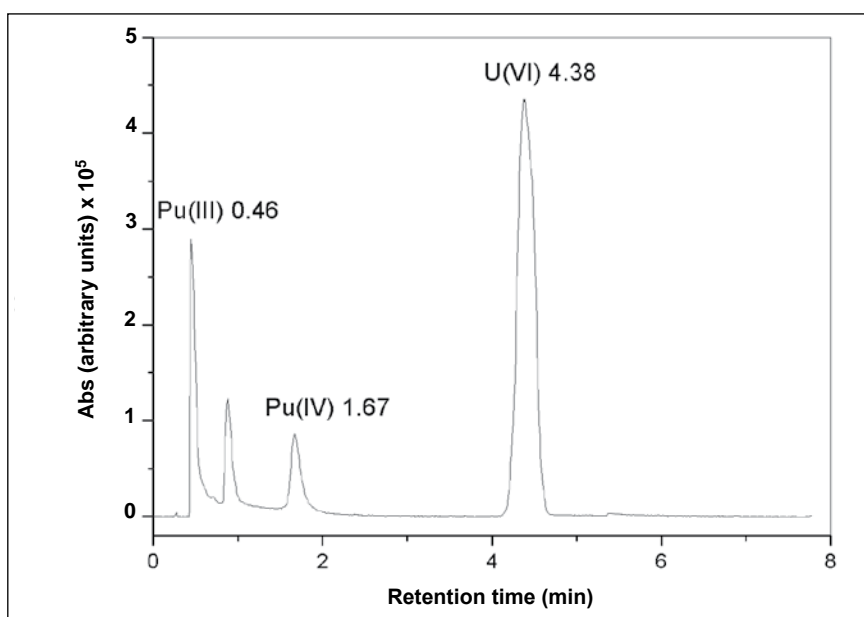
Fig. 3 *Separation of uranium and plutonium from dissolver solution of spent fuel*

IV.5 Thermochemistry of Some Ternary Oxides of Relevance to Fast Reactor Fuels

Information on the thermodynamic quantities of the compounds that could be formed through the possible interactions between fuel, fission products and the constituents of the clad and coolant is important in evaluating the performance of uranium plutonium mixed oxide fuel during its irradiation in a fast breeder reactor. RE_6UO_{12} (RE = Lanthanide metal) type of compounds with a rhombohedral structure are known to exist in the system RE–U–O. These compounds are formed in a fuel pin under transient conditions. Rare earths and tellurium are among those fission products that are formed during the burn up of the nuclear fuel. An understanding of the thermochemistry of these compounds of tellurium with the rare earth oxides is useful in predicting the integrity of the fast reactor fuel pins.
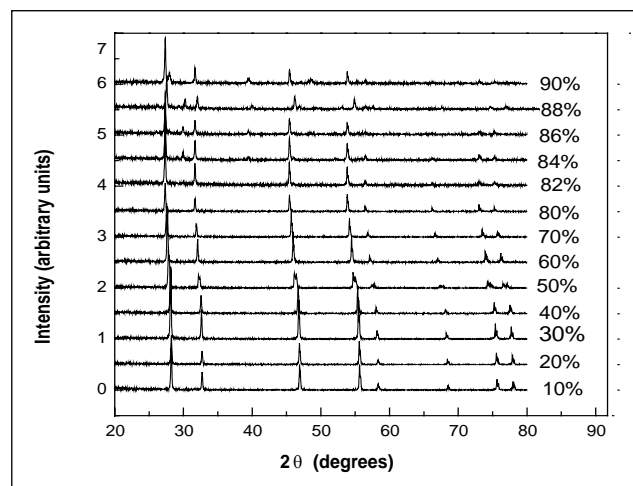
Fig. 1 *XRD patterns of $(U_{1-y} La_y) O_{2\pm x}$ prepared by combustion route show second phase only after 82% lanthanum oxide*
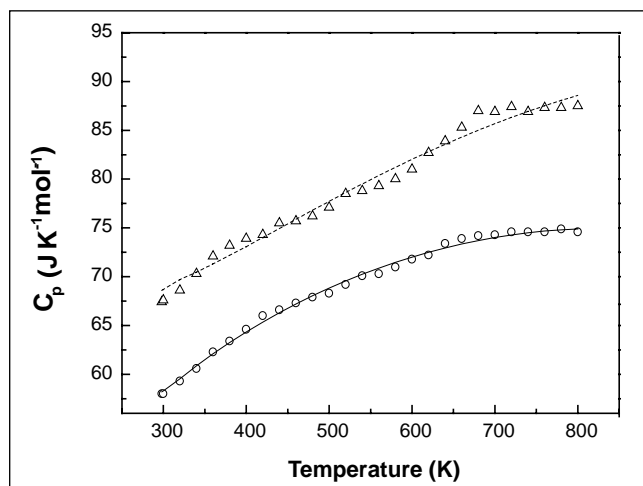
Fig. 2 *Heat capacity of $(U_{1-y} La_y) O_{2\pm x}$. The points are measured values and the curve is fitted to data*

Titanate ceramic formulations are relevant to nuclear waste forms and have evolved as an alternative from the original polyphase assemblage. These could plausibly accommodate a wide range of fission products, actinides and process chemicals. Titanates containing alkaline earths such as $BaTiO_3$ are the most promising candidates in such applications. Hence the thermodynamic stability of $Ba_{1-x}Nd_xTiO_3$ (in which neodymium simulates the behaviour of a transuranium counterpart) was studied.

Heat capacity measurements on some rare earth uranates

Solid solutions of $(U_{1-y}La_y)O_{2\pm x}$ (y=0.1–0.9) were prepared by the citrate gel-combustion and were characterised using HPLC, ICP-AES and XRD (Figure 1). The terminal solubility of La_2O_3 in UO_2 was determined with the help of XRD and was found to be 0.80 to 0.82 mole fraction of the former (y). Interestingly a lower solubility limit (y=0.7) was obtained when this solid solution was synthesised by using the conventional solid state route. The value obtained by using the citrate gel-combustion, more appropriate for this method ensures mixing down to the nano meter scale right from the start of the synthesis. Heat capacity measurements on $(U_{1-y}La_y)O_{2\pm x}$ (y = 0.2, 0.4) were carried out for the first time in the temperature ranges 298-800 K and 800-1600 K, by using differential scanning calorimetry (DSC) and drop calorimetry respectively (Figure 2).

Thermodynamic stability of M_2TeO_6 (M = La, Pr, Nd or Sm)

As a part of the ongoing thermodynamic investigations on
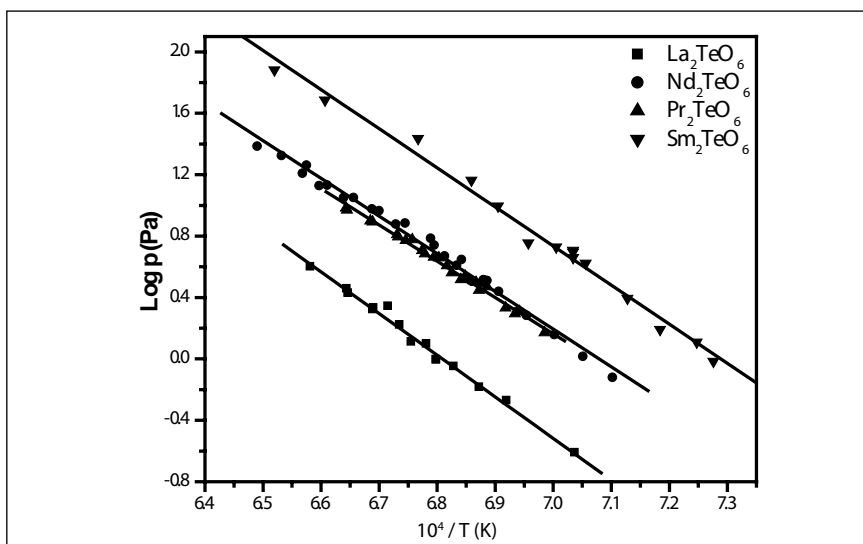
Fig. 3 *Temperature dependence of the vapour pressure of TeO_2 (g) over $M_2TeO_6 + M_2O_3$, (M = La, Pr, Nd and Sm)*

M	log p (Pa) = A – B / T(K)		Range of Temperature in K	p (Pa) at 1450 K	Δ_fG^o (M_2TeO_6) = -A + B T (K)	
	A	-B			-A	B
La	18.47	27127	1421-1320	0.6	2395	0.5563
Pr	16.71	23639	1432-1505	2.6	2348	0.5332
Nd	17.39	24559	1408-1541	2.8	2358	0.5314
Sm	18.56	25469	1374-1533	9.9	2399	0.5714

Table 1 : Vapour pressure and Δ_fG^o (M_2TeO_6)

the rare earth tellurates, the vapour pressures of M_2TeO_6 (where M = La, Pr, Nd or Sm) were determined by using a transpiration technique that employs a horizontal thermal analyser. From the measured partial pressure of TeO_2 (g) over the mixture M_2TeO_6 and M_2O_3, the standard Gibbs energy of formation of M_2TeO_6 was determined for the first time. This TG based transpiration technique, was validated by measuring the vapour pressure of pure TeO_2 (s) in the range 884–987 K. These data yielded a ΔH^0_{298} value of 269.7 ± 0.6 kJ.mol^{-1} for the enthalpy of sublimation (third-law method) of TeO_2 which compared well with the data reported in

the literature. The temperature dependence of vapour pressure of TeO_2(g) over the mixture M_2TeO_6 (s) + M_2O_3(s) generated by the incongruent vapourisation reaction:

$$M_2TeO_6\,(s) \rightarrow M_2O_3(s) + TeO_2(g) + 1/2O_2(g)$$
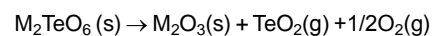
is shown in Figure 3. The linear least squares regression analysis of these vapour pressure data is summarised in Table 1.

The standard Gibbs energy of formation of M_2TeO_6(s) was derived by using the vapour pressure data in conjunction with auxiliary data for the other coexisting phases in the vapourisation reaction.

IV.6   Estimation of Oxygen Potential of the U-Pu-O Mixed Oxide Fuel

A thermochemical method for the estimation of oxygen potential for the uranium-plutonium mixed oxide fuel was developed with the help of certain generalisations derived through the analysis of similar methods reported in the literature. Within the scope of thermochemical method, the mixed oxide (MOX) system is visualised as a pseudo-quaternary solid solution of UO_2-U_cO_d-PuO_2-Pu_aO_b, where *a,b,c* and *d* are stoichiometric coefficients. For the purpose of modelling, the quaternary is subdivided into solid solutions of lesser components as shown in Figure 1.

A Pu_2O_3-type phase is used to describe the hypo-stoichiometric fuel and U_4O_9-type phase is used to describe the hyper stoichiometric fuel. Thus, the hypo- and hyper-stoichiometric MOX can be represented by two pseudo ternary systems Pu_aO_b-PuO_2-UO_2 and U_cO_d-UO_2-PuO_2 systems respectively. Juxtaposition
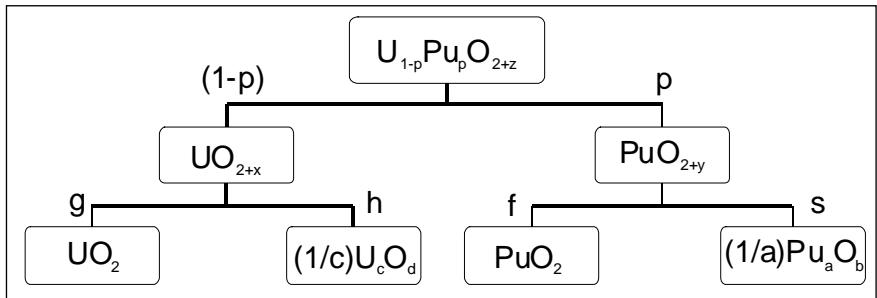
Fig. 1   *Schematic representation of MOX solid solution*

of the pseudo ternaries across UO_2-PuO_2 boundary gives a 'diamond plot' which can be used to generate several stoichiometric correlations relevant to the estimation of oxygen potential (Figure 2). The initial estimate of the composition is generated from the considerations of this 'diamond plot'. The oxygen potential pertaining to a given composition at a desired temperature is obtained by solving the non-linear expressions generated by invoking the equilibrium constraint viz., constancy of the oxygen potential in the Pu-O and U-O pseudo-binary subsystems. It was found that for compositions away from the exact
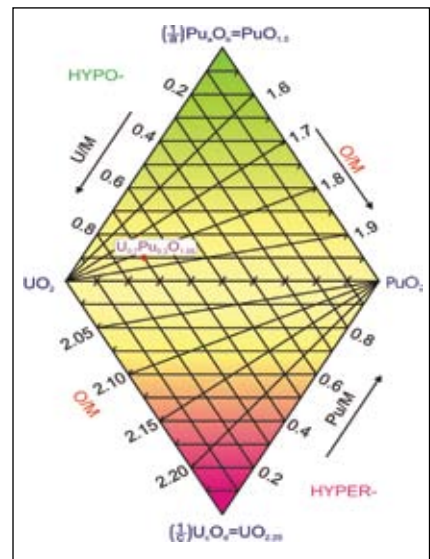
Fig. 2   *Diamond plot representing hypo and hyper stochiometric U-Pu-O system*
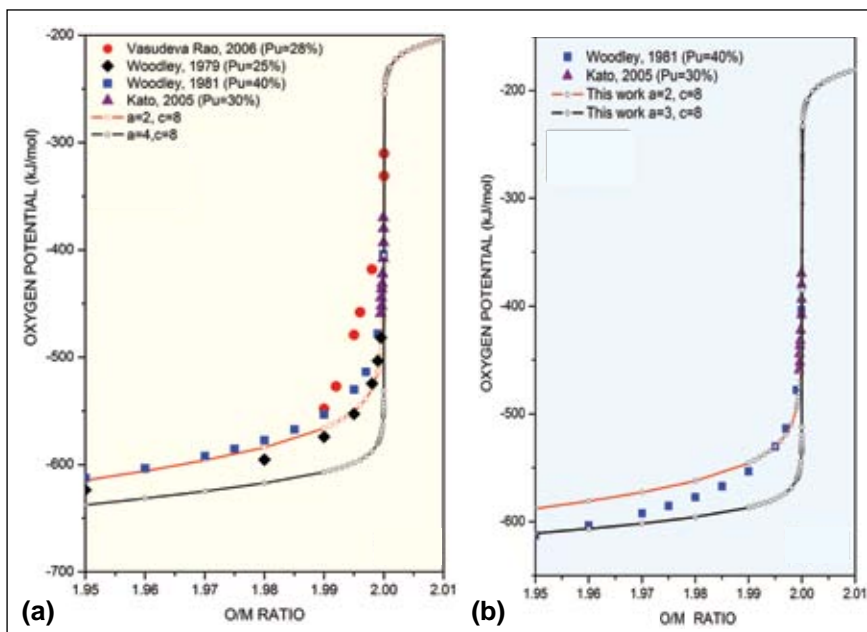
Fig. 3   *Variation of oxygen potential with O/M for at 1273 K for (a) Pu=0.28 (b) Pu=0.44*
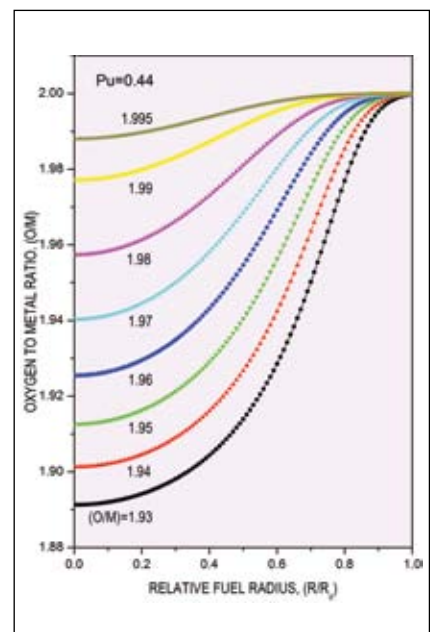
Fig. 4   *(O/M) redistribution for $(U_{0.56}Pu_{0.44})O_{2-z}$*

stoichiometry, the initial estimate of the oxygen potential obtained from the 'diamond plot' was adequate. However, at the regions close to the stoichiometry, several iterations were required before converging on to a consistent value by using the equilibrium constraint.

The current approach generalises the thermochemical models reported in the literature using the parameter *a* and *c*. It was proved that the configurational entropy is related to the model parameters and it affects the slope of oxygen potential vs. (O/M) curve near exact stoichiometry.

From the analysis of literature by Woodley and Adamson for Pu=0.25 at 1273 K, typical values for *a* and *c* were arrived at as two and four respectively. This was used further to generate the oxygen potential for $(U_{0.79}Pu_{0.21})O_{2-x}$ and $(U_{0.72}Pu_{0.28})O_{2-x}$ relevant in the context of PFBR and $(U_{0.60}Pu_{0.40})O_{2-x}$ relevant in the context of test pin irradiation in PFBR, shown in Figure 3. The estimated result is compared with literature data and the comparison is reasonable. Using this model and the method suggested by Ewart et al. (1984), the radial redistribution of oxygen across a fuel pellet was generated for Pu=44 and is shown in Figure 4.

A new thermochemical model was developed in order to estimate and predict the dependence of the oxygen potential of the fuel on the oxygen stoichiometry. It was also demonstrated that this model could be gainfully applied for predicting the radial distribution of oxygen potential in a fuel pellet.

IV.7   Studies on the Electrorefining of U-Zr Alloys

In order to recover the actinides and separate them from the fission product elements the spent fuel needs to be reprocessed. U-Pu-Zr alloy fuel used in fast reactors would be reprocessed by using a high temperature electrochemical method. This pyrometallurgical technique is called as electrorefining. The latter involves the dissolution of the spent fuel in a halide mixture (LiCl-KCl) followed by electrolysis. Uranium and plutonium are recovered as cathode deposits at the end of this process. The cathode is usually made of solid metal or liquid cadmium. Use of liquid cadmium provides several advantages. For instance, it facilitates the simultaneous deposition of uranium and plutonium. Subsequently uranium and plutonium are recovered from the cathode deposit by distilling out the salt and cadmium. Currently a process that involves the use of a fluoride containing melt is being thought of as a potential alternative to the electrodeposition and recovery of uranium and plutonium from the chloride melts. The electrochemical behaviour of actinides and fission products in these fluoride based melts are also being studied worldwide. The fluoride based process is being thought of as an alternate to the direct electrochemical reduction of actinide oxides. Thus, it is evident that the studies related to the dissolution of the spent fuel in the molten salt mixture as well as the data pertaining to the electrochemistry of deposition on the liquid cadmium cathode play an important role in understanding the pyrochemical reprocessing.

In view of the above, studies were carried out on: i) electrochemistry of uranium deposition from an alloy of U-Zr (10%), ii) electro-chemical behaviour of Ce^{3+}, Zr^{4+} and U^{4+} in LiF-CaF$_2$ eutectic and iii) demonstrative trials on cadmium distillation by using an equipment that was developed in-house.

The feasibility of anodic dissolution of the spent fuel was explored by using U-Zr (10%) alloy as the test specimen. The cyclic voltammogram shown in Figure 1 pertaining to the deposition of uranium from this alloy, on a liquid cadmium cathode (at 698 K) reveals that uranium deposits at a more anodic potential at the liquid cadmium cathode than at a solid cathode. This difference in the deposition potentials could be attributed to the thermodynamic stability of the compound UCd_{11}. The anodic dissolution of U-Zr (10%) showed
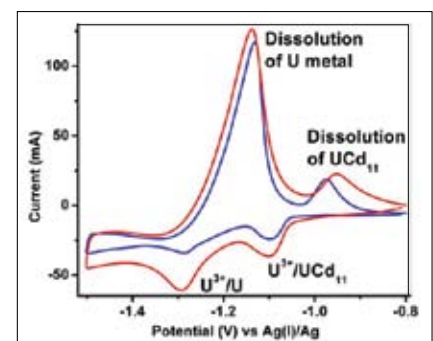
Fig. 1 *Cyclic voltammogram of U at the liquid cadmium cathode (698 K)*
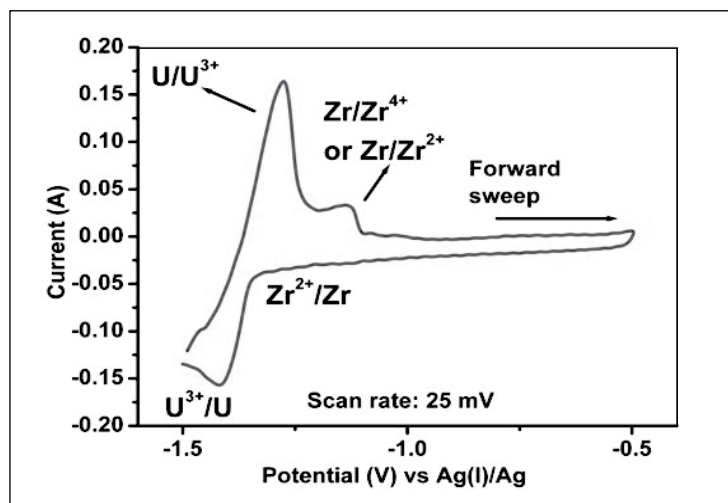
Fig. 2 *Cyclic voltammogram-U-10 % Zr alloy in LiCl-KCl eutectic (683 K)*
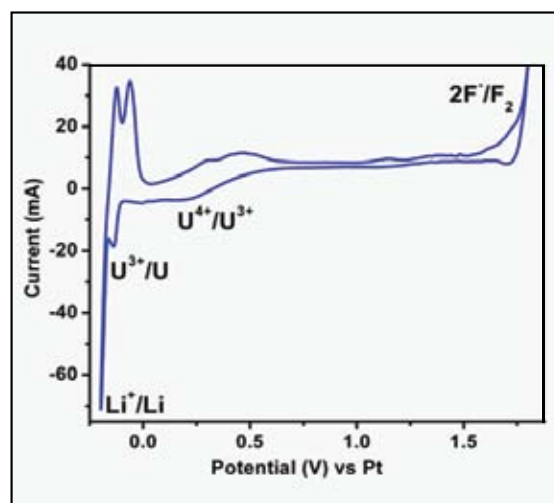
Fig. 3 *Cyclic voltammogram - UF$_4$ in LiF-CaF$_2$ eutectic (1123 K)*

that the potential pertaining to the dissolution of uranium (U/U^{3+} redox couple) is reversible while that pertaining to the dissolution of (Zr^{2+}/Zr redox couple) is not fully reversible. These studies indicate that it is indeed possible to selectively dissolve uranium by applying a suitable potential in presence of zirconium in the LiCl-KCl salt mixture (Figure 2). Studies on the electrochemical behaviour of U, Ce and Zr in the LiF-CaF$_2$ melt (1123 K) showed

that UF$_4$ gets reduced to metallic uranium through a two step process that involves the formation of U^{3+} (Figure 3).

Studies were carried out on the distillation of cadmium by using a trial assembly made of graphite that was designed and fabricated in-house. This resistively heated distillation set up showed that quantitative removal of cadmium from the cathode deposit could be achieved.

These investigations have demonstrated that anodic dissolution of the fuel is quite a possibility and could also facilitate the selective dissolution of uranium and zirconium.

In order to understand the efficacy of this process further investigations on the dissolution of uranium in the presence of plausible fission products and noble metals are necessary.

IV.8 Studies on Control Rod Materials for Fast Breeder Reactors

Ignition behaviour of elemental boron powder

High-density boron carbide pellets containing boron enriched in ^{10}B (65 at %) will be used in the control rods of the prototype fast breeder reactor (PFBR). These pellets are prepared by reacting elemental boron (produced through molten salt electrolysis method) with graphite. Elemental boron powder is highly susceptible to oxidation. Thus the study on the ignition of boron powder is relevant

in identifying the ideal conditions for its safe handling and storage. A study was carried out in order to assess how the rate of heating, size of the constituent particles and the residual oxygen present in the gas phase influence the ignition of boron.

It was observed that the ignition temperature (T$_{ig}$) linearly increases with the size of the particles at a given heating rate. The powder with finer particles provides greater surface area and is thus more

reactive. It was observed that the powder whose constituent particles had an average size of 32 μm or lower could be handled safely without the risk of ignition up to 783 K in air. These observations testify the conclusion that the oxidation of the boron powder at room temperature is a kinetically hindered process.

The dependence of T$_{ig}$ and the gain in weight during the oxidation on the partial pressure of oxygen (*Po$_2$*) for powders with particles in

the size range 10-32 µm is shown in Figure 1. It was observed that a threshold, Po_2 of $2×10^3$ Pa, is required in order to initiate the ignition. At lower pressures only a benign oxidation prevails as indicated by the marginal gain in weight. It is seen from Figure 2 that T_{ig} falls exponentially with increasing Po_2 and beyond a certain value of Po_2 ($> 4 × 10^4$ Pa) it remains constant.

These experiments revealed that it is safe to handle powdered boron (having a particle size distribution suitable for the fabrication of B_4C) in air.

Thermodynamic stability of TiB_2

TiB_2 is a refractory intermetallic compound with high hardness, low density, high electrical conductivity, good thermal shock resistance, chemical inertness, excellent wear and corrosion resistance and high elastic modulus. These properties render it suitable for many applications such as in the manufacture of wear resistant parts, ballistic armour, cathodes and thermocouple sheaths, crucibles for molten metals, metal evaporation boats and cutting tools as well as in tribology. The neutron absorption properties of ^{10}B coupled with the high temperature stability of TiB_2 (containing ^{10}B) makes it a candidate material for the manufacture of the control rods for the fast breeder reactors. The thermodynamic properties of TiB_2 and information on its stability at high temperatures are of relevance to fast reactor technology. Hitherto the Gibbs energy of TiB_2 has not been measured experimentally, although estimates have been reported. Hence the Gibbs energy of formation of this compound was measured experimentally.
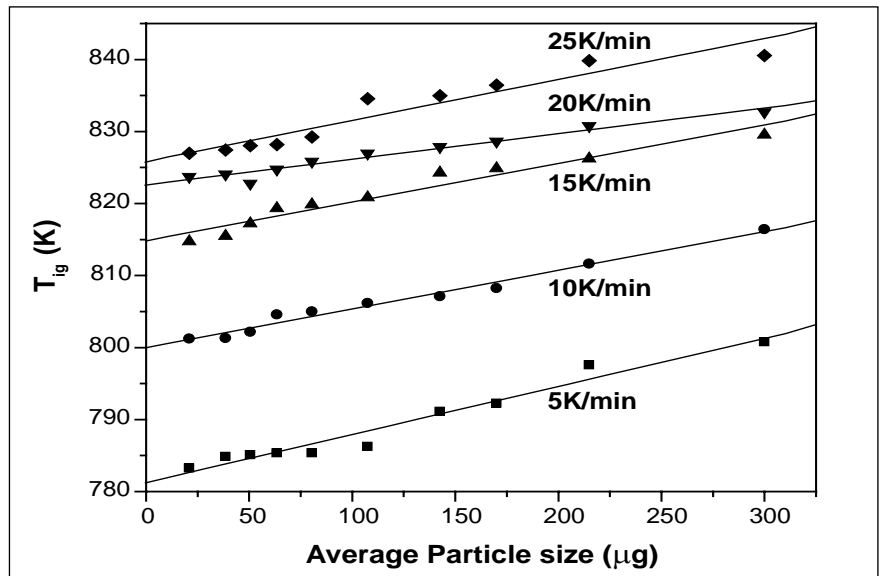
Fig. 1 *Dependence of the ignition temperature of boron powder on the size of its constituent particles*
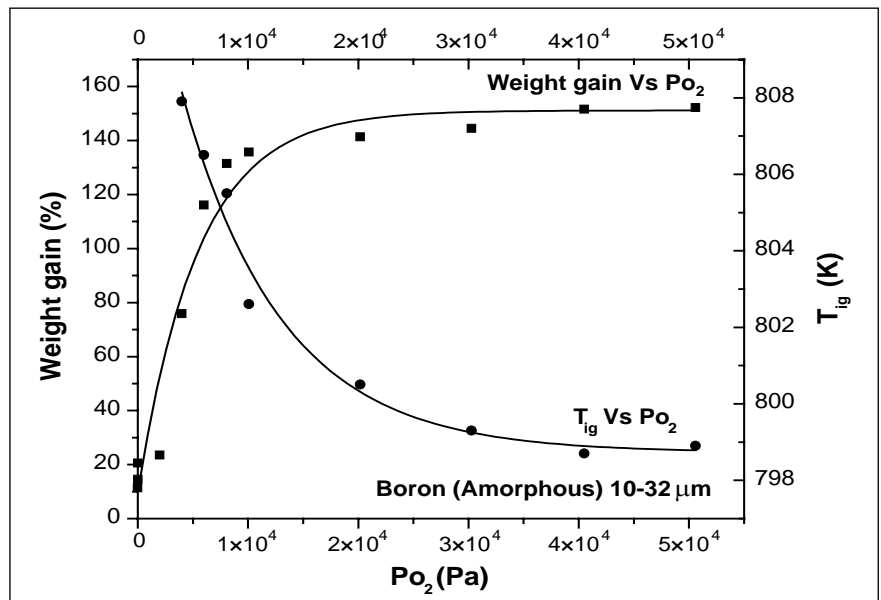
Fig. 2 *Correlation between the residual oxygen pressure and ignition temperature of the boron powder*
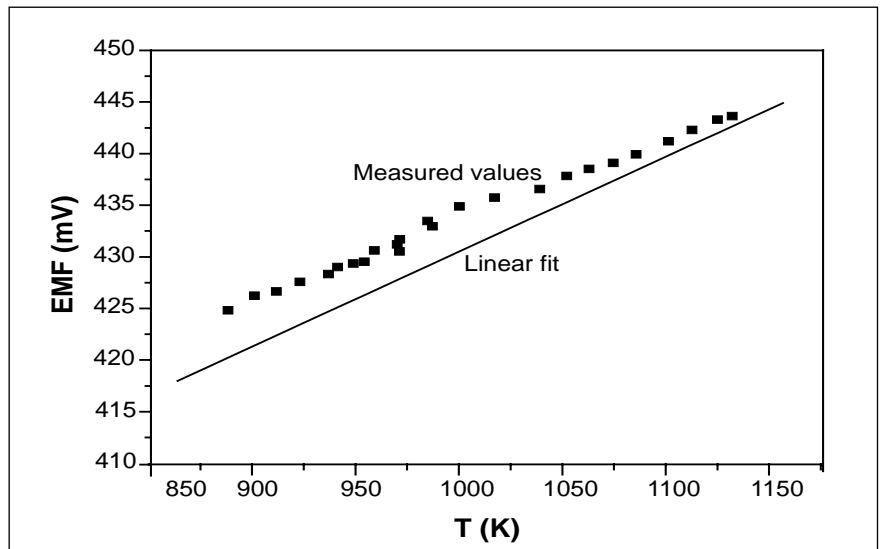
Fig. 3 *Temperature dependence of the emf values*

The Gibbs energy of formation of TiB_2 was derived from the experimentally determined values of the emf of a galvanic cell that employed YDT as the solid electrolyte and a mixture of Ni, NiO (or Fe, FeO) as the reference electrode. These galvanic cells could be represented as follows.

Cell (I): Pt, TiB_2 (s), TiO_2 (s), B (s) | YDT | NiO (s), Ni (s), Pt and

Cell (II): Pt, TiB_2 (s), TiO_2 (s), B (s) | YDT | FeO (s), Fe (s), Pt

The temperature dependence of the EMF measured by using the cell (I) is shown in Figure 3.

Enthalpy increments on TiB_2 were measured by using inverse drop calorimetry over the temperature range 583-1769 K. The heat capacity, entropy and the free energy function have been derived from these experimental data in the temperature range 298–1800 K. The mean value of the standard enthalpy of formation of TiB_2 ($\Delta_f H°_{298}<TiB_2>$) was obtained by combining the $\Delta_f G°$ values with the free energy functions of $\Delta_f H°_{298}$ TiB_2 derived from the drop calorimetry data. The mean values of $\Delta_f H <TiB_2>$ derived from the $\Delta_f G°$ data obtained from cell I and II were found to be -322 ± 1.2 and -323.3 ± 2.1 kJ mol^{-1} respectively. These values were found to be in agreement with the assessed data.

The Gibbs energy of TiB_2 was determined experimentally for the first time.

IV.9 Glass and Glass-Ceramic Matrices for the Immobilisation of Radioactive Waste: Synthesis and Physicochemical Characterisation

High-level radioactive liquid waste (HLW) is generally immobilised in a suitable glass or glass-ceramic matrix. Many new candidate matrices have emerged in the recent past like, Iron Phosphate Glass (IPG) and calcium chlorapatites based glass ceramics. These were tested for the immobilisation of the high-level radioactive nuclear waste expected from fast reactor fuel reprocessing by the PUREX process. Iron phosphate glass waste form containing 20 wt% of simulated High-level radioactive nuclear waste corresponding to the FBTR fuel after a burn-up of 150 GWd/t was prepared and characterised for its thermo-physical properties. Simulated FBTR waste oxides (20 wt% loading) were homogenised with Fe_2O_3 and ammonium dihydrogen phosphate and melted at 1323 K in an electric furnace. The melt was quenched to room temperature in air; the amorphous nature of the glass waste form (named as IP20FBRW to signify 20 wt% loading of simulated FBR waste) was confirmed by X-ray diffraction. SEM micrographs showed the glass to be smooth and homogeneous. The density of IP20FBRW was found to be 3.1 g/cc, which is higher than the bare iron phosphate glass (2.9 g/cc), indicating the effect of incorporated waste in the matrix. The glass transition temperature
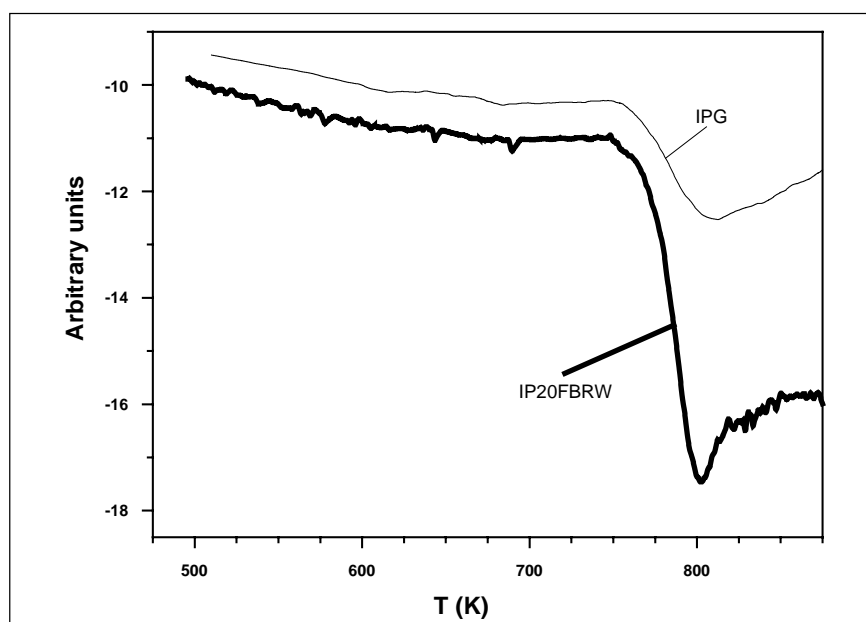
Fig. 1 *DSC curves of iron phosphate glass and IP20FBRW showing the glass transition temp (T_g)*
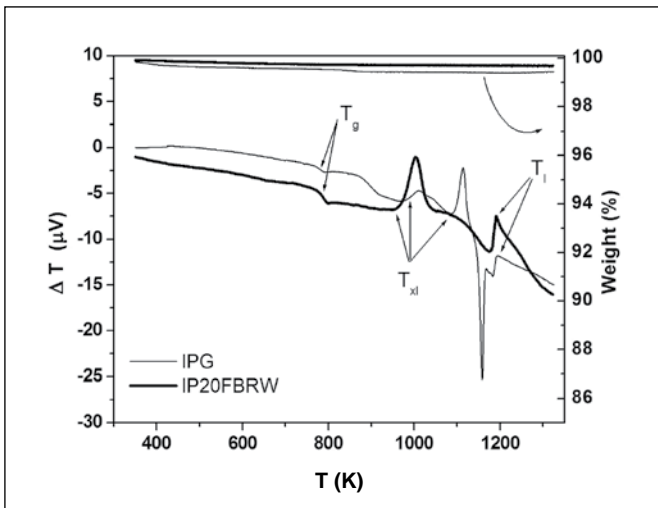
Fig. 2 *TGA/DTA curves of IPG and IP20FBRW*
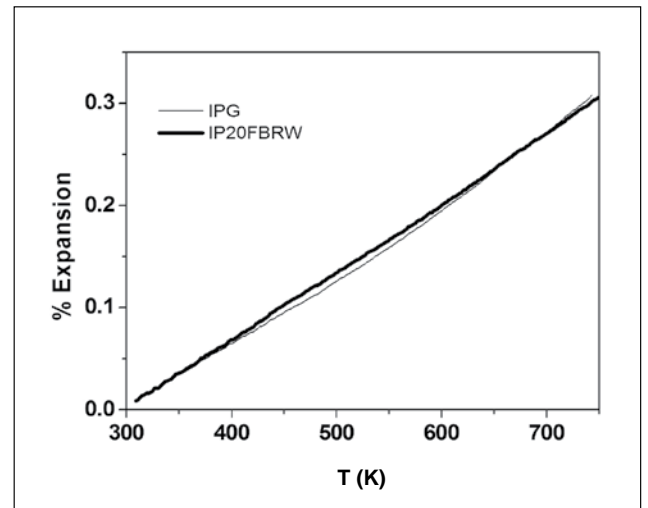
Fig. 3 *Linear thermal expansion behaviour of glass and the glass waste form*

(T_g) of IP20FBRW was found to be 785 K which is same as that of the pristine iron phosphate glass, as shown in Figure 1. The presence of the alkali/alkaline earth elements modify the glass network and hence lower the glass thermal stability, whereas the transition metal oxides act as intermediates and increase the thermal stability of the glass. Since the waste oxides contain both types of oxides, the T_g of the waste form is not much altered from that of iron phosphate glass. No detectable weight loss was observed up to 1300 K in air as revealed by thermogravimetry of IP20FBRW and iron phosphate glass (Figure 2). The DTA patterns show the liquidus temperature (T_l) along with the glass transition temperature (T_g) and crystallisation temperature (T_{xl}) of IP20FBRW and iron phosphate glass. The thermal expansion behaviour of iron phosphate glass and IP20FBRW is shown in Figure 3, which clearly indicates that the thermal expansion of the IP20FBRW is similar to that of bare iron phosphate glass. This reveals that the expansion behaviour is not altered by waste loading. This also agrees well with the observation that thermal stability of IP20FRBW iron phosphate glass is practically the same as that of pristine iron
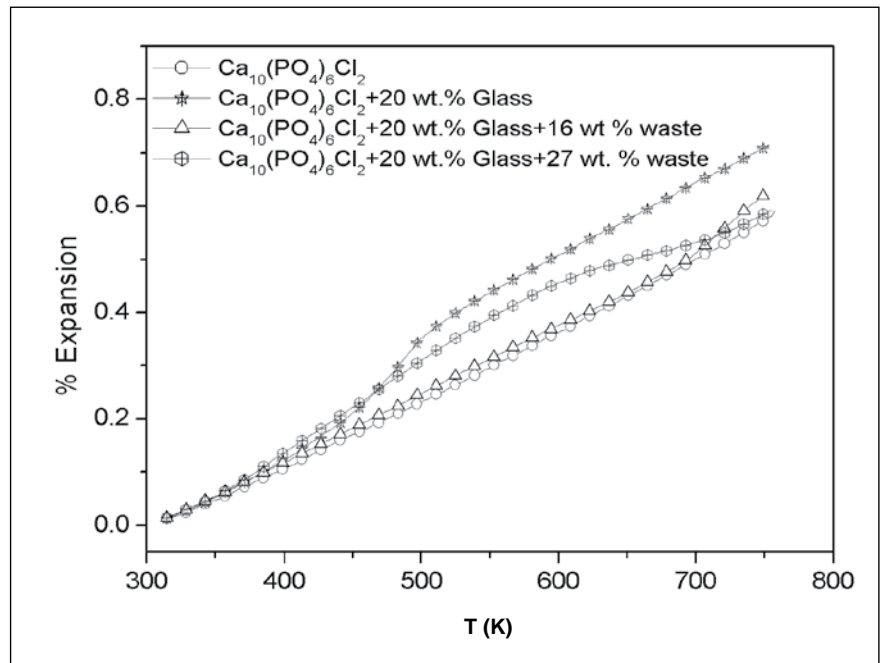
Fig. 4 *Bulk linear expansion of Ca-chloroapatite and chloroapatites glass-ceramics measured by dilatometry*

phosphate glass. The studies show that iron phosphate glass is a promising matrix for fast reactor high-level radioactive nuclear waste disposal.

HLW from non-aqueous pyro-metallurgical methods, such as metal electrorefining yields the HLW in chloride form. The iron phosphate glass is not a suitable matrix for this chloride waste. Researchers have demonstrated a method to immobilise chloride waste in zeolites, and converting it to a glass

bonded sodalite, but the waste loading is low. Chlorapatites are another class of halide-containing ceramics that can be exploited for this purpose. Ca-chloroapatites glass-ceramic compositions with up to 32 wt% simulated waste loading were prepared and characterised.

The simulated glass-ceramics were synthesised by taking the required amounts of apatite-forming agents, glass-forming agents and a simulated chloride waste composition (2.63 wt%

CeCl$_3$ +1.38% BaCl$_2$ +1.74% CsCl + 11.23% NaCl + 12.08% NdCl$_3$ + 70.91 wt% (45 wt. % LiCl- 55 wt % KCl) eutectic) in appropriate ratios, mixing and grinding thoroughly and heating at 773-1023 K for three hour in air. The nominal waste loading was in the range 16-32 wt%. The products were characterised by XRD, TGA/DTA, and SEM-EDAX and thermodilatometry.

The XRD patterns of the glass-ceramics showed that only single phase chlorapatites is formed as a crystalline phase for chloride waste loading up to 32 wt% on heat-treatment at 1023 K for three hours in air. However, inclusions of cubic NaCl and KCl were detected by SEM and EDAX in the product with 32 wt% waste loading. The bulk thermal expansion behaviour of Ca-chlorapatites, chlorapatites glass-ceramics and 16-27 wt% waste loaded glass-ceramic bodies (~10 mm dia and 10 mm height, heat-treated at 1123 K/3h) is shown in Figure 4. The percentage linear thermal expansion in the temperature range 298-700 K is about 0.5 for Ca-chlorapatites and the 16 wt % waste loaded apatite glass-ceramic. The coefficient of thermal expansion for the two is about 12.5 x10^{-6} K^{-1} in this temperature range. A large positive change of slope of the thermal expansion curve is seen for the waste loaded glass-ceramic (16%) around 700 K which is attributed to the glass transition phenomenon in the glass phase. In the case of the 27 wt% waste loaded glass-ceramic and the chlorapatites glass-ceramic without waste loading, a totally different thermal expansion behaviour is observed; investigations are in progress to understand this phenomenon.

The products heat-treated at 1023 K for 3 hours were washed with de-ionised water and the solution analyzed by ion selective electrode technique. The results showed that leaching of cloride ion is below detection limit (10 ppm); rare earths were found to be below the detection limit of ICP-OES (0.5 ppm) in the case of 16 wt% waste loaded glass-ceramic; for the 27 and 32% waste loaded compositions, the leaching was found to be more significant.Thus the investigations show that Ca-chlorpataites glass-ceramics are capable of fixing significant concentrations of simulated chloride waste (~ 15%).

IV.10   Physical Properties of Post-PUREX Solvents

After recovering U, Pu, Np and Tc from spent nuclear fuel by aqueous route (PUREX process), a highly active waste stream is generated which has traces of U, Pu, Zr, heat-emitters like Cs and Sr, trivalent actinides (Am, Cm) and trivalent rare-earths and all the rest of fission products. This waste stream can be processed by a combination of post-PUREX processes, shown schematically in Figure 1 which shows the use of CCD-PEG and reversed TALSPEAK processes for the above task. The CCD-PEG process is based on usage of a synergistic
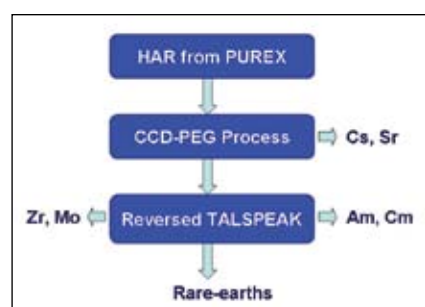
Fig. 1 *A schematic of Post-PUREX processes*
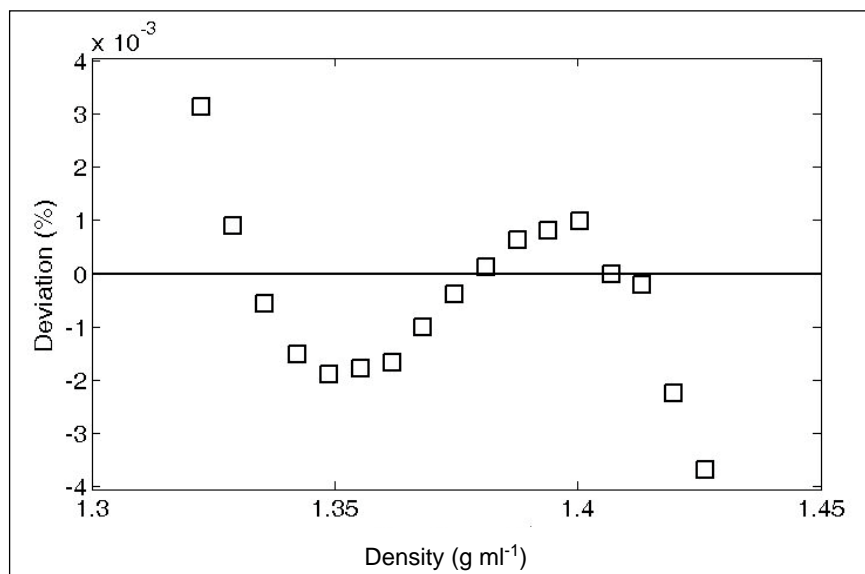
Fig. 2 *Plot of deviations for the density of the special diluent, FS-13 (mean deviation = – 0.00049319%, standard deviation = 0.0015961%)*

solvent mixture of chlorinated cobalt dicarbollide (CCD) and polyethylene glycol-400 (PEG-400) in a speciality diluent Phenyl Trifluoro Methyl Sulphone (FS-13) for selective extraction of Cs and Sr from waste radioactive solutions. Reversed TALSPEAK process uses di-2-ethyl hexyl phosphoric acid in dodecane with TBP as phase modifier. Both the processes use task-specific stripping agents for back extraction of designated components.

For the estimation of physical properties and partition coefficients, as in-house solvent extraction code SIMPACTR (Simulation program for Actinide recovery at source) is developed. Experimental data was generated as listed under, which will be used as input data for the code.

a) For CCD-PEG process, density and viscosity data for pure FS-13, pure PEG-400, PEG-400 in FS-13, HCCD/PEG-400 in FS-13 has been generated as per established ASTM standards. Surface tension and IFT determinations are in progress. For stripping agent (Guanidine carbonate), aqueous density, apparent molar volume determinations, water activity values were experimentally determined and osmotic coefficients and activity coefficient in aqueous solutions were predicted. Figure 2 shows plot of deviations for the density (as recorded at different temperatures) of FS-13 diluent.

b) For Reversed TALSPEAK process, density and viscosity data for pure D2EHPA, pure TBP, D2EHPA in n-dodecane, TBP in n-dodecane and D2EHPA/TBP in n-dodecane has been generated as per established ASTM standards. For task specific-stripping agent (citric acid, lactic acid, DTPA), aqueous density, apparent molar volume, water activity values were experimentally determined. Osmotic coefficients and activity coefficients in aqueous solutions were predicted.

IV.11   Studies on Plutonium Polymerisation and De-polymerisation

During the solvent extraction operation in CORAL with the modified PUREX process, there can be conditions in which plutonium polymerisation can occur which may lead to loss of plutonium especially during process upsets. One such condition is possible during co-stripping, where, a low acid strip is used to reduce the plutonium in the lean organic. Polymerised plutonium can deposit as coating in process vessel or may go along with the aqueous wastes since they are not extractable. A method is developed for the recovery of plutonium from Ce(IV) bearing solution.

Experimental studies involve generation of plutonium polymer
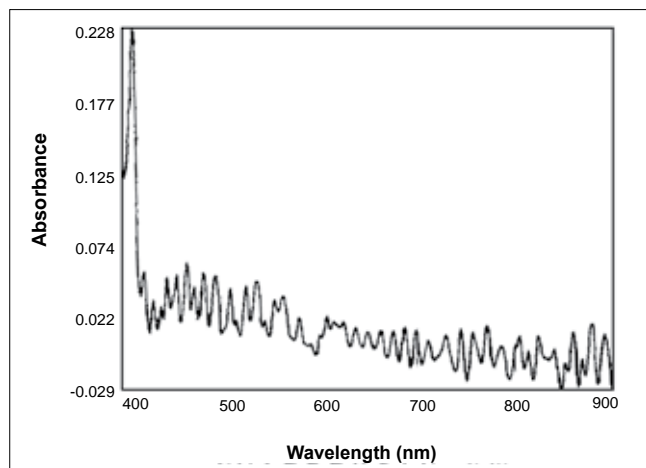
Fig. 1   *Spectrum of solution in the presence of Pu Polymer*
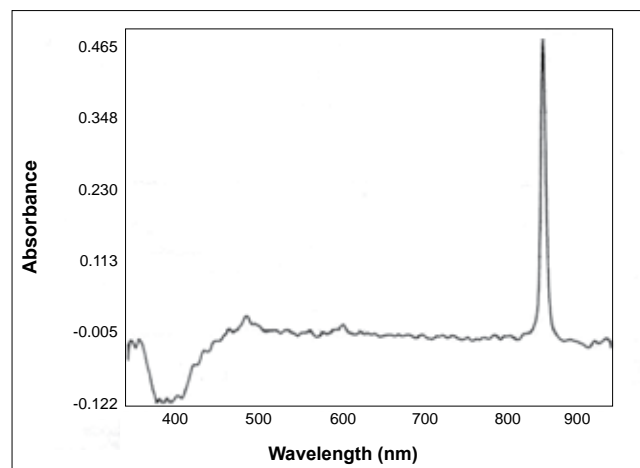
Fig. 2   *Absorption spectrum of the solution after de-polymerisation treatment*

from pure plutonium solution. The absorption of this solution is given in Figure 1. After subjecting the solution to the conditions of de-polymerisation using ammonium nitrate, the absorption spectrum was again taken which is given in Figure 2. The experimental studies indicate that using this process, it is possible to convert the plutonium polymer to ionic form, namely, Pu(VI) nitrate. Also, it is possible to detect the polymerisation using absorption spectra.

IV.12 Laboratory Studies on Aqueous Phase Reduction of Plutonium for Partitioning of Uranium and Plutonium

Several methods have been deployed for the separation of uranium and plutonium from the feed solution which is decontaminated from fission products in the PUREX process. The process based on uranous nitrate to reduce plutonium from IV to III valency for stripping preferentially plutonium from loaded organic is employed in most of the reprocessing plants. This method requires large excess uranous requirement, typically around ten times the stoichiometric amount. This is primarily due to the low K_d values of U(IV), the instability of Pu(III) in the organic phase as well as parasitic oxidation reactions. As the concentration of plutonium in fast reactor fuel reprocessing is high, alternate strategies have to be evolved to reduce this uranium load. Hence an alternate process, called aqueous phase partitioning, is being developed.

In this process, the aqueous phase containing Pu(IV) and U(VI), after co-decontamination cycle of extraction and stripping, is conditioned with externally generated U(IV) to reduce plutonium to III valency. This solution is then subjected to extraction conditions using 30% TBP which extracts uranium preferentially leaving plutonium in the aqueous phase.

Table 1 : Effect of time on the extraction of plutonium after addition U^{4+}			
Ageing period (hrs)	Plutonium		Uranium
	Aqueous (g/L)	Organic (mg/L)	Organic (g/L)
0	5.8	65	41.51
1.0	5.7	56	43.40
3.0	5.8	64	45.48
24	5.9	60	45.78

Table 2 : Effect of Pu^{3+}/U^{4+} on extraction separation uranium and plutonium (A/O=1)			
$Pu^{3+} : U^{4+}$	Plutonium		Uranium
	Aqueous (g/L)	Organic (mg/L)	Organic (g/L)
1 : 0.5	5.7	65	41.51
1 : 0.7	5.7	52	45.22
1 : 1	5.5	39	49.06

Experiments were conducted to study the stability of Pu(III) in the aqueous phase as well as the stoichiometric excess requirement of U(IV) for effective partitioning.

The stability of Pu(III) in the aqueous solution as a function of time is studied with a feed solution (acidity 3.7 M) of Pu(IV) and U(VI). A solution containing U(IV) 29 g/l was added to an extent of stochiometric equivalent (Pu:U^{4+} :: 1:0.5). The conditioned aqueous solution, after different periods of ageing, was equilibrated with 1:1 volume ratio of 30% TBP and the concentrations of total plutonium and total uranium were analysed in the two phases. From the data (Table 1), it can be seen that Pu(III) formed is stable and the pickup of plutonium in organic even after twenty four hours is nearly the same as that of the one immediately after adding U(IV).

The stoichiometric excess requirement was conducted with the same solutions as described earlier. Table 2 gives the variation

of U (IV) addition. It can be seen that near stoichiometric requirement only is required for effective reduction of Pu(IV) since the specification of plutonium contamination in uranium is 500 mg/kg of plutonium whereas around 1500 mg/kg is achieved in a single contact itself. The results indicate that a counter current extraction-scrub bank can be designed for separating plutonium and uranium which will meet the required specifications of product by this process.

IV.13 Development of Radiation Resistant Polymer – Ceramic Composites

Radiation damage in polymer materials results in the deterioration of mechanical properties such as tensile strength, elastic modulus, impact strength, shear strength and elongation. Radiation normally affects polymers in two basic mechanisms. They are (a) chain scission, a random rupturing of bonds, which reduces the strength of the polymer and (b) cross linking, which results in the formation of large three-dimensional molecular networks. Polymers containing aromatic molecules generally are much more resistant to radiation degradation than are aliphatic polymers. Among the commercially available aromatic polymers, polyetheretherketone (PEEK) is a linear, high performance and semi-crystalline thermoplastic polymer material. It possesses a variety of beneficial properties which include good process abilities, high mechanical strength and excellent stability in many harsh environments. Since PEEK is semi-crystalline, it is insoluble in all common solvents and has excellent chemical resistance to a very wide range of organic and inorganic liquids. PEEK melts at around 623 K and is highly resistant to thermal degradation. Its structure is shown below.
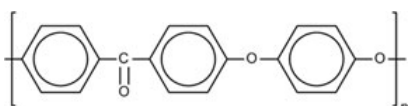
For specific applications of polymer materials in nuclear industry, they are expected to withstand radiation doses better than one gigarad, which is also the radiation tolerance limit of PEEK. The deterioration of polymer materials in ionising radiation is reported to be suppressed by the addition of ceramic fillers. Hence, PEEK was blended with varying percentage (5, 10, 15, 20 and 25%) of nano-alumina powder and were exposed to γ radiation after fabricating thin sheets in order to assess the radiation stability of the composites towards radiation by way of determining the mechanical properties of the composites before and after irradiation and comparing the results with those of pure PEEK. Specimens were removed from the γ chamber at intervals of cumulative dose rates 2.5×10^8 (starting from 10^8 up to 10^9 rads) and mechanical properties such as hardness, tensile strength, toughness, elongation at break, heat deflection temperature and dynamic mechanical properties were measured. To estimate the magnitude of improvement in radiation resistance of PEEK induced by
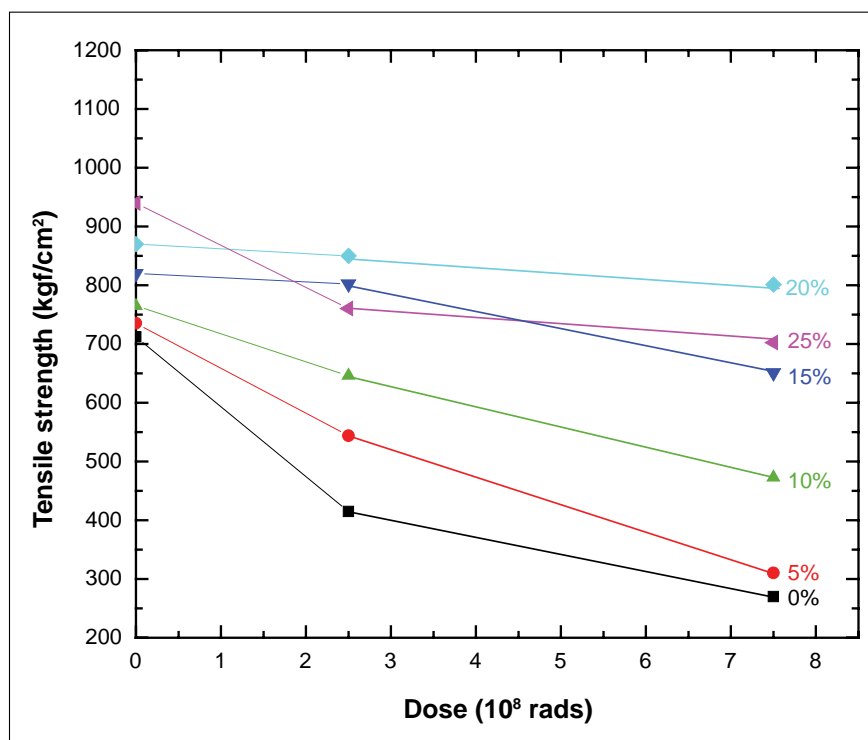
Fig. 1 *Tensile strength for irradiated PEEK and its composites with varying % of Al_2O_3 as a function of dose rate*

the ceramic filler, the mechanical properties of unirradiated specimens were also determined.

Hardness values (Rockwell M scale) measured for PEEK and its composites revealed an increase in hardness at higher doses owing to the increase in brittleness of the polymer. For pure PEEK, hardness after irradiation had increased by 11% (after 2.5×10^8 rads) and 26% (after 7.5×10^8 rads). The percentage increase in hardness for + 5% nano alumina composite was 7% (after 2.5×10^8 rads) and 16% (after 7.5×10^8 rads) and those values for + 25% nano alumina were 2 and 3% respectively. As alumina acts as a stabiliser, the extent of radiation damage to the polymer gets reduced, thereby reducing the percentage increase in the hardness values.

Tensile strength values obtained from stress-strain curves for irradiated PEEK and its composites are plotted in Figure 1 as a function of dose rate. The tensile strength value for pure PEEK before

irradiation was computed to be 712 kgf/cm^2. This value decreased by 42 and 62% after exposing to 2.5×10^8 and 7.5×10^8 respectively. It is evident from Figure 1 that the decrease in tensile strength after irradiation for PEEK–alumina composites was lower than that for pure PEEK as alumina retards the degradation of PEEK by acting as particle reinforcement to the polymer base.

Owing to chain scission polymers become hard and brittle and the elongation at break values decrease. The elongation at break values for pure PEEK before and after irradiation to 7.5×10^8 rods were determined to be 4 and 1% respectively. The percentage decrease in elongation at break for pure PEEK after irradiation to 7.5×10^8 rads was found as 69% and that for composite with 25% nano alumina was computed to be 40% for the same dose.

The decrease in toughness values for the irradiated composite specimens were also calculated to be much lower than the value

measured for PEEK. Typically, the percentage decrease in toughness after exposing to 7.5×10^8 rads was 53% for PEEK + 15% nano alumina sample whereas for PEEK the decrease in toughness was 88% after irradiation.

The change in glass transition temperature, heat deflection temperature and the modulus values measured for the irradiated composites uphold the reliability of other mechanical properties reported here for the composites. All these results corroborate the fact that alumina acts as a stabiliser and inhibits the degradation of PEEK during irradiation. It is also apparent that to improve the radiation resistance of PEEK, the weight of filler alumina required for stabilisation need not be more than 10–15%, because no drastic change in the mechanical properties could be observed above this composition besides fabricability problems arising for higher alumina content. Resistance of PEEK to gamma rays may be improved further by stabilising the radicals with alumina fibre reinforcement.

IV.14 Development of Nitric Acid Grade High Nitrogen 304L Stainless Steels for Reprocessing and Waste Management Applications

In the spent nuclear fuel reprocessing plant, excellent corrosion resistant materials are required as the nitric acid solution used in the PUREX process and powerful oxidisers from the fission products can significantly influence the corrosion processes. AISI type 304L stainless steel (SS) is extensively used for the fabrication

of vessels, tanks, piping and equipment in reprocessing plants. However, in highly oxidising nitric acid environment i.e.,concentration ($\geq$ 8N), temperature ($\geq$ 353 K), impurities (S, Si, B, P etc) and ionic species (Fe^{4+}, Cr^{6+}, Pu^{6+} etc), SS are susceptible to severe intergranular corrosion (IGC), even if the alloys are not sensitised.

Nitric acid grade (NAG) SS is an alloy with controlled chemical impurities like S, B, P etc., and with higher Ni, Cr, Si etc. to improve intergranular corrosion resistance under aggressive nitric acid conditions. AISI type 304L SS, and its improved varieties with extra low-carbon and restricted levels of C, Si, P, S, and Mo (AISI
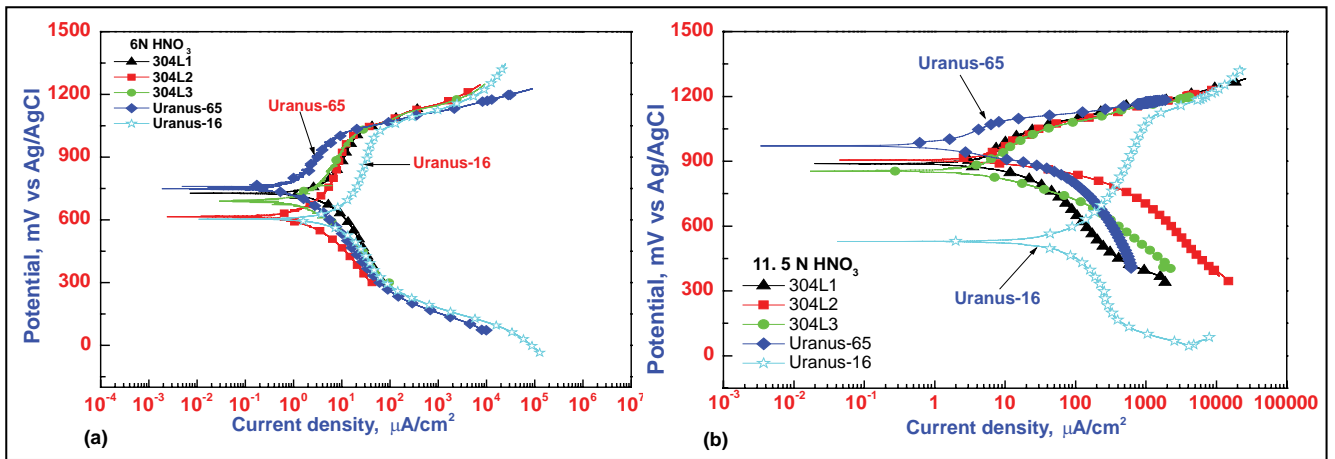
Fig. 1 *Potentiodynamic polarisation plots of different nitric acid grade stainless steel measured in (a)6N HNO$_3$ and (b) 11.5 HNO$_3$*
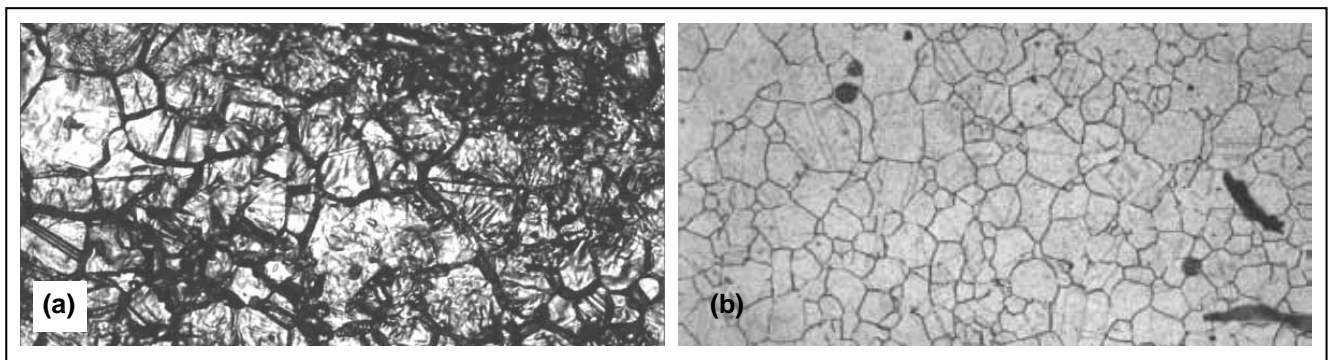
Fig. 2 *Typical microstructure of nitric acid grade stainless steel ; (a) Uranus-16 after polarisation and (b) nitric acid grade 304L1 SS*
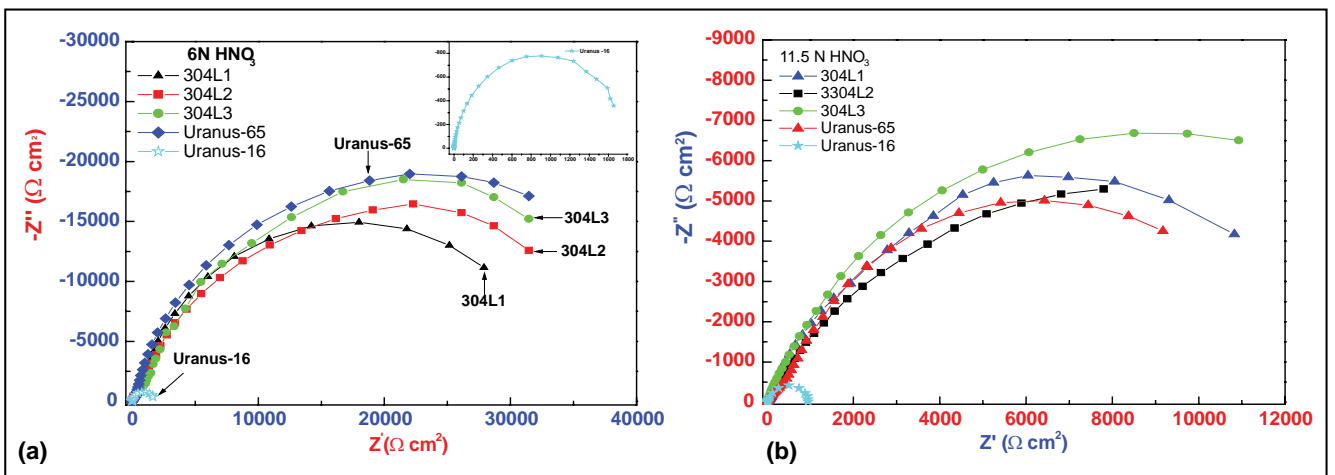
Fig. 3 *Nyquist plots of different nitric acid grade SS measured under OCP in (a) 6N HNO$_3$ and (b) 11.5 HNO$_3$*

type 304ELC), with Nb (AISI type 347), with Ti (AISI type 321), or AISI type 310L SS and its equivalent with neobium stabilisation and high chromium content, have been used in several reprocessing plants in the world. Present work provide data and information related to correlation between alloy composition and HNO$_3$ concentration of various new and

indigenously developed nitric acid grade stainless steel.

The corrosion resistance of new and indigenously developed nitric acid grade stainless steel designated as 304L1, 304L2 and 304L3 and two commercial nitric acid grade SS designated as Uranus-16 similar to 304L composition and Uranus-65 similar to type 310L SS

are investigated. In Figure 1(a), the results of anodic polarisation in 6N HNO$_3$ shows that the indigenous nitric acid grade 304L SS and Uranus-65 alloy exhibited similar and higher corrosion resistance compared to Uranus-16 alloy. The better performance of Uranus-65 SS is attributed to higher Cr (24.97 %) and Ni (19.60 %) content. In higher concentration

of 11.5N HNO_3 (Figure 1(b)), the decrease in corrosion resistance of nitric acid grade SS could be corroborated to the morphology of corrosion attack (Figures 2(a) & (b)). The non-uniformity of the attack observed after the polarisation test in the nitric acid grade stainless steel (Figures 2(a) & (b)) can affect the passive film property and intergranular corrosion resistance.

The typical Nyquist plots measured using electrochemical impedance spectroscopy in 6N (Figure 3(a)) and 11.5N HNO_3 (Figure 3(b)) revealed only one time constant with of an unfinished semi-circle arc for all the samples. Distinct difference in the impedance spectra could be observed between the different nitric acid grade alloys. The three nitric acid grade 304L stainless steel and Uranus-65 alloy showed similar and higher semicircle arc radius compared to Uranus-16 alloy in 6N HNO_3 (Figure 3a). However, the semicircle arc radius is lower in higher concentration of 11.5N HNO_3 (Figure 3b) which is due to involvement of autocatalytic metal dissolution which will proceed at higher rates in higher concentration.

The present study has provided critical factors involved in material degradation processes of different nitric acid grade SS to be used in reprocessing plant. The overall outcome of the investigation revealed that corrosion resistance of indigenously developed NAG 304L SS are comparable to commercially available high chromium and nickel Uranus-65 stainless steel alloy.

IV.15   Electroformed Seamless Ni-W coated Nickel Crucibles for Molten Salt Environments

Pyrochemical reprocessing of spent metallic fuels utilises molten LiCl–KCl eutectic salt at 673 K for unit operations like salt purification and electro-refining. Due to high temperature operation in molten chlorides, pyrochemical reprocessing requires salt purification vessels made of highly corrosion resistant materials.

Electroforming is an effective and economical alternative for fabricating seamless precision parts that are difficult to make by conventional manufacturing means. Electroformed nickel shows excellent strength, toughness, and ductility and is extremely resistant to corrosion in a wide range of environments. Electrodeposition of nickel–tungsten alloys has been utilised for various applications due to their unique combination of mechanical, tribological, magnetic, and electrical properties and, good resistance to strong oxidising acids, and to high temperature corrosion. Therefore electroformed nickel (EF Ni) and electroformed nickel-tungsten (EF Ni-W) coating on electroformed nickel were proposed as candidate materials for salt purification application and corrosion studies were carried out in molten LiCl–KCl salt.

The electroformed nickel and electroformed Ni-20 wt % W used in the present study was developed through collaborative R & D with Central Electrochemical Research Institute (CECRI), Karaikudi. The dimensions of electroformed plate with (50 μm) and without Ni-W coating obtained were tested in molten LiCl (44.48 wt%)–KCl (55.52 wt%) eutectic salt in air.

The percentage weight loss of the electroformed nickel, and electroformed Ni-W exposed to molten LiCl-KCl salt at 673, 773 and 873 K for two hours in air is shown in Figure 1. The results have shown that at 873 K the percentage weight loss for electroformed nickel is 15.6% while the weight loss for electroformed Ni-W at the same temperature is only 7.0%. The banded features exhibited in the as received condition disappear on dissolution resulting in a smooth and porous surface. After the corrosion test a salt film formed on electroformed nickel which is highly brittle and light green in color and got detached from the sample, from all sides. Investigations on the surface morphology of the cross
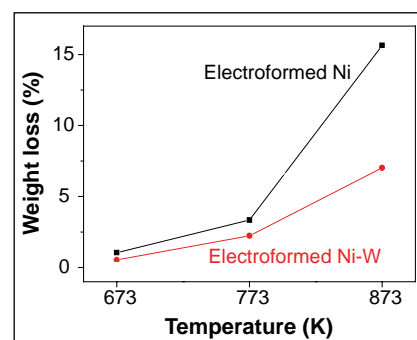
Fig. 1   Percentage weight loss of EF Ni and EF Ni-W at various temperatures in molten LiCl-KCl salt for 2 hours in air
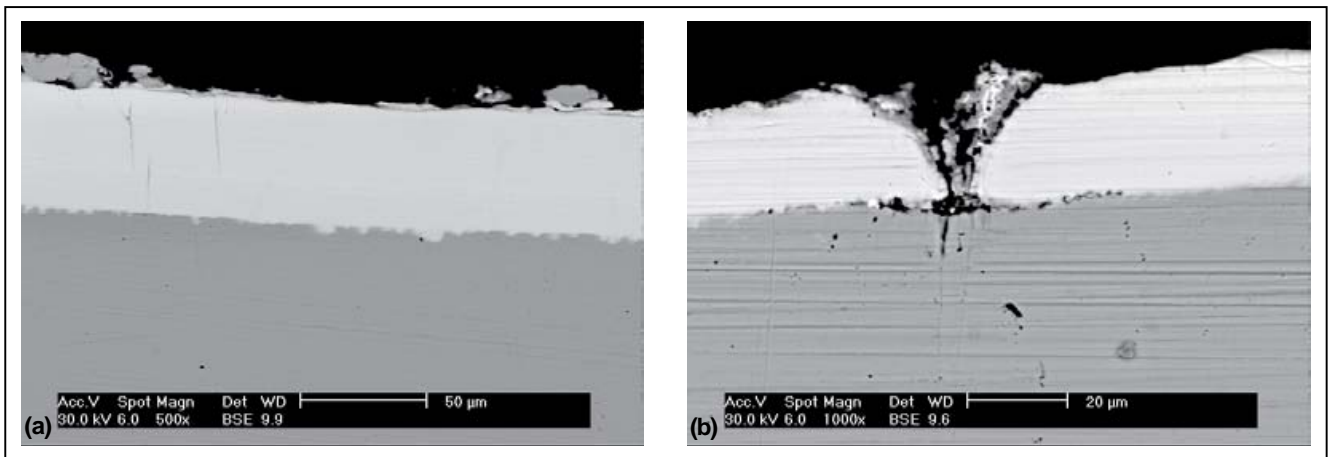
Fig. 2   Cross section microstructure of electroformed Ni-W (a) As received and (b) Molten salt tested

section of the salt film revealed two distinct porous layers within the salt film; nickel rich and nickel depleted layers of NiO and KCl. This indicated that the porous thick NiO film formed on electroformed nickel, allows the penetration of salt, thus accelerating the corrosion.

The results of electroformed Ni-W coating in molten LiCl-KCl salt in air indicated that the coating has exhibited high hardness as well as good corrosion resistance. The average microhardness value from the coating and from the substrate were found to be 665 and 328 VHN, respectively. These studies showed that no salt film was observed on the Ni-W coated surface, while the salt film similar to that formed on electroformed nickel was formed on the uncoated sides. The improved corrosion resistance of electroformed Ni-W in the present study was attributed to the tungsten rich NiO layer formed on the surface. Characterisation of the tested surface indeed showed enrichment of tungsten on the surface and the presence of NiO along with Ni-W solid solution. As can be seen from Figure 2 the disintegration of coating by opening up of a pre-existing crack in the Ni-W coating occurs due to the penetration of the molten salt. Based on the results of these studies, the parameters for deposition of electroformed Ni-W were optimised for crack free coating and prototype salt purification vessel was fabricated as shown in Figure 3. This study established

Fig. 3   Electroformed Ni crucible (Ni-W coated)

the feasibility to fabricate seamless corrosion resistant salt purification vessel. This vessel will be used in the mockup experiments using salts and characterisation of the vessel will be carried out in future for material selection and qualification.

IV.16   Grain Refinement in Ti-5Ta-1.8Nb Alloy Achieved by Severe Deformation Followed by Annealing

The Ti-5Ta-1.8Nb alloy, an α-β alloy of titanium is an alternate structural material for reprocessing applications due to its excellent corrosion resistance and weldability. Titanium and its alloys are also well known for their very high ductility but show poor yield strengths which limit their application as load bearing components. A possible method to strengthen the alloy is to engineer the grain size to finer dimensions so that large number density of grain boundaries impedes the
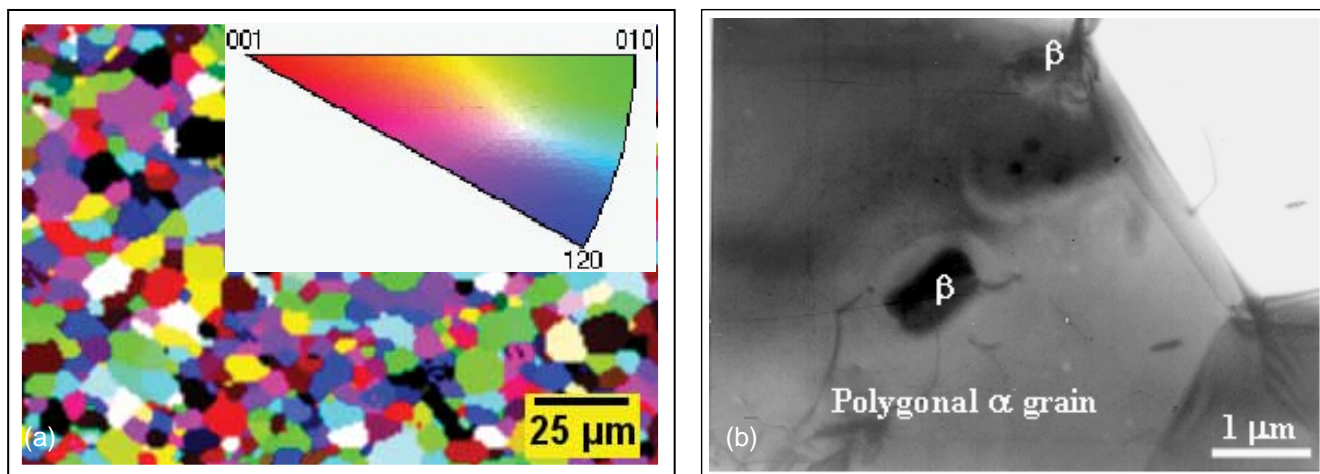
Fig. 1   *(a) Orientation map of the starting material showing equiaxed polycrystalline grains, IPF legend is shown in the inset and (b) TEM bright field image showing the polygonal α-Ti and embedded β-Ti grains*

movement of dislocations, thus enhancing the yield strength. Severe plastic deformation may be employed to obtain increased yield strength of titanium alloy. Rolling is one of the simplest methods to impart deformation to metals. Rolling at sub-zero or cryogenic temperatures has the advantage, since dynamic recovery effects at room temperature or higher can be suppressed. Thus, in case of cryo-rolling, high strain hardening is achieved, which results in formation of highly deformed and sometimes even fragmented grains. But the excessive hardening leads to severe loss of ductility and also the defect-laden fragmented grains are likely to be unstable under operating conditions at elevated temperatures. The

microstructure may be stabilised by annealing at temperatures below the recrystallisation temperature. It may be mentioned here that although typical recrystallisation temperature is about 0.3 T_m (T_m: melting temperature; $T_{m\text{-}Ti} \sim 829\,K$) for titanium alloys, its effects may set in quite early in these materials owing to very high defect density and presence of large number of boundaries. Therefore, the safe operation temperature limit for the cryo-rolled alloy needs to be determined.

The effect of heavy rolling (upto 99.97%) under cryogenic conditions (cryo-rolling) and subsequent annealing at various temperatures for different time durations are presented in this

article. Microstructure, microtexture and crystallography of the material under different processing conditions are studied using scanning and transmission electron microscopy, electron back scatter diffraction (EBSD) and X-ray diffraction (XRD) techniques. These results are correlated with hardness.

Figure 1 (a) shows the EBSD orientation map of the starting material, which is inverse pole figure (IPF) coloured. It can be seen that the alloy is poly-crystalline with random oriented grains. Equiaxed grains measuring about 8 μm are seen. Figure 1 (b) shows the bright field transmission electron micrograph revealing the larger polygonal α-Ti (hcp) grains
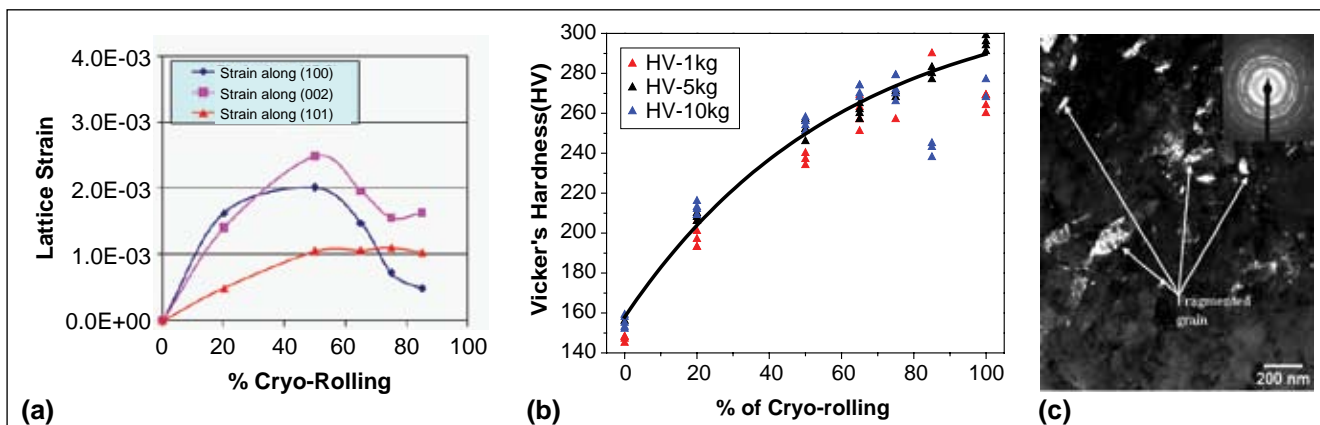
Fig. 2   *(a) Lattice strain calculated from XRD spectra as a function of degree of deformation (b) Variation of hardness as a function of degree of deformation, both of which exhibit a maxima and (c) TEM dark field image showing grain fragmentation for the 99.97% cryo-rolled material*

with inter and intragranular β-Ti (bcc) of relatively smaller size. The hardness of the alloy in this condition was found to be ~150HV.

Figure 2(a) shows the lattice (micro) strain as measured from peak shift in the XRD spectra along the prism plane (100), basal plane (002) and pyramidal plane (101) for various degrees of cryo-deformation. It is observed that the micro-strain is positive indicating lattice expansion. It is also observed that maximum micro-strain occurs at about 50% of cryo-rolling whose value is ~0.33% along the 'a' and 'c' axes of the α-Ti unit cell indicating a uniform expansion of the lattice. The resultant volume expansion of the unit cell is ~ 0.98%. Beyond 50% of cryo-rolling relaxation of the lattice is observed. Figure 2(b) shows the variation of Vickers hardness with cryo-rolling. Hardness was found to increase exponentially with increase in deformation. Figure 2(c) shows the TEM dark field image of the 99.97% cryo-rolled material revealing all the α-Ti grains along (002) direction. The grain sizes are observed to be in the range 50–200 nm; a remarkable reduction in size from the starting value of ~ 8μm (Figure 1(a)). Thus, grain refinement by means of heavy deformation is established. Although relaxation in micro-strain beyond 50% of cryo-rolling was observed (Figure 2(a)) it is not found to have any effect on the macroscopic property of the material (Figure 2(b)). The

relaxation in micro-strain may be attributed to defect annihilation by creation of new surfaces through grain fragmentation. However, the increase in the number of grain boundaries which offer hindrance to movement of dislocations results in the observed increase in hardness. Therefore the hardening phenomena observed here is due to the interplay between dislocation density and grain size effects at higher deformation regimes.

Figure 3 deals with the variation of mechanical properties during annealing, a detailed analysis of which can yield valuable information about the kinetics of the recovery-recrystallisation process. Figure 3(a) shows the dependence of hardness (in Vickers unit) on time of annealing in the temperature range 573 – 873K for the 85% cryo-rolled material. While the hardness remains nearly constant at 573K, it softens at higher temperatures in an exponential manner with the rate being higher at higher temperatures of annealing. Figure 3(c) shows a similar viewgraph for the 99.97% cryo-rolled material. In this case the material begins to soften even at 573K since recovery and recrystallisation is expected to begin at lower temperatures for higher degree of deformation. Figure 3(c) shows the Arrhenius analysis of the hardness values at different annealing temperatures. The activation energy (ΔE) for the recovery/recrystallisation process

was evaluated as ~ 0.27 eV (26 kJ/mol) for both 85% and 99.97% cryo-rolled samples. Literature reports suggest that this value is much less than the ΔE for diffusion of cold-deformed α-Ti (~96 KJ/mol) but is more than that reported for cold sprayed CP-Ti (~ 13 kJ/mol). The present results suggest that the high density of defects and grain boundaries result in the nucleation rate being exceedingly high making grain refinement possible.

Figure 4 (a) shows the orientation map of the specimen cryo-rolled upto 99.97% and then annealed at 773 K for three hours. The image is IPF coloured, colour codes of which are given by the IPF in the inset. It is observed that the average grain size is about 2.1 μm, still only about 25% of the starting grain size. Figure 4(b) shows the (002) pole figure of this material. The pole figure reveals that the material is crystallographically textured such that the 002 plane normals of α-Ti are inclined with respect to the sheet normal by 35°. The texture is similar when annealed at higher temperatures and for longer durations, hence it may be designated as the typical recrystallisation texture for this material.

To summarise, it can be said that significant grain refinement down to about 50nm can be achieved in the Ti-Ta-Nb alloy by means
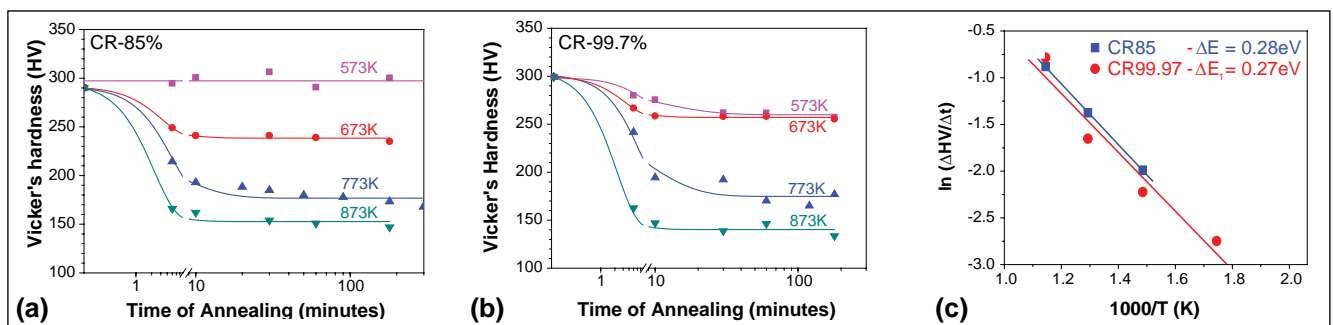
Fig. 3 *Variation of hardness with time for (a) 85% and (b) 99.97% cryo-rolled materials during annealing at various temperatures and (c) Arrhenius plot of the initial rate of recovery*
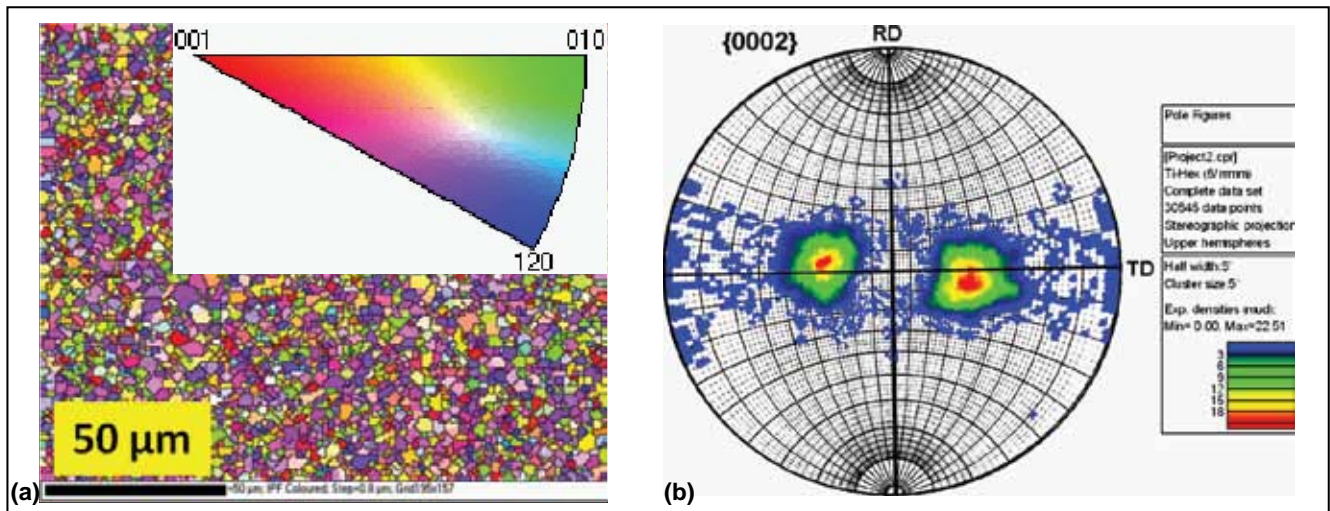
Fig. 4 *(a) EBSD orientation map for the 99.97% cryo rolled material that is annealed at 773K for three hours showing fine grains measuring 1-2 µm and (b) pole figure along the (002) plane showing strong crystallographic texture*

of cryo-rolling, resulting in a two-fold increase in hardness with a concomitant increase in the yield strength of the material. However, the material properties are stable only upto about 573K beyond which it softens due to recovery and recrystallisation. Controlled softening of the matrix is necessary from workability (ductility) point of view. It was shown through this work, that when annealing is carried out below the recrystallisation temperature, grains measuring about 2 µm can be obtained with retention of hardness about 50% higher than the starting matrix. These results demonstrate that the TiTaNb alloy can be engineered to have significantly high yield strength without much loss of ductility, known as 'high tensile ductility', so far demonstrated only for fcc metals, leading to possibilities of using the material for load bearing applications in highly oxidising environment.

IV.17   Development of a Multi-Robotic System for DFRP Analytical Cell

Remote sampling system is an application specific integrated robotic control system in DFRP cell (Figure1). It consists of various robots viz. Sample Handling Robot (SHR), Capping/Decapping Robot (CDR) and Pipette Robot (PPR), tip rack and accessories. This sampling system has dedicated GUI based software, which can control the operation of all robots in programmed mode or manual
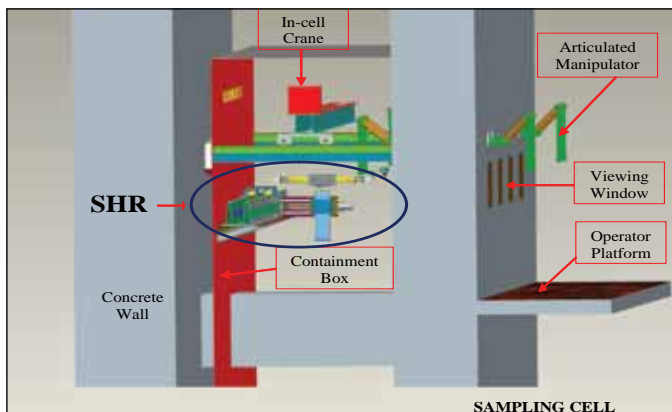
Fig. 1   *Sampling cell*
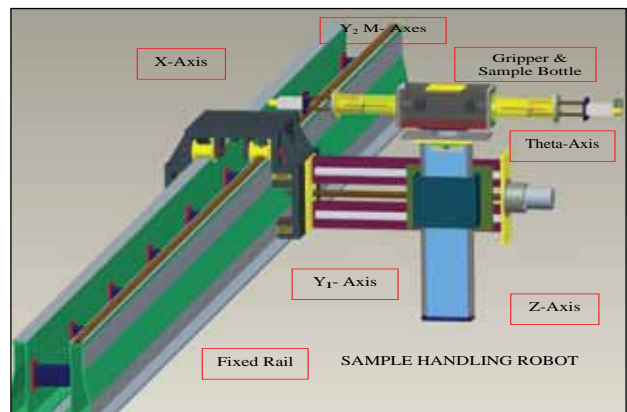
Fig. 2   *Sample handling robot*

mode and also it has data logging system for storing information of samples and other operational relevant data.

The conceptual design of comprehensive remote sampling system for remote sampling of process liquid in the DFRP analytical cell is completed and fabrication process is in progress. The major tasks of this sampling system is to collect sample bottles from various predefined locations and move the sample bottles through different stations for various operations like de-capping, sample collection, capping, transporting the sample bottle to analytical cell, pipetting, rinsing and disposal of used sample bottle, pipette tip etc. In this remote sampling system sample handling robot plays a vital role in completing the analysis cycle. Apart from the operational requirement it has many constraints and challenges like remote assembly and disassembly of robot using 250 kg capacity in-cell crane and nitric acid fumes and radiation environment compatibility.

SHR is designed in modules to facilitate remote assembly/ disassembly and maintenance. It has six degrees of freedom and is a cantilever configured custom built robot. The entire design concept is enabling provision for remote assembling and dismantling of SHR using the 250 kg capacity in-cell crane and articulated manipulators which are present inside the cell. The cantilever configuration was adopted for sample handling robot to have obstacle free travel with the presence of pipelines inside the cell. Yet another challenge addressed was how to make the robot remotely removable for any maintenance inside the cell (Figure 2). A specially designed fixed rail configuration is adopted which gives self aligning during remote assembly and topple free operation of the robot.

Capping/Decapping Robot is designed with two sub-systems, one for bottle handling and the other is for cap handling. One common bottle gripper is provided in the bottle handling unit. It has two motors, one for gripping of

bottle and the other for rotation of bottle. A self compliance is provided in all the cap gripping heads to adjust with small misalignment in the start of the thread and also to accommodate the axial travel during capping and decapping.

Pipette robot is a cylindrical configured robot. It has base rotation, vertical travel and horizontal travel and a pipette head. The prototype pipette head is already manufactured and tested for its accuracy. The pipette head is demonstrated within 2 % error.

Stepper motors are used in the entire robotic systems. The stepper motors perform better in open loop control as usage of any feedback devices are prone to fail in this environment.

A GUI based software to control the operation of robotic control system for remote sampling will be developed. This software can control the operation of various robots in a programmed mode or online mode through pendant.

IV.18 Pyrohydrolysis Method for the Determination of Fluoride and Chloride in Uranium Oxide and Boron Carbide

Determination of chloride and fluoride is important in the quality control of nuclear materials, due to their implications in corrosion processes. Pyrohydrolysis is the recommended ASTM procedure for the determination of these halides in uranium oxide and boron carbide. In this method, the sample is kept in a quartz boat and heated to a high temperature

(~1273 K) in a quartz tube under a flowing stream of argon, saturated with water vapour. The pyrohydrolysis reaction converts the fluorides and chlorides in the sample into HF and HCl, which is carried away by the flowing argon. The Ar / (HF, HCl) mixture that exits, is passed through a water cooled condenser in order to condense the halides and is

eventually collected in a suitable buffer solution.

A pyrohydrolysis apparatus (Figure 1) was designed and fabricated as per the ASTM method. Using this apparatus the analytical procedure for the determination of fluoride and chloride in uranium oxide and boron carbide was standardised. In the

pyrohydrolysis of boron carbide, U_3O_8 was added as the accelerator for the release of halides.

Standardisation was carried out by using a spiked standard of uranium oxide and boron carbide. Sodium acetate buffer solution was used for collecting the condensate. Appropriate ion selective electrodes were used for the determination of fluoride and chloride. Excellent recovery (~ 95%) was obtained for both chloride and fluoride. When one

gram of the sample was taken the detection limit of fluoride and chloride was found to be 2.5 and 25 µg/g respectively.

The standardised procedure is now being regularly applied for the analysis of uranium oxide microspheres obtained from the sol-gel method and boron carbide samples. The results obtained by using this method, corroborated well with the results obtained on identical samples analysed by BARC.

Fig. 1 *Photograph showing the apparatus used for carrying out pyrohydrolysis*

IV.19 Enhancing the Availability of Hot-Cell Equipments through Novel Maintenance Approaches Combining Direct and Remote Repairs

A large number of remotely operated equipments confined to the inert atmosphere shielded hot cells of the Radio Metallurgy Laboratory and dedicated to the Post-Irradiation Examination of FBTR fuel and structural materials have served nearly fifteen years without any direct contact repairs / maintenance. This is largely due to the prudent design philosophy adopted for the in-cell equipments which envisages long term maintenance-free operation with provision for essential remote repairs using master slave manipulators. However, unexpected failures of the following in-cell equipments necessitated direct contact repair. The carriage drive mechanism (CDM) of the neutron radiography system was unavailable due to failure of a transmission coupling. An in-cell crane became inoperative due to the overlapping of steel rope on the groove of steel drum. In both cases,

contact repairs complemented by remote operations were carried out with minimum man-rem expenditure and without spread of contamination by evolving special methodologies.

Attempts for remote repairs of the carriage drive mechanism using specially designed gadgets assisted by CCD cameras and LED array lighting indicated that due to the complexity involved and the inaccessibility of some of the components, it is preferable to carry out the work by resorting to direct contact repair. A meticulous step by step procedure was evolved for carrying out this contact repair.

In order to facilitate repair work without man-entry into the hot cell, a scheme was made to dissemble the affected module of the system remotely and to locate it within the hot cell such that it is accessible from a specially established work

area outside the hot cell by opening the hot cell door. Before opening the door, the inert atmosphere in the hot cell needs to be converted to air. Radiation field in the cell estimated by direct measurements through master slave manipulator port openings and also using TLDs inserted and withdrawn from the hot cell indicated about 150 mGy/h. Radiation level in the work area was brought down to about 300 µGy/h by relocating to the extent possible all radioactive sources from this hot cell to the adjacent hot cells as well as by cleaning the hot cell floor using remote gadgets.

To further minimise the exposure of personnel during contact repair, all repair activities were divided into sub-activities and detailed procedures and check lists were prepared after validating them through a number of rigorous mock-up drills. The extent and duration of contact work was planned to

Fig. 1 *Photograph showing personnel engaged in the repair of in-cell crane*

Fig. 2 *Photograph showing personnel engaged in the repair of CDM*

be minimised by executing all possible sub-activities through master slave manipulators as far as possible. Action plan was prepared for facing anticipated problems and to keep the corresponding tools and gadgets ready.

To avoid over exposure/spread of contamination and particulate ingestion by personnel, all the participants of the campaign were trained rigorously before the actual work regarding the essential principles of time-motion management, health physics, ventilation and air monitoring, rubber station dress codes and other general safety provisions. Full dress rehearsal was carried out wearing fully ventilated suit/ frog-man suit and breathing apparatus.

For effective coordination between the groups of personnel working simultaneously at various locations such as the operating area, isolation area, warm work area, and control room, audio-visual communication was established during the repair campaign. This was useful particularly during the in-cell crane repair (see Figure 1), where the crane module had to be lifted up through a roof plug opening after
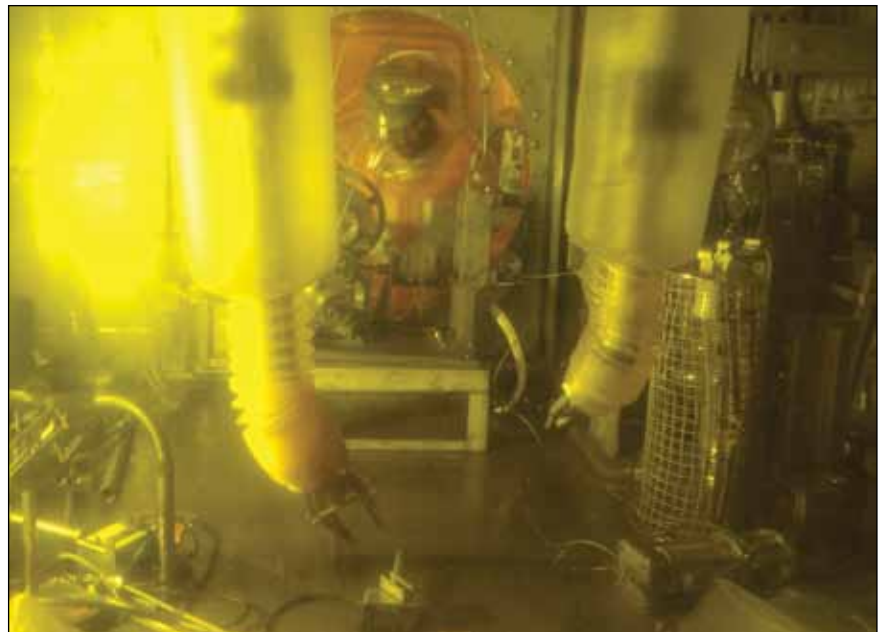
Fig. 3 *CDM under contact repair as seen through shielding glass window*

removing the roof shielding block weighing eighteen tonnes. Taking advantage of the rare opportunity offered by the opening up of an active operating hot cell, house keeping of the concerned hot cell, which normally gets bogged down by various constraints, was carried out effectively by segregating and disposing materials that have outlived their useful life.

Workmen wearing fully ventilated suits and respirators did the contact repair on carriage drive mechanism from behind the

hot cell assisted by master slave manipulators controlled from the operating area (see Figures 2 & 3). The repair campaigns were completed systematically by following all safety procedures with very minimum man-rem expenditure of the order of about 3 mSv distributed among six persons. The above activities have boosted the confidence level of personnel and has prepared them for planning and taking up more challenging jobs in radioactive environments.

IV.20 Development of Remote handling equipment for Demonstration Pyrochemical Processing Plant

A pilot facility is being built in Radiochemistry Laboratory for developing and demonstrating a viable technology for manufacturing metallic fuels using pyrochemical reprocessing technique. As this process involves handling of highly radioactive spent fuels in high purity inert atmosphere, all process operations and associated handling have to be necessarily carried out using remote techniques. Radioactive cells essentially require handling equipment such as an in-cell crane and power manipulator for handling heavy equipment. For demonstration of the remotisation of the process steps inside the containment box in the upcoming pilot pyrochemical reprocessing facility, a special in-cell crane with a power manipulator has been developed. The in-cell crane with power manipulator (IC&PM) is designed and developed to operate in high purity argon atmosphere and is modular and compact. Modularity of the system is essential for remote maintenance and assembly. Since the space inside the process containment box is at premium, compact

design and high work volume of IC&PM to containment volume ratio were the design criteria considered during the design stage. Careful selection of motors for the system was carried out and brushless DC (BLDC) servo motors have been selected for all motions to achieve compactness, maintenance-free operation, high mean time between failures (MTBF), high efficiency, and wide range of speeds. The drag chains carrying the cables have been designed for remote engagement and disengagement during remote interventions.

The in-cell crane is designed for a safe working capacity of 500 kg. The containment box is 5300 mm long, 2000 mm wide and weighs 2500 kg. The in-cell crane has long travel (3925 mm), cross travel (1500 mm) and a hoist (2296mm (1796 mm and - 500 mm)). Due to the compactness, the span of 1850 mm is obtained and the approach has been maximised. The long travel wheel carriage houses the in-cell crane and power manipulator. Due to the low clearance between the ceiling of the containment and the crane

(39 mm), rope drive has been chosen for long travel with a continuous rope tensioning arrangement as shown in Figure 1. The compactness of the crab has been obtained by the optimisation of the component layout and housing the hoist motor within the rope drum (Figure 2). The drive transmission to the long travel is by a penetrating shaft from outside the containment box. Drive shaft is provided with double mechanical seal with purging facility to reduce the leak rate to 0.05% of the containment box volume per hour. In cell crane is operated through remote pendent, which communicates with the motion controller and variable frequency drives. The power manipulator has seven degrees of freedom viz, cross travel (C.T), azimuth (rotation about vertical axis), vertical "Z" motion, shoulder arm, elbow arm, wrist extension, wrist rotation, in addition to gripping motion of the tongs. At the end of the power manipulator, a modular gripper with a force sensor is provided as an end-effector. Figure 3 shows the photograph of the power manipulator.

Fig. 1 *View of the wire rope tensioning arrangement*

Fig. 2 *Optimisation of the component layout*

Fig. 3 *Photograph of power manipulator*

Users can set the gripping force (0-136 kgf) from the control panel depending upon the nature of the object being handled. Speed of each axis can be varied using the pendant according to the requirement. The in-cell crane and power manipulator have been tested and validated for the performance prior to installation at site. The IC&PM has been installed in the process containment box, and functional trials have been carried out. The performance and ease of operations in the containment box are found satisfactory. Trials in air are being carried out using in-cell crane and power manipulator. Figure 4 shows the IC & PM installed in the containment box.

Fig. 4 *In-cell crane with power manipulator installed in the containment box*

IV.21   Fast Reactor Fuel Cycle Facility

Work on design of the Fast Reactor Fuel Cycle Facility (FRFCF) to close the fuel cycle of Prototype Fast Breeder Reactor (PFBR) is being piloted by IGCAR with technical support from BARC and NFC. A preparatory project for development of site infrastructure and engineering of FRFCF has been sanctioned and is in progress. Approval of AERB for the site has been obtained. Technical investigations of the site like geotechnical investigations, hydro-geological studies and estimation of design basis flood level have been completed. Basic infrastructure like approach roads, construction power supply system, workshop and storage/construction office space has been created at the site to reduce the lead time required to commence the construction work once the FRFCF project is sanctioned. Review of the preliminary safety analysis report by Project Design Safety Committee for FRFCF and specialist working groups is in progress. Consultants have been appointed to carry out preliminary design of conventional

Fig. 1 *View of the workshop building of FRFCF project*

Fig. 2 *View of Infrastructure buildings for FRFCF project*

systems and assist in preparing cost estimates for the detailed project report. They would also carry out the detailed design and prepare the tender documents. Detailed project report for FRFCF is planned to be submitted for financial sanction during the last quarter of the financial year 2009-10.

IV.22 Innovative Engineering for Equipment Building and Development of New Experimental Facilities

The chemistry of nuclear fuel cycle often calls for innovative experiments involving highly specialised requirements. To meet such experimental programmes it is necessary to custom build equipment and develop engineering methodology to fabricate unique accessories. These applications include development of sophisticated instrumentation as well as involved mechanical engineering. Some typical examples of such innovative engineering in support of the research on the chemistry of nuclear materials is presented here.

A. Ultra sensitive thermal probe for an in-house solution calorimeter

A sensitive thermal probe has been developed for use with a

Fig. 1   *Dilatometer assembly*

solution calorimeter built in-house. This probe is highly sensitive and would be used to measure the heat evolved during the dissolution of substances resulting in a rise in temperature only to the tune of a few Kelvin. Typical applications of this device include isoperibol solution calorimetry for the assay of special nuclear materials, thermometric titrations, bio medical applications etc.

A special probe was constructed using the YSI 44000 series thermistor (10 kΩ at 298 K) with a sensitivity $\Delta R/R$ as 426×10^{-5} at 298 K. A novel adaptation of a lock-in amplifier circuit is made to make linear measurement over a change of 10% $\Delta R/R$.

In order to achieve a wide dynamic range along with good linearity, the DC voltage (proportional to the resistance) is first converted into a frequency signal by a VFC circuit. Subsequently the resultant frequency is counted for a period of 400 milli seconds in order to generate 100000 counts on full-scale. A microcontroller takes care of the control and measurement of the integrating type analog to digital converter (ADC).

The thermal probe was placed in a glass beaker containing water and the beaker was in turn immersed in a water bath that was maintained at 299 K. The thermal probe was connected to the electronic module and the measured counts were converted into resistance and further into temperature.

B. Development of instrumentation for high temperature dilatometer for metallic fuel fabrication facility

A high temperature dilatometer system housed in an inert atmosphere glove box is being developed as a part of the metallic fuel preparation facilities in our laboratory. This model is an enhanced version of our earlier model of the dilatometer. In this system the push rod assembly along with LVDT is located inside the glove box while the furnace assembly is placed outside the latter. The experimental facility is shown in Figure 1. The instrumentation essential for carrying out the experiment, control of the furnace, measurement of experimental parameters, system surveillance etc. were developed.

The instrumentation used for the measurement is based on a microcontroller that transmits the measured data to a personal computer. The signal processing operations such as linearisation, cold junction compensation, signal averaging etc. are carried out by using the personal computer with the help of the Visual Basic software.

Fig. 2   *Fuel pin scanner assembly*

C. Development of instrumentation for fuel pin scanner

Microspheres of uranium plutonium mixed oxide fabricated through the sol-gel process would be vibrocompacted into fuel pins. These sphere-pack fuel columns need to be examined for their density and uniformity. A fuel pin scanner (Figure 2) that functions based on the principle of gamma absorptiometry was developed for this purpose. In this procedure a strong ^{137}Cs γ emitter is used as the transmission source. The activity of the source (~10 μCi), as it is transmitted through the fuel pin is measured by using a LaBr scintillation detector fitted with a 2 mm wide slit and a 2" SS collimator.

In order to assess the performance of this system a was carried out by using a surrogate vibro-packed fuel pin with UO_2 in order to get the density distribution. The step scan experiment was conducted for the pin with a step size of 2 mm, and a counting period of 200 seconds and with three iterations. This experiment revealed that the positioning precision and the counting consistency are satisfactory.

D. An automated and remotely operated sintering furnace housed inside a special glove box

A remotely operated facility for the fabrication of sol gel based test fuel pins has been set up at our centre. Among the various steps in the fabrication of the fuel, sintering of the micro-spheres is crucial. This comprises of several operations that involve both the handling of the delicate micro spheres as well as the programmed operation of the furnace. Sintering is carried out in a tungsten mesh furnace at 2173 K under argon–hydrogen atmosphere. The furnace is housed inside a special glove box and various services like vacuum and gas lines are connected through special leak tight feed-throughs. A heavy duty lifting mechanism facilitates lifting of the top dome of the furnace and a pneumatically operated mechanism actuates the lid to open the furnace chamber for charging of the microspheres. The hoisting mechanism is a telescopic three stage drive occupying only a limited head room. The moving gantry stage and the attached end effectors have an overall positioning accuracy of ±0.5 mm in order to avoid collision with the thermal shields. All the complex operations are integrated and controlled from the operating area through a camera assisted viewing system. A photograph of this furnace is shown in Figure 3.

Fig. 3   *The sintering furnace housed inside a glove box*

E. An experimental facility for the measurement of solidus and liquidus temperatures in plutonium bearing fuels

The solidus point corresponds to the temperature at which the first spec of liquid appears while heating an alloy, while the liquidus temperature refers to the point at which it completely liquefies. Experimentally determined value of the solidus temperature of a nuclear fuel is required for estimating the upper limit of its center line temperature. The spot technique is a method which is quite useful in carrying out such measurements. Recently an experimental system that employs the spot technique was designed and commissioned where the solidus and liquidus temperatures of alloys could be measured over a wide range of temperatures (1273 to 2273 K). This facility is enclosed in a glove box, in order to facilitate measurements on plutonium bearing compounds. Photograph of the experimental system is shown in Figure 4. This experimental technique involves heating the sample held in a Knudsen effusion cell (K Cell) by radiofrequency induction under vacuum. The sample surface is monitored remotely by using a telescopic device. After complete liquefaction of the metal the molten surface of the sample reflects the image of the K-Cell as a black spot. At temperatures

Fig. 4   *Experimental assembly used in the "spot - experiment"*

between the solidus and liquidus this surface produces broken spots. An accurate measurement of the temperature of the sample is made with the help of a pyrometer that is focused on to a black body hole drilled on to the K-Cell bottom.

In order to validate the accuracy of the experimental measurements, the solidus and liquidus in the system Cu-Ni were measured. The results obtained in this investigation could reproduce the assessed data within 5 K.

F. Development of an innovative welding methodology for fabrication of online hydrogen sensors for liquid metal fast reactors

Liquid sodium is used as the coolant in the primary/secondary loop and steam is used in the tertiary loop for power generation in liquid metal fast breeder reactors. The liquid sodium in the secondary loop is separated from high pressure steam in the tertiary loop by thin walled steel tubes at the steam generator. Development of any defect in steel tubes during reactor operation would lead to sodium-water interaction resulting in generation of large amount of heat. It is necessary to detect leak of steam into sodium at the inception stage. Since sodium temperature is greater than 673 K, the hydrogen and sodium hydroxide produced in the sodium-water reaction would completely dissolve in sodium. This would cause an increase in the hydrogen concentration in sodium. Hydrogen sensors need to be used in order to detect such failures at their very inception. Manufacture of this sensor involves machining and assembly of intricate parts with very close alignment tolerances and welding of components

made out of dissimilar materials like pure iron and stainless steel (Figure 5). These sensors have been fabricated by adopting stringent dimensional control, proper sequencing and innovative mock-up trials. An automated TIG welding (orbital welding process) has been used in order to produce high quality welds. The whole assembly was subjected to helium leak testing under pressure and found the leak rate was within the acceptable limit of 1×10^{-7} Pa l sec^{-1}.

G. A quadrupole mass spectrometer based facility for understanding oxide – analyte interactions

Sensors based on semiconducting oxides as thick films made out of the nano crystalline powders or as thin films are being developed for measuring low and ultra low levels of gases such as hydrogen, ammonia and NO$_x$ which are of interest and also for monitoring environmental pollution. These devices comprise a tailored oxide thin film that is sensitized to the analyte by modulating its (surface) conductivity. The development of such sensors necessitate the characterization of the analyte-sensor interaction. In order to carry out such investigations a quadrupole mass spectrometer system was established (Figure 6). This QMS system was calibrated with mixtures containing known concentrations (0.5 to 1.2 ppm) of He, Ne, Ar, CO$_2$ and Kr. The signals obtained with the gaseous products (N$_2$O, NO$_2$ and NO) emanating from a decomposing lead nitrate specimen (573 K) showed that this system could be effectively used for understanding the interaction of analyte species with metal oxide surfaces.

Fig. 5 *Electrochemical hydrogen meter (ECHM) – Probe: typical*

Fig. 6 *Quadrupole mass spectrometer based facility for understanding analyte – oxide interactions*
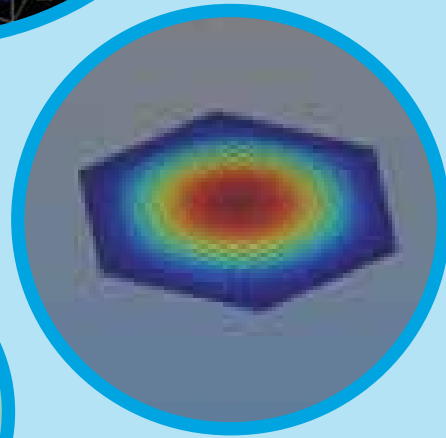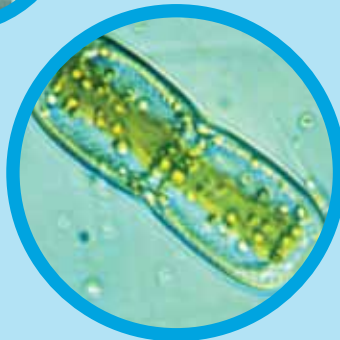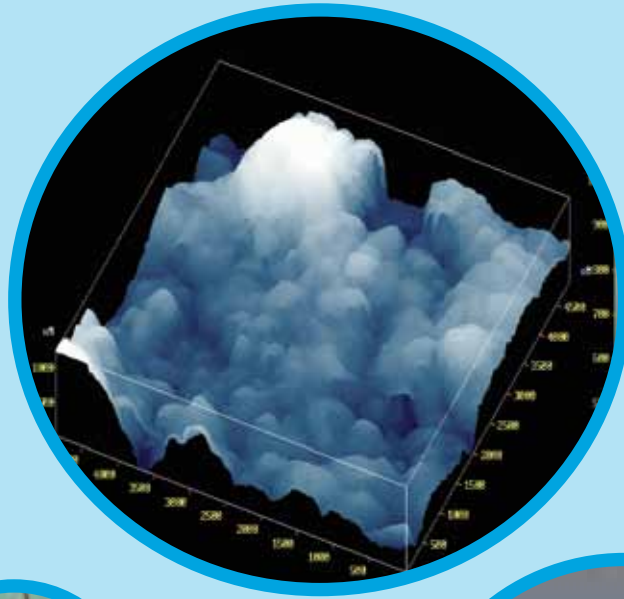
CHAPTER V

Basic Research

V.1 Defect Detectability in Austenitic Stainless Steel by Lock-in Thermography

Lock-in thermography is an advanced infrared imaging technique that has been successfully used for inspection of quantitative characterization of surface, subsurface defects, features and measurement of thermo-physical properties. The main advantage of lock-in technique is its invariance to surface conditions apart from the other advantages such as capability to inspect large areas rapidly, repeatability and sensitivity. The lock-in thermography uses a periodic sinusoidal thermal excitation in order to derive information on reflected thermal wave phase and magnitude.

Stainless steel 316 finds extensive applications in the nuclear and other industries as a structural material. At the Quality Assurance Division, detailed experimental investigations have been undertaken to establish the limit of defect detectability in stainless steel.

AISI 316 plates of dimensions 150×100 mm and thicknesses of 4 and 7 mm with simulated defects (circular holes and notches with depth ranging from 5 to 100% of the wall thickness) were investigated using lock-in thermography. Phase angle measurements were obtained for a range of thermal excitation frequencies (0.005-0.5Hz) for each of the defects. An optimum excitation frequency was established in each case. Figure1 is the photograph of a typical sample used for experimentation.

A focal plane array camera (Model CEDIP Silver 420M) was used for experimentation. The 320 x 240
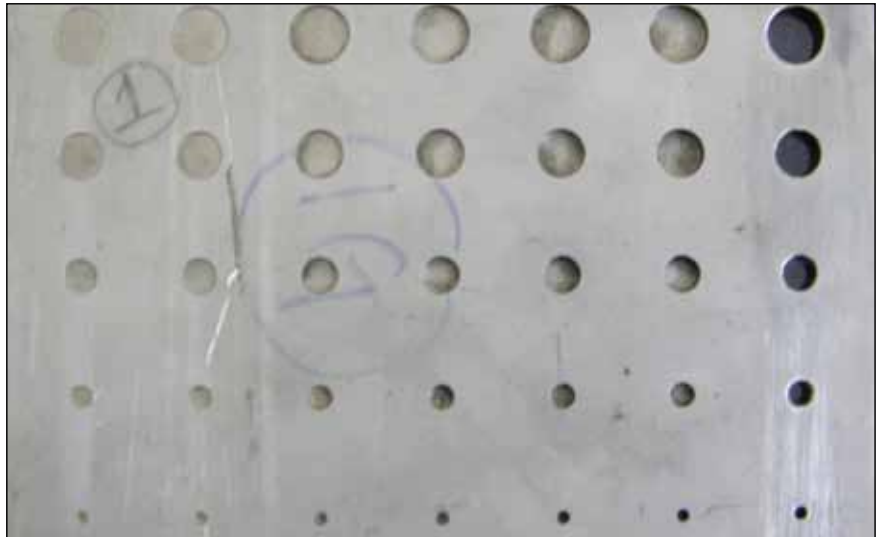
Fig. 1   Photograph of samples with flat bottom holes

detector array captures the IR radiation in the 3-5 μm spectral band at a frame rate upto 200 Hz. A lock-in module (CEDIP Altair LI) and a signal generator provided the modulated thermal source which is synchronized to the recording process of thermal images. Two halogen lamps of 1000 W each illuminate the component during the less than five minutes exposure while the infrared camera acquires the thermal images. The phase angle between the sinusoidal illumination of the sample surface and the local thermal wave response is colour coded and visualized on the screen as phase angle image of the inspected surface area.

Figure 2 is the phase image of the sample while Figures 3 and 4 depict the variation of phase contrast as a function of defect depth and defect diameter. It can be observed that as the depth of the defect from the surface increases, the phase contrast decreases and with the diameter of the defect it increases. It can also be observed that the maximum depth
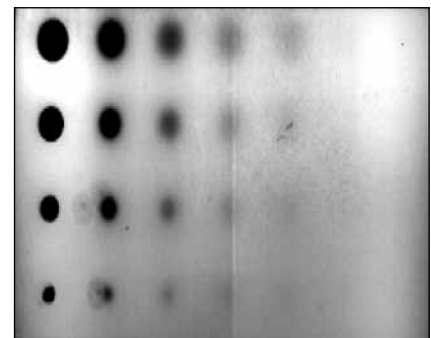
Fig. 2   Phase image of sample

of the defect that can be detected by this method in SS 316 is about 3 mm. Analysis also revealed that both defect depth and its diameter play an important role in detectability. In general only if the diameter to depth ratio exceeds three the defect becomes detectable. Experiment also revealed that frequency of modulation plays a significant role in limiting the contrast sensitivity of defects.

Experiments clearly revealed that lock-in thermography is well suited for depth resolved measurements. With appropriate calibration, the defect depth can be estimated based on phase angle measurements. In SS
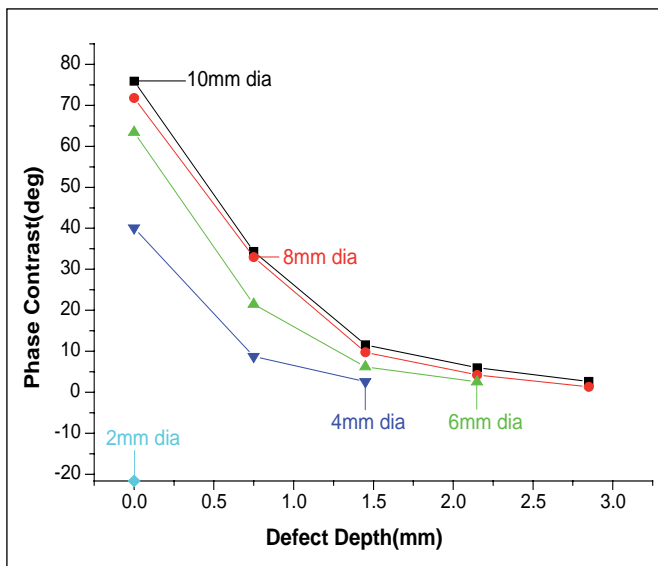
Fig. 3 *Variation of phase contrast with defect depth*
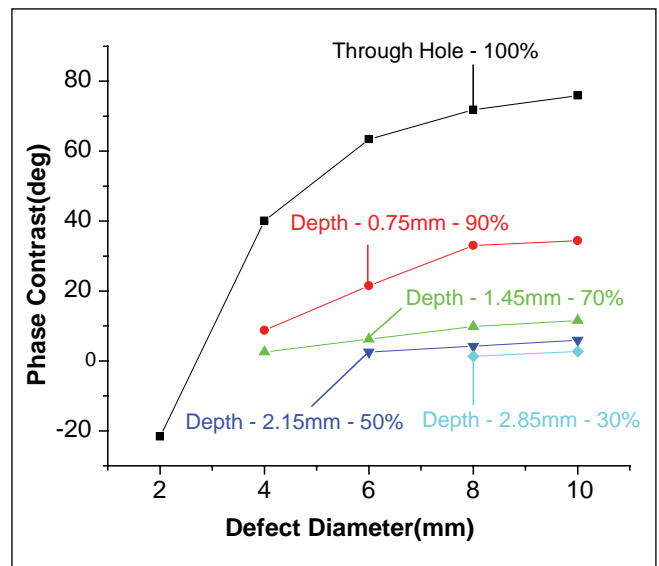
Fig. 4 *Variation of phase contrast with defect diameter*

316, defects can be detected only if the defect diameter to depth exceeds three. Lock- in thermography can be an ideal choice to complement conventional techniques such as ultrasonics and radiography especially for the detection of defects located close to the surface. An additional advantage of this technique is that the accessibility to one side is adequate for inspection and large surface area can also be covered. However, reliable characterization requires establishing the optimum modulation frequency.

V.2 Studies on the CrNbO$_4$ and In$_{2-x}$Mn$_x$O$_{3-d}$ for Wide Dynamic Range Sensing of Hydrogen

Fast breeder reactors use liquid sodium as the coolant. In the rare event of an accidental leak in the steam generator section of a fast reactor, ingress of high pressure steam into liquid sodium would cause a violent reaction leading to the complete failure of the structural components. In this reaction, hydrogen is produced. The latter owing to its sluggish dissolution in sodium, especially at lower temperatures, could escape into the cover gas. This would happen when the temperature of the liquid sodium coolant is rather low, viz. about 523K. Typical situations when such conditions prevail include low power operation and the start up of the reactor. Hence, it would be prudent to monitor the hydrogen content of the cover gas. This would provide a vital clue about the occurrence of such a sodium leak as mentioned above.

Currently a thermal conductivity detector (TCD) based sensor system is being used for monitoring hydrogen in the argon cover gas. The lower limit for the detection of hydrogen by this sensor is typically about ~20 vppm. The detection limits of this sensor could be enhanced such that it spans over concentrations ranging from a few percent of hydrogen (in argon) down to 5 ppm. This enhancement was achieved by combining this sensor with another tin oxide based sensor. Even though the performance of this combined sensor was found to be satisfactory, in order to enhance the reliability it was found desirable to use another system based on a single sensor that would sense hydrogen at varying concentrations in the range mentioned above.

In an attempt to find materials suitable for sensing hydrogen in streams in which the concentration of the latter ranges from trace levels to a few percent, two different types of materials were chosen.
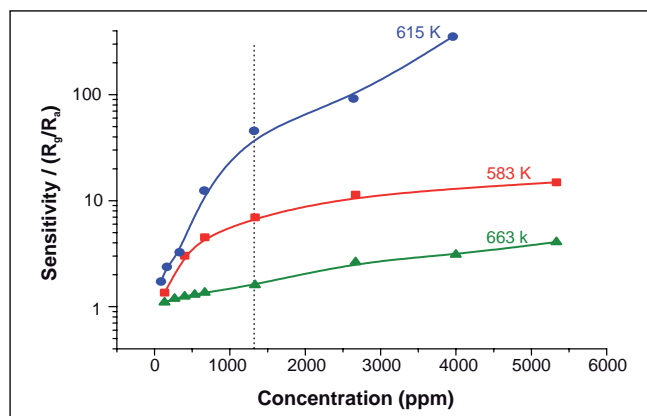
Fig. 1 *The plot of sensitivity as a function of concentration of H_2 of $CrNbO_4$ at different operating temperatures*
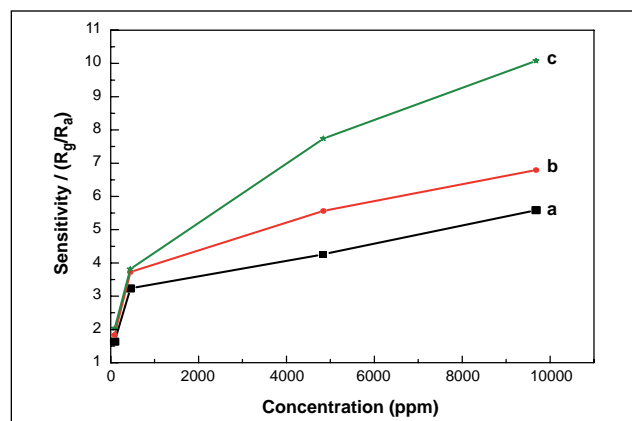
Fig. 2 *Calibration traces (towards hydrogen) for In_2O_3 containing (a) 1 mol % (b) 2 mol % and (c) 1.5 mol % of Mn_3O_4 at 623 K in air*

The first of these was based on $CrNbO_4$ and the second on $In_{2-x}Mn_xO_{3-d}$ (x = 0.1, 0.5, 1, 2, 5, 10 and 25 mol%). These samples were prepared in the form of porous pellets, characterized by different physicochemical techniques and were investigated for their hydrogen sensing properties.

Porous pellets of $CrNbO_4$ were exposed to hydrogen in the concentration range of 100 ppm to 0.4 % H_2 in air. The operating temperature was varied from 583 to 663 K. The sensitivity (defined as the R_g/R_a) of this sensor to different concentrations of hydrogen as a function of the operating temperature is depicted in Figure 1. A sensitivity of seven was observed for a stream having 1320 ppm H_2 at 583 K. When the temperature was raised to 613 K the sensitivity increased to a

value of forty six. Further increase in temperature, however, brought down the sensitivity to a value of about two. Further at 613 K this sensor responds to even higher concentrations. The use of pellets in place of films led to rather large response and retrace times of three and fifteen minutes respectively, at 613 K.

Hydrogen sensing studies on In_2O_3 containing 1, 1.5, 2, and 5 mol% Mn_3O_4 were found to give reasonably good sensitivity towards hydrogen gas. Typical response times were found to be one and seven minutes for 1 % and 100 ppm of H_2 respectively and the retrace times were found to be of the order of a few hours. Figure 2 shows the calibration graphs for three compositions of In_2O_3 doped with manganese, namely 1, 1.5 and 2 mol% of

Mn_3O_4 in In_2O_3 at 623 K. As is seen from this figure the change in slope was observed at 500 ppm of hydrogen. This plausibly is due to a change in the mechanism of the reaction responsible for the sensing action. It is surmised that the initial part of the sensing is facilitated by the chemisorbed oxygen while in the later stage it is brought about by the lattice oxygen lying beneath the chemisorbed layer.

These studies have demonstrated that it is possible to design a new sensor that could cover the entire range of concentrations of relevance to fast reactor applications. Further work is in progress to fine tune the properties of the ternary oxide based sensors in order to device a suitable hydrogen sensor with a wide dynamic range.

V.3 Research and Development on Reduced Activation Ferritic Martensitic Steels

Energy derived from the nuclear fusion reaction between light elements is regarded as the ultimate future source of energy for mankind.

India is a part of the international efforts to harness the fusion energy through its participation in International Thermonuclear

Experimental Reactor (ITER). The development of blanket material facing the plasma is considered as one of the challenges to realize the
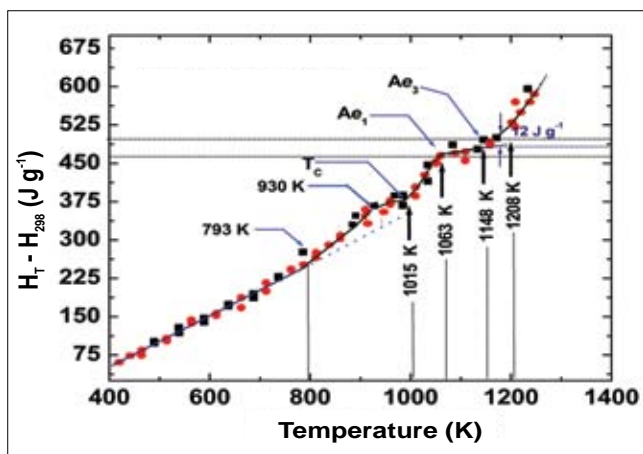
Fig. 1 *Temperature dependence of enthalpy increment for the indigenously developed RAFM steel. The temperatures marked pertain to the sequence of different phase changes on-heating*
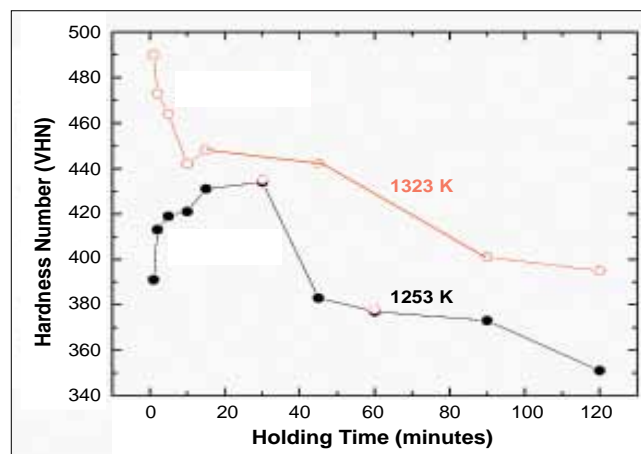
Fig. 2 *Variation of Martensite start (M_S) and finish (M_f) temperatures for RAFM steel with cooling rate transformation as a function of cooling rate*

fusion power plant. The material is required to be highly non-radioactive with high void swelling resistance (upto 200 dpa) in high energy neutron spectrum and of moderate creep strength. High chromium ferritic steel because of its inherent void swelling resistance is considered for development of the blanket material. The material is being developed in collaboration with MIDHANI, Hyderabad. The chemical composition of conventional grade 91 steel (9Cr-1Mo-0.06 Nb-0.2V-0.05N (wt %)) has been modified with the substitution of highly radioactive elements, Molybdenum and Niobium by Tungsten and Tantalum, respectively. Strict control has been exercised on the radioactive trace elements (Mo, Nb, B, Cu, Ni, Al, Co, Ti) and on the elements that promote embrittlement (S, P, As, Sb, Sn, Zr, O). These elements have been restricted to ppm levels. The RAFM steel has been produced by proper selection of raw materials and by employing VIM and VAR melting routes with strict control over the parameters of forging, rolling and heat treatments. The normalizing and tempering heat treatments of the rolled product are optimized at 1253 K for 30 minutes and

1033 K for 60 minutes respectively considering the austenitic grain growth and hardness. This steel has a tempered martensitic structure with intergranular $M_{23}C_6$ and transgranular MX (M = Ta, V) type of precipitates.

Study of martensitic transformations

In order to enable a comprehensive characterisation of the thermal stability of this indigenous steel upon various heating and cooling heat treatment schedules, an in-depth calorimetry study has been initiated using inverse drop calorimetry (IDC) and heat-flux differential scanning calorimetry (DSC). The former technique measures the temperature variation of enthalpy increment in a very sensitive manner that captures the occurrence of various phase changes either by a gentle inflection or a distinct change in slope of the enthalpy versus temperature curve.

In Figure 1, a typical portrayal of one such drop calorimetry curve for the martensitic RAFM steel is illustrated. It is quite revealing to know that at about 793 K, the hard dislocation - rich martensite

structure begins to relax with a gentle rise in the enthalpy curve. At about 930 K, there is another plateau, which signifies the exothermic onset of $M_{23}C_6$ carbide precipitation. In a similar fashion, the onset of magnetic to non magnetic phase change, followed by gradual formation of austenite at Ae_1 and its supposed completion at Ae_3 etc. are all clearly marked by distinct features in the basic enthalpy – temperature curve. The data on enthalpy variation with temperature at phase transformation domain can be modelled to obtain heat capacity change due to phase transformation. Thus, it is possible to obtain an estimate of thermal properties from drop calorimetry measurements. While drop calorimetry measurements yield equilibrium on-heating phase change information of a martensitic structure, it does not yield dynamics of martensite formation upon cooling from high temperature austenite. In order to resolve this issue, dynamic or scanning calorimetry studies were carried out on samples that are cooled in a controlled manner from about 1253 to 1273 K.

Under varying cooling rates in the range 1 to 100 degree/minute. The DSC results yield accurate values

of the start and finish temperatures of martensitic transformation as a function of cooling rate.

In Figure 2, this result is graphically portrayed for the indigenous RAFM steel. It is very clear that for very low cooling rates less than about 5-6 degree/minute, 100 percent martensite formation is not realised in case of W and Ta added RAFM steel. Infact, the critical cooling rate for martensite formation is estimated to be about 5 degrees per minute for this composition. One other remarkable aspect of martensitic transformation is the role of holding time in the austenite phase on M_S and M_f temperatures. It is clear that holding time decides the prior austenite grain size as well as the extent of hard carbide particle dissolution. This latter phenomenon indirectly contributes to obtaining small austenite grain sizes at 1253 K austenitizing. This is remarkably illustrated in the martensite hardness variation with holding time, as depicted in Figure 3.

It emerges that in the initial phase, the martensite hardness exhibits a pronounced rise with increasing holding time at 1253 K , as during this phase the undissolved carbide particles serve to pin the austenite interfaces from coarsening. This small austenite promotes finer martensite laths with considerable carbide particles retained in the quenched microstructure. On the other hand, a prolonged holding time results in appreciable carbide dissolution and hence in lesser pinning effect. The somewhat coarsened austenite grains serve to enhance the M_S temperature. It is remarkable to observe that a slight enhancement in the austenitising temperature to 1323 K, results in the continuous decay of martensite hardness with holding time.
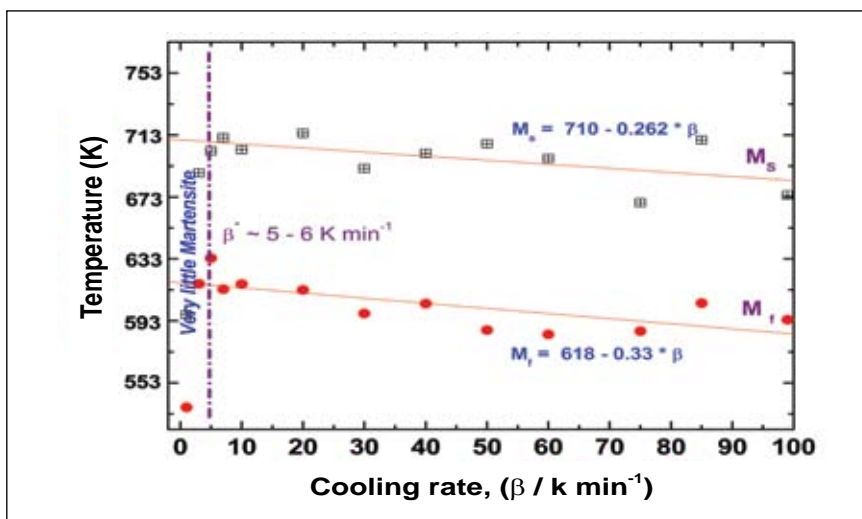
Fig. 3   Effect of austenitising time and temperature on martensite hardness
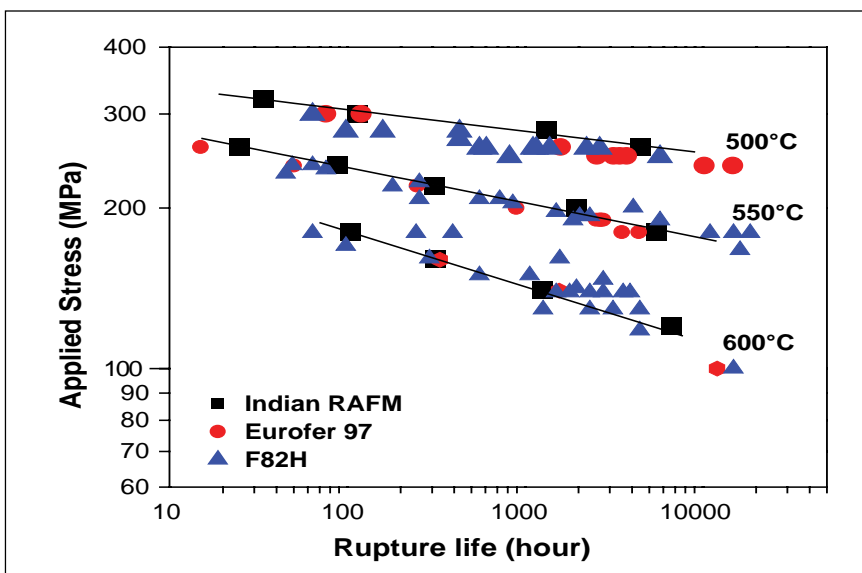
Fig. 4   Creep rupture strength of Indian RAFM steel, compared with those of internationally developed RAFM steel (Eurofer 97, Europe)

Thus, the kinetics of martensitic transformation in a RAFM steel is a sensitive function of the choice of the solitionising temperature and time. With a view of ensuring finer austenite grain size of about 25 microns, a somewhat low austenitising temperature of about 1253 K is prescribed for RAFM. This choice is fully supported by the experimental findings. The effect of replacing Mo by W and Nb by Ta and V in RAFM has subtle but definite effects in influencing the characteristics of martensitic transformation, as for example revealed in a slight enhancement of the critical cooling rate.

Determination of mechnical properties

In order to ascertain the mechanical properties for fusion energy application, Charpy V-notch impact, tensile, creep and fatigue properties of the steel have been evaluated. The ductile to brittle transition temperature (DBTT) (based on 68 J criteria) is estimated to be around 193 K and meets the requirements. Tensile and creep rupture strength of the indigenously developed steel are comparable with those of internationally developed RAFM steels as depicted in Figure 4.

V.4 Positron Annihilation Studies of Reduced Activation Ferritic/Martensitic Steels

Towards mitigating the problems of void swelling and transmutation-induced radioactive elements, martensitic/ferritic steels are considered as candidate structural materials in fission and fusion reactors. Although the conventional 9Cr-1Mo ferritic/martensitic steels have excellent void swelling resistance, it is necessary to modify them by replacing some alloying elements like molybdenum and niobium with tungsten and tantalum respectively to reduce the activation problems. In order to obtain a fundamental understanding of the occurrence and thermal stability of defects as well as precipitates in the matrix we have carried out positron annihilation, hardness and microstructural studies on a 9Cr reduced activation ferrtic/martensitic steel, commonly referred as EUROFER97. This steel was normalised for 0.5 hour at 1253K followed by tempering for 1 hour at 1033K. Isochronal annealing treatments were carried out from 300 to 1273K with a holding time of 1 hour at each 50 K step in a vacuum of $< 10^{-6}$ torr. Positron lifetime measurements,

hardness and optical microscopy were carried out on these samples.

Figure 1 shows the variation of microhardness as a function of the annealing temperature. As can be seen, the hardness remains more or less constant within the limits of experimental error upto 1100 K, beyond which it exhibits a steep increase. SEM studies have revealed that the microstructure remains stable upto 870 K and metal carbide precipitation sets in beyond 870 K. However, beyond 1273 K, the martensite structure is seen by SEM due to the transformation of high temperature austenite, which is consistent with the increase seen in the hardness measurements.

Figure 2 shows the variation of positron lifetime and Doppler broadening line shape S-parameter as a function of the annealing temperature. It should be noted that only one lifetime component was resolved for all annealing temperatures. As-tempered sample shows higher positron lifetime and S-parameter as compared to reference Fe. This reveals that the tempering treatment retains a large concentration of point

defects detectable by positron. Defect-free lifetime in pure Fe as well as in complex Ti-stablised stainless steel is ~110 ps, while the vacancy lifetime is 175 ps while the saturation lifetime is ~165 ps for cold worked steel. The value 148 ps of the mean lifetime in the present sample can be understood as arising from such vacancy-impurity complexes. Considering the sensitivity and selectivity of positrons to point defects and its low concentration detection limits, three distinct annealing stages viz., a steep reduction from 300 to 700 K, a broad maximum between 700 and 1100 K and further a maximum between 1100 and 1300 K, are observed. While the first two stages could not be seen by hardness, only the third stage is visible in a macroscopic bulk parameter like hardness. The initial decrease in positron lifetime and S-parameter upto 700 K can be understood as due to the annealing of point defects, which are "quenched-in" due to prior heat treatment procedures. Similar defect recovery is also seen in austenitic steels subjected to room temperature deformation and proton irradiation.
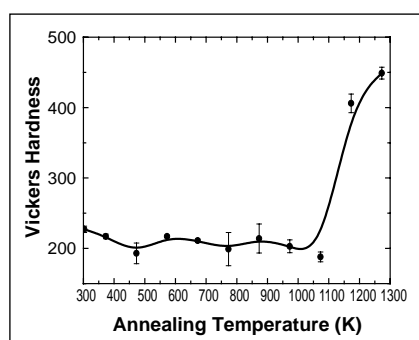
Fig. 1 *Variation of vickers microhardness as a function of annealing temperature*
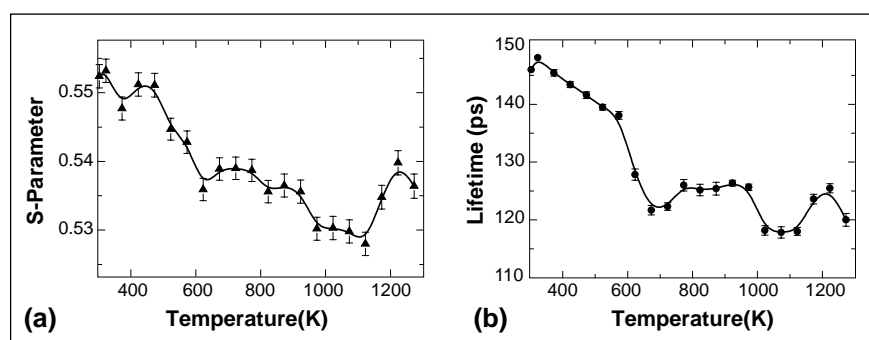
Fig. 2 *Variation of (a) S-parameter and (b) Positron lifetime as a function of annealing temperature*

The broad maximum seen between 700 and 1100 K is attributed to the nucleation and growth of metal carbide precipitates. In order to understand these variations observed for the positron annihilation parameters beyond 700 K, ab-initio positron lifetime and Doppler broadening curves were calculated using MIKA-Doppler code. Our preliminary computations seem to suggest that positrons annihilate at small vacancy defects in the as-quenched state, while they detect mostly carbon deficient metal carbide precipitates in the temperature interval between 700 and 1000 K. It is well known that both $M_{23}C_6$ and MC type carbides are formed during tempering treatment and hence the 'as received' normalised and tempered sample already contains the $M_{23}C_6$ carbides together with nanoscale metal carbide precipitates found homogeneously in the bulk. However, additional precipitation and coarsening of precipitates can arise during annealing in the temperature range of 700 to 1000 K. Further, as the dislocations are more mobile at these temperatures the martensite lath structures start arranging. This type of intra-grain MC formation is also reported in Ti bearing austenitic steels. Accordingly, the broad maximum around 700 to 1000 K is attributed to the formation of additional carbide precipitates and their coarsening.

The observed increase in hardness, lifetime and S-parameter above 1100 K arise due to formation of a martensite phase with a high defect density. However, further studies are needed in order to understand the decrease seen at 1273 K for both lifetime and S-parameter, while the hardness reveals high density of defects. In summary, positron annihilation measurements have shown microstructural changes upto 700 K, not detectable by macroscopic mechanical properties.

V.5 Improving the Antimicrobial Properties of Titanium by Surface Modification using Nanotechnology

Titanium has been chosen as condenser material for the PFBR to avoid steam side corrosion problems that can affect the integrity of sodium cooled steam generator. Routine water treatment programme would not keep the condenser tubes free from microorganisms over a long period. In this context, surface modification techniques for making titanium surface antimicrobial assume relevance. Applying nanostructured coatings of antimicrobial metals such as copper on the surface of titanium would be a viable option. Copper and copper-nickel thin films on titanium surface using different methods such as DC magnetron sputtering, pulsed laser deposition, and electroless plating have been developed. Based on the particle size of the coating and reduction in the attachment of bacterial cells on the coated surfaces in a laboratory study, electroless copper coating was found to be a better antibacterial surface. Moreover, electroless-plating technique is more amenable for application in small diameter tubes such as condenser tubes. The electroless copper coating procedure and the results of bacterial attachment studies are presented.

Copper electroless bath solution used contains copper sulphate ($CuSO_4.5H_2O$) which serves as source of copper ions, sodium potassium tartarate ($C_4H_4KNaO_6.4H_2O$) acting as a complexing agent, sodium hydroxide (NaOH) as a pH controller, and formaldehyde (37 wt %) as a reducing agent. The

Fig. 1 *Titanium surface with and without copper coating*

electroless deposition of copper on polished titanium substrate was done under thermostatic condition at 328K and pH of the solution was controlled at 12.5-13 using NaOH. The deposition time was for five minutes. Figure 1 shows photograph of titanium surface with and without copper coating. The thickness of electroless deposited copper films was measured by weight gain method as 120 nm. The GIXRD pattern showed three
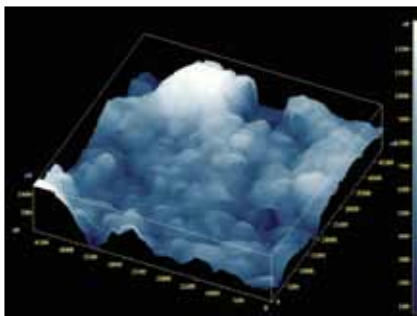
Fig. 2 *AFM image of the copper thin film formed on titanium surface by electroless coating technique*

distinct peaks at 2θ=43.4°, 50.6° and 74.2°, which correspond well with the three most intense peaks of copper in JCPDS number 040836 and the other diffraction peaks corresponds to titanium substrate. By using Scherrer formula, the calculated particle size was found to be around 21 nm. Figure 2 shows the Atomic Force Microscopic image of electroless deposited copper film with a roughness less than 20 nm.

Exposure studies of the electroless-copper plated titanium surfaces were conducted under laboratory conditions using seawater obtained from the outfall of Madras Atomic Power Station (MAPS) having about 0.1 to 0.3 ppm residual chlorine. After seventy two hours of exposure, three specimens (triplicate experiments) along with uncoated titanium were withdrawn and used for estimating the total viable count of bacteria in the biofilm by Zobell marine agar as per APHA standards. Results are expressed as number of cells per square centimeter. Epifluorescence microscopic observation of the surfaces was also carried out after staining, to view the attached organisms. Results (Figure 3) clearly showed about one order of magnitude reduction in number of cells by culture method and no microbial cell was seen on electroless- plated surface, microscopically.

Future studies are planned to be carried out to standardize this technique to coat inner surface of titanium tubes with nanocrystalline Copper layer or a combination copper and nickel. Stability of these layers will also be studied.
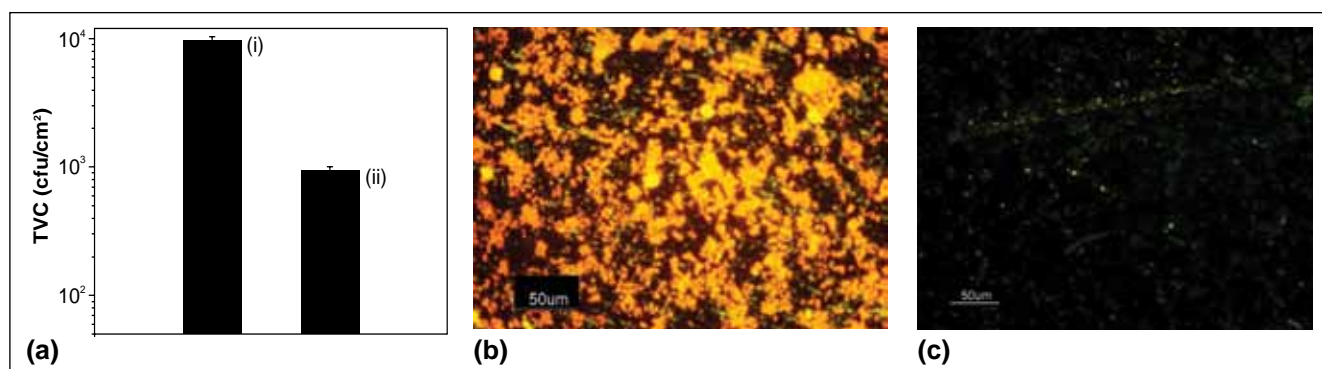
Fig. 3 *(a) Bacterial counts in (i) 0.1 and (ii) 0.3 ppm residual chlorine conditions (b) Epifluorescence micrographs of biofilms on Ti control and (c) Electroless copper coated surface*

V.6 Vaporization Studies by Knudsen Effusion Mass Spectrometry and Transpiration Thermogravimetry

Thermodynamic investigations are being carried out in order to understand the vaporization behaviour of materials of relevance to fast reactors. Knudsen effusion mass spectrometry (KEMS) and transpiration thermogravimetry (TTG) are the techniques that permit such studies on vaporization under dynamic conditions.

The binary and ternary systems containing tellurium are relevant to fuel-clad chemical interactions (FCCI) in mixed-oxide fueled fast breeder reactors. The system Ru-Te is one of the subsystems of relevance in this context. Hence vaporization studies were carried out on this system by using KEMS.

Boric acid is one of the starting materials in the manufacture of boron carbide. The latter is used in
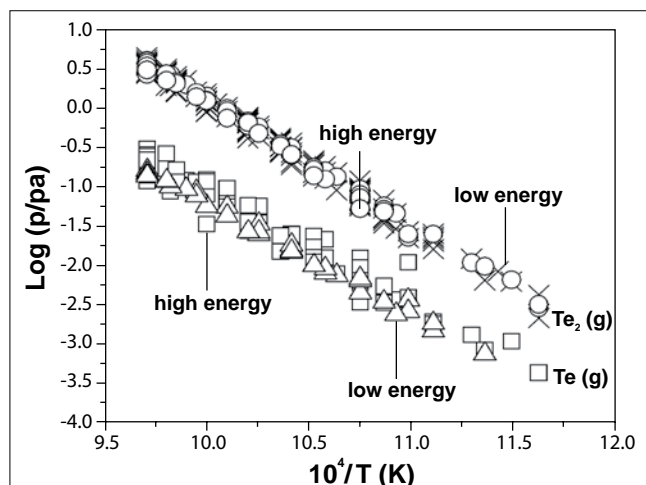
Fig. 1 $p(Te_i)$ $(i = 1, 2)$ over $(Ru + RuTe_2)$ as a function of temperature
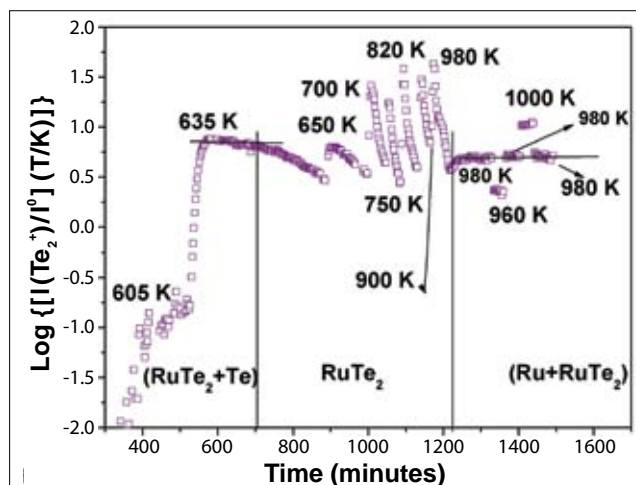
Fig. 2   Variation of $I(Te_2^+)$ as a function of time at different temperatures; starting composition of the sample: 69.5 at % Te

the manufacture of control rods used in fast reactors. The thermodynamic characterization of boric acid is relevant in this context. Furthermore, only a very few vaporization studies exist on boric acid (all essentially by transpiration methods), the results of which show huge discrepancies in the vapor pressure and the enthalpy of sublimation. Hence the vapourisation of boric acid was investigated by using both KEMS and TTG.

Ru-Te system

Te_2^+ and Te^+ were the ions detected in the mass spectra of the equilibrium vapor. The vaporization experiments involved measurement of Te_2^+ and Te^+ intensities as a function of 1) temperature over $(Ru+RuTe_2)$ (860-1030K); 2) time starting with $(RuTe_2+Te)$ samples - at various isothermal sections as the continuous shift in the composition (towards Ru-rich values) was occurring; and 3) temperature on the residues of the above experiments which belonged to $(Ru+RuTe_2)$. Figure 1 shows the values of the partial pressures of $Te(g)$ and $Te_2(g)$ deduced at various temperatures from many runs of measurements over $(Ru + RuTe_2)$. The enthalpy changes for the incongruent vaporization reactions

$RuTe_2(s) = Ru(s) + (2/i)Te_i(g)$ $(i = 1$ and 2) were subsequently deduced. Figure 2 shows the results of one of the homogeneity range experiments, mainly performed in order to determine the Te- and Ru-rich boundary compositions of the $RuTe_2$ phase. The Ru-rich boundary values were relatively consistent (i.e. within the uncertainties associated with such experiments) and close to stoichiometric value, but the Te-rich boundary values showed

some dependence with the starting composition or the amount. The ongoing experiments with a newer initial composition are in progress to resolve this disconcerting result on the Te-rich boundary.

H₃BO₃ system

Before undertaking the study of boric acid by TTG, a commercial TG apparatus was rendered amenable for good transpiration measurements by optimizing and
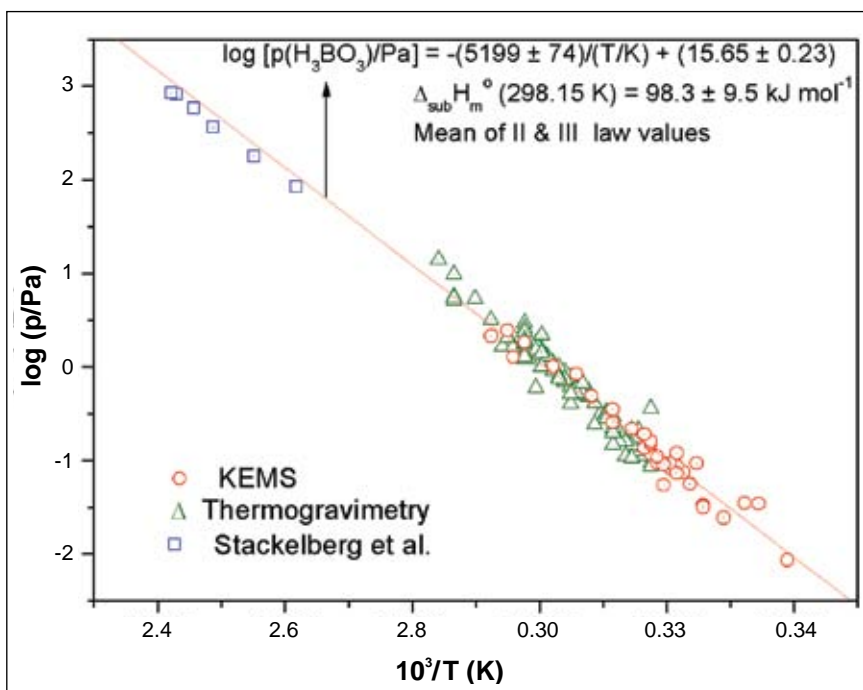
Fig. 3   Vapor pressure of boric acid as a function of temperature (295–413 K)

testing the methodology on three systems (Te, CsI, and TeO_2), which have been previously established by us to vaporize congruently (through KEMS).

The KEMS measurements showed $H_2BO_2^+$ and $H_3BO_3^+$ (as major ionic species); and HBO_2^+ and $H_3B_3O_6^+$ as minor species at the highest temperature. The relatively higher appearance potential for the ion $H_2BO_2^+$ and similar temperature dependence for both $H_2BO_2^+$ and $H_3BO_3^+$ led us to conclude that electron impact ionization of $H_3BO_3(g)$ generate $H_3BO_3^+$ as parent ion and $H_2BO_2^+$ as a fragment ion. The ion intensities of $H_2BO_2^+$ and $H_3BO_3^+$ were measured as a function of temperature (295-342 K) and the partial pressure of $H_3BO_3(g)$ was deduced using pressure calibration measurements on mercury, another low temperature system. The TTG measurements involved the use of argon as the carrier gas for vapor transport and derivation of vapor pressures of $H_3BO_3(g)$ through many flow dependence runs (at 336 and 349 K) and temperature dependence runs (315 to 352 K). The TTG measurements were also conducted on mercury to obtain confidence on the values of pressure measured at such low temperatures. The thermodynamic parameters, both the enthalpy of sublimation and vapor pressures of $H_3BO_3(g)$ obtained by both KEMS and TTG are in excellent agreement amongst themselves as well as with those determined by Stackelberg et al. (Z. Elektrochem. 43 (1937) 14) by using the transpiration method at relatively higher temperatures (382-413 K) with steam as the carrier gas. Figure 3 shows the results of our study and those of Stackelberg et al., adopted by JANAF.

The data on the vapour pressures of boric acid was obtained by two different techniques viz., KEMS and TTG and was shown to be in agreement with the measurements reported in the literature. This would provide useful inputs to the various unit processes involved in the manufacture of boron carbide for control rod applications.

V.7   Study of the Ageing Behaviour of M250 Grade Maraging Steel

M250 grade maraging steel is used as a structural material due to its ultra-high yield strength combined with good fracture toughness. This steel achieves its superior mechanical properties after ageing for an appropriate duration at an appropriate temperature as a result of formation of fine intermetallic precipitates of $Ni_3(Ti, Mo)$ and Fe_2Mo. At larger ageing duration (e.g. 40 to 100 hours at 755 K) formation of reverted austenite degrades the mechanical properties. As precipitation of these intermetallic phases and reversion of austenite have opposing effects on hardening, the resultant overall hardening levels off after reaching a maximum. Hence, studies for nondestructive characterization of microstructural changes that take place in this steel during isothermal ageing at 755 K for varying durations of 0.25, 1, 3, 10, 40, 70 and 100 hours were carried out by using X-ray diffraction (XRD), nonlinear ultrasonics (NLU) and eddy current (EC) techniques.

X-ray profiles were recorded between 36-122° with a step size of 0.02° and dwell time of four seconds with $CuK\alpha$ radiation for all the samples. XRD peak profile analysis is a powerful tool for the characterization of microstructures in crystalline materials. The peak profile broadens when the size is small or when the material contains lattice defects which occur due to the presence of dislocations and due to coherency strains caused by precipitates. The approach of Williamson–Hall modified by Ungár and Borbély accounting for the anisotropic strain broadening has been used to estimate the apparent crystallite size and the normalized mean square strain. The changes in microstrain and hardness with ageing are shown in Figure 1. The similarity of the observed change in the normalized mean square strain and hardness with ageing prompted the use of normalized mean square strain to study the kinetics of precipitation by employing Johnson-Mehl Avrami equation i.e., $f = 1 - e^{-tk^n}$ where f is the fraction of precipitates transformed at the ageing temperature, t is the ageing time, k is the reaction rate constant and n is the Avrami exponent. The fit of the equation obtained from the normalized values of mean square
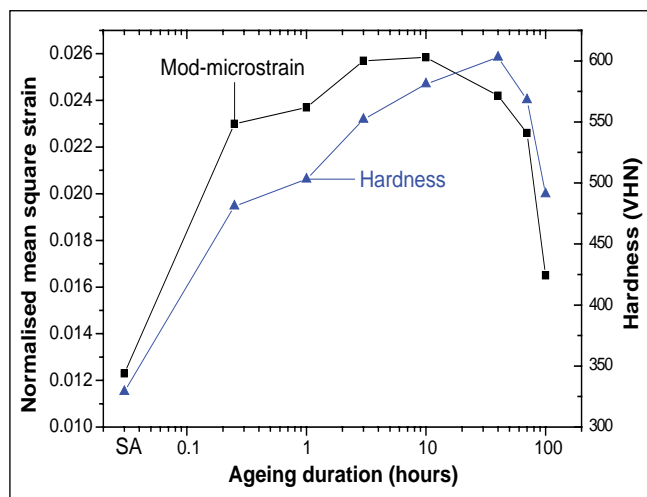
Fig. 1 *Variation of normalized mean square strain and hardness with ageing at 755 K. SA denotes solution annealed*
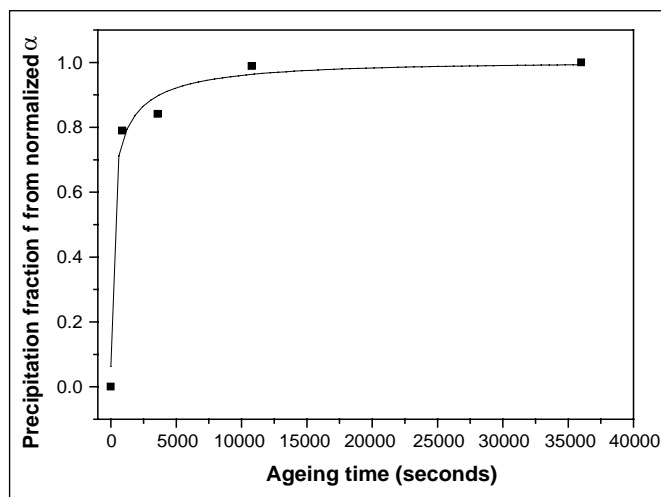
Fig. 2 *Change in precipitation fraction with ageing from normalized mean square strain*

strain is shown as a plot in Figure 2. The Avrami exponent estimated from this fit is 0.34 ± 0.08 which matches well with the published data of 0.39 and 0.35 at 755 K.

In non-linear ultrasonic technique, a high amplitude ultrasonic wave of a particular frequency (5 MHz) is made to propagate through the material and the second harmonics (10 MHz) generated due to elastic and plastic interaction of ultrasonic waves with dislocations, precipitates, micro-cracks, damage etc. are detected and used for characterization. The amplitudes of fundamental (A_1) and second harmonics (A_2) are measured using the pulse inversion technique and the ratio of these amplitudes gives the non-linear ultrasonic parameter β, given by, $B = \frac{8}{K^2 a}\left(\frac{A_2}{A_1^2}\right)$, where K is the material constant and a is the thickness of the material. The β-parameter gives volumetric information about the microstructural changes taking place in the material. The variation of β-parameter with ageing is shown in Table I. The β-parameter is found to marginally decrease upon ageing for 0.25 hours and increases continuously up to 10 hours followed by a decrease till 100 hours of ageing. The decrease

in β-parameter at 0.25 hours is attributed to the combined effect of recovery of martensitic substructure that decreases β and increase in coherency strains (Figure 2) due to precipitation of very fine Ni_3Ti precipitates that increases the β parameter. Upon further ageing, the β-parameter is found to increase and reaches a peak value at 10 hours due to the large coherency strains from both Ni_3Ti intermetallic precipitates that have grown to a critical size and the Fe_2Mo intermetallic precipitates that just initiate in the low-carbon soft martensite matrix. Beyond 10 hours of ageing, β-parameter is found to decrease as a result of coarsening of precipitates and formation of reverted austenite. Coarsening of Ni_3Ti intermetallic precipitates reduces the coherency strains originating from the precipitate-matrix lattice misfit while increase in volume fraction of soft reverted austenite decreases the nonlinear behavior of this material.

In the eddy current technique, the coil impedance is influenced by changes in electrical resistivity and magnetic permeability as a result of microstructural changes that take place in the material. The impedance change measurements
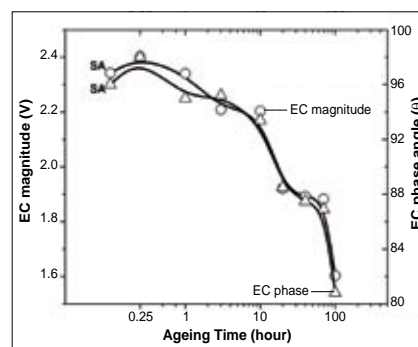
Fig. 3 *Variation of eddy current magnitude and phase with ageing*

Table I : Changes in β with ageing	
Ageing time (h)	*β parameter*
Solution annealed	*0.09122*
0.25	*0.08932*
1	*0.10193*
3	*0.12057*
10	*0.14461*
30	*0.13985*
40	*0.13308*
70	*0.12937*
100	*0.12074*

were carried out using transmit-receive coil (T/R) type probe. The variation in the magnitude of eddy current and phase with ageing time is shown in Figure 3. The increase in the induced voltage from solution annealed condition to 0.25 hours is attributed to the increase in magnetic

permeability (due to recovery, i.e. removal of quenched-in point defects and dislocation annihilation). Subsequently, the electrical resistivity is found to decrease due to the combined action of recovery and precipitation of intermetallic precipitates. The larger decrease in magntidue and phase angle for specimens aged above 10 hours is attributed to the formation of non-magnetic reverted austenite in addition to the continuous precipitation of intermetallics (Ni_3Ti and Fe_2Mo).

While the increase in microstrain at 0.25 hours of ageing can be used to infer very early precipitation, the increase in β and microstrain can be attributed to the increase in volume fraction of precipitates causing coherency strains to increase. The formation of reverted austenite causes a decrease in amplitude of eddy current and is also observed in XRD peaks by the formation of the FCC phase. These observations clearly show that a combination of X-ray diffraction, nonlinear ultrasonics and eddy current techniques can be used to characterize the complex microstructural changes that take place in M250 grade maraging steel.

V.8 Design and Simulation of Capacitive Micromachined Ultrasonic Transducer and Cantilever Based Sensors

Various finite element modeling (FEM) is being used for designing and simulating the functions MEMS based sensors. The main advantage of FEM simulation in MEMS device design is that it provides design optimization by varying geometry, layer dimension and materials of the device before the actual fabrication. This article describes the design and simulation of two different MEMS sensors. First the optimum design parameters of a capacitive micro electro-mechanical ultrasonic transducer is discussed followed by the positional sensitivity of a nano cantilever based mass sensor, using "*Intellisuite*" - a commercial MEMS CAD tool.

Capacitive micromachined ultrasonic transducer design

MEMS based capacitive Micromachined Ultrasonic Transducer (cMUT) is a competitive candidate for high performance ultrasonic imaging arrays in a wide frequency range which provides additional advantages like higher bandwidth, non-contact, means of measurement etc. over conventional piezoelectric transducers. At our Centre, cMUT for NDT applications is being developed in collaboration with IISc, Bangalore and CEERI,

Pilani. The shape of the poly silicon membrane was regular hexagon with an edge length of 50 μm and thickness of 1 ìnch. On top of it an aluminium electrode was selected with a dimension of 50 μm edge length × 1 μm thickness. The structure was meshed and all the edges were fixed using boundary condition and frequency analysis was performed. Figure 1(a) shows the fundamental mode vibration of a cMUT cell. From the FEM analysis frequency of vibration was found to be at 2.4 MHz, which is close to the experimentally observed result of the fabricated device using laser doppler vibratometer. The DC
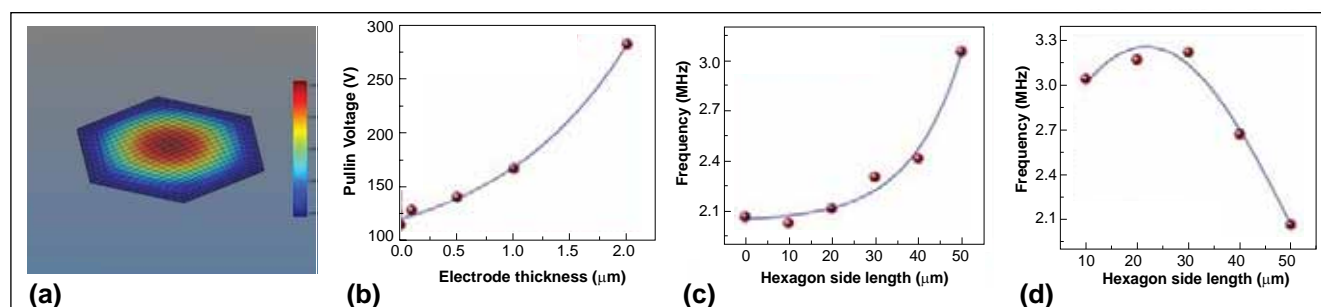
Fig. 1 *(a) First vibrational mode of single cell cMUT, (b) Variation of pull-in voltage with electrode thickness, (c) Variation of natural frequency with electrode outer area, and (d) Variation of natural frequency with electrode inner area*
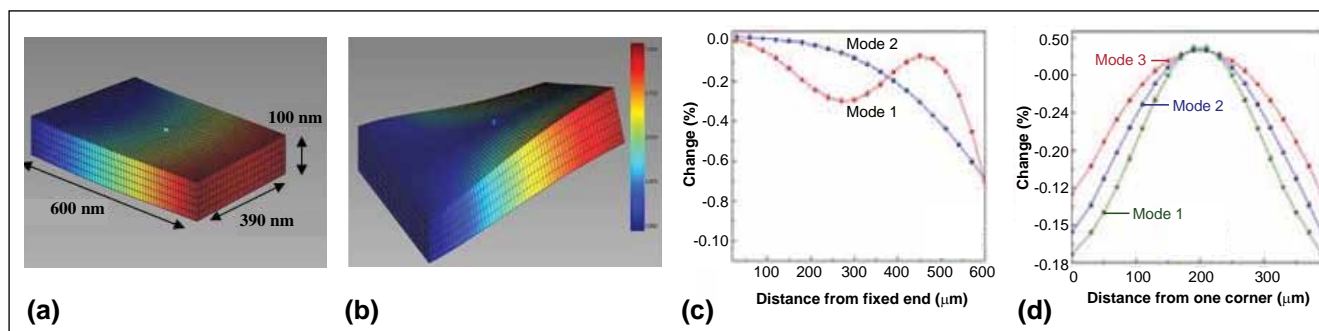
Fig. 2 *(a) Bending mode of the cantilever, (b) Torsional mode of the cantilever, (c) Change in frequency due to added mass along the length axis in bending mode, (d) Change in frequency due to added mass along the width axis in torsional mode*

bias at which the top membrane touched the bottom plate is known as pull-in voltage and is an important parameter in the design of a cMUT. To determine the optimum pull-in voltage value for the designed cMUT, a static analysis was performed. Figure 1(b) shows the variation of the pull-in voltage with electrode thickness and it is evident from this figure that the pull-in voltage increases with the electrode thickness. Variation of natural frequency of the membrane with varying electrode area was also studied and the results obtained are shown in Figures 1(c) and 1 (d). Apart from this, transient analysis for the prediction of ultrasonic power is in progress.

Cantilever design

Nano mechanical cantilevers show great promise when operated in dynamic mode for sensor applications and systems capable of detecting masses in the atto and zepto gram range have been reported recently. Interestingly, the mass sensitivity of these cantilevers depends highly on the position of the mass loading on the cantilever. In the present work, mass and position sensitivity of a nano cantilever based mass sensor are simulated by using FEM analysis. Vibrational mode simulations have been performed for a polysilicon cantilever which is 600 nm long, 390 nm wide and 100 nm thick, using the FEM analysis. Figures 2(a) and 2(b) show the fundamental bending (380 MHz) and torsional mode (1179 MHz) vibrations of the designed cantilever.

A gold bead (cube of 10 nm^3, weighing $\approx$ 19.3 ag) was placed on the cantilever at regular positions along the length and width axis and the simulations were performed.

By comparing unloaded case, mass sensitivity was estimated at every position. Figures 2(c) & 2(d) show the variation of percentage change in natural frequency with respect to unloaded cantilever for gold bead positioned along the length axis for bending and along the width axis for torsional modes respectively. From these figures some interesting observations can be made. In all the cases change in natural frequency is always negative. Bending mode shows maximum sensitivity for the central tip loading and torsional mode shows maximum sensitivity for mass loaded at tip corner. In general, higher modes are more mass and position sensitive. In summary, we find that the influence of the gold coating area and position on the natural frequency shift is a very important parameters in determining the optimum performance of a cantilever based mass sensor.

V.9 High Temperature X-ray Diffraction Studies on Phase Stability of Al$_2$O$_3$/ZrO$_2$ Multilayers Prepared by Pulsed Laser Deposition

Alumina-zirconia composites are commonly coated, where a ceramic material is required with a combination of hardness and toughness. As thin films, alumina-zirconia has been focused mainly on thermal barrier coatings (TBC). TBCs are deposited on combustion lines, first–stage blades, and vanes

and other hot path components of gas turbines either to increase the inlet temperature with a consequent improvement of the efficiency or to reduce the requirements for the cooling system. The combination of high hardness of alumina (Al_2O_3) with the low thermal conductivity of zirconia (ZrO_2) will contribute to the development of functionally graded thermal barrier coatings with higher wear and oxidation resistance. Development of Al_2O_3 / ZrO_2 nanolaminated composite coating is an important method to thermally stabilize the high temperature tetragonal zirconia phase at room temperature. The present work has focused on the development of new nanolaminate thin-film structures of zirconia-alumina. Alumina has been chosen in order to stabilize the tetragonal phase at temperatures as low as possible. Preparation of the multilayers of ZrO_2/Al_2O_3 films by PLD and the study of their microstructure and thermal stability form the major objectives of the present work. The determination of crystallite size, lattice parameters, percent thermal expansion and thermal expansion coefficients of

the tetragonal phase have been reported.

Multilayers, which consisted of Al_2O_3 layer of 5 nm thickness and ZrO_2 layer of varying thicknesses from 5 to 20 nm were deposited on (100) Si substrates at an optimized oxygen partial pressure of 3×10^{-2} mbar at room temperature. The multilayer thin film samples were analysed by using high temperature X-ray diffraction (HTXRD) in a INEL XRG – 3000 diffractometer attached with a curved position sensitive detector and Buhler 2.4 HDK high temperature camera. Study of the structural and thermal expansion behaviour as a function of temperature in the range 298 -1373 K in vacuum in the order of 2×10^{-5} mbar was carried out. Cross-sectional transmission electron microscopy (XTEM) investigations were carried out on a JEOL 2000 EX II (T) high resolution transmission electron microscope operated at 200 kV.

The cross-sectional transmission electron microscopy of the multilayer films deposited at 298 K shows the formation of multilayers
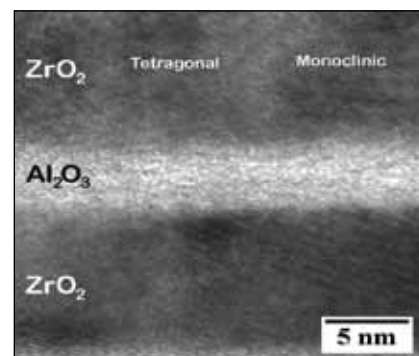
Fig. 1 *Cross-sectional TEM of the as-deposited Al_2O_3/ZrO_2 (5 nm /15 nm) multilayer deposited at 298 K*

with uniform thickness, a mixture of monoclinic and tetragonal phases of zirconia and amorphous alumina (Figure 1). Figure 2(a) shows the HTXRD of the multilayers of alumina / zirconia (5 nm /20 nm) in the temperature range 298-1373 K. It is interesting to note that the alumina remains in an amorphous state throughout the entire range of annealing temperatures. However, broadening of the peak at an angle of 32º because of the overlapping of peaks of (-111) of monoclinic and (101) of tetragonal phases. At 873 K, the film shows crystalline nature of zirconia. Strong peaks corresponding to tetragonal phase
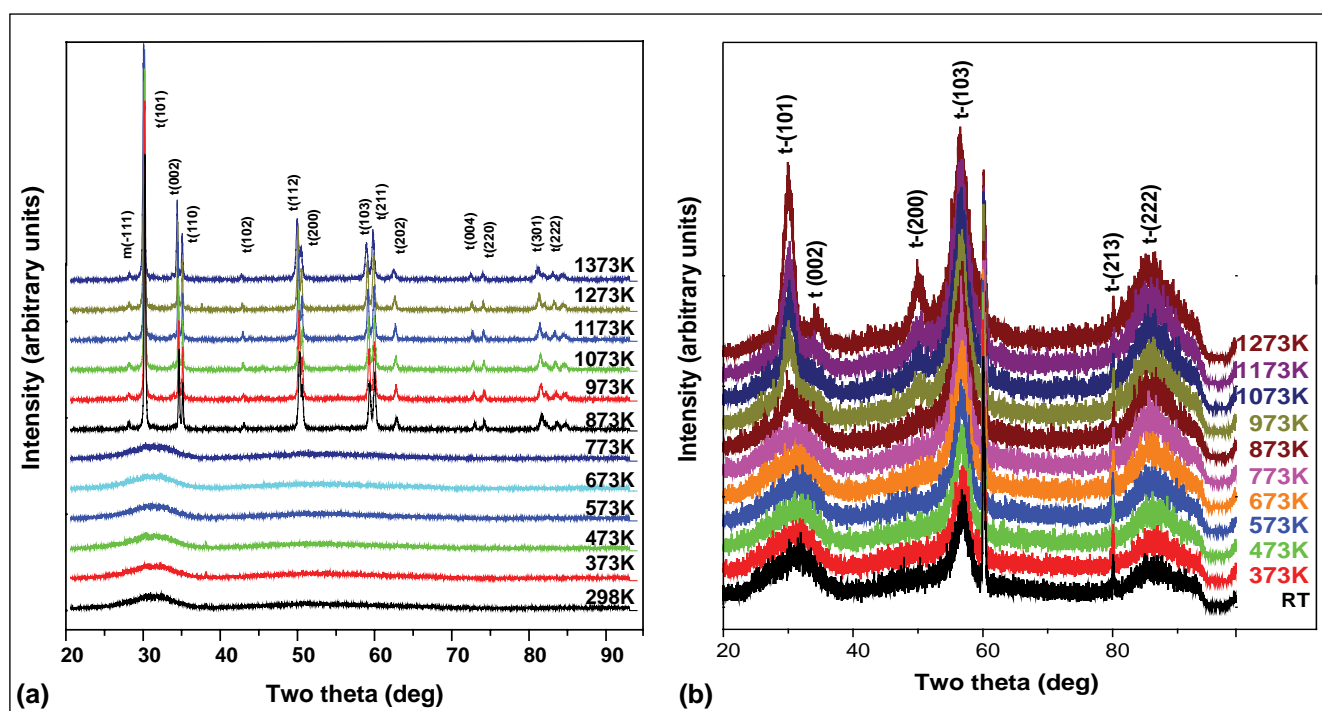
Fig. 2 *HTXRD patterns of Al_2O_3/ZrO_2 multilayer films deposited at 298 K (a) 5 nm/ 20 nm and (b) 5 nm/ 10 nm*

and a weak peak corresponding to monoclinic zirconia are observed. The mean thermal expansion coefficients have been calculated along a and c axes using the following expressions :

$$\alpha_a = \frac{1}{a_{C_r}} \left[\frac{a_T - a_{C_r}}{T - C_T} \right]; \; \alpha_c = \frac{1}{c_{C_r}} \left[\frac{c_T - c_{C_r}}{T - C_T} \right]$$

Where a_T and c_T - the lattice constants at temperature T, α_a, and α_c - the thermal expansion coefficients of cell parameters a and c, respectively, C_T is the critical temperature at which crystallization of the film is observed. The mean thermal expansion coefficient of tetragonal zirconia is 4.69×10^{-6} K^{-1} along the a-axis, while it is 13.68×10^{-6} K^{-1} along the c-axis in the temperature range of 873-1373 K (Table 1). The thermal expansion coefficient along c-axis is about three times that of a-axis.

The Al$_2$O$_3$/ZrO$_2$ (5 nm/15 nm) multilayer film showed the amorphous nature at $\leq$ 573 K. The HTXRD studies showed that crystallization temperature of tetragonal zirconia is 673 K. The mean thermal expansion coefficient is found to be 4.14×10^{-6} K^{-1} along the a-axis and 8.32×10^{-6} K^{-1} along c-axis in the temperature range 673 - 1473 K (Table 1). The thermal expansion coefficient along c-axis is found to be about two times higher than that along a-axis.

Figure 2 (b) shows the HTXRD of Al$_2$O$_3$/ZrO$_2$ (5 nm /10 nm)

Table 1 : Layer thickness versus crystallization temperature and thermal expansion coefficients (TEC)				
Al$_2$O$_3$/ ZnO$_2$ layer thickness (nm)	Crystallization temperature (K)	Phases	Mean TEC $\times 10^{-6}$ along	
			a-axis (K^{-1})	c-axis (K^{-1})
[5/20]$_{40}$	873	M, T	4.69	13.68
[5/15]$_{40}$	673	M, T	4.14	8.32
[5/10]$_{40}$	300	T	8.75	8.2
[5/5]$_{40}$	300	T	—	—

multilayer film indicating the formation of a tetragonal phase at room temperature. There is no monoclinic phase in the film the mean of which was found to be in the range 298-1273 K. The broadness of the peaks clearly indicates the increased nanocrystalline nature of the film consisting of the crystallites of sizes in the range 6-10 nm. The mean thermal expansion coefficient has been found to be ~8 K^{-1} along both a- and c-axes (Table 1).

The HTXRD studies illustrate the stabilization of metastable phase of zirconia by forming multilayers of zirconia and alumina. Here, alumina influences the growth of the zirconia layer and provides a template for the stabilization of metastable phase of zirconia. The layer thickness of zirconia has been found to be the most important influencing parameter on stabilization of tetragonal zirconia. In the present work, we observe

an increase in the volume fraction of the tetragonal phase with the decrease of ZrO$_2$ layer thickness. Also, when the thickness of zirconia layer is $\leq$ 10 nm, the formation of the tetragonal zirconia is noticed. For instance, when the ZrO$_2$ layer thickness is in the range 5-10 nm, all the peaks corresponding to the tetragonal phase are noticed (Figure 2b). The thermal expansion coefficient is in the ratio 1:3 along a- and c -axes for Al$_2$O$_3$/ZrO$_2$ (5 nm/20 nm), while it is 1:2 for the Al$_2$O$_3$/ZrO$_2$ (5/15 nm). The thermal expansion coefficient is higher and almost equal along both the crystallographic axes for the 5nm/10 nm multilayer films (Table1). A similar result is also obtained for the Al$_2$O$_3$/ZrO$_2$ (5/5 nm) multilayer film. This study demonstrates the feasibility of stabilizing the metastable zirconia phase by the suitable selection of thickness of zirconia layer and the template layer of a few nm thick alumina.

V.10 Reversible Zippering of Chains in Magnetic Nanofluid under External Magnetic Field

Magnetic colloids can be easily manipulated with an external magnetic field and hence they are exciting systems both from fundamental and application points of view. Complete understanding of the structure, phase behavior, and dynamics of strongly interacting dipolar magnetic fluids is still a

considerable challenge in soft matter physics. In the presence of an external field, the magnetic colloids experience attractive force along the field direction and repulsive normal to it. Therefore, on slowly increasing the magnetic field from zero to high value, the magnetic fluid undergoes several interesting structural transitions. Using time dependent light scattering measurement at constant ramping of external magnetic field values, investigations have been carried out on metastable structures formed in a magnetically polarizable media. The structures inside the dipolar fluid for different regimes of magnetic field are modeled by considering linear aggregation at the first and lateral aggregations at the next higher critical fields. Based on these modeled structures, the reason for the experimentally observed scattered patterns and their variations at the critical fields are explained. The increase in the stability of the system due to the structural reorganization at the critical fields is explained on the basis of energy argument.

The dispersion used in the present studies was a magnetic nanofluid where the particle size is less than the incident light wavelength $\alpha < \lambda$. The forward transmitted light intensity was measured as a function of time at different applied magnetic field. A stable colloidal suspension of magnetite (Fe_3O_4) nanoparticles of average diameter 6.5 nm was used. The ferrofluid sample is taken in a quartz cuvette and kept inside a solenoid, where magnetic field is varied by changing the current passing through its coil using a DC power supply. The direction of magnetic field is parallel to the light propagation. An amplitude and frequency stabilized polarized He-Ne laser (Spectra-physics) of wavelength 632.8 nm with an output power of 1 mW is

used as a light source. The light intensity is measured by using a photo multiplier tube (PMT) (Oriel). The output of the photo multiplier tube is fed to readout through a current amplifier with variable gain. The analog output from the readout is connected to a 12-bit analog-to-digital converter (ADC) that is interfaced with a computer. For observation, the scattered light from the sample is projected on a screen and recorded using a charge coupled device (CCD) camera. The transmitted light intensity through the sample has been acquired as a function of time at different external magnetic field values. The variation in the magnetic field within the sample was less than 1% and the variation within the laser spot diameter was less than 0.01%.

Figure 1 shows the normalized transmitted intensity as a function of time required for the stabilization of intensity at different critical magnetic fields for different concentrations. At the critical fields, the intensity

starts to decrease with time till it reaches a minimum value. After the minimum, the transmitted intensity again increases till its value gets saturated at a particular time. For all the concentrations of the sample, five 'critical' fields are observed as the magnetic field is increased up to 200 Gauss. Figure 2 shows the evolution of scattered pattern with their corresponding surface plots at the fifth critical magnetic field for 0.649 vol. % of the sample. Calculations show a decrease of energy of the system due to dipolar interactions at different critical fields, confirming the coarsening of the field induced structures that lower the system energy.

The transmitted intensity and the scattered pattern show time dependent variation at different critical fields upon slow ramping of external field. Several critical fields are observed at a regular interval of 20 Gauss after the first critical field. At each critical field, the transmitted light intensity decreases drastically followed by
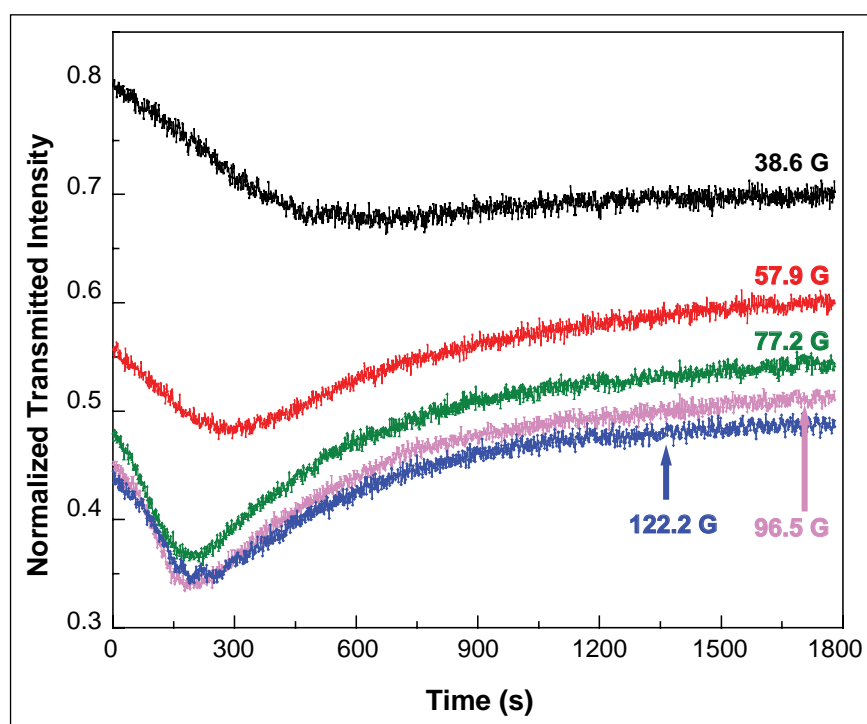
Fig. 1 *Normalized transmitted intensity as a function of time required at different critical magnetic fields for a concentrations of 1.078 vol. % of ferrofluid sample*
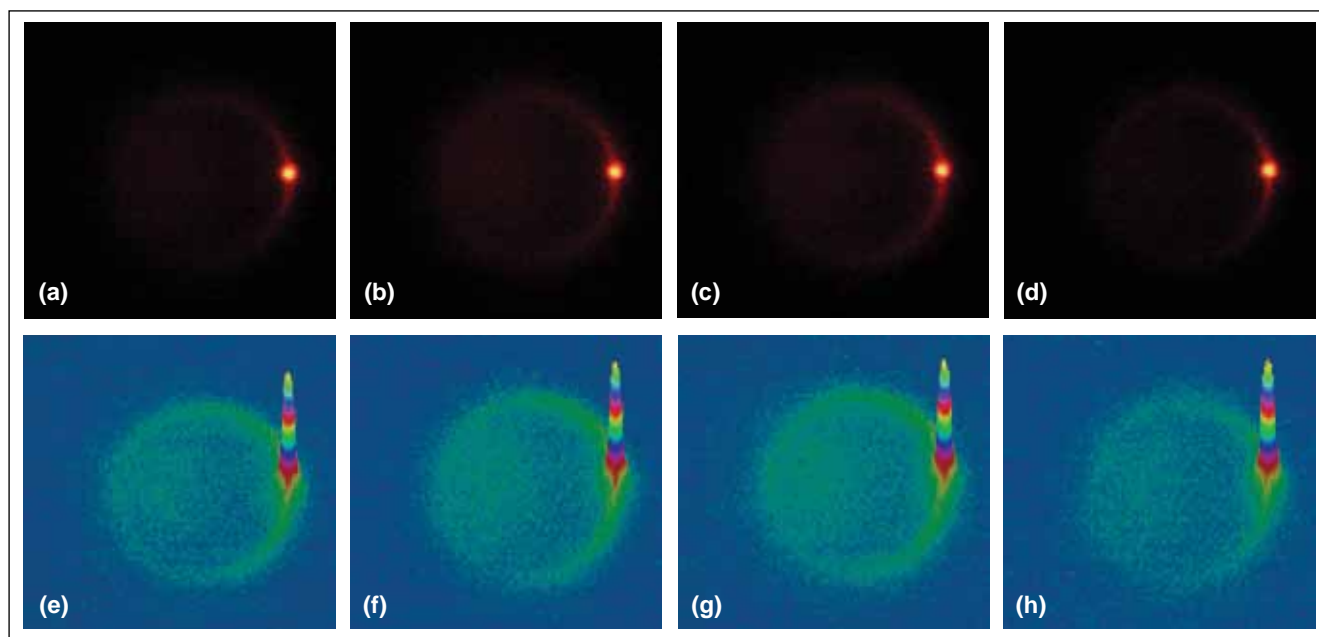
Fig. 2 *The evolution of scattered pattern (a, b, c, d) with their corresponding surface plots (e, f, g, h) at the fifth critical magnetic field for 0.649 vol. % of the ferro fluid sample*

the formation of a ring like pattern on a screen placed perpendicular to the field direction. The observed critical fields are attributed to zippering transitions of the chains due to attractive energy well when the chains are of different lengths or shifted with respect to one another.

V.11   Phase Transitions in Thermo-Responsive Nanogels

Nanoparticle dispersions are studied with considerable interest not only because of the fundamental interest in understanding the co-operative phenomena such as structural ordering, crystallization and glass transition using these systems but also for their practical use in a wide range of disciplines, including photonics, optics, sensing, drug delivery and bio-separations. Some of these applications use ordered arrays of these nanoparticles organized by using processes such as self-assembly, sedimentation, centrifugation etc. A system of monodisperse nanoparticles can serve as super-atoms and exhibit structural ordering analogous to that observed in atomic/molecular systems. In the case of conventionally investigated nanoparticle dispersions such as polystyrene, polymethyl-methacrylate, silica etc., the particle size is fixed and temperature (T) is not a controllable parameter to investigate the phase behavior. However there exists a novel nanoparticle dispersion that comprises thermo-responsive nanogel particles, where the particle size is tunable by varying the temperature and hence the volume fraction ϕ and the interparticle interactions. Thus it will be of interest to investigate the phase behavior of these nanogel dispersions by varying the temperature and we show that the phase behaviour is quite different from hard-sphere suspensions which are known to exhibit only a fluid–solid transition at $\phi \cong 0.5$.

In order to investigate the phase behaviour of thermo-responsive nanogels, we have synthesized an aqueous dispersion of thermo-responsive poly N-isopropylacrylamide (PNIPAM) nanogel particles by free radical precipitation polymerization. Samples of varying number density, n_p have been probed for their temperature dependant phase behaviour using static and dynamic light scattering techniques (SLS/DLS). The effect of temperature on particle size was carried out on a dilute sample (labeled as S1) with

n_p = 4.36 $\times$ 10^{11} cm^{-3} using the dynamic light scattering technique. At 298 K the average hydrodynamic diameter of the nanogel particles was found to be 273 nm. Upon increasing the T, the particle size decreased and at 305.4 K the nanogel particles suddenly collapsed to 110 nm. This sudden transition volume of the particle is identified as the volume phase transition (VPT). This transition is found to be reversible upon lowering the temperature and the transition occurs due to the hydrophilic nanogel particles turning to hydrophobic.

Sample with increased n_p = 4.36 $\times$ 10^{12} cm^{-3} (labeled as S2) appeared slightly turbid but did not exhibit iridescence even after repeated annealing. The time averaged scattered intensity $I_s(q)$ measured as a function of scattered wave vector, q on sample S2 showed a well defined peak (Figure 1) suggesting the liquid-like ordering of particles. Upon increasing the temperature, the peak height was found to decrease without a shift in the peak position (Figure 1). Beyond 305 K the peak disappeared indicating a gas-like disorder in sample S2. The transition from liquid-like state to gas-like state is identified by monitoring this peak intensity I_{max} as function of T (inset in Figure 1). For the first time a change in slope but not a sudden jump in I_{max} at ~ 304.5 K has been observed. This suggests that across the transition there is no variation in n_p. Hence this transition is identified as fluid (liquid-like) to fluid (gas-like) transition. The absence of change in n_p across this transition suggests that the interparticle interactions are repulsive.

Another sample that was ten times more concentrated than sample S2 with n_p = 8.71 $\times$ 10^{13} cm^{-3} (labeled as S3) showed iridescence upon
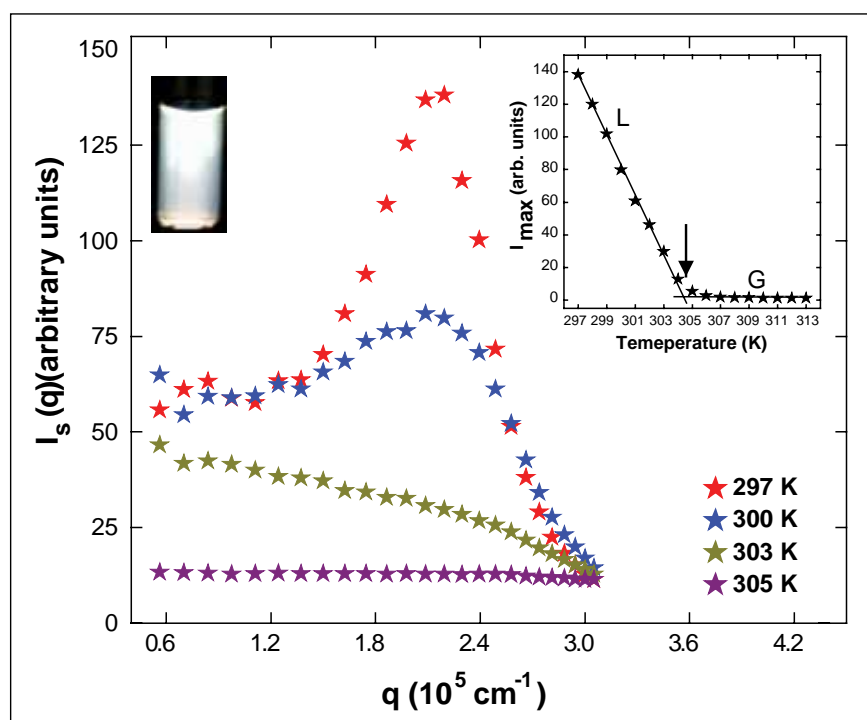
Fig. 1   *Scattered intensity $I_s(q)$ as a function of q for sample S2 at different temperatures. Insets show photograph of sample S2 and the peak intensity $I_{max}(q)$ as a function of T. Arrow indicates the fluid (liquid-like (L)) to fluid (gas-like (G)) transition temperature (~304.5 K)*
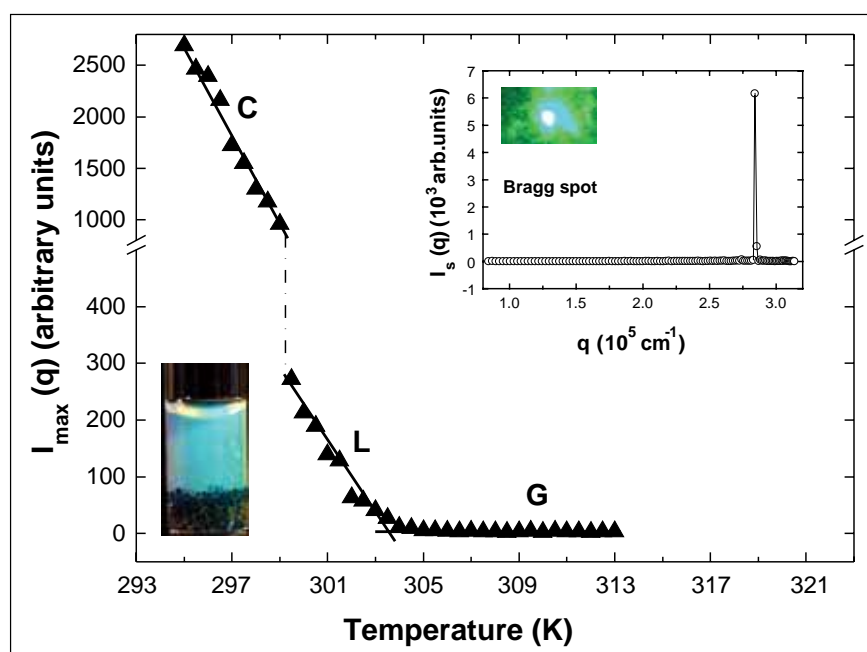
Fig. 2   *Bragg peak intensity $I_{max}(q)$ as a function of T for sample S3. C, L, and G represent the temperature region where sample exhibited crystalline, liquid-like and gas-like disorder, respectively. Insets show the photograph of sample S3 exhibiting iridescence, Bragg spot and the Bragg peak from crystallites in sample S3*

repeated annealing above volume phase transition and the iridescence is due to the Bragg diffraction of visible light. A sharp Bragg peak at $q = 2.84 \times 10^5$ cm^{-1} (inset Figure 2) was observed by performing static light scattering measurements using a 488 nm argon ion laser. These observations of iridescence and a sharp Bragg spot (inset in

Figure 2) suggest that the sample S3 is crystalline and has several single crystals. The melting transition of this PNIPAM nanogel crystal is identified by monitoring the Bragg peak intensity I_{max} as a function of temperature (Figure 2). The sudden drop in I_{max} at $T = 299.2$ K is due to the melting of these crystals into a liquid-like state. Further, the Bragg peak position remained the same across the melting transition, which suggests no change in n_p across this transition. Upon increasing the temperature beyond the melting point of PNIPAM nanogel crystals, the peak intensity decreased and showed a change in slope at 303.5 K. Beyond 303.5 K, the structural ordering in the suspension is found to be "gas-like" similar to that observed in sample S2. Thus the change in slope observed at 303.5 K is due to the occurrence of a fluid to fluid transition.

At temperatures below volume phase transition the PNIPAM nanogel particles are highly water swollen and hence the dielectric constant of these nanogel particles is almost the same as that of water. This results in a van der Waals attraction between the nanogel particles negligible at temperatures below volume phase transition and it is expected that the dispersion of these particles would behave as hard-spheres up to the volume phase transition. Hence this dispersion is expected to exhibit crystallization at a volume fraction $\phi = 0.5$. However the volume fraction of the crystallized sample S3 was determined to be 0.93 at 298 K and 0.85 close to its melting. Such high values of ϕ suggest that these particles are soft spheres. Further no change in number density in their in samples S2 and S3 which exhibited fluid-to-fluid and melting transitions respectively as a function of T. These observations indicate that the interparticle interactions between the PNIPAM nanogel particles are "soft-sphere repulsive" below volume phase transition and are responsible for the observed phase transitions. The phase transitions reported here are useful for developing temperature sensors, optical switches and in drug delivery applications.

V.12   Studies on Gallium Nitride Nanostructures

After the fascinating success of Si in electronic processing, GaN is the most potential candidate for changing the quality of life with its exclusive optoelectronic properties. The use of GaN as a blue light source has the potential market for printing, high density DVD memories and white light based (using diode laser based RGB) compact display devices. High power and high speed electronic devices operating at high temperature including High Mobility Electronic Transistor (HEMT) structure using GaN is another vista of this new generation material. The successful production of high quality GaN nanostructures opened up the possibility of device application in these low-dimensional systems. The understanding of optical properties and phase transition in the GaN nanostructures are important as an evolution of defect process. Lattice vibration of GaN nanostructures of the vibrating surface optical modes are on the verge of opening new applications.

GaN nanostructures were grown primarily using chemical vapor deposition technique following the vapor-liquid-solid process. The samples were grown at 1173K on c-Si substrates, pre-coated with gold catalyst of diameter ~5 nm, using molten Ga as the source material and NH_3 (10 sccm) as the reactant gas in a tubular furnace. The reactor chamber was pre-evacuated to a pressure of 10^{-3} mbar before starting the growth process at atmospheric pressure in the presence of NH_3 gas. Gold catalysts are grown using DC sputtering technique.

Defect evolution in single nanowire

Morphological and structural studies in the pristine nanostructures with field emission scanning electron microscopy (FESEM) and high resolution transmission electron microscopy (HRTEM) studies (Figure 1a) confirmed the growth of highly crystalline wurtzite (h-) GaN with zone axis lying along [001] direction as calculated from the corresponding diffraction pattern (inset in Figure 1a).

It was shown (Figure 1b) that dynamic annealing (defect-annihilation) processes in h-GaN become relatively efficient during heavy-ion bombardment at an optimum fluence of 5×10^{15} cm^{-2}. Ion-beam-generated Frenkel pairs, which survive the ultra short duration quenching
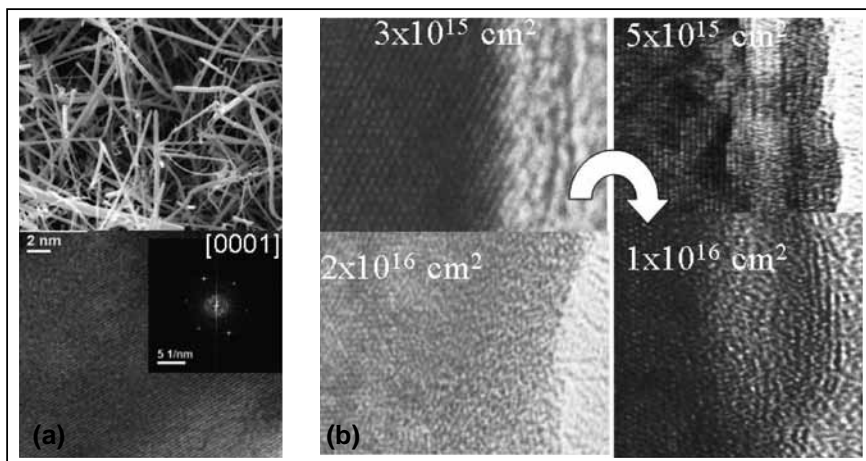
Fig. 1 *(a) FESEM image showing random oriented pristine GaN nanowires and corresponding HRTEM lattice image of the h-GaN nanowire, inset shows the SAED pattern with zone-axis lying in [0001] direction. (b) HRTEM image of sample irradiated at fluences of ~ 3×10^{15} - $2 \times 10^{16} cm^{-2}$ shown clockwise using mono-energetic (spread <0.2%) 50 keV Ga^+ FIB with current ~1.3 nA at flux $5 \times 10^{12}\ cm^{-2}\ sec^{-1}$*
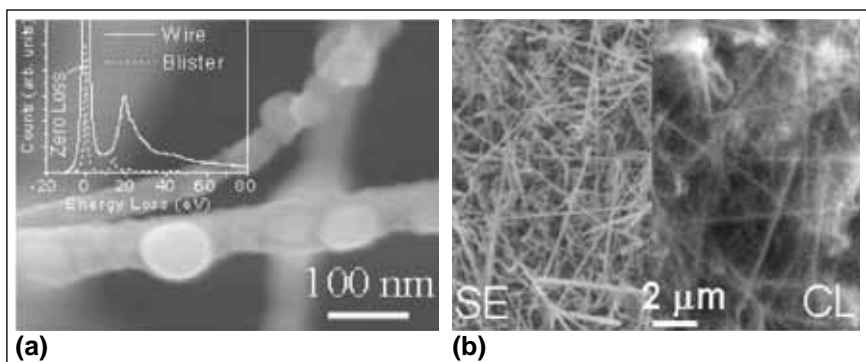
Fig. 2 *(a) ESEM images of GaN samples irradiated at fluences of $2 \times 10^{16}\ cm^{-2}$. Inset shows plasmon loss spectra corresponding to nanoblister and nanowire region. (b) Secondary electron (SE) and cathodoluminescence (CL, excited at 3.3 eV) images at 4K showing large of the nanowires are in cubic phase*

(~10^{-10} sec) of collision cascades, are mobile in *h*-GaN even at liquid-nitrogen temperature. Under these circumstances, a vacancy (or interstitial) cluster is likely to experience annihilation by trapping of the mobile interstitials. Therefore, an efficient dynamic annealing is expected. Presumably, the high diffusivity of mobile point-defects (interstitials) in the high-curvature geometry of nanowires makes this effect even more pronounced than that reported for the ion irradiated epi-GaN. However, the dynamic annealing process is a non-equilibrium process and hence the evolving structure never leads

to perfect ordering. In fact, other competitive processes can force the structure to be less ordered at a slightly higher fluence > $1 \times 10^{16} cm^{-2}$.

Nanoblister formation beyond the fluence of amorphization

The formation of nanoblisters for the GaN sample irradiated at a fluence of $2 \times 10^{16}\ cm^{-2}$ is shown in the FESEM image (Figure 2a). Inset shows the electron energy loss spectrum (EELS) in the plasmon-loss region corresponding to blister and nanowire regions show presence of pure Ga (13.6 eV) and GaN (19.6 eV), respectively.

Disintegration and accumulation of lattice atoms were found to be the dominant mechanisms for the formation of metallic α-Ga nanoblisters.

Hexagonal-cubic phase transformation in single nanowire

Hexagonal to cubic phase transformation is studied in self-ion implanted GaN nanowires. Optical photoluminescence and cathodoluminescence (Figure 2b) studies along with high-resolution transmission electron microscopic structural studies were performed to confirm the phase transformation. The potential reason may be that the fluctuations in the short-range order induced by enhanced dynamic annealing (defect annihilation) with the irradiation process stabilize the cubic phase and cause the phase transformation. It is known that the enhanced dynamic annealing in as-irradiated samples with short-range order appear at an optimum fluence of $5 \times 10^{15}\ cm^{-2}$ for efficient annealing.

Blue shift of yellow luminescence band : A promising technique for white light emission

The yellow luminescence band at 2.2 eV in GaN nanowire shows a blue shift with accumulation of nitrogen vacancies during the, chemically clean, self-ion irradiation process with a blue luminescence band observed at ~ 2.8 eV for the sample containing large nitrogen vacancy related point-defect clusters at the fluence of amorphization. The blue shift of the yellow band in self-ion implanted GaN nanowire, as observed in the present study, may be correlated to the formation of nitrogen vacancies introduced during the irradiation process. Presence of various bands can form the white light source.

Surface optical phonon in GaN nanostructures

In addition to the optical phonons (Figure 3a), Raman peak around 673 cm^{-1} is observed for GaN nanowires. Calculation in the cylindrical geometry for the surface optical (SO) phonon modes in GaN show values close to that of the new Raman mode. The effect of surface modulation assisted electron-SO phonon scattering is made responsible for the pronounced appearance of SO phonon modes.

The dispersion relation of the SO mode is calculated using appropriate parameters (Figure 3b) given by

$$\omega^2{}_{so} = \omega^2{}_{TO}(\varepsilon_0 - \rho_{nx}\varepsilon_m)/(\varepsilon_\infty - \rho_{nx}\varepsilon_m)$$
$$\rho_{nx} = (K_1(x)\,I_0(x)) / I_1(x)\,K_0(x))$$

where ε_0 (=10.4) and ε_∞ (=5.8)
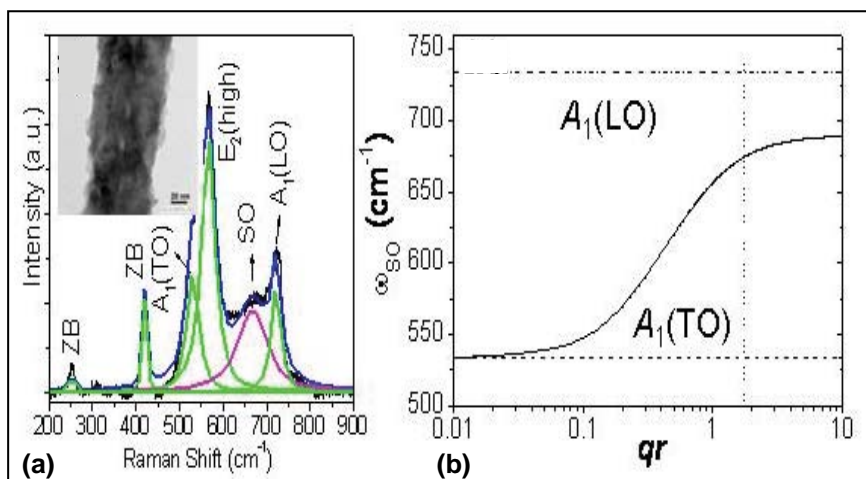
Fig. 3 *a) Raman modes for GaN with the unknown mode designated as SO mode. A typical surface modulation in GaN nanostructure is shown in the inset and b) Dispersion relation of A1 symmetry of SO mode. Horizontal full and doted lines correspond to the values of LO and TO mode frequencies, respectively, with a vertical line indicating the value of q for the SO mode at 673 cm^{-1}*

are the static and high frequency dielectric constant of the material, and ε_m (=1) is for the medium. I_j, and K_j are the modified Bessel functions and $x=qr$ (r radius of nanostructure, and q as wave vector).

V.13 Nanomechanical Characterization of TiN/TiAlN and TiN/NbN Nanoscale Multilayers

Modern synthesis techniques like Magnetron Sputter Deposition and Pulsed Laser Deposition have aided the field of materials science to synthesize *a priori* tailored novel materials for application in areas of technological importance. The repeating layered architecture of two materials with nanometer scale dimensions, the so called "multilayers or superlattices", is an emerging class of artificially engineered protective coatings that has been the subject of intense experimental and theoretical investigations. TiN, which was initially used for applications as hard coatings for special tools, later found diversified applications viz., in solar cells, selective transparent films for high temperature photothermal conversion, local interconnects in CMOS technology, aesthetic and chemically inert applications and diffusion barrier in semiconductor technology. The various attempts to improve upon its properties such as hardness, toughness, oxidation resistance and corrosion resistance led to the development of multilayer coatings. Two such material systems are TiN/TiAlN and TiN/NbN.

We have precisely engineered and synthesized multilayer thin films of Ti$_{1-x}$Al$_x$N/TiN (x=55%) on SS 304 LN steel substrates by reactive magnetron sputtering of various bi-layer thicknesses starting from 8 to 60 nm to understand their interphase and mechanical properties. The objective of using TiAlN as one of the sub-layers is to provide stability against oxidation at higher temperatures. This is due to the formation of a very dense and strongly adherent Al$_2$O$_3$ surface layer. Grazing Incidence X-ray Diffraction (GIXRD) profile exhibited broad peaks corresponding to cubic TiN. This represents the nanometric multilayered thin films. The profiles also revealed the formation of metastable TiAlN with 'NaCl' crystal structure. Cross sectional TEM images of multilayer thin films with 7 nm and 30 nm (single layer thickness) are shown in the Figure 1. It is understood from the Cross sectional TEM images that the interface between the layers is sharp and clear. The nanoindentation hardness versus thickness of individual layer of multilayers is shown in Figure 2. The hardness of
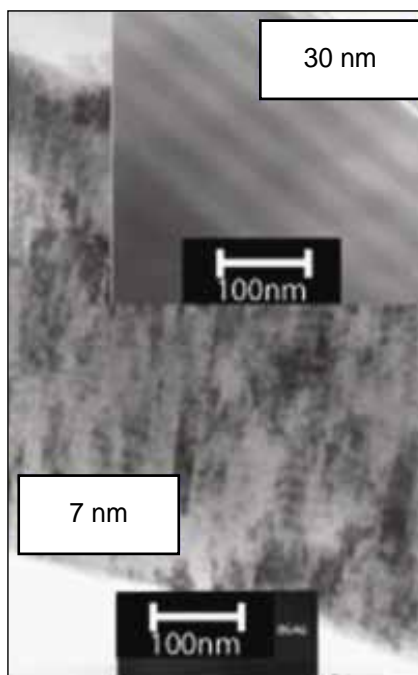
Fig. 1 *X-TEM image of multilayer thin films with individual layer thickness of 7 nm and 30 nm*

these thin films varies from 28 GPa to 34 GPa for the bilayer thicknesses of 8 to 30 nm, respectively. The decrease in hardness has been observed for a bilayer thickness of 30 nano meter. Reverse Hall-Petch relationship for a bilayer thickness of 30 nano meter has been also observed.

Reactive Pulsed Laser Deposition is a single step process wherein the ablated elemental metal reacts with a low pressure (1.0×10^{-2} to 1.0×10^{-1} mbar) ambient gas to form a compound. A novel Secondary Ion Mass Spectrometry based methodology was evolved for the optimization of important process parameters aimed at the synthesis of nano-structured stoichiometric TiN and NbN thin films. NbN/TiN coatings were

synthesized through sequential ablation of Ti and Nb targets using nanosecond pulsed Nd:YAG laser (1064 nm; 5 ns; 900 mJ) in nitrogen environment. We studied the evolution of structure, composition and morphology of monolithic thin films as a function of important process parameters. Under optimal deposition conditions, the hardness of both TiN and NbN films were found to be ~ 30 GPa. Parameters thus optimized were used to synthesize TiN/NbN multilayers, with individual layer thicknesses varying from 25 to 500 nm. The resultant multilayer coatings were evaluated for hardness and other mechanical properties using nano-indentation, scratch adhesion tester and nano-tribology. The hardness of this multilayer substantially increased to ~45 GPa.
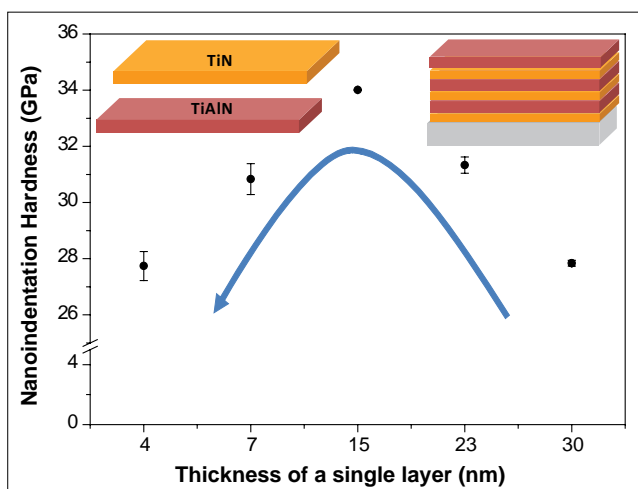
Fig. 2 *Nanoindentation hardness vs single layer thickness of multilayer thin films exhibiting reverse Hall-Petch relationship*
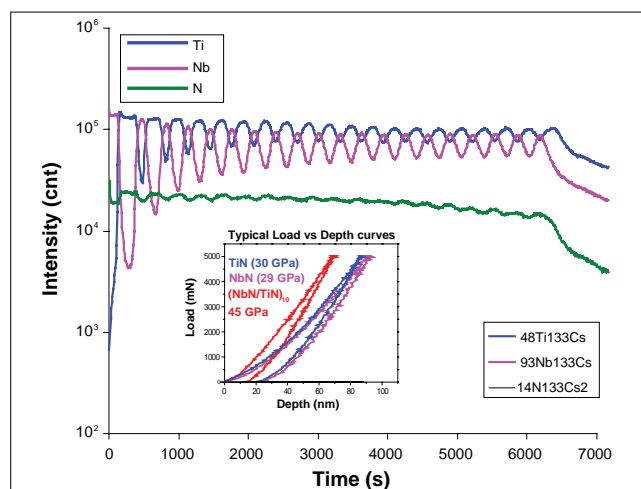
Fig. 3 *SIMS depth profile showing (TiN/NbN) multilayer and (Insert) typical nano-indentation curves along with hardness*

V.14 Discovery of Superconductivity in Rutheniun Substituted BaFe$_2$As$_2$

Research in condensed matter physics has focused on understanding superconductivity in Fe based compounds in the past two years. Several families

of superconductors have been discovered providing a fertile ground for extensive research, reminiscent of the hey days of high temperature superconductors.

These compounds contain Fe tetrahedrally co-ordinated to the anion, but with the Fe atoms placed in a square planar network. The first of these compounds to be

discovered were of the general formula LnOFeAs (Ln=early rare earth) popularly termed 1111. Subsequently compounds of the type MFe_2As_2 (M=Ba,Sr,Ca,Eu) termed as 122, LiFeAs, FeSe and more recently Sr_2VO_3FeAs have been discovered. Superconductivity occurs at the expense of the spin density wave ground state, by substituting F at O site in the 1111 compound and by K at the Ba site in the 122 compounds, suggesting that magnetism and superconductivity are competing orders. In the LiFeAs, FeSe and Sr_2VO_3FeAs systems no such spin density wave state is seen in the chemical vicinity and the systems seem to be self doped. Despite the initial expectation of very high transition temperatures and frenzied search for newer superconductors, the T_C in these systems is capped at 55 K for $SmOFeAs_{1-x}F_x$. The 122 family is the most well studied in these FeAs superconductors since single crystals were available at a very early stage. It has been shown in these double layer arsenides that superconductivity is robust to substitution at the Fe site by Ni and Co, unlike in the cuprates. Another unusual feature of these arsenide superconductors is that pressure and strain can destabilize the spin density wave order in the system and induce superconductivity without any external chemical substitution. Despite the vast body of research on a wide variety of compounds, the exact mechanism of superconductivity has yet to be pinned down. In these arsenides it appears that fluctuations present in the system due to the proximity to the quantum critical point, could originate the superconducting pairing interactions.

Two classes of these compounds, viz., $BaFe_2As_2$ and FeSe have been synthesized. Here we present our finding that isoelectronic substitution of Fe by Ru can also induce superconductivity in $BaFe_2As_2$ in a select range of Ru concentration. The $BaFe_{2-x}Ru_xAs_2$ samples were synthesized from stoichiometric mixtures of Ba, FeAs and RuAs under 50 bar of Ar pressure in a stainless steel chamber at 1233 K for 8 hours. The FeAs and RuAs precursors were synthesized in the same set up from intimate mixtures of elemental powders by heat treatment (carried out at 873 K for 16 hours) with intermediate grinding. These samples were handled in a helium filled glove box. The structural parameters were measured by X-ray diffraction, which indicates that the a-lattice parameter increases monotonically and the c-lattice parameter decreases with the Ru content. This results in a steady reduction in the c/a ratio and a small increase in the cell volume with the Ru concentration. The temperature dependence of resistivity was measured in all these samples in the temperature range 4.2 K to 300 K. The pristine sample shows a well known spin density wave anomaly at ~150 K (see Figure1) corresponding to the opening of the gap in some regions of the Fermi surface, due to perfect nesting. This anomaly is seen to shift to lower temperatures with increase in Ru content, as indicated in Figure 1 by the "✱" marking. Filamentary superconductivity is seen at x=0.625 in $BaFe_{2-x}Ru_xAs_2$. For x=0.75 both bulk superconductivity and magnetic transitions are seen, with the superconducting transition showing zero resistance. The superconducting transition with zero resistance is seen to persist upto a composition of x=1.125, whereas filamentary
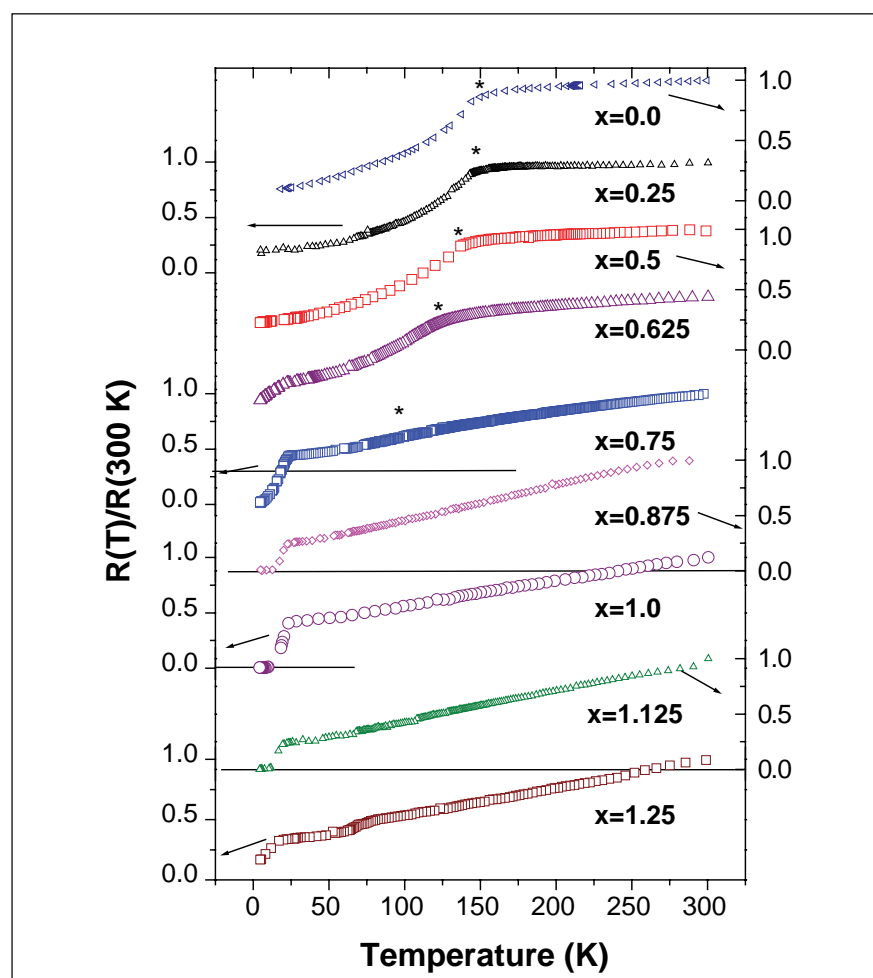
Fig. 1 *Variation in resistivity with temperature in $BaFe_{2-x}Ru_xAs_2$ for various nominal Ru fractions x indicated*
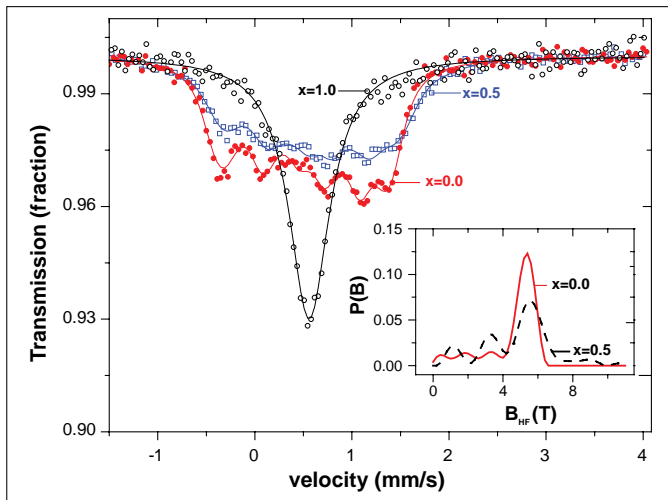
Fig. 2 *Variation of the transmitted intensity versus the velocity of the Mossbauer spectra measured at 5 K in BaFe$_{2-x}$Ru$_x$As$_2$ samples with x= 0.0, 0.5 and 1.0. Inset shows the fit of the hyperfine splitting in terms of magnetic field distribution*
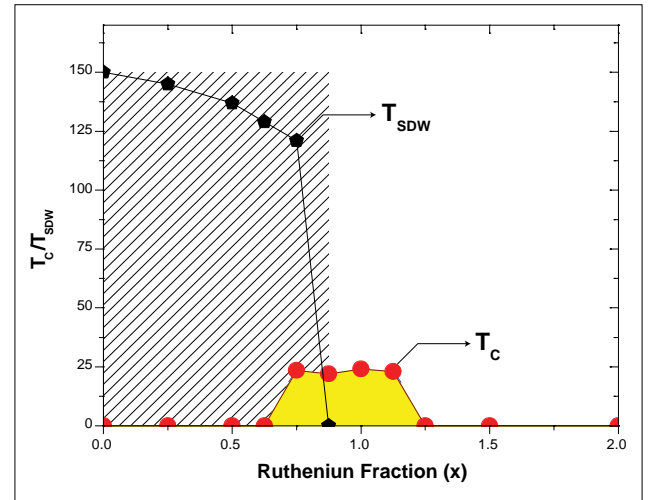
Fig. 3 *The variation of the SDW transition temperatures and superconducting onsets as a function nominal Ru fraction x. SDW and superconductivity states co-exists for the x = 0.75 sample*

superconductivity is observed for x=1.25. The diamagnetic signals confirming bulk superconductivity is seen in the fraction range x= 0.75 to 1.125. To examine the disappearance of the magnetic order with Ru substitution, Mossbauer measurements were carried out at 5 K in the transmission geometry in these samples with x= 0.0, 0.5 and 1.0 (see Figure 2). A magnetic ground state is clearly seen in the sample with x=0.0 as revealed by the appearance of a six finger pattern. This six finger pattern progressively collapses with the Ru content and is altogether absent in the superconducting sample with x=1.0. This clearly indicates that magnetism is killed in this superconducting composition. The variation SDW transition T$_{SDW}$ and the superconducting transition temperature T$_C$ obtained from R(T) graphs for various Ru composition are plotted against nominal Ru composition in Figure 3. The phase diagram clearly indicates that for low concentration the SDW ground state is stabilized, which gradually transforms to the superconductivity state with increase in Ru composition. Superconductivity is stabilized only over a small region of Ru concentration of $\cong$36 % to

66%. Superconductivity and SDW co-exist in the low Ru concentration region.

To understand how Fermi surface nesting, essential for the SDW state, is affected, electronic structure calculations for BaFe$_2$As$_2$, BaFe$_{1.5}$Ru$_{0.5}$As$_2$, BaFeRuAs$_2$ and BaFe$_{0.5}$Ru$_{1.5}$As$_2$ by considering appropriate supercells were performed. These were carried out using the full potential linearized plane wave plus localized orbitals (FP-LAPW+LO) method with the WIEN2k code. The generalized gradient approximation was used for the exchange interaction. These calculations were done with 1000 K points in the full Brillouin zone, with the ground state relaxed structure obtained using the same technique. These calculations reveal that the density of states at E$_F$ is substantially suppressed with Ru substitution. The magnetic moment calculated using the spin polarized calculations also indicate a reduced moment with increase in Ru substitution. The system seems to be electron doped with Ru substitution.

To summarise, Ru has been substituted at Fe site in the BaFe$_2$As$_2$ structure, inducing superconductivity in a select Ru composition range. Co-existence of SC and SDW orders is observed for a small composition regime. Disruption of the magnetic order with Ru substitution has been followed by Mossbauer spectroscopy, carried out at 5 K. Although Ru is larger than Fe, structural parameters reveal that c- lattice parameter shrinks but the a- lattice parameter increases resulting in a decrease in c/a ratio and in the increase lattice volume. Band structure calculation indicate Ru-As bond hybridisation is larger than that of Fe-As, which leads to depletion of density of states at E$_F$. The increased hybridization could also increase the inter-planar hopping and lead to a distortion of the two dimensional Fermi-surface disrupting the condition for perfect nesting. This could be the origin of the destabilization of SDW, favouring of the superconducting ground state. A detailed understanding of the parameters crucial for the observation of superconductivity, might help identify newer substituents that could induce superconductivity.

V.15 Investigation of the Metal Insulator Transition in GdBaCo$_{2-x}$Ni$_x$O$_{5.5}$ using Infrared Spectroscopy

Oxygen deficient layered perovskites of the formula LnBaCo$_2$O$_{5+\delta}$ have attracted considerable attention in recent years due to the unique combination of electrical and magnetic properties that they posses. The oxygen content in these compounds play a very crucial role in determining transport and magnetic properties of the latter. Materials with δ = 0.5 exhibit a metal to insulator transition (MIT) at ~ 370 K (T$_{MIT}$) in addition to several magnetic transitions. Chemical substitution of the cobalt sublattice in GdBaCo$_2$O$_{5.5}$ with nickel is seen to suppress the T$_{MIT}$. While detailed studies have been carried out to understand the origin of this metal to insulator transition, in the present work we have used infrared spectroscopic studies to investigate the interplay between metal to insulator transition and the structural aspects. Room temperature far infrared absorption spectroscopic measurements were carried out on GdBaCo$_2$O$_{5.5}$ in the range 125-650 cm^{-1} and thirteen infrared active phonon modes have been identified for the first time. *Ab initio* lattice dynamical calculations using VASP simulation program, helped in preliminary mode assignments. In situ variable temperature far infrared absorption spectroscopy was carried out to follow the phonon modes in both undoped and Ni doped GdBaCo$_2$O$_{5.5}$, across the T$_{MIT}$, in an effort to understand the nature of this transition. Figure 1 shows a select set of as recorded far infrared spectra of GdBaCo$_2$O$_{5.5}$ in the range 125-650 cm^{-1}, spanning the T$_{MIT}$ (370 K). Prior to the T$_{MIT}$, in the insulating state, the spectrum exhibits sharp and highly resolved
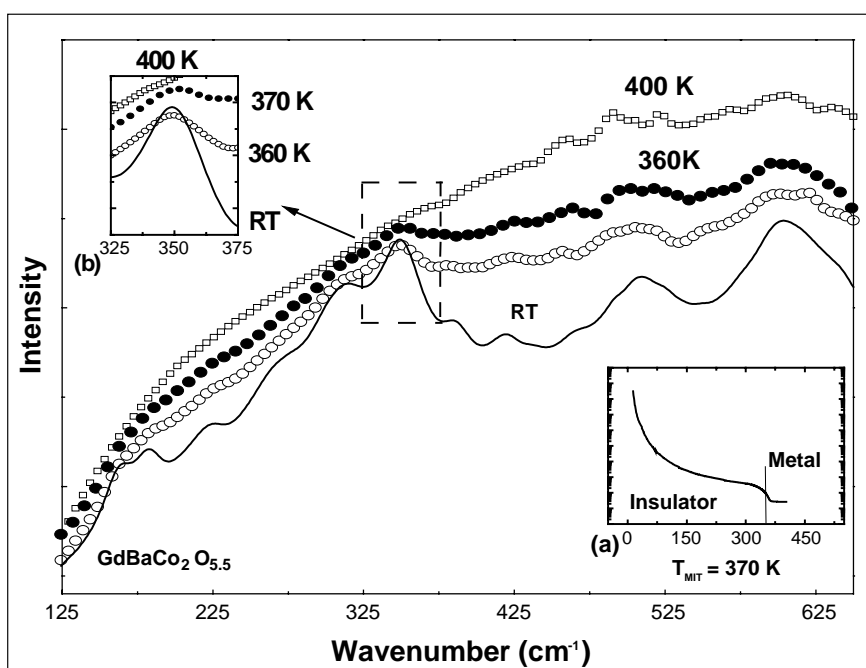
Fig. 1 *Far infrared absorption measurements of GdBaCo$_2$O$_{5.5}$ across T$_{MIT}$. Inset (a) Temperature dependence of resistivity in the range 4.2K – 400K Panel and (b) shows detailed evolution of the bending mode across T$_{MIT}$*
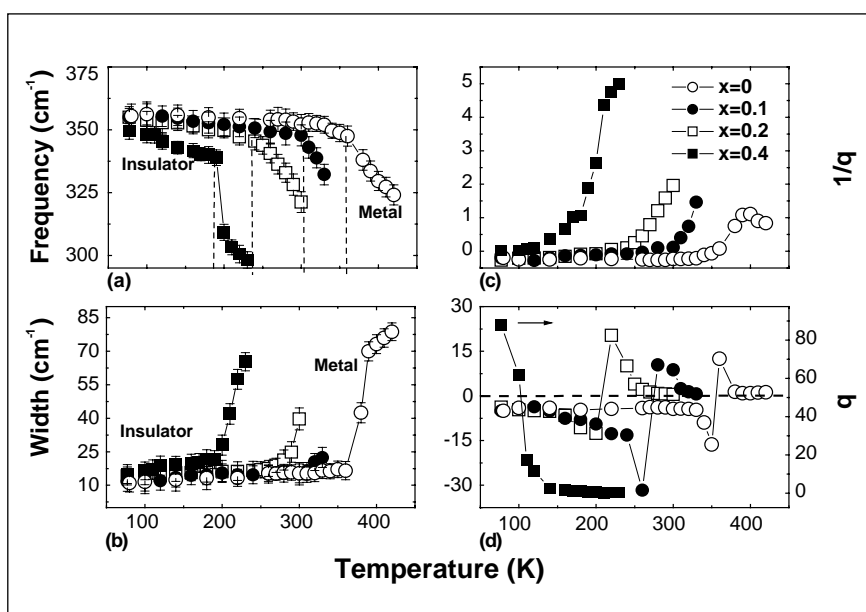
Fig. 2 *Variation of line shape parameters across T$_{MIT}$. Note the suppression of T$_{MIT}$ with increasing nickel contents*

phonon features. With an increase in the temperature, an increase in the electronic absorption background is observed along with a systematic decrease in the phonon intensities accompanied by an evident broadening. For temperatures beyond T$_{MIT}$ the phonon modes are observed to be totally screened by the increased electronic absorption background, and the spectrum becomes totally

featureless, signaling the transition to the metallic state. Detailed analysis of the bending mode at 350 cm^{-1} revealed anomalous changes in the line shape parameters that correlate well with the transition temperatures. (Figures 2(a) and 2(b)). A sharp decrease in the phonon frequency associated with an anomalous increase in their line widths indicative of extensive electron-phonon interaction effects, signals the transition to the metallic state. Additional support for the interaction of this mode with the free electrons in the medium is provided by changes observed in the variation of the asymmetry parameter '1/q' (Figure 2(c)) and the Fano parameter 'q' (Figure 2(d)) that also correlates with T_{MIT}. A clear indication of the suppression of the T_{MIT} with increasing nickel contents is also seen. The fact that the bending mode exhibits an abrupt softening at the T_{MIT} is indicative of increased bond angles between the octahedra / pyramids thus suggesting delocalization of charge carriers along all directions leading
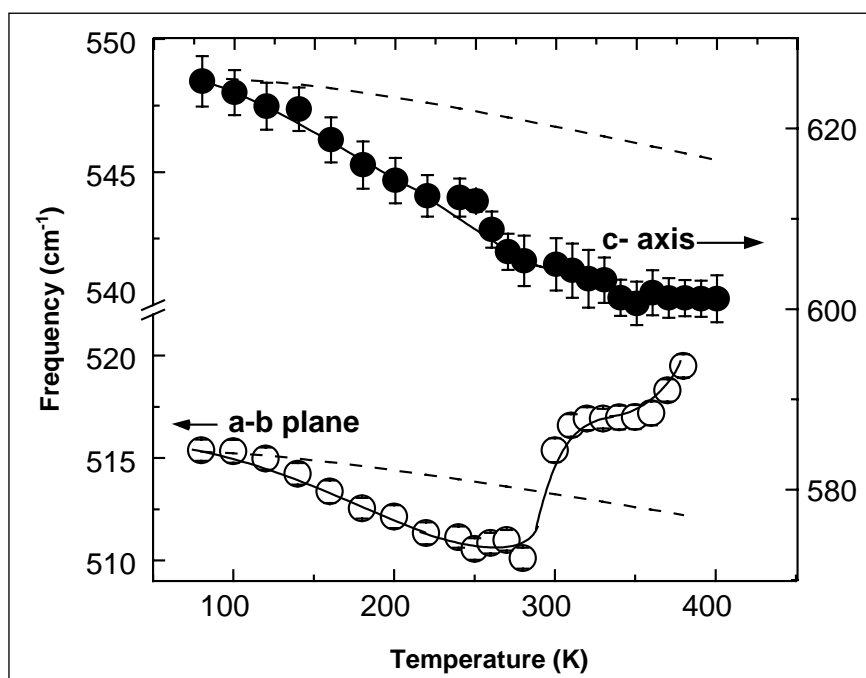
Fig. 3 *Variation of the octahedral stretching modes across T_{MIT}. Dotted lines refer to the expected variation based on cubic anharmonicity model*

to the observed metallic state. Analysis of the octahedral stretch modes of GdBaCo$_2$O$_{5.5}$ (Figure 3) reveals an evident contraction of the octahedra along the a-b plane (515 cm^{-1} mode) associated with an elongation along the c axis (603 cm^{-1} mode) as the system enters the metallic state. These distortions are expected to modify the crystal field splitting energies, thus reducing the band gaps resulting in the observed insulator – to metal transition. The above observations clearly provide evidence for a structural link associated with the insulator to metal transition.

V.16 Ion Beam Studies of Ultrananocrystalline Diamond

Ultrananocrystalline diamond (UNCD) is relatively a new material in the family of carbon nanomaterials. Ultrananocrystalline diamond is a fine grain material with 3 to 5 nm diamond grains bound by thin grain boundaries as seen in the XTEM image in the inset of Figure 1. Generally, the interface region between the two phases forms the grain boundaries, but in the case of ultrananocrystalline diamond, the intergrain amorphous phase with sp2 content and bonded hydrogen is so thin (~1 nm) that the whole of it constitutes the grain boundary. The surface is smooth and pinhole free as seen in the FE-SEM image presented in Figure 1 and it can form conformal coating on various substrates with reproducibility. Ultrananocrystalline diamond has all the good properties of diamond. While the film
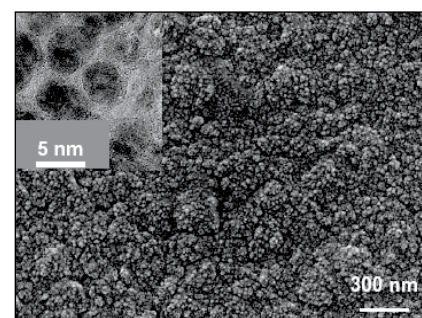
Fig. 1 *FE-SEM image of UNCD film. XTEM image is in the inset*
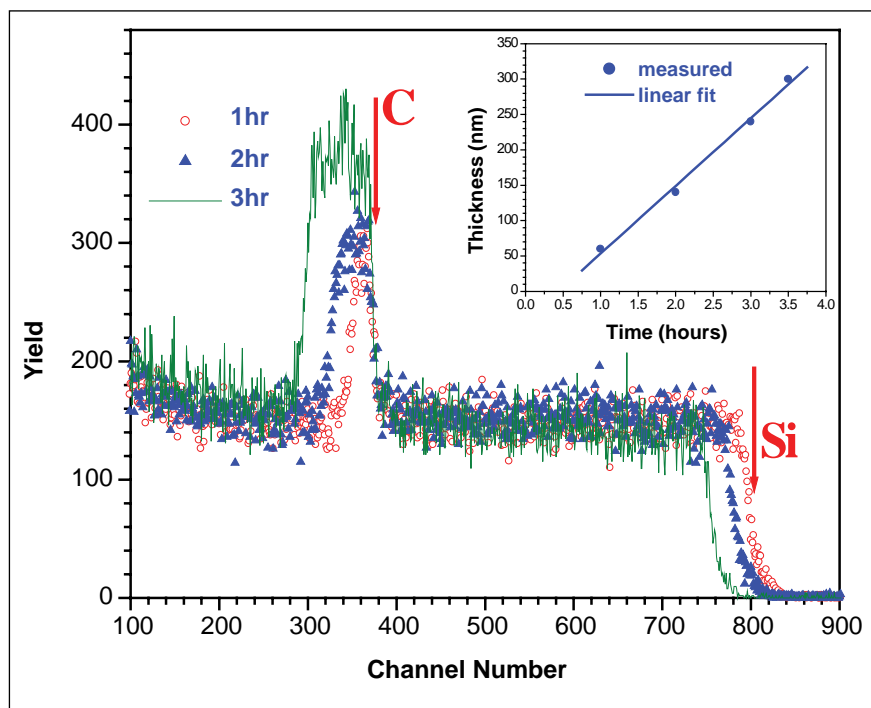
Fig. 2   *RBS spectra from UNCD films on Si with different growth time. Variation of thickness with growth time is in the inset*

properties are found to depend on the grain size, it is the structure of the grain boundaries which mainly determines the electrical and optical characteristics. The surface can be made hydrophobic or hydrophilic by the plasma treatment with H_2 or O_2 and can be functionalised to be used as a gas sensor or bio-sensor. It has applications in MEMS, flat panel displays, surface acoustic wave telecommunication devices, ultra-low friction and wear coatings for mechanical pump seals and tools, in-vivo biomedical implants, etc. Ion beam characterisation for studying the growth process of Ultrananocrystalline diamond and modification of these films for enhanced field emission is reported.

During CVD growth of conventional diamond film from H_2+CH_4 plasma, it is known that stress gets relaxed at about 1 mm thickness. For studying the corresponding behaviour in ultrananocrystalline diamond, its film is grown on Si substrates from Ar +CH_4 plasma in microwave plasma enhanced CVD

growth with very high renucleation density for different durations at a power of 1200 W and a pressure of 120 torr. Figure 2 shows Rutherford backscattering spectra (RBS) with 3.6 MeV (which has enhanced cross-section for carbon) of the ultrananocrystalline diamond films. The value of thicknesses extracted from the spectra is shown in the inset which shows a linear behaviour with growth time.

GIXRD measurements show that the film is strained. Strain reduces with increase in thickness and remains saturated after 165 nm. This implies that intrinsic stress in the film due to grain boundaries relaxes at this thickness. The reduction in strain is accompanied by increase in defect density. Raman measurements are also consistent with GIXRD results.

As Ar +CH_4 plasma is used during the growth of ultrananocrystalline diamond, hydrogen is also present in the film. H-termination is responsible for negative electron affinity (NEA) in CVD diamond

which lowers the work function and makes it a suitable candidate for cold cathode field emission devices. It is important to study the distribution of hydrogen in the Ultrananocrystalline diamond films and is studied with Elastic Recoil Detection Analysis (ERDA). Elastic recoil detection analysis spectra with 2.8 MeV He^{++} from the samples of different thicknesses are shown in figure 3. The width of hydrogen signal increases with thickness indicating that hydrogen is distributed through out the film thickness. Hydrogen profile is also measured in nanodiamond films with different grain sizes of 5, 100, 800 and 1000 nm. It is seen that hydrogen content decreases with an increase in grain size. This implies that hydrogen is at the grain boundaries and its concentration is proportional to the area of the grain boundaries cutting through the film.

Ion implantation in ultranano-crystalline diamond can cause doping, desorption of hydrogen, interchange between sp2 and sp3 bonded carbons, broadening of grain boundaries and introduction of defects which can affect the field emission properties. Low dose ion implantation in ultrananocrystalline diamond introduces defects which enhance field emission but the property reverts back upon annealing. High dose nitrogen implantation gives rise to good field emission even after annealing, but it makes a major part of the film into nanographite. Multiple energy nitrogen implantation at low doses and high substrate temperature is found to be a better method which distributes the implanted nitrogen throughout the film with a lesser density of defects which can anneal out. The implanting order of energies is also important. Figure 4 shows the field emission data from ultrananocrystalline
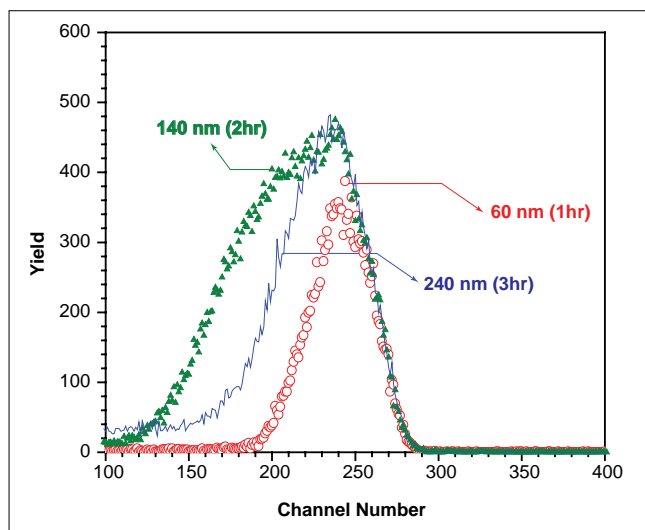
Fig. 3 *ERDA spectra of UNCD films on Si with different thicknesses*
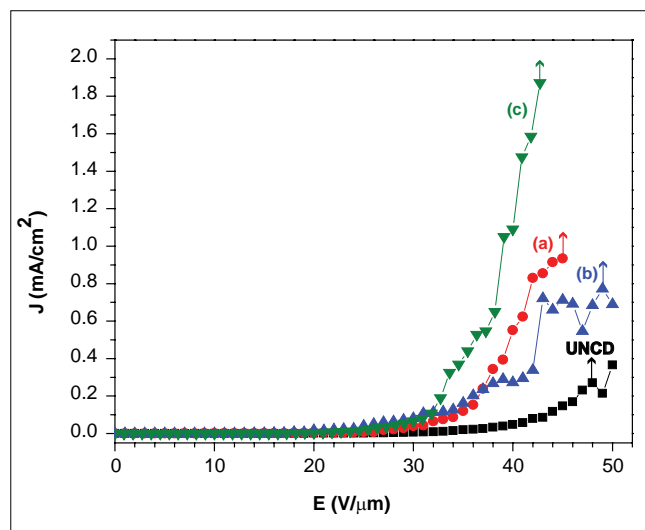
Fig. 4 *Field emission measurements from N-implanted UNCD films*

diamond films implanted with nitrogen ions of (a) 100 keV, (b) 200, 150, 100, 50 keV and (c) 50,100, 150, 200 keV at 573 K to a total fluence of 4×10^{14} ions/cm^2. The sequence (c) gives the best field emission property with a turn on voltage of 7 V/mm

and higher current density. Nitrogen is expected to diffuse into the grain boundaries and introduce more sp2 content, thereby enhance the field emission which is quite stable. Doping with Li and B ion implantation at room temperature has been tried out with out

any success. 100 MeV Ag^{9+} irradiation in ultrananocrystalline diamond is also found to be useful which induced the formation of interconnected sp2 nano-cluster networks, facilitating the electron conduction and enhancing the field emission properties.

V.17   Sterate Coated Mg(OH)$_2$ Nano Powders

Commercially available Dry Chemical Powder (DCP) which is being used to fight conventional fire is also recommended for

sodium fire fighting, mainly because of its easy availability. However, it has been proved that many other powders are much more effective.

Hence a structured R&D programme has been initiated. In this context, Mg(OH)$_2$ is being assessed for its sodium fire fighting ability, based
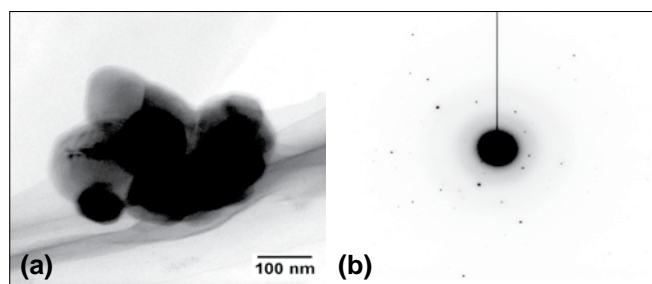
Fig. 1 *(a) [A01-1] Bright-field image showing a typical nanoparticle cluster supported on amorphous carbon film. (b) Diffraction pattern from selected area of the cluster. The spots have been measured and found to correspond to Mg(OH)$_2$*
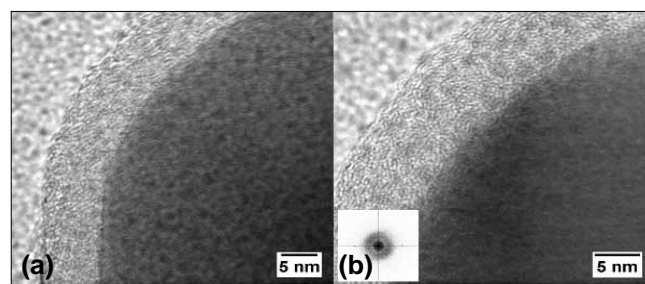
Fig. 2 *Phase contrast images of the (a) Edge of the left-most nanoparticle cluster. The width of the coating is uniformly 8 - 9 nm. (b) Faint 0.24 nm fringes seen correspond to the (101) planes of Mg(OH)$_2$. This is also indicated by spots in the power spectrum provided as inset*

on its reported superior cooling rates on conventional fires and higher enthalpy of decomposition. Nanoparticulates of the same has been successfully prepared and assessed for size and composition. The powder was characterised using XRD, as well as TEM. From the XRD pattern it is confirmed that the stearate coating does not alter the basic characteristics of the $Mg(OH)_2$.

High Resolution Transmission Electron Micro-scopy (HRTEM) images indicate that nanoparticles of magnesium hydroxide were seen to occur in small lump. Crystallite sizes are in the range 80 – 120 nm (Figure 2(a)). Since very few particles were found and their orientation could not be changed, the diffraction pattern (Figure 2(b)) consisted of very few spots, that could be indexed to $Mg(OH)_2$ structure. Figure 3 (a & b) show higher magnification phase

contrast images of the edge of the left-most particle in Figure 2 (a). It is seen that the layer covering the nanoparticle cluster is 8 – 9 nm thick and is amorphous. It can be clearly distinguished from the amorphous carbon support film that is seen in the top left corner of the images. In Figure 3 (b), faint 0.24 nm fringes corresponding to (101) plane spacing of $Mg(OH)_2$ can also be seen. The fringes are not very distinct since the particles are thick.

V.18 Compton Scattering Study of Electron Momentum Distribution in Lithium Fluoride

The Compton profile studies on ionic solids, particularly alkali halides with NaCl structure, have been the subject of great interest both experiment and theoretically. Amongst all the alkali halides the fluorides have been theoretically predicted to give larger anisotropy and it has been shown that the relative anisotropy of fluorides decreases as one goes from lithium to higher alkali atoms. Lithium fluoride is the simplest of all typical ionic solids. It has a NaCl structure and ten electrons per unit cell. For these reasons it has been the subject of intensive theoretical investigation and measurement. Yet another reason for the present study is its widespread use in thermoluminescence dosimetry. Its properties are well studied and it is possible to compare the high-energy irradiation effects of other types of luminescence excitations. In contrast to the other alkali halides, LiF is a more complicated material for the luminescence spectroscopy since its spectra, besides intrinsic

self trapped exciton emission bands, usually consists of the bands assigned to radiation defects and trace impurities. The latter bands are typical for LiF because of its relatively high melting temperature. An understanding of the ground state electronic structure is necessary in order to explain the chemical bonding and other properties.

In this study, we report the first ever ^{137}Cs Compton spectroscopy study of LiF with an improved momentum resolution of 0.39 a.u. obtained by using the 662 keV Compton spectrometer. Also the HF-LCAO theoretical results were tested for the first time at this energy. The spherical average Compton profiles of LiF are deduced from Compton scattering measurements on a polycrystalline sample at a γ ray energy of 662 keV. There are also compared with the spherical average and directional Compton profiles of LiF calculated using the CRYSTAL98 software suite.

Crystalline orbitals were generated from self-consistent Hartree–Fock method applied to Linear Combination of Atomic Orbitals (LCAO). The directional Compton profiles and their anisotropic effect were also calculated by using the same HF-LCAO approximation. The calculation was performed at the characteristic crystal structure (rock salt) by using the experimental lattice parameters (a ¼ 4.0173A°) according to Wyckoff. Default tolerances were used in these calculations, with reciprocal space integration being performed at twenty nine points in the irreducible wedge of the first Brillioun zone. Calculation was performed with high quality all-electron basis sets, namely 6–1G for Li^+, and 7–311G for F^-. All these basis sets for the present system are available in optimised form in CRYSTAL98 code.

The differences (DJ(q)) between the spherical average experimental and convoluted theoretical
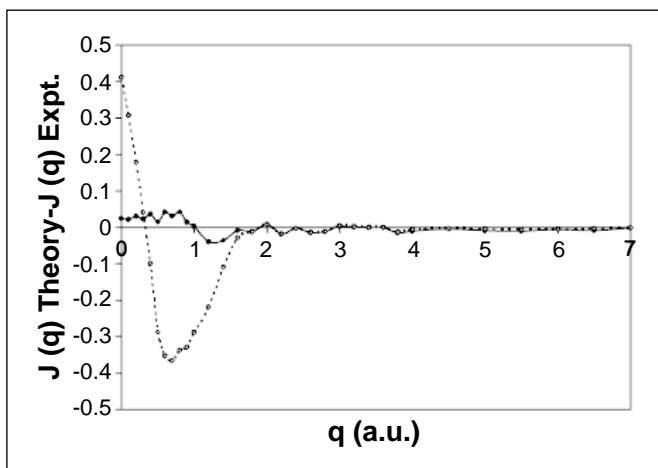
Fig. 1 *Difference in Compton profiles of theory and experiment of lithium fluoride. Solid line represents the difference of HF-LCAO and experiment*
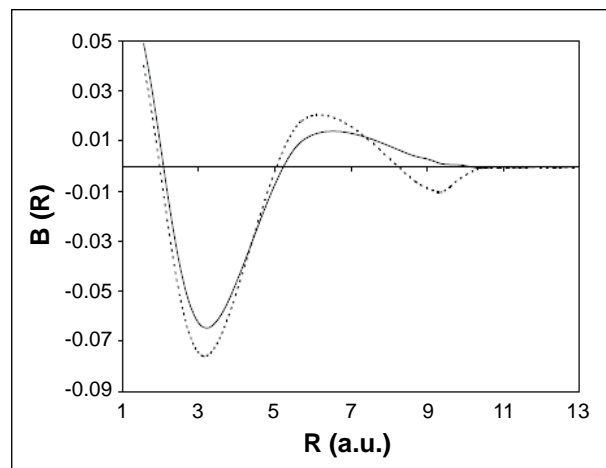
Fig. 2 *Reciprocal form factor B(R) of lithium fluoride. The broken curve represents the experiment and solid line represents the HF-LCAO theory*
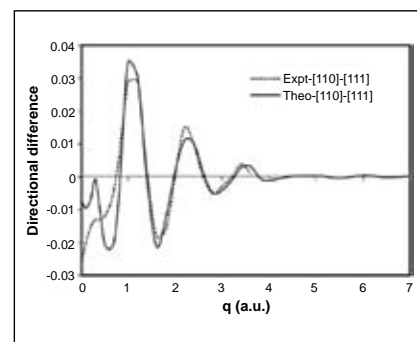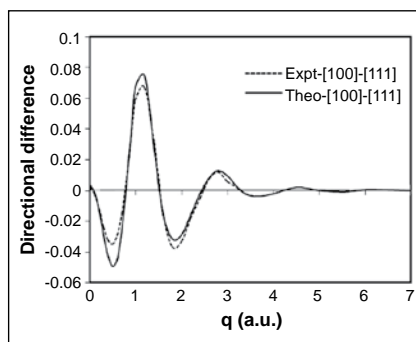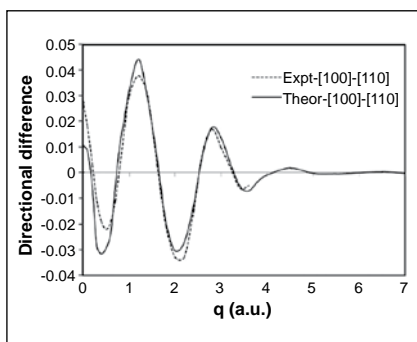
Fig. 3 *Difference between [100-110], [100-111] and [110-111] Compton profiles. The present theory using self-consistent Hartree – Fock wave functions employed on linear combination of atomic orbital (HF-LCAO) approximation is shown as solid line. Experimental results are shown as dotted line*

Compton profiles of lithium fluoride are shown in Figure 1. It is seen that at lower momentum region the deviation is more for free atom values compared to HF-LCAO calculations. At the higher momentum region the agreement between experiment and free atom profile are found to be good. Our present experimental data are found to compare well with the available experimental Compton profiles obtained by means of 59.54 keV γ rays. As a further check, the reciprocal form factors B(R) were also determined by transforming the Compton profiles with a fast Fourier transform (FFT) program. The results are shown in Figure 2. The most meaningful test of these wave functions is carried out by comparing the anisotropies. We have demonstrated that our calculations agree well with experimental data recorded with 159 keV γ-rays (Figure 3)

The fact that the [110]–[111] anisotropy in the case of LiF is very small in the high momentum region (Figure 3) is because both the directions cut the [100] bond at roughly the same angle, and thus to the first-order the bond looks the same. Further for the difference Compton profile [100]–[111], a significant effect is seen for momentum values q $\leq$ 1.8 a.u., where a pronounced minimum is observed around q = 1.4 a.u. However, the J[110]–J[111] curve has an amplitude roughly one half of the amplitude of the other two anisotropy curves. Thus, one can conclude that the crystal direction [100] is the nearest neighbor (Li–F), which has been found to be a special one.

V.19 Improvement in Spatial Resolution of Raman Distributed Temperature Sensor using Path Delay Multiplexing

Optical fiber based Raman Distributed Temperature sensors (RDTS) with inherent advantages such as immunity to electromagnetic interference, flexibility, low material reactivity and long transmission distances, are widely used for distributed and continuous temperature monitoring of oil plants, nuclear reactors, power cables and environmental monitoring. Feasibility of using RDTS for high temperature measurements up to 973 K has been demonstrated earlier. The major limitation of RDTS is its spatial resolution capability. The spatial resolution depends on the pulse width of the laser used. A typical RDTS uses 5 ns pulse width laser and has spatial resolution of 1 meter. Many groups have worked towards increasing the spatial resolution of the system. The methods involve ultra low pulse width lasers and associated modifications in electronics.

A simple but powerful technique to improve spatial resolution is developed using path delay multiplexing. In this method, the sensor fiber is multiplexed to the RDTS through a coupler. One arm of the coupler is larger than the other by a length equal to half the spatial resolution of RDTS. The extra length, introduces path delay in RDTS measurement.

The fiber can be considered to be sectionalised, each of length equal to the spatial resolution of RDTS. When the RDTS measures temperature, due to multiplexing, there are two sets of temperature measurement over a single sensor fiber (Figure 1). The temperature measured is lower than the actual temperature since it is averaged over 1m zone. The temperature measurements over the section of
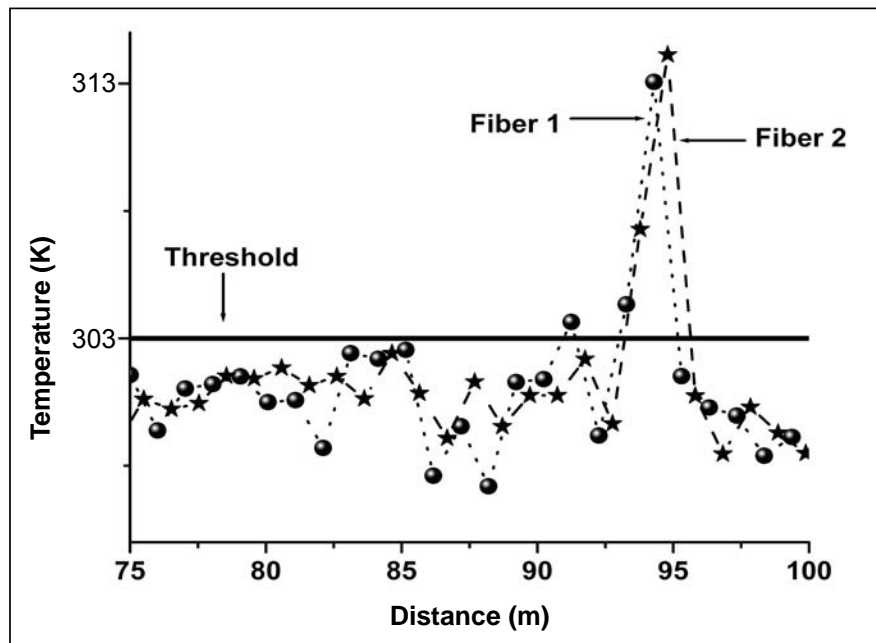
Fig. 1 *Temperature measurement by fiber 1(dotted line) and fiber 2 (dashed line). The two scan differ by path length =L/2. The spatial resolution is 1.02m*
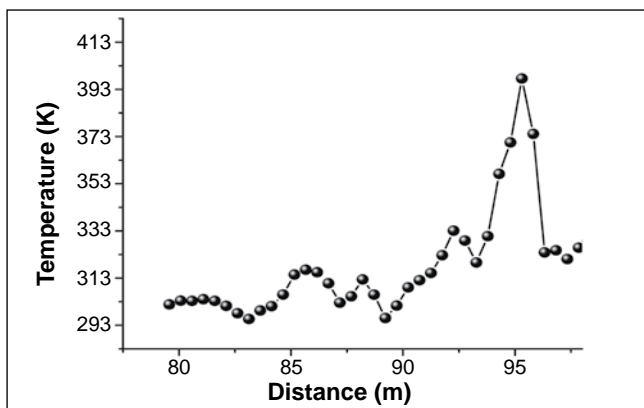
Fig. 2 *Temperature reconstructed with spatial resolution of 0.51m. Note error propagation along the length of the fiber*
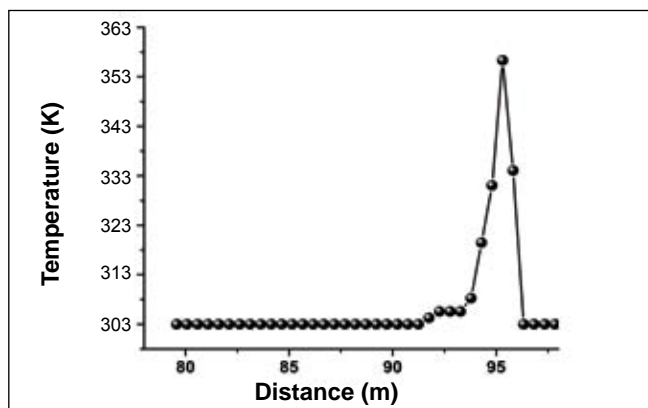
Fig. 3 *Temperature reconstructed with spatial resolution of 0.51 m after applying a threshold filter*

overlap can be formulated into a set of algebraic equations. The number of equations, thus formulated is one less than the number of overlap sections. This can be solved if temperature of at least one section is known apriority. This condition is achieved by maintaining the leading section of the fiber sensor at known temperature. The set of equations is then solved through iterative method. However, though the resolution has improved, the resulting temperature is still not close to the true temperature profile (Figure 2). This is because of the iterative method where the error propagates along the length of the fiber. To overcome this, a simple threshold is applied to the temperature measures of fiber 1 and fiber 2 before iteration. This yields, accurate measurement resolved over every half a length of spatial resolution (Figure 3).

This simple technique allows spatial resolution to be improved by n times, if the number of path delays introduced is n-1.

V.20 Magnetocardiographic and Magnetoencephalographic Studies using a SQUID Based Four Channel System

Magnetocardiographic (MCG) and Magnetoencephalography (MEG) involve non-invasive measurements of the magnetic fields associated with the physiological activities of human heart and human brain respectively and represent the most challenging applications of SQUID (Superconducting Quantum Interference Devices) sensors. These fields (~100 fT to ~ 100 pT) are very small and are virtually immeasurable by any other sensor technology. A magnetically shielded room with an attenuation of 70 dB at 1 Hz, improving to 100 dB at 100 Hz has been installed at our center, to shield the much larger ambient noise. A four channel MCG/MEG system, comprising of four independent SQUID channels has been established inside the magnetically shielded room and is coupled to a fast data acquisition system, using a 24 bit Delta- Sigma ADC for each channel. The overall white noise of the system was measured to be 12 fTHz$^{-1/2}$ in each channel.

Magnetocardiography is morpho-logically similar to ECG as both arise from the electrical activity of

Left Panel: SAMCG of a 47 year Old femal with normal ECG : Subject ID 616B

Right Panel: Top ECG of 68 year old male identified with LBBB; Bottom : MCG
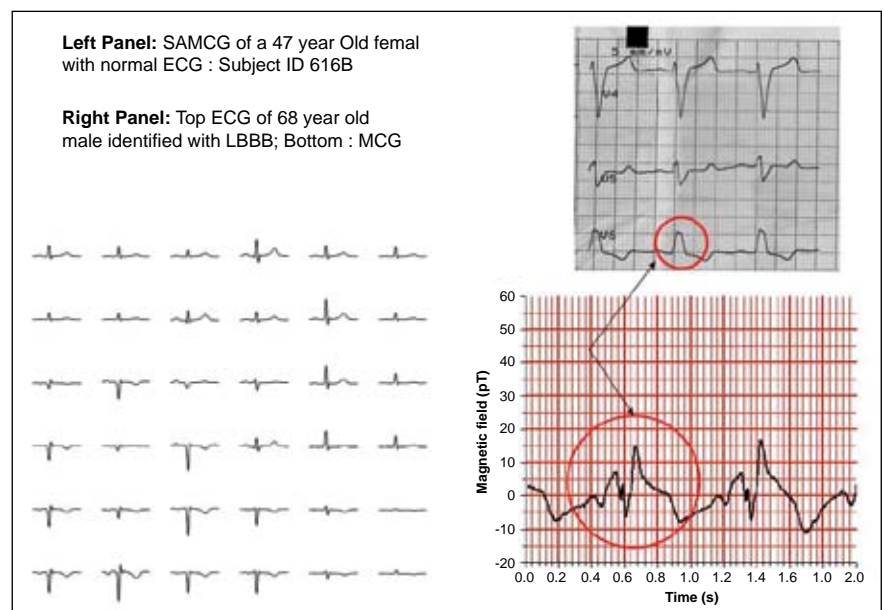
Fig. 1 *MCG of a normal subject and that with a cardiac anomaly*

the heart. The former presents a better source localization accuracy, due to a variety of reasons. Not yet a routine clinical tool, MCG has been reported to be superior in several clinically important problems in the assessment of the risk of life-threatening arrhythmias, localization of cardiac activation, arrhythmia causing regions etc. An MCG study was carried out at our Centre on about 40 subjects (both normal and with cardiac dysfunctions), in collaboration with the DAE Hospital, Kalpakkam, to assess the potential of this technique. As an illustration, Figure 1 shows the MCG traces (magnetic field in pico Tesla vs. time in seconds) of a normal subject measured over the chest on a grid of 36 equi–spaced positions, each trace averaged over several cardiac cycles. The regularity and expected symmetry across the spatial positions is clearly seen.

For a patient diagnosed with a left bundle branch block (LBBB) anomaly, while the ECG shows the widened QRS complex and the characteristic notched R wave, the corresponding MCG (two cardiac cycles are shown at a position in the middle of the chest) shows a distinctly split R wave, representing the delay in the depolarization of the left ventricle compared to the right ventricle. MCG has the potential to emerge as a powerful diagnostic tool complementing the standard ECG.

MEG measures electrical activity of the brain and is capable of better spatial localization of the sources in the brain compared to the conventional EEG. Figure 2 shows the spontaneous brain activity of a subject during non REM (Rapid Eye Movement) sleep measured over the occipital lobe of the brain. The four stages of sleep and the corresponding brain rhythms are clearly seen.

Response of the brain to the presentation of external stimuli, like visual, auditory or tactile is very small in magnitude, of the order of 100 fT and can nevertheless be measured. Figure 3 shows the auditory evoked response of the brain to a presentation of 1 kHz pure tone, measured at 128 locations equispaced over the temporal lobe of the brain. The tone was amplitude modulated at 23 Hz (with a depth of modulation of about 95%) and the measured evoked response is the average of a multitude of time locked responses obtained by presenting identical stimuli in succession, using the stimulus presentation instant as trigger.

Reconstruction of sources from the measured magnetic field distribution in both the MCG and the MEG is known as the "inverse problem"; this is generally ill-posed and its solution is expected to provide information on the electrophysiology of the heart during a cardiac cycle in the case of MCG and a glimpse into the way information is processed in the brain in MEG. For a reliable source reconstruction, it is important to simultaneously measure the magnetic field at a large number of positions using a multichannel measurement system. A 19 channel system is presently being assembled; when commissioned, this system will be used to study MCG and MEG in collaboration with cardiologists and neurologists.

Fig. 2 *Brain rhythm recorded in MEG showing the four stages of sleep*
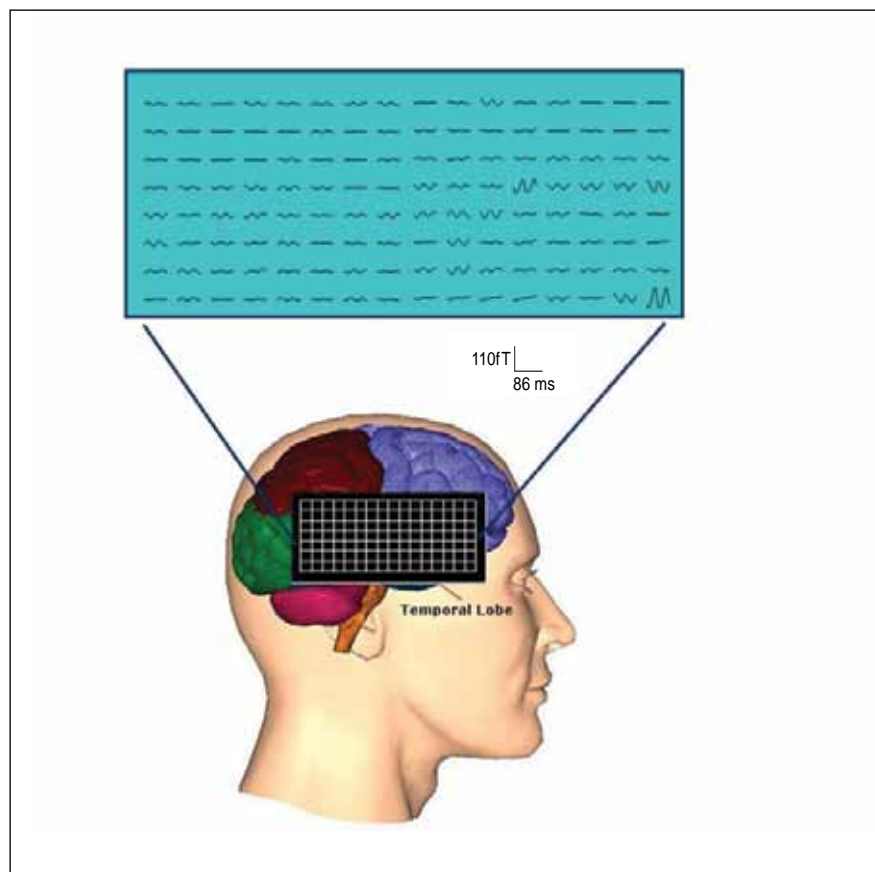
Fig. 3 *Cortical response measured over the temporal lobe in response to an auditory stimulus*

V.21 Embedded Designs for Bio-medical Applications

The advances in sensor technology and read-out electronics with intelligent programmable system on a chip as well as cost effective software application packages supports the novel design approach in many application areas. This article deals with some exciting and challenging new embedded electronic designs for bio-medical investigations to support the human health and enhance the quality of life. It describes about two specific examples, indigenously designed for bio-medical application to support the brain neuron analysis.

Programmable delay timer design for transcranial magnetic stimulator (TMS)

Transcranial motor evoked potentials are used to monitor spinal cord integrity intraoperatively. Magnetic transcranial motor evoked potentials (tcMMEPs) are obtained by stimulation of the motor cortex with a magnetic stimulator. Sri Chitra Tirunal Institute of Bio-medical Science & Technology (SCT), Trivandrum, has a new Transcranial magnetic stimulator, to the motor area of the brain, which produces an evoked response in the hand muscle of a patient, which has to be recorded with an Electromyography (EMG) system. transcranial magnetic stimulator with an electromyography machine has been connected with electrical stimulators to record the evoked response and perform operations such as averaging. Both transcranial magnetic stimulator and electromyography have a triggering input & output, so that each one of them could activate the other depending on the requirement. Some protocols proposed to be used with transcranial magnetic stimulator (TMS) & Electromyography require triggering TMS after a preset delay. Also the functional mismatch between Transcranial magnetic stimulator & Electromyography causes large number of missed triggers leading to technical difficulties (unnecessary exposure of patient to high magnetic fields). The fixed triggering between the magnetic simulator and recorder causes repeated analysis and investigations for patients to observe and record their neuron motor response for the triggered magnetic field. The need for a programmable delayed trigger signal has been identified and implemented for recording the data, after the impulse of a magnetic field as per the user adjustable time delay with respect to the distance of the sensor mounted reference to the simulating point.

This design also configures the input/output specification of the different electronic circuitry between the two independent units, simulator and recorder. An indigenous interface embedded design with a Programmable System on-chip (PSoC) has been implemented to accept any trigger between Transcranial magnetic stimulator and electromyography systems with a very short rise time, and provides proper recording of data with a single attempt. The interface unit has been implemented successfully (Figure 1) with the Transcranial magnetic simulator (TMS) setup at SCT, Trivandrum, and found to be working satisfactorily as per the feedback from the user.
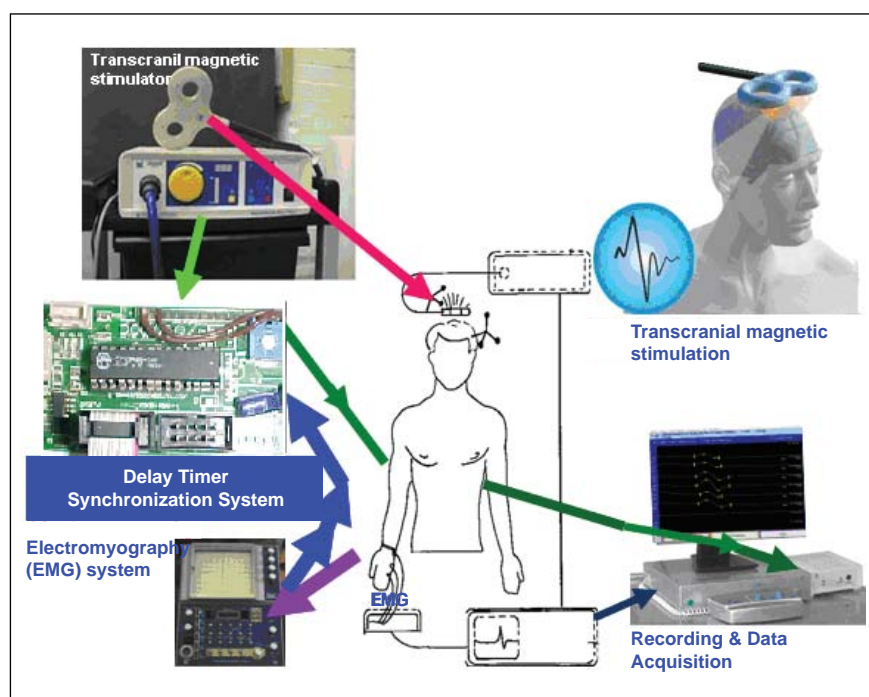
Fig. 1 *Transcranial Magnetic Stimulator (TMS) and Electromyography System (EMG) interfaced with the embedded design for synchronisation in event recording, for research and therapeutics in movement disorders*
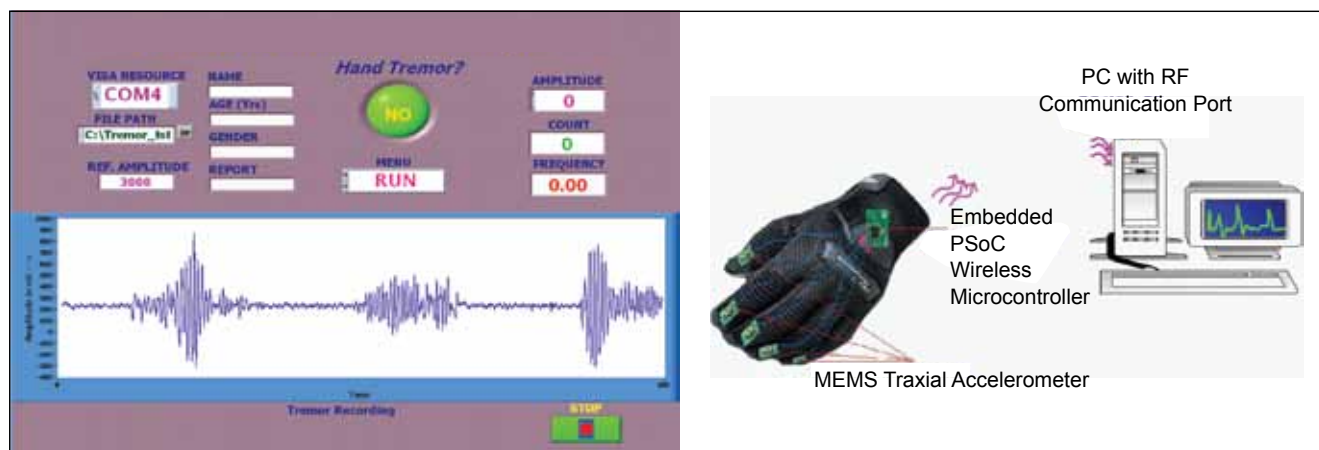
Fig. 2   *Embedded wireless MEMS glove for hand tremor sensing and analysis using commercial MEMS accelerometer (shown in left), a graphical user interface design for acquiring on-line data, on-line analysis and saving the data in a user specified file path (shown on the right)*

Design and development of MEMS accelerometer based wireless glove

Figure 2 shows an embedded design with the commercial MEMS accelerometer based wireless system for hand tremor analysis. A wireless MEMS glove with single axial MEMS sensor has been designed and fabricated to monitor and measure the severity of various movement disorders such as tremor, bradykinesia (slow and irregular movements), gait disorders and dystonia (twisting movements and sustained postures). A wireless embedded design with a Programmable System on Chip interfaced with the MEMS accelerometer and communicate the data in a wireless way to a PC for further analysis.

The virtual instrument program written in LabVIEW, (a graphical language to interact with PSoC embedded design) provides on-line plotting and analysing frequency, amplitude and count with respect to the lower level threshold of vibration to identify the tremor. The designed glove is working successfully and is ready for clinical test and analysis. This design is easy to wear by the patient located in a remote clinical investigation room, 300 meters away from the PC. The supported chargeable battery can work for more than a week when fully charged (with the help of a PC through the USB port).

V.22   Calibration of Phoswich Based Lung Counting System using Realistic Chest Phantom

The low yield of lower energy photons and the severe attenuation of these photons in the chest wall and the rib cage make the monitoring of actinides (Pu & Am) in lungs a challenging one. The variation of chest wall thickness and fat to muscle composition among individuals further complicates the calibration of lung monitors. One needs specialised phantoms for calibration. IGCAR has recently procured a special realistic
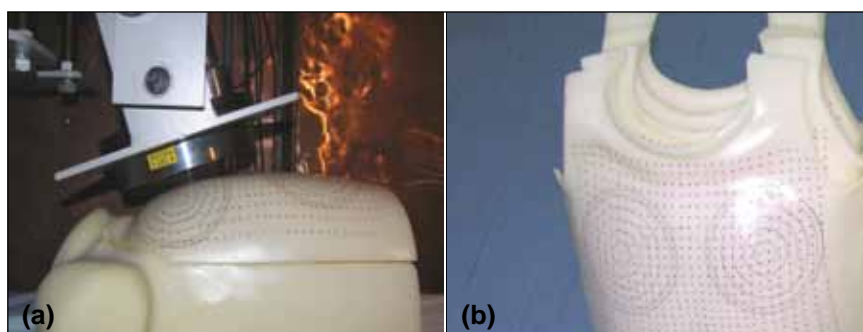
Fig. 1   *(a) Realistic chest phantom and (b) Chest overlays*

chest phantom known as LLNL phantom (Lawrence Livermore National Laboratory) phantom. This phantom (Figure 1(a))

contains various organs of thoracic region, which are made of tissue equivalent materials. This phantom also contains activity tagged lung sets and also chest overlays (Figure 1(b)) of varying thickness and fat / muscle compositions. Using this phantom, phoswich detector has been calibrated with [241]Am activity tagged lung set.

Phoswich lung counting system with PSD electronics

A phoswich system consists of 203 mm dia x 3mm thick NaI(Tl) sandwiched with 203 mm dia x 50 mm thick CsI detector along with pulse shape discrimination (PSD) electronics for effective background counts reduction in lower energies. The system is housed inside a low background shield room.

Realistic chest phantom (LLNL phantom)

The phantom consists of a shell with synthetic rib cage, which is constructed to represent a standard reference man used for radiation protection purposes. It has internal organs such as lung, liver, lymph nodes, heart, and stomach contents, all of them constructed using synthetic substitutes representing human tissues and whose shape and size are as per the standard reference man. This phantom has a top cover plate made out of synthetic substitutes (including ribs). The material of construction of this phantom simulates the attenuation properties equivalent to that of human tissue (with varying compositions of muscle and fat) for low energy gamma photons. The phantom also has three set of overlays with varying muscle to fat ratios, viz., (i) 100% muscle 0% fat, (ii) 50% muscle 50% fat and (iii) 13% muscle 87% fat and four different overlays each combinations with varying chestwall thicknesses (22,
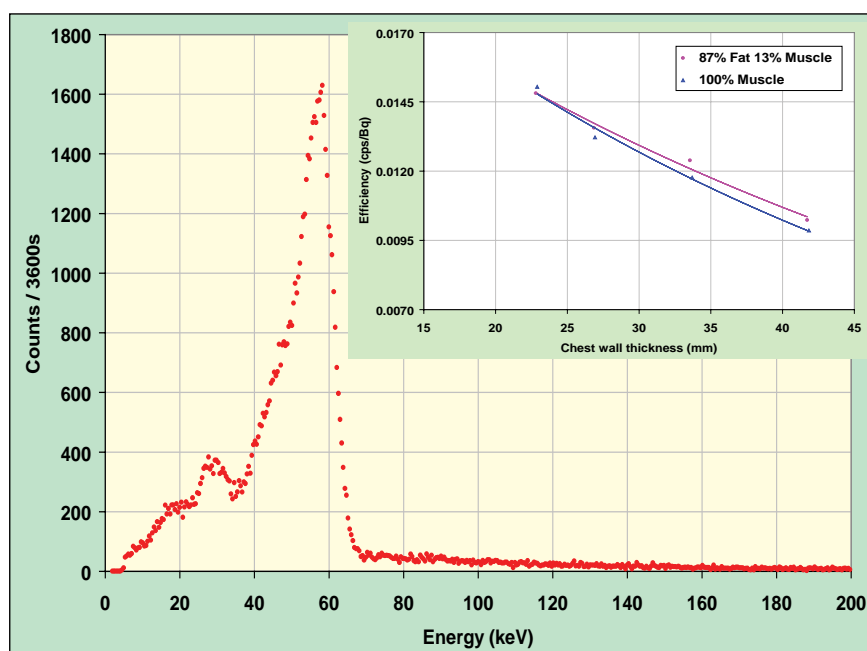
Fig. 2 *Typical spectrum of phantom loaded with [241]Am (Inset) Calibration factor*

27, 32 & 40 mm). The phantom was procured with activity ([239]Pu, [241]Am, natural U, enriched U and natural Th) tagged lung sets and a liver tagged with [241]Am.

Calibration with [241]Am loaded lung set

[241]Am activity tagged lung was placed inside the phantom, keeping all other organs inactive. The measurements were performed with all the overlays of various types and thicknesses. The 59.5 keV gammas were used for the measurement. Figure 2 shows the typical spectrum taken with phantom loaded with [241]Am tagged lungs. The calibration factors obtained are shown in inset of Figure 2.

Activity estimation

Except for freshly separated plutonium, aged plutonium is expected to have [241]Am activity (4 to 8%), which is formed from the [241]Pu. The estimation of plutonium activity can be indirectly done from the measurement of [241]Am activity in lungs. The pre-requisite is the knowledge of plutonium isotopic composition. Using [241]Am as tracer, smaller level of plutonium could be detected. Thus, the established calibration factors will be used to measure Pu/Am contamination in lung. Based on the subject chestwall thickness and the fat/muscle composition right efficiency factors will be selected and used for activity estimation.

Validation

As part of IAEA intercomparison exercise, RSD has received similar type of lung phantom called JAERI phantom with undisclosed amount of americium activity. Using the present calibration factor the activity in the JAERI phantom is estimated to be 498 Bq. The actual activity present in the phantom is 420 Bq. This comparison ensures the validity of our calibration factor and procedure.

The state of the art calibration tool for lung counting system, Realistic Chest Phantom, was procured first time in our country. This helped us in establishing calibration factors for the measurement of plutonium and amerecium in lung.

V.23   In-Situ Mussel Shells Open-Close Status Detection and Logging System

Chlorination has been proven as the suitable biofouling control method and has been widely used in industrial establishments using water as coolant for various cooling purposes. Of the various methods of chlorination, pulse chlorination has been proposed as an effective tool for controlling bivalves, such as mussels. Green mussel is one of the major fouling species at MAPS (70%). As soon as it senses chlorine it closes its shells and so also filtration, a process solely responsible for feeding and respiration of these organisms. They tend to open their shells after a certain period of time and immediately closes if the chlorine presence in the water continues. This is an effective method for avoiding its growth and settlement. However, instead of chlorinating continuously, chlorine can be injected at intervals coinciding with the closing and opening intervals of the mussel shell (pulse chlorination) to take advantage of this behaviour. Knowledge on this time interval between closing and reopening of the mussels will be useful for deciding the optimum frequency of pulse chlorination so that operational cost and environmental damage due to chlorine is minimised. However, this interval is not generic and information on the

same is not available in literature. A microcontroller based system is designed to detect and log these time intervals.

Various sensor choices were analysed to detect the shell movement of mussels. The ohmic contact sensing method may fail due to insufficient pressure made on the contacts by the mussels and rusting due to corrosiveness of sea water in which mussel. Inductive techniques attempted by earlier researchers, were also tried during this experiment. But the signal chain required to bring the information to the digital domain in the above technique is lengthier. So a magnetic reed relay along with a tiny magnet is exploited to detect the shell movement of mussels.

A magnetic reed relay with polypropylene encapsulation is used for corrosion resistance and water proofing. It is a miniature reed relay, which is activated when it is exposed to magnetic flux. One shell of the mussel was attached with the magnetic reed relay and the other shell was attached with a small magnet of size 3 mm diameter and 1 mm height. Both the reed relay and the magnet are very light weight items. The magnetic coupling between the magnet and the reed

relay becomes stronger when the shells are in closed position and the relay is activated. When the mussel starts opening its shells the magnetic coupling become weaker and it deactivates the reed relay. The relay and the magnet were connected with the mussel shells through a paper clip and a plastic wire respectively (Figure 1). The switching distance between the relay and the magnet can be adjusted by bending the plastic wire. Enamelled copper wire was used to interconnect the reed relays with the circuit. Since it is a coil winding wire, having thin cross section, the stress on the relay arrangement affixed on to the mussels would be minimal. To withstand the sea water environment such an enamel wire is used. The soldered parts of the reed relay with the interconnecting wires were sprayed with an 'electrical resistive and anti corrosive coating' to prevent them to make any electrical contact through the sea water. The magnet is also sprayed with anti corrosive coating.

The detection and acquisition system is shown in Figure 2. It is designed around PIC16F877A microcontroller. It is a microchip product that follows flash technology. The 'Normally

Fig. 1   *Open-close detection system deployed on a mussel*
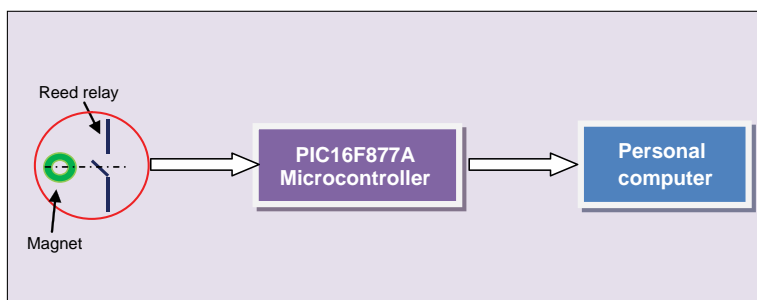
Fig. 2   *Block diagram of the mussel shell position detection and logging system*

Open (NO)' contact of the reed relay which is mounted on to one of the shells of the mussel is connected between the +5V power supply and the I/O port pin of the microcontroller. Relay outputs from up to ten mussels can be connected with specific I/O port pins. Whenever the shells of any mussel closes, the appropriate relay is activated and +5V will appear at the port pin. The program scans the ports to get the information from the mussels. The inbuilt hardware USART is programmed to send this information to the host PC through RS232 communication channel. The communication speed is set at 9600 bits/sec with odd parity check. The MAX232

chip is used for converting TTL to RS232 level converter. The microcontroller is programmed by CCS-C compiler. The host PC is programmed in LabView7.1, graphical programming language.

The experimental run on this investigation may prolong for more than two days. Thus continuous data acquisition may require a large memory to hold the data. To avoid this, acquired data is compared against the previous data. If the comparison indicates no change in the mussel shell status, then the data will be discarded. Any change in the incoming data compared to the previous one is resultant of the change in the
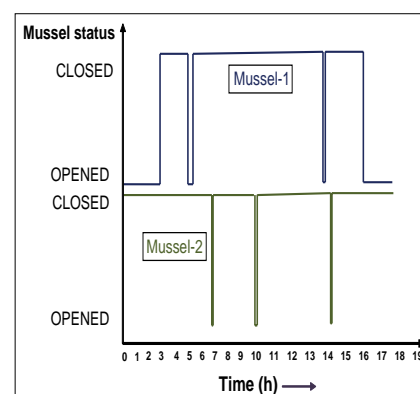
Fig. 3 *Status of mussel shells in the time scale*

shell position of the mussel, and hence that data will be stored. The resultant data contains information about change in valve positions of mussels with respect to time as shown in the Figure 3.

V.24 Studies on Precipitation Reaction using Conductometric Technique

High performance conductivity monitoring system using pulsating sensor was used for basic understanding in precipitation reaction. A well known precipitation reaction (reaction of KCl and $AgNO_3$) was chosen to demonstrate the concept. Different processes involved in precipitation reaction were clearly understood from online conductometric titration plot using a high resolution conductometric titrator developed in-house.

An online titration plot using our indigenously developed titrator for precipitation reaction of KCl and $AgNO_3$ is shown in Figure 1. A slight decrease in conductivity before the end point is due to replacement of chloride ion by slightly less mobile nitrate ion. When titration was carried out using very dilute reactants the nature of the titration

plot completely changed as shown in Figure 2. The conductivity shows a gradual increasing trend to attain a maximum value beyond which it starts decreasing and again it shows rapid increasing tendency due to accumulation of unreacted $AgNO_3$. In order to understand this phenomena, titration was carried out by manual addition of $AgNO_3$ in small steps of volume (20 µL steps) using a Hamilton syringe. The shift in conductivity which showed the progress of reaction was captured online. Figure 3 shows a real time conductivity plot both in time and volume domain during addition of $AgNO_3$ to KCl. It is interesting to note that the region-1 of Figure 2 is composed of two linear regions. Since the titration was carried out using very dilute solutions the ionic product in first few additions was
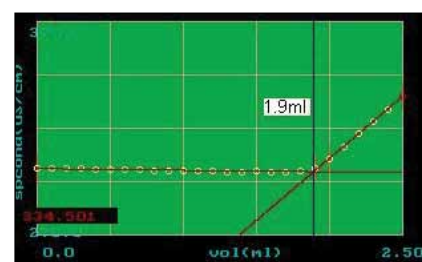
Fig.1 *A typical online conductometric titration plot for precipitation reaction of $AgNO_3$ and KCl, [Cl^-] : 28 ppm Cl^-.*

below the solubility product of AgCl. Hence AgCl was not precipitated. The increase in the conductivity in region-1 of Figure 3 was due to AgCl which remained in ionic form. The slope change at region-2 was due to super saturation, a meta stable state, where nucleation started. Due to super saturation associated with nucleation a major part of AgCl remained in solution
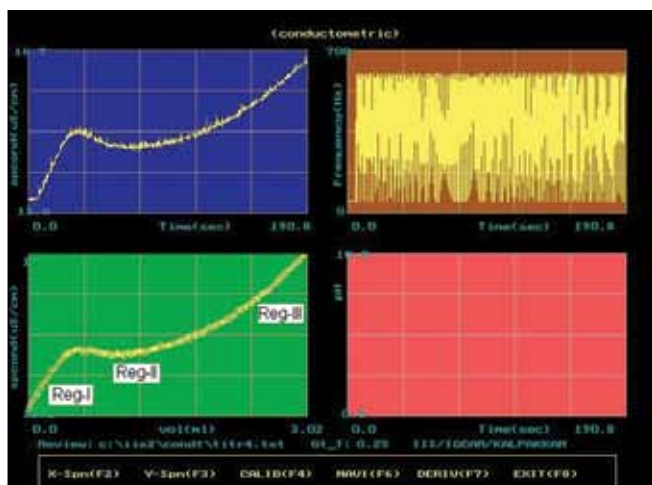
Fig. 2   *Online titration plot of a precipitation reaction using very dilute reagents. (KCl versus AgNO₃, 35 ml 0.07 mM KCl titrated against 1 mM AgNO₃)*

Fig. 3   *A real time conductivity plot both in time and volume domain during addition of 1mM AgNO₃ to 35 ml of 0.07 mM KCl in 20 micro litre steps*

and a few minute AgCl particles participated in nucleation. Hence the rate of increase in conductivity at region-2 was less than that at region-1 in Figure 3. The conductivity increased and attained a maximum value which implied that the growth of nucleation was progressively increased in region-2. After attaining a maximum value

the conductivity showed a sudden decreasing tendency as shown in Figure 2. This is due to the sudden destruction of meta stable stage and initiation of precipitation. The commencement of super saturation and precipitation is easily traced from real time conductivity plot. Besides understanding the phenomena during precipitation

reaction, a new approach on determination of solubility product was evolved from this work. From the concentrations of silver and chloride ions corresponding to the beginning of super saturation region (refer point 'S' in Figure 3) the solubility product of AgCl was evaluated which agreed well with the literature data.

V.25   Redox Titration at Trace Level

Potentiometric titration even at a few ppb (µg/l) level concentration is realised by using 'rapid titration facility with pulsating sensors' developed in IGCAR. The measurement approach followed for high precision and high resolution (sensing a shift in potential of 0.1 mV) potential measurement in an electrochemical system is described below.

The *electrochemical motive force* of a chemical system, sensed across two appropriate electrodes dipped

in solution within a cell, is directly converted to digital pulse frequency using a specially designed *V to F* converter. The frequency at any given time is related to the *electrochemical motive force* at that instant. Pulses are counted for a given duration through a personal computer or in some case by using an external pulse counter for determination of frequency at desired intervals, and thus one can follow the time dependent change in *emf* caused by progressive chemical reaction with a reactant. For rapid titrations, the reactant is

added in quick succession using a laboratory made solution dispenser or for very accurate analytical work using a Hamilton syringe. One channel follows the real time change in potential during titration whereas the other channel keeps track of the drops, simultaneously, for automatic generation of reactant volume versus *electrochemical motive force* data. Titrations, including data unfolding for precise end points, are usually completed within a couple of minutes.

The potential of this innovative measurement approach is

demonstrated in two well-known systems (i) assay of dissolved oxygen and (ii) assay of residual chlorine in aqueous solutions at ppb level. Winkler chemistry is strictly followed for assay of dissolved oxygen in which after proper chemical treatment the liberated iodine is titrated against standard sodium thiosulphate solution. The high resolution potentiometric measurement technique evolved in this Centre could capture the change in potential at the end point in solutions containing dissolved oxygen at a few ppb level. Due to evolution of this primary analytical technique for dissolved oxygen at sub-ppm and at a few ppb level, it is proposed to adopt this offline titration technique for calibration of online dissolved oxygen analysers commonly used in nuclear power stations. A sample containing dissolved oxygen down to 10 ppb with RSD 1.5% was easily measured by following this technique. A schematic diagram of the titration facility is shown in Figure 1. The marine chemists and the environmental scientists always look for a simple and reliable technique for determination of residual chlorine in water. In nuclear power plant where sea water is used as coolant in condenser, frequent monitoring of residual chlorine is needed to have a control on chlorine dosing. Considering this requirement a simple user friendly REDOX titration technique was evolved using pulsating potentiometric titrator. The method involves the oxidation of iodide by residual chlorine to generate iodine which is further titrated by using sodium thiosulphate. Though the technique is widely used as a primary method for assay of chlorine in several ppm level, due to evolution of our high resolution pulsating potentiometric titrator it is possible to develop appropriate methodology for analysis of
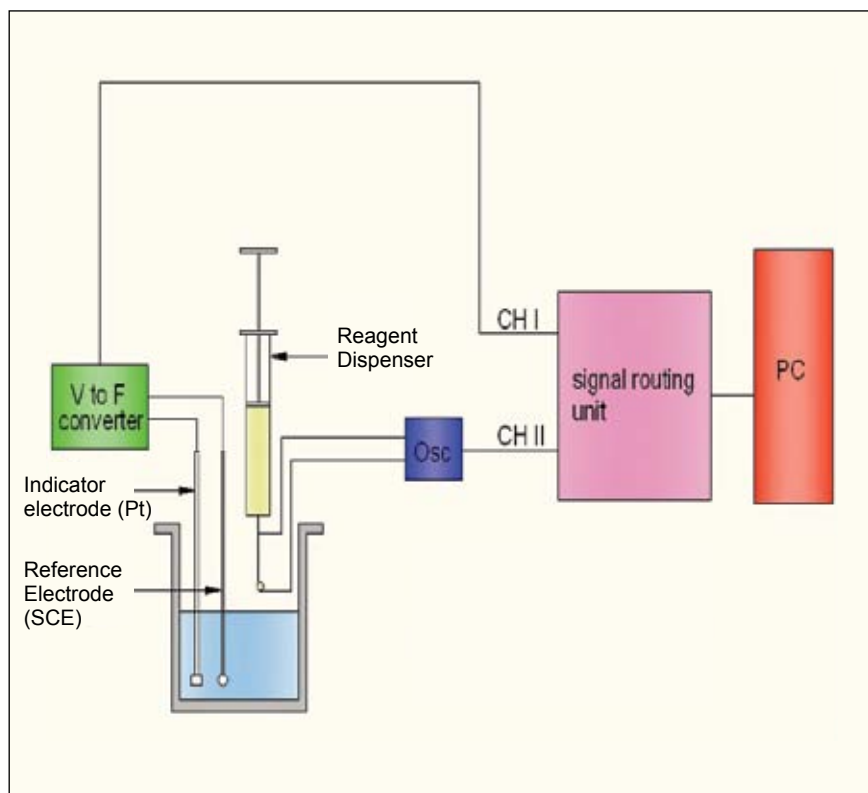
Fig. 1 *Schematic diagram of potentiometric titration facility with pulsating sensors*
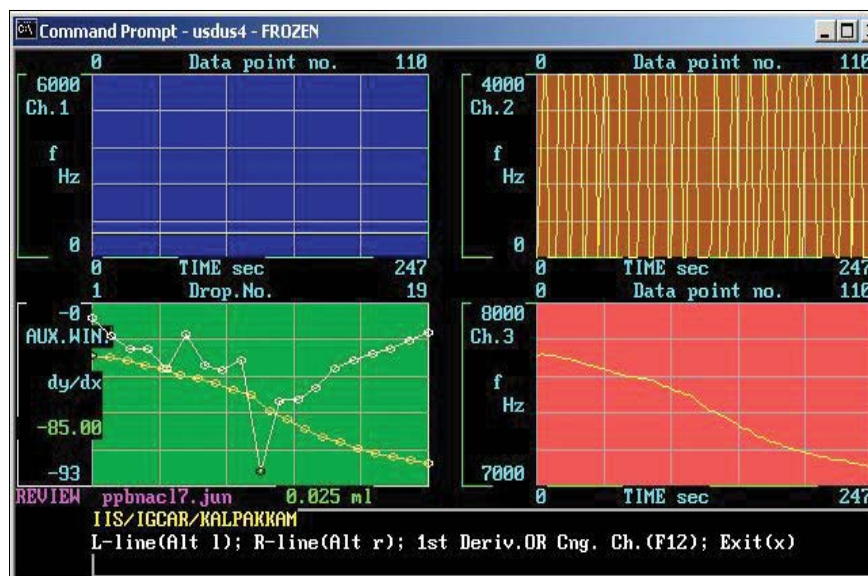
Fig. 2 *Online titration plot for assay of residual chlorine in 3% NaCl matrix at 35 ppb level (Ch.2 : discrete steps of addition of standard $Na_2S_2O_3$, Ch.3: Real time titration plot, Ch.4: Titration plot and corresponding first derivative plot to get information on end point)*

residual chlorine at ppb level. Water sample containing residual chlorine down to 25 ppb (RSD 1%) was easily analysed by using this novel technique. Rare information is available for assay of chlorine at such a low level even by using other optical techniques reported in literature. Figure 2 shows an online titration plot and its first derivative plot for assay of chlorine at ppb level.

V.26 Towards Development of a Novel Technique for Void Fraction Measurement in Coolant Circuit of PHWR

Detailed research and development work is in progress to bring out new PHWRs of 700 MWe capacity in which about 4 to 6% steam will be available in primary coolant circuit. Moreover, a new class of reactor such as Advanced Heavy Water Reactor is likely to come up in near future in which the primary coolant circuit is designed for about 18% steam. Hence, in such type of reactors it is essential to have online monitoring of void fraction (VF) during reactor operation from the safety point of view.

Towards this direction a PC based plug-and-play type stand-alone real-time system with very little auxiliary hardware has been developed for on-line determination

Fig. 1 *Photograph of a typical conductance probe mounted vertically in test section of SF*

of void fraction in steam-water system. Initial laboratory studies were conducted by designing appropriate pulsating conductance sensor to respond rapid changes in conductance as the compressed argon gas from a cylinder was passed into water taken in a specially designed perspex cell. A pair of stainless steel electrodes vertically mounted on it sensed conductance both in homogeneous water phase and in heterogeneous water and gas phase. The sudden drop in conductance was due to accumulation of voids created during passage of compressed gas into water.

The digital pulses as the primary signal, which are generated by direct conversion of conductance to frequency with the help of a laboratory made miniature device, are fed to a PC directly through its parallel port without any add-on card. The pulse frequency at a given moment carries information with respect to the voids in heterogeneous phase at that instant. With successful achievements in measurement of voids in water–air mixture, further experimental campaigns were conducted in steam–water system of a specially designed simulated
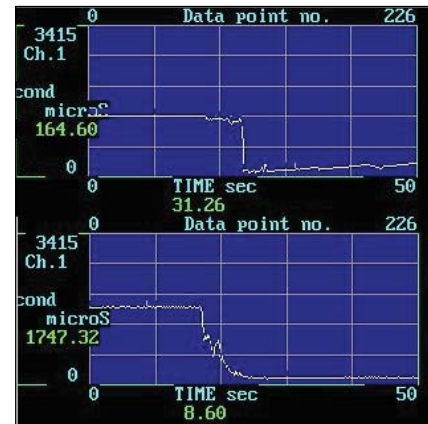
Fig. 2 *A screen capture view during a hot run in SF (above) by suddenly opening and (below) by gradually opening the valve*

test facility at Jadavpur University (JU), Kolkata. Experiments were carried out in two different test conditions (i) Cold run – at room temperature, 90 bar pressure (ii) Hot run – at 523 K, 90 bar pressure. Encouraging results obtained from the above campaigns inspired us to carry out this activity to meet the actual reactor requirement. Figure 1 shows the photograph of conductance probe used in test section of simulated test facility. The results in a typical experimental campaign are shown in Figure 2.

V.27 Heat Evolution of Flyash Concrete

In nuclear power plant structures mass concreting is required in sections such as foundation, RC walls etc. As the hydration of cement is exothermic and thermal conductivity of concrete is relatively

low, it acts as an insulator, and in the interior of a large concrete mass, it results in a large temperature rise. While cracking due to heat of hydration can not be altogether avoided, it is possible to limit the crack width by replacing one big crack with numerous small cracks distributed along the full dimension of the section by providing reinforcement where tensile stresses are developing. This procedure is highly uneconomical and laborious and construction time is affected, leading to highly congested reinforcement. Addition of mineral admixtures such as flyash and there by reducing the total quantity of heat generated is a most viable option.

Using flyash replacements at varying mix proportions specimens were developed in two categories viz. M50 and M35 grades of concrete. They were given designations such as 585F50 where

585 denotes the total binder weight in kilograms and F50 denotes 50% replacement of cement by flyash, aggregates of coarse and fine sands were apropriately used. Field tests were conducted to measure and compare the heat of hydration in concrete specimens of control concrete mix(mix without flyash) and fly ash concrete.

Calibrated resistance thermometer detectors (RTD) were placed and temperature data was measured at every one hour interval for first 72 hours and then every 2 hours up to a period of 7 days. Atmospheric temperature and relative humidity were also noted at same frequency as mentioned above. Observations are graphically represented in Figure 1.

The results showed reduction in peak temperature rise in mass concrete to the extent corresponding to the amount of
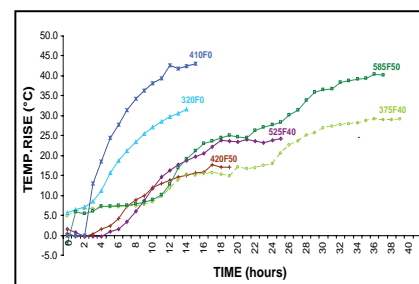
Fig. 1 *Age of peak curves for M50 and M35 grade concrete*

replaced cement. Flyash typically reduce the rate of strength gain, lower the heat of hydration, reduce the rate of stiffness development and thereby typically reduce the potential for cracking.

Hence, the flyash concrete can be utilised for the construction of Nuclear Power Plant structures, thereby reducing the congestion of thermal reinforcement, increasing the lift dimensions etc. leading to economy and ease of construction.

V.28 Variations in Phytoplankton Community Structure in The Coastal Waters of Kalpakkam

Phytoplankton, the microscopic plant components of aquatic system constitutes the most vital component of the biological community as primary producers. In marine ecosystem, about 95% of the total primary production through photosynthesis is contributed by the phytoplanktons. The plankton flora comprises of diatoms, dinoflagellates, cyanobacteria, silicoflagellate etc. however, diatoms dominate the phytoplankton assemblage. For assessing the fisheries yield, it is important to have knowledge on phytoplankton abundance and

variability. In addition, phytoplankton assemblages are often used as the indicators of water quality including pollution. Moreover, baseline data on phytoplankton assemblage is of prime importance to evaluate future impact studies. In view of this a study has been undertaken to assess the qualitative and quantitative aspects of phytoplankton community in the coastal waters of Kalpakkam around which, a hub of industrial activities are in progress. Seawater samples were collected weekly for a period of two years from the coastal waters and phytoplankton enumeration and identification

were carried out following standard procedures.

The results showed a considerable increase in the number of phytoplankton species (216 species) as compared to the earlier reports (60 species). Well pronounced fluctuation (about ten times) in phytoplankton density was observed during the course of present study with a minimum density 0.43×10^5 cells l^{-1} in the month of March and maximum 1.5×10^6 cells l^{-1} in August. A reduction of 4-10 times in population density was observed as compared
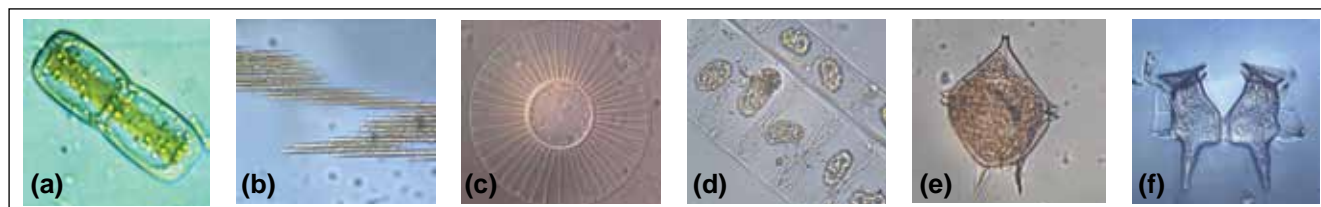
Fig. 1 *Phytoplanktons observed during various seasons (a) Amphiprora paludosa (b) Bacillaria paradoxa (c) Peridinium pallidum (d) Dinophysis caudata (e) Planktoniella sol and (f) Bellerochea malleus*

to the earlier reports, possibly due to increase in turbidity level during the post-Tsunami period, which might have hindered the light penetration in the water column leading to low phytoplankton production. Heavy phytoplankton proliferation was observed during summer and pre-monsoon period, which might be due to relatively stable as well as optimal conditions of salinity, temperature, light and nutrient levels prevailed during summer and upwelling and vertical mixing that occurs during pre-monsoon (August – September). However, prevalence of relatively high concentration of nutrients (phosphate, nitrate, silicate) during monsoon months could not support the growth and proliferation of phytoplankton. During this period, low salinity, low light penetration, high turbidity and low temperature inhibited phytoplankton growth in spite of abundant availability of nutrients. A positive correlation between phytoplankton and salinity indicated the prime role of salinity in controlling the phytoplankton community structure among various other parameters at this location. During summer and pre-monsoon period, the nitrogen: phosphorous (N:P) ratio remained low as compared to normal 16:1 (Redfield's ratio), which indicated that phytoplankton consumed nitrogen preferentially to phosphorous. During monsoon period the N:P ratio were relatively high which is indicative of the terrestrial contribution of nitrogen as well as its non-utilisation. Silicate:

nitrogen (Si:N) ratio showed higher values than the Redfield value (1:1), which indicated that silicate was not limiting for the production and development of phytoplankton, especially for diatoms. Similarly, silicate: phosphate (Si:P) values were also very high (compared to Redfield's ratio – 16:1) indicating the insignificant role and high bioavailability of silicate for primary production in this coastal water. In conclusion it is the nitrogenous nutrients which could limit the phytoplankton growth and proliferation at this location.

Between the two forms of diatoms, centric (mostly floating forms) and pennate (mostly attached forms), pennates (Figure 1(a) and 1(b) dominated the plankton community during pre- and post-monsoon periods. However, during monsoon period, centrics (Figure 1(c) and 1(d) dominated over pennates. In general, dinoflagellates dominated the coastal waters next to the diatoms. Among dinoflagellates, *Prorocentrum micans* and *Protoperidinium* sp (Figure 1(e) and 1(f) were commonly observed, but as expected their percentage contribution was very meager as compared to the diatoms. Dinoflagellates are more mobile and more buoyant than diatoms as they have two pronounced flagella. Moreover, they are dominant producers in calm and downwelling waters. Considering the fact that coastal zone is very dynamic and turbulent as compared to oceanic waters, dinoflagellates were very scanty in the coastal waters.

Another important feature of this study was the characterisation of transition period by phytoplankton. Transition is a period during which the water mass neither moves south nor north. It almost remains lull. This occurs when monsoonal wind changes from south to north and vice-versa, and associated with it a change in coastal water current direction takes place. The present study describes the transition period, when water current changed from north to south. There are two types of water masses during this period, i.e. southern sub-surface water, which flows from south to north and northern surface water, which flows reverse of SSW. No phytoplankton species was observed as indicator of southern sub-surface water in the present study, in contrast to earlier report. Significant decrease in phytoplankton density (pre-transition- 1.38×10^6 cells l^{-1}; transition - 0.52×10^6 cells l^{-1}; post-transition - 0.15×10^6 cells l^{-1}) and number of phytoplankton species from pre-transition (127) to transition (109) followed by post-transition (76) were observed. Present study indicated that, species abundance could be an indicator of the presence of different water mass in the coastal waters of Bay of Bengal. Presence of *Eucampia cornuta* indicated the transition lull period and presence of *Skeletonema costatum*, *Chaetoceros curvisetus* and *Pseudonitzschia delicatissima*, indicated the arrival of northern surface water.

CHAPTER VI

Infrastructure Facilities

VI.1 Advanced Visualisation Centre – Innovation in Seeing and Simulation of Reality

Visualisation has been used as an effective tool for understanding or to communicate ideas ever since the existence of humans in the globe. Now, in the era of communication and information technology, visualisation techniques have grown by in leaps and bounds. In our Centre we are designing and developing complex nuclear reactors such as Fast breeder reactors and therefore, it is essential to have a facility which will facilitate in design, construction, maintenance of breeder reactors limiting not only to reactor but also for any other complex visualisation system. With this objective, a world class fully immersive advanced visualisation centre has been setup to visualise the models of fast breeder reactors and associated fuel cycle facilities.

The design drawings have come a long way from the earlier drawing boards using T-squares to the present 3D–modelling softwares. The models designed in 3D software being seen in normal displays will not give the 3rd dimension fully. To enable depth perception of 3D models, these models are split into two images one for left eye and another for right eye and thus present them to each eye, accordingly which is achieved using stereoscopic display systems, to make the environment fully interactive and immersive, virtual hand with force feedback systems are used.

Advanced visualisation system

The advanced visualisation centre has been set up at Computer Division. It has a seating capacity of twenty persons. A special silver coated screen of size 16'×9' has been mounted. The display technology uses a passive circular polarised stereo projection. Two high definition projectors of resolution 1920 x 1080 pixels and 6500 luminance have been installed. The entire room is acoustically treated for complete immersion. A powerful high-end graphics workstation with dual graphics cards supporting stereographic with 3GB of video memory to process any large set of graphical data has been connected to the projector through a video processor. Variable luminance lighting system has been provided. All the equipments are connected to a wireless touch panel control system for smooth operation of the system. For excellent clear sound effects digital 2.1 sound systems has been integrated. To view the models (Figure 1) specific visualisation software has been installed in the workstation for 3D projection as well as for integrating with the hand glove and force feedback system.

For interactive and immersive applications virtual hand consisting of hand glove and force feedback system has been configured and installed. Using this, a person can touch, grasp and get a feel of the physically defined objects inside a plant which will be useful for commissioning and maintenance of the plant (Figure 2).

Applications

- *Fully immersive plant walkthrough*
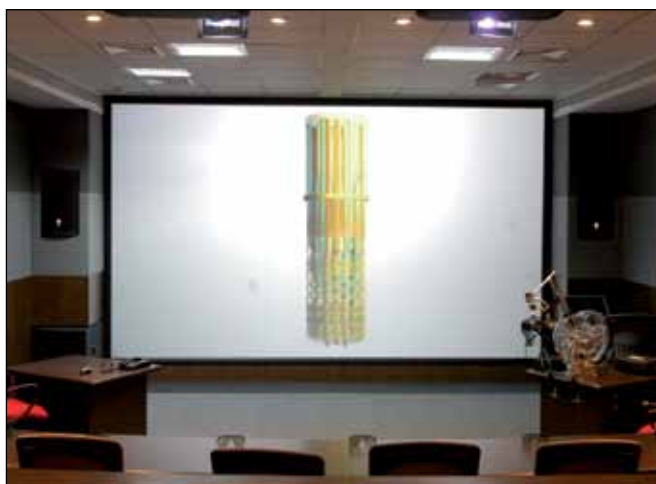
Fig. 1 *Visualisation display of 3D model of PFBR control plug*
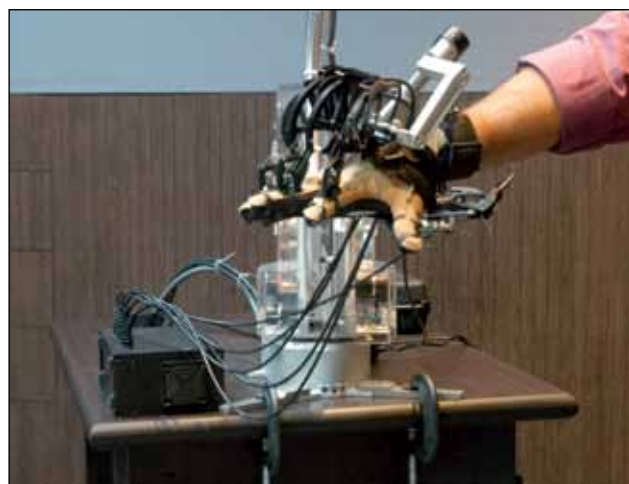
Fig. 2 *Cyber glove with force feedback device*

Basic walkthrough of a plant including many human-centered activities can be simulated in full one-to-one scale, such as navigation, orientation, object identification and manipulation.

• *Scientific data visualisation*

The scientific data like geological modeling, Finite Element Method data from simulation or experiments can be viewed to allow the exploration, analysis and understanding of the data.

• *Training*

Virtual Reality walkthrough of a plant can be used for training operators/ engineers about the entire plant which will serve as a bridge between theory and operations.

• *Design review*

A mock design review could be performed looking for any errors and inconsistencies. For example, enough space might not be there for making a weld in a pipe.

• *Construction review*

Construction activity review can be done by turning on/off of the respective models and see the progress of construction of a plant.

• *Equipment installation*

Interactive installation sequences of complex large equipments can be studied.

• *Maintenance training*

The system can be used as a maintenance training and simulation tool.

VI.2   HEPA Filter Testing Laboratory

HEPA Filter Testing Laboratory (HFTL), was commissioned in the year 2008 and is dedicated to test HEPA filter banks of active facilities of the centre. A test rig facility is also functional for undertaking the testing of individual fresh HEPA filters as per IAEA technical series 122 (Figure1). The test rig is mainly used for pre-procurement testing of HEPA filters and testing of procured filters by various facilities before installation in the filter banks.

HEPA filters along with pre-filters are assembled in a frame work to constitute a filter banks capable of handling the requisite quantity of air. The performance of the filtration system may be impaired due to leakage paths between the filter gaskets and the frame at various stages. Therefore, though the filters are tested randomly for their particulate removal efficiency at the time of procurement, it becomes mandatory to test the filtration

Fig. 1   *HEPA filter testing rig*

system in-situ at regular interval to ensure that it meets the regulatory requirements laid down in the technical specification document of any plant.

The laboratory since inception has undertaken in-situ testing of HEPA filter banks of all the active facilities and Iodine filters of FBTR periodically.

In addition to regular testing, special works like testing of Deep Bed Filters of Reprocessing Development Laboratory were undertaken successfully without much personnel exposure and any contamination incidents (Figure2). On receipt of the request, steps were initiated immediately to undertake the testing of deep bed filters while at the same
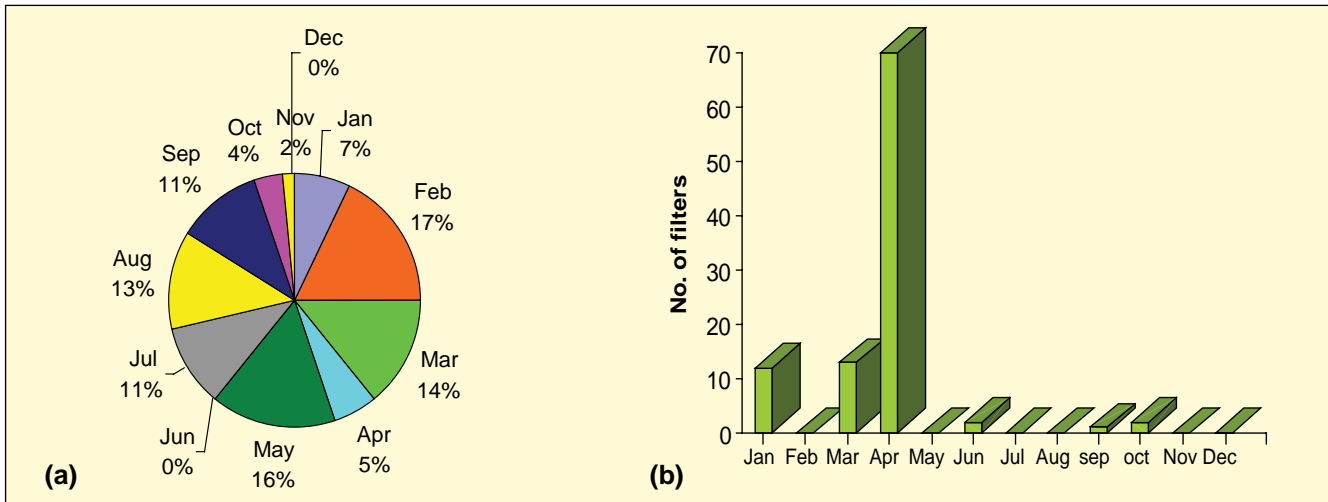
Fig. 2   *Test conducted during Jan-Oct 2009 (a) In-situ test and (b) Rig test*

time avoiding the contamination of particle counter. To avoid the contamination of 'particle counter' while testing, it was decided to check the downstream particle counts from deep bed filters after calibrating the upstream counts at the HEPA laboratory itself. This problem was overcome by suitably calibrating the aerosol generator to produce aerosol particles at particular number concentration by using same air velocity of the DBOG blower.

HEPA filter testing laboratory personnel have undergone explicit training for, carrying out HEPA filter testing as well as Iodine filter testing and they are duly qualified with certificate after the examination conducted by the Superintendent, Air Cleaning Services, CWMF, and Plant Superintendent, CWMF, Kalpakkam. The quality anagement system of HFTL adopts four levels of documents viz. Level 1: Quality Manual, Level 2: Quality Procedure,

Level 3: Work Instruction and Level 4: Quality forms. A clear documentation procedure is adopted for the receipt of the requests from various laboratories and reports of the filter testing by the lab. With a view to further improve our quality oriented services in line with international standards, we are aiming for the accreditation from NABL (National Accreditation Board for testing and calibration laboratories).

VI.3 Design of 1MeV Radio Frequency Quardrupole linear Accelerator for $^9Be(d,n)^{10}B$ based Pulsed Neutron Source

IGCAR requires a compact neutron source for applications such as active neutron interrogation of the hull and radioactive waste, benchmark shielding experiments, neutron activation analysis of very short-lived reaction products and study of trace element. A compact Radio Frequency Quadrupole (RFQ) LINAC based pulsed neutron source is being built using $^9Be(d,n)^{10}B$ reaction for the neutron

flux of the order of 10^9 n/s as shown in Figure 1.

The deuterium ions produced by an ion source having initial energy, 25 keV, will be accelerated by the radio frequency quadrupole linear accelerator to the final energy of 1MeV and bombarding on Beryllium target results in neutron beams. The radio frequency quadrupole is a linear accelerator which focuses,

bunches and accelerates the ion beam simultaneously using RF field. The sequence adopted for the design of RFQ accelerator is as: beam simulation → 2D vane simulation → 3D vane simulation
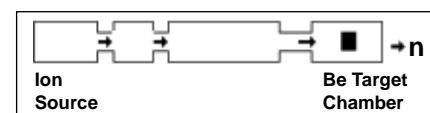
Fig. 1   *The schematic diagram of neutron source*

→ Thermal analysis → Fabrication drawing. For each steps different computer codes have to be used to simulate and optimise the radio frequency quadrupole vane/beam parameters. The radio frequency quadrupole beam simulation and the 2D vane shape simulation have been completed and the radio frequency quadrupole 3D vane shape simulation is in progress. The specification of the neutron source is summarised in Table 1.

Radio frequency quadrupole bean simulation and analysis

The challenge in the radio frequency quadrupole beam dynamic simulation is its short length with following constraints: (i) maximum possible transmission efficiency (>95%) with no localised beam energy loss distribution (ii) minimum radio frequency quadrupole length (~1.2m) (iii) acceptable ratio between the beam radius and the minimum bore radius less than 0.9 (iv) E_{kilp} not more than 1.8 and (v) less energy spread with minimum emittance growth. The radio frequency quadrupole beam simulation has been carried out with the code LIDOS.RFQ. The graphical approach is used to optimise Radio frequency quadrupole parameters for the beam simulation. The general method to optimise the RFQ beam simulation is the conventional approach given by the inventor Kapchinskiy and Tepliakov. With the conventional approach the radio

frequency quadrupole has been found to be of 1.65 m length using E_{klip} of 1.8 and having transmission efficiency more than 90%. For the same input parameters beam simulation has been optimised with the non-conventional approach in which the focusing strength is varied from zero to a maximum and then decreases so that the average focusing parameter is almost same as that of the conventional approach.

Using this non-conventional approach, the radio frequency quadrupole has been designed with same length (1.65 m) but higher acceleration efficiency (95%). There are mainly two ways to reduce the length of radio frequency quadrupole for same transmission efficiency: (i) using higher E_{klip}, (ii) using ion source of low beam energy and emittance. The various options for optimizing the radio frequency quadrupole beam simulation have been summarised. The beam simulation with the lower input beam energy is most suitable design for a compact 1 MeV radio frequency quadrupole design (Figure 2). However the beam acceleration efficiency (92.7%) is lower than the beam acceleration efficiency (95%) obtained for the simulation with higher input beam energy. In order to get the same beam current at the target, the input beam current has been enhanced in the beam simulation to 15 mA from 10 mA. In the error analysis, the

Table 1 : Neutron source	
Parameter	**Value**
Accelerated beam	Deuterium ion
Input/Output beam energy	0.025/1MeV
Beam current	10mA-15mA
Pulsed width	100 μ sec
Repetition rate	10Hz
Duty factor	10^{-3}
Neutron yield	10^9n/sec

transmission efficiency is analysed for the deviation of various radio frequency quadrupole parameters such as input beam energy and current, Radio Frequency source frequency and vane voltage using the code LIDOS.RFQ.

RFQ 2D vane design

SUPERFISH code is used to optimise the two-dimensional transverse vane geometry. The radio frequency quadrupole vane shape geometry has been optimised for the maximum Q-value, minimum power loss and less E_{klip}. The vane voltage of 50.1 kV and bore radius 1.95mm (obtained from LIDOS) used as input of SUPERFISH, the radio frequency quadrupole vane is designed. The dipole mode frequency obtained from SUPERFISH is 343.66MHz. Figure 3 shows the 2D transverse RFQ vane with the quadrupole mode field distribution.
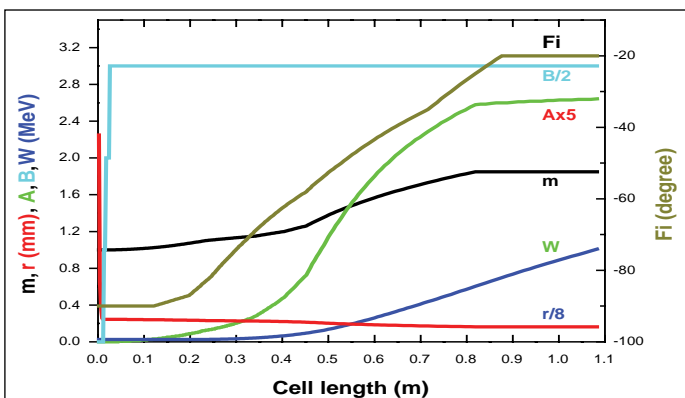
Fig. 2   *Variation of parameters with RFQ length*
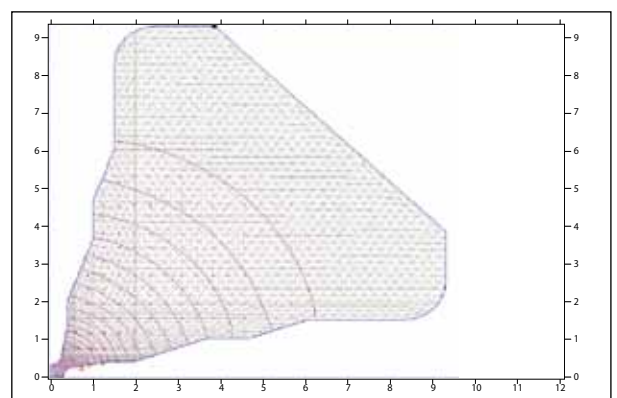
Fig. 3   *RFQ 2D vane shape with electric field lines*

159

VI.4 In-house Development of Radiation Monitor using Dual Phosphor

In a nuclear facility, area and personnel monitoring, play a key role in restricting the radiation exposures to ALARA (as Low As Reasonably Achievable) for occupational workers. Due to the high potential for contamination of α, β and γ in reprocessing plants, a variety of detectors are used. For example, ZnS (Ag) detector is used for α and GM detectors for β and γ are normally used. Instead of using two separate monitoring systems, a dual phosphor system based on plastic scintillator for monitoring both was conceived. This concept reduces the number of instruments as well as the surveillance and maintenance load. Such radiation monitors are not available in India though are commercially available abroad.

The pulse outputs from photo multiplier tube were analysed using a newly designed pulse discriminating logic circuit; on the basis of different pulse heights for α and β,γ the pulses are separated and recorded in the respective channels for display. Different electronic circuit configurations were evaluated to improve the overall efficiency and to reduce the cross-talk and, above all to improve the signal-to-noise ratio to achieve lower minimum detectable activity value.

The response of the sandwich detector and cross-talk (defined as the counts due to alpha particles that might get registered in beta channel and vice versa) was studied in detail for alpha and beta sources of different energies. It is known that the cross-talk due to beta particles in alpha channel would be negligible (<2%) and hence the major emphasis while designing the electronic configuration was given to reduce the alpha cross-talk in beta channels. After arriving at the correct discriminating logic and delay-time triggering logic, the cross-talk has been reduced to <7% for alphas in beta channel which is comparable with the commercial system available in abroad and also well within the acceptable cross-talk of 10%.

Three different thicknesses of plastic scintillator (0.5, 1.0 and 2 mm) were employed in the studies to arrive at an optimum thickness of plastic scintillator. The background counts should be the least to achieve lower minimum detectable activity and this is especially important for alphas since the annual limit on intake (ALI) value for alpha emitting radio nuclides is less by three to four orders of magnitude as compared to $\beta\gamma$ ones. On the basis of both percentage efficiency and minimum detectable activity considerations, the optimum thickness was found to be 0.5 mm.
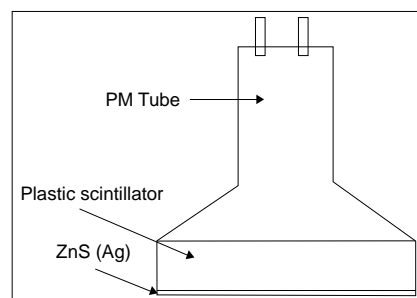
Fig. 1 *Schematic of dual phosphor detector*

The efficiency factor for alpha is very much comparable and it is far superior for betas. For medium energy beta particles (0.7 MeV), the system has five times better efficiency. In fact, the beta particles having very low energy (0.156 MeV) can also be detected in the newly developed system which is not possible with the existing conventional system. The shape and size of the dual phosphor ensures uniform source response. minimum detectable activity values for alpha particles in both the newly developed dual phosphor system and the existing one are less than 1 Bq. The minimum detectable activity value for alpha is marginally higher. However, this is insignificant when one compares with the derived working level value of 250 Bq for radioactive contamination in hands for alpha. For beta, the minimum detectable activity values are far lower for the dual phosphor based hand-contamination-monitor.

VI.5 Precision Air-Conditioning for High Density Cluster Room at Computer Centre

Computer Division is equipped with High Density Cluster room to cater to the needs of high performance computing requirements of the Centre. The temperature and humidity inside the

cluster room should be maintained precisely. Variation in temperature and humidity beyond specified limits can cause electric static discharge and damage the electronic components of the computing system. Hence, precision air-conditioning system was installed at Computer Centre cluster room to maintain the temperature precisely between 19 to 294 K and relative humidity at 50±1% to provide the suitable conditions.

The precision air conditioning system has a high sensible heat ratio and a high airflow rate per ton of refrigeration compared to conventional air conditioning. The precision air conditioning system is equipped with cooling, heating, humidification and de-humidification components which will work independently or in combination to achieve the required conditions of the room. The conditioned air is distributed uniformly throughout the room using floor discharge grilles as shown in Figure1.

The following are the special features of precision air-condition system.
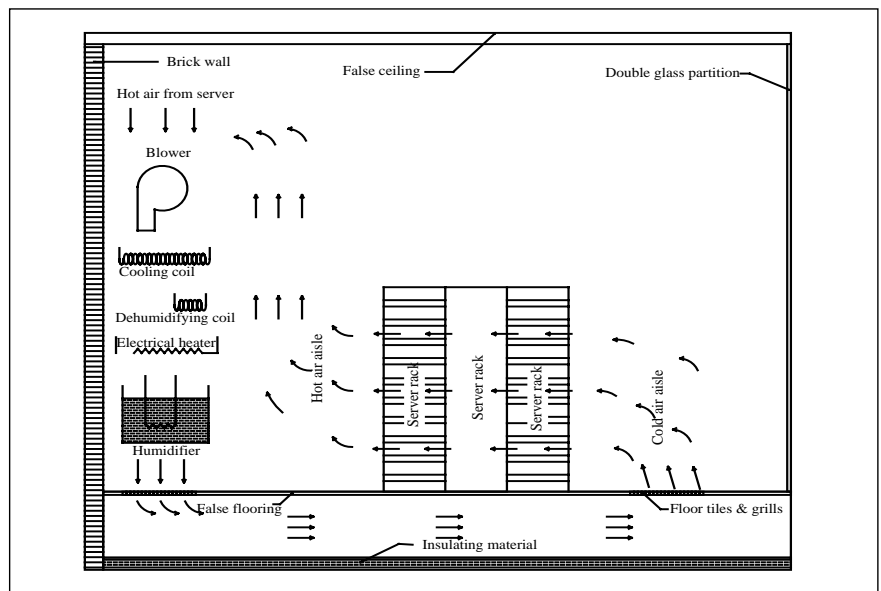
Fig. 1 *Schematic layout of important components for precision air-conditioning*

- Thermal insulation of false flooring and double walled glasses are provided to avoid condensation.

- Intelligent capacity control system for auto switching off the compressors and fans in steps during lean periods.

- Separate dehumidifier and humidifier circuit to maintain and control humidity.

- Automatic operation of units

- Remote monitoring and control of the units using building management system.

- Display of working parameters and trend monitoring to assess the healthiness of machine, alarm conditions, fault conditions and their previous history etc.

- The under deck is provided with water under flow (**WUF**) alarm to indicate water collection inside the deck.

VI.6   Information Retrieval Effectives and New Gateway of SIRD

Scientific Information Resource Division (SIRD) has always been the forefront in utilizing the advancements in the information technology for effective dissemination of information.

The electronic information resources are accessible to the users of our Centre from any where any time, and in appropriate format, across the Kalpakkam campus. Intensive initiatives have been taken to build various repositories like IGC Publications, Research articles of IGCAR, Knowledge Management Documents of Fast Reactor, Image archives, etc.

To enhance the usage of library resources, the library gateway page http://vaigai has been redesigned from user point of view to incorporate more dynamic features and ease of access.

The new web page has more organised links and other features like Cascaded Style Sheets, XML, JavaScript and Ajax based programs, photo gallery of the month, bulletin board service what's new service, etc.

VI.7 Development of Fluoride Treatment System for Societal Application

Fluoride contamination in potable water is prevalent in many parts of world. Fluoride was observed in ground water in Andhra Pradesh, Rajasthan, Tamil Nadu etc in India. Dharmapuri District has the highest concentration of fluoride in Tamil Nadu. While the permissible fluoride level in drinking water is 1.5 mg/l, certain place in this district has fluoride as high as 15 mg/l, which causes dental, skeletal and non-skeletal fluorosis. IGCAR had earlier developed a two-stage treatment process, for fluoride bearing effluents generated from elemental boron plant, with lime treatment followed by reverse osmosis to bring down the fluoride concentration from 1000 mg/l to 1 mg/l. Based on this experience, experiments were carried out for removal of fluoride from drinking water. A process was developed to reduce fluoride from 15 mg/l to less than 1mg/l by passing it through a calcium carbonate column followed by Reverse Osmosis. A defluoridation demonstration plant, consisting of pre-treatment unit, RO-plant and storage tank of 200 litre capacity, was designed, fabricated and commissioned at Avaranagattur village, Dharmapuri District (Figure 1). The fluoride level in the treated water was less than 0.2 mg/l, which is well below the permissible limit. Reject water containing about 25 to 30 mg/l of fluoride was passed through a percolation pit consisting of calcium carbonate the fluoride level was brought to 5 mg/l level and charged back to the ground water.

Fig. 1 *View of the plant in Dharmapuri*

VI.8 Management Information System for Capital Project Budget Monitoring

Planning Division, IGCAR has been shouldering the responsibility of budget expenditure monitoring and control of capital projects of IGCAR under all the sectors, viz., R&D, Industries and Power sectors. In order to effectively monitor the budget expenditure and provide information and exception reports to the budget coordinators, an online Management Information System (MIS) has been developed and deployed. The system has been developed using PHP (an open source scripting language) and is hosted on website of Planning Division (http://plan/) which is accessible to all users and budget coordinators in IGCAR.

Following MIS reports are available in this system:

• Expenditure Details: This report provides project-wise, sector-wise expenditure, booked under capital projects, between date ranges.

• Balance Payments: An information report on balance payment of purchase orders under capital projects.

• Tender Enquiry to be Issued: This report provides information about indents raised but tender enquiry to be issued at Madras Regional Purchase Unit (MRPU). It helps reducing time lag between indent and tender enquiry phase.

• Purchase Order to be Released: It is an exception report providing information like indent date, tender due date and current status of indents for cases where purchase order is to be released by MRPU.

• Purchase Recommendation/ SPC Approval Pending: This report provides project-

wise, purchase case file-wise or tender due date-wise details of cases where purchase recommendation or Stores and Purchase Committee (SPC) approval is to be obtained.

- Purchase Order Released: It is an information report giving details purchase order issued during a period, project-wise or case file-wise.

- Purchase Order Delivery date expired/expiring shortly: This report gives information about purchase orders where delivery date as per purchase order is expired or going to expire in a given period.

- Tenders Opened/Being Opened Shortly: An information report for indentors about indents for which tenders are already opened or quotations received and tenders will be opened shortly.

- Indent Status: An online status of indents at MRPU or local purchase section. The search facility is provided based on indent number, case file number, purchase order number Item name or by indentor. This module provides chronological status of indents, purchase order and payment details.

- IGCAR Payments: This module displays report) on expenditure incurred on major works, project-wise, sector-wise and voucher-wise. It also provides work order search facility and payment details for a given work order.

The Management Information System helps in monitoring the budget / expenditure patterns and also initiating corrective action, in time, to meet the project as well as budget targets.

VI.9   Commissioning of Fire Water System

Fire safety is very important for nuclear installations and extinguishing fire within short duration is the most important criteria to mitigate more hazardous consequences. The primary objective of fire water system of IGCAR is to protect the facilities, laboratories and other common service buildings from the fire hazards using water which is an excellent extinguishing agent except incase of certain specific fires.

The existing fire water system is combined with domestic and process water supply network and has already exceeded a life span of thirty years. Hence, it has been decided to provide a new fire water system for IGCAR.

The hydraulic design of the distribution system has been carried out using the computer software LOOP Version 4.0 developed by UNDP.

The important features of the new fire water system are as follows:

- Total length of fire water line is about 14.5 Km with Ductile Iron pipes of diameters 100 , 200 and 250 mm.

- Total number of hydrants is 133. There are forty isolation valves, eight scour valves and ten air valves in the system.

- The new network system has been designed with ring main headers with a diagonal link. Alternative flow path of water is available to the hydrants in case of maintenance work.

- The rate of water discharge is 4500 lpm at any point of network. Ductile Ironpipes and specials are used to give longer life and

Fig. 1   *Demonstration of fire water system at CDO*

higher resistance of pressure and anti corrosive effects.

- The new fire water system replaces the dead end of lines with ring headers which will ensure availability of water at all times.

- It provides fire hydrants where the locations are anticipated for jungle fire. It complies with the codal requirement of independent fire water system. It keeps the fire water

system under constant desired pressure.

• It is also complementing FBTR/ DPEND fire water system, whenever back up is needed and future expansion is also possible from this system to cover 11th and 12th Plan facilities and buildings.

• The underground sump of capacity 450 m^3 is located near the steelyard. The underground sump has a dead storage of 300 m^3 of water exclusively reserved for the fire fighting operations. The source of water to fire water system is from Edaiyur wells of IGCAR and also from IGCAR /

BARCF reservoir through OHT / UG sump of IGCAR as a backup.

The interim commissioning of the newly dedicated fire water system of IGCAR is completed and demonstrated (Figure 1). The system ensures fire safety for all the facilities in IGCAR in the future.

VI.10   Here Nature is Moulded at its Best……

Landscape development in and around IGCAR has been designed to maintain aesthetic excellence keeping high standards of environmental protection mainly to emphasize sense of place and permanence of our Centre.

To preserve the nature, the development has been emphasised on the preservation of plant specimens and groupings of local and native species which are representative of our region and hence calls for less maintenance. Some salient features are as given below.

Man made water cascades are used to create interest and focus. Each fountain is unique in design and style as the one near IGCAR gate, with a majestic water sheet fountain and the one in front of Homi Bhabha Building (HBB), with the vibrant flowing water cascade. Art work, landscape elements, structures, lighting and other features are used to support the image and identity.

To depict sculptured relics of Mamallpuram, the fountain at IGCAR gate, is designed as water sheet-focal point with the radial piers and stone pillars with a capital

and planters around. A sheet of water falls in between the piers which are emphasised by the stone pillars in front of them. The elegance of the pillar is enhanced by the Corinthian capital and fluted grooves engraved on it. The piers are finished with natural granite stone slabs and stone pillars to give sculptured look and the planters are finished with clay tile to give an earthy look. Foxtail Palm trees are planted behind the waterfalls and thick bamboo groove is planted behind the backdrop wall to make a natural setting for the waterfall.

The primary area opposite to Homi Bhabha Building is enhanced with the landscaped lawn dominated by the fountain to create an intimate warm inviting environment to the visitors and employees. Free standing water cascade of random stone cladding with invisible joint and mortar makes the fountain the focal point. The planting around the waterfalls makes varied visual aesthetic of subtropical nature. The entire landscape near Homi Bhabha Building is full of contours and mounds created as per natural contours of the site to make the profile interesting and continuous. Rocks were used randomly in the lawn to replicate local topography.

Fig. 1   *Landscape at structural mechanical laboratory*

The landscape in front of Structural Mechanical Laboratory (Figure 1) is developed with well manicured lawn, pebble garden, shrubs and ground cover. It is developed by retaining the existing plantations and emphasised with pebbles around. This includes fox tail palms for vertical emphasis of Structural Mechanical Laboratory, shrubs for screening at a variety of heights and ground covers to reduce weed growth and provide visual interest.

At the Raja Ramanna Auditorium the work of covering is takenup with provision to keep the view of the landscaped garden dominated by the sunken court that is lined with granite seating along stoned pathway under pergolas. Every step has been ensured to preserve the harmony with nature.

AWARDS & HONOURS

Dr. Baldev Raj, has been conferred with

- **Distinguished Materials Scientist Award** by the Materials Research Society of India for the year 2009.
- "**FICCI Award**", the highest recognition for an individual by the Federation of Indian Chamber of Commerce and Industry (FICCI) for the outstanding contributions to Science and Technology in the context of Industries and Society.
- **1st Dr. Homi J. Bhabha Centenary Year Award** by Nayudamma Centre for Development Alternatives, Nellore for the year 2009.
- "**Pandit Jawaharlal Nehru National Award**" in the field of Engineering & Technological Sciences, Department of Science & Technology, Government of Madhya Pradesh for the year 2007, awarded in the year 2009.

He has been selected as the **Vice President, Academia NDT International** and **Vice President (Academic, Professional & International Affairs)** of the Indian National Academy of Engineering (2008-2011).

He has been nominated as **Chairman**, **NTPC Energy Technology Research Advisory Council, National Thermal Power Corporation of India Ltd.**

He has been appointed as

- **Distinguished Professor**, **Institute of Chemical Technology (Deemed University), Mumbai.**
- **Adjunct Professor and Honorary Consular General, Department of Electrical and Computer Engineering**, Michigan State University, USA.

He has been elected as

- **Vice President by the Board of Directors of International Institute of Welding**.
- **Member of the International Nuclear Energy Academy.**

He has been invited to be a Member of

- **Advisory Committee for Shanti Swarup Bhatnagar Prize 2009 (Engineering Sciences).**
- **Australia-India Science & Technology Research Award** on "Energy Generation in a Low Carbon Future" instituted by Australian Academy of Technological Sciences and Engineering in association with Australian Government's Australia India Council.
- **Scientific Advisory Council of School of Engineering Science & Technology**, Central University of Hyderabad.
- **Board of Advisors, "The Al Gore Sustainable Technology Venture Competition, India".**
- **Advisory Board of Summer School on Modeling**, **Experimentation & Validation (MeV)**, Idaho National Laboratory, Argonne National Laboratory & Idaho State University, 2009.
- **Dr. Yellapragada SubbaRow Award Committee** for the year 2010.
- **Scientific Advisor to Proposal for Singapore Institute of Nuclear Science & Engineering Research (SINSER)**, National University of Singapore.

He has been invited to be a Patron of **Society for Failure Analysis**.

He has delivered

- **Smt. Rukmini Lakshmipathy Endowment Lecture**, Women's Christian College, Chennai.
- **2nd Y.M. Mehta Memorial Award Lecture**, Indian Institute of Metals (Vadodara & Mumbai Chapters).
- **DAE Raja Ramanna Lecture in Physics**, Jawaharlal Nehru Centre for Advanced Scientific Research, Bengaluru.

Dr. U. Kamachi Mudali, Reprocessing Research & Development Division, Reprocessing Group has been awarded "**NIGIS Meritorious Contribution Award**" of NACE International Gateway of India Section, Mumbai for the year 2008-09.

Dr. S. Ningshen, Corrosion Science & Technology Division, Metallurgy and Materials Group has been awarded "**Mascot National Award – 2009**" by the Electrochemical Society of India.

Dr. (Smt.) Saroja Saibaba, Physical Metallurgy Division, Metallurgy and Materials Group has been selected as **Fellow of The Indian Institute of Metals** from April 2009.

Dr. Sumantra Mandal, Materials Technology Division, Metallurgy and Materials Group has been selected as an **Associate of the Indian Academy of Sciences**. He has also received "**2009 Young Metallurgist of the year**" award in the 'Ferrous Category' from Ministry of Steels, Government of India.

Dr. B.V.R. Tata, Condensed Matter Physics Division, Material Science Group has been awarded the **MRSI Medal** for the year 2009 by Materials Research Society of India (MRSI).

DAE AWARDS

Department of Atomic Energy has instituted annual awards for excellence in Science, Engineering and Technology in order to identify best performers in the area of Research, Technology Development and Engineering in the constituent units (other than Public Sector Undertakings and Aided Institutions). The Young Scientist, Young Engineer, Young Technologist, Homi Bhabha Science and Technology Award and Scientific and Technical Excellence Award fall under this category. Group Achievement awards for recognition of major achievements by groups have also been instituted. Life time Achievement Award is awarded to one who has made significant impact on the DAEs programme. They are the icons for young scientists and engineers to emulate. The awards consist of a medallion, citation and cash prize.

The recipients of the awards from IGCAR for the year 2008 are:

Homi Bhabha Science and Technology Award: Dr. N.Sivaraman, CG

Young Applied Science & Technology Award: Shri M.G.Hemanath, FRTG

Young Engineer Awards: Shri T.Gokulakrishnan, EIG and Shri A.Ravishankar, MMG

Scientific & Technical Excellence Award:

Shri B.K. Nashine, FRTG, Dr. S. Murugan, Dr. R. Sandhya and Dr. Saroja Saibaba from MMG, Shri P. Puthiyavinayagam, REG and Dr. D. Ponraju, SG.

Meritorius Award:

Shri M. Ganapathy, CG, Shri S. Chandran, Shri R. Devan, Shri A. Dorai, Shri K. M. Natarajan from ESG, Shri A. T. Loganthan and Shri A. Rajan from FRTG.

Group Achievement Awards:

Establishment of the Unique and State of the Art Accelerator Facility for Experimental Studies & Ion Beam Simulation of Radiation Damage

Dr. K.G.M. Nair, Group Leader, Dr. S. Amrithapandian, Shri S. Balaji, Shri V. Baskaran, Shri C. David, Shri R. Dhandapani, Shri K. Dasarathan, Shri A. Dhanusu, Shri P. Gangopadhyay, Shri J.C. George, Shri P. Magudapathy, Dr. B.K. Panigrahi, Dr. Sandip Dhara, Dr. B. Sundaravel, Shri K. Suresh, Shri S.K. Srivastava from MSG.

Design, Construction, Commissioning and Operation of the Pilot Plant for the Cover Gas Purification System of PFBR

Shri C. R. Venkata Subramani, Group Leader, Shri R. Parandhaman, Shri R. Parthasarathy, Smt. D. Sai Subalakshmi, Shri D.K. Saxena and Shri K. Swaminathan from CG, Shri S. Alexander

Xavier, Shri A. Ashok Kumar, Shri S.Chandramouli, Shri T. Chandran, Shri M.G. Hemanath, Shri K. Jayagopi, Shri S. Krishnakumar, Shri P. Mohanraj, Shri D. Muralidhar, Shri B. Muralidharan, Shri R.K. Murthy, Shri R. Punniyamoorthy, Shri J. Prem, Shri Rafiq Basha, Shri S. Ravishankar, Shri S. Shanmugam, Shri M. Shanmugasundaram, Smt. C. Sundari, Shri V. Tharmaraj, Shri Vivek Nema from FRTG, Shri M. Rajan (Retired) from SG, Shri D. Jambunathan (Retired) from ROMG.

Remote Sealing of Biological Shield Cooling Coils

Dr. A. K. Singhal, BARC, Group Leader, Shri K.A. Gopal, MMG, Shri U. Chandrangadan, Shri K. Ganapathy Subramanian, Shri D. Loganathan, Shri N. Manimaran, Dr. B.S. Panigrahi, Shri R. V. Ramesh, Shri M.Savarimuthu, Shri P. Sekhar, Shri R. Sekar, Shri A. Suriyanarayanan from ROMG, Shri Vimal Kumar, TC&QCS, Shri A.K. Chhabra, Dr. Hemant Sodey, Dr. S. Prabhakar, Shri Sushil A Tiwari, Dr. P. K.Tewari from BARC.

Insitu Repair Welding of Steam Turbines of NPCIL

Dr. A. K. Bhaduri, Group Leader, Shri M. Arul, Shri Chitta Ranjan Das, Shri N. Dhakshanamoorthy, Shri R. Gnanasekaran, Shri D. Manokaran, Shri V. Ramasubbu, Dr. Shaju K. Albert, Shri P. Sukumar from MMG, Shri P.M. Ajith Kumar, Shri N. Dhanasekaran, Shri S.P. Jaishankar, Shri M. Kuppan, Shri M. Krishnamoorthy, Shri A. Mohamed Muneer, Shri A.S.L.K. Rao, Shri A.G. Sarangapani, Shri P. Sivaraman, Shri C. Subramanian from ESG.

Design and Manufacture of Grid Plate For PFBR

Dr. P. Chellapandi, REG, Group Leader, Dr. A.K. Bhaduri, Shri Hemant Kumar, Dr. Shaju K. Albert from MMG, Shri Abishek Mitra, Shri V. Balasubramaniyan, Shri Bhuwan Chandra Sati, Shri S.Jaisankar, Shri S.Jalaldeen, Shri V. Kothandam, Shri R.Manu, Shri D.Naga Sivayya, Shri K.Natesan, Shri U. Parthasarathy, Shri P. Puthiyavinayagam, Shri V.Rajan Babu, Shri C.Raghavendran, Shri G.R.Ravi Prasan, Shri S.D.Sajish, Shri Sebasti John, Shri P. V. Sellaperumal, Shri P. Selvaraj, Shri R.Sritharan, Shri R.Suresh Kumar, Dr. K.Velusamy, Shri G.Venkataiah from REG.

Design & Manufacture of Steam Generator For PFBR

Shri T.K. Mitra, BHAVINI, Group Leader, Dr. B. Venkatraman, ESG, Dr. R.K.Dayal, Dr A.R. Hasan Shaikh, Shri A. Sivakumar, Shri G. Srinivasan from MMG, Shri Amitava Biswas, Shri Amzad Pasha, Shri S. Athmalingam, Shri S. Chandrasekar, Dr. P. Chellapandi, Shri V. Devaraj, Shri Jainendra Kumar Dubey, Shri S. Jalaldeen, Shri P. Jayaraj, Shri K. Madhusoodanan, Shri R. Nanda Kumar, Shri K. Natesan, Shri U. Parthasarathy, Shri V. Rajendran, Shri S.D Sajish, Shri S. Satheesh Kumar, Shri L. Satish Kumar, Shri P.Selvaraj, Shri R. Srinivasan, Dr. K. Velusamy from REG, Shri N. Kasinathan from SG.

IGCAR Publications

Pie chart values: 244 (Internal Reports), 357 (Journal Articles), (60) (Articles in press), 25 (Books / Book Chapters), 274 (Conference Papers)

Legend:
- Journal Articles
- Articles in press
- Books / Book Chapters
- Conference Papers
- Internal Reports
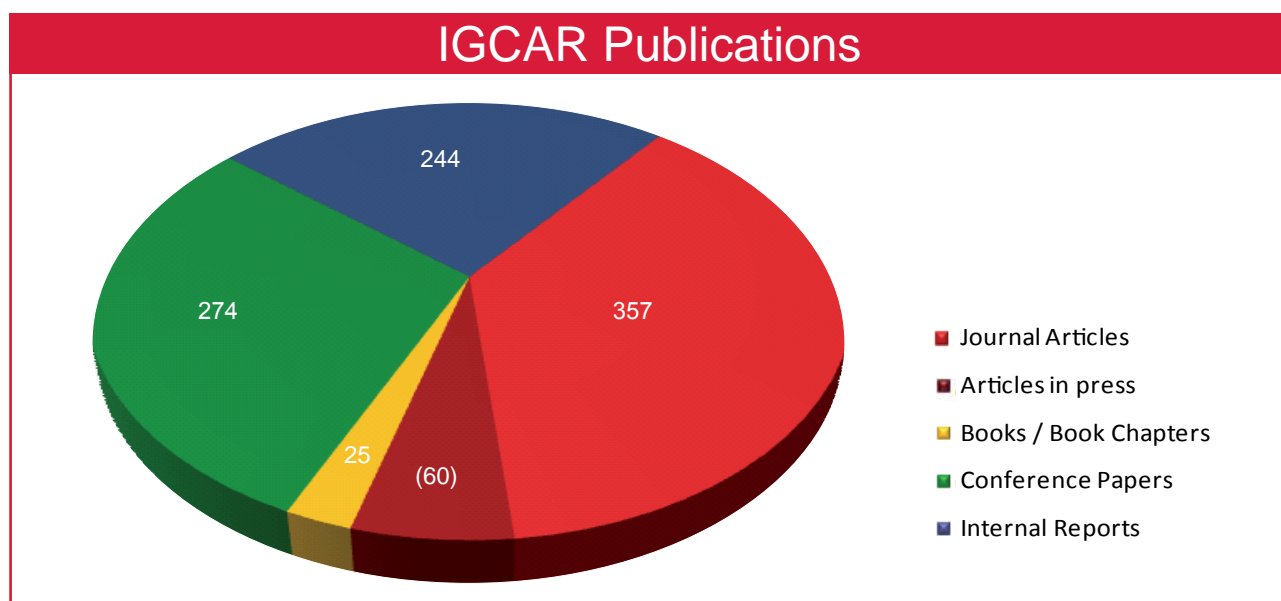
PATENTS

A Process for the Treatment of Cellulose based Waste for Removal of Hazardous Materials and Recovery of Valuables. Ch. Jagadeeswara Rao, K.A. Venkatesan, K.Nagarajan, T.G. Srinivasan and P.R. Vasudeva Rao. Application No. 2017/MUM/2008, Dated 22/09/2008.

EMINENT LECTURE SERIES

Department of Atomic Energy is commemorating the Birth Centenary of Dr.Homi Jehangir Bhabha, the founder father of Atomic Energy Programme in India during 2008 to 2009. As part of the birth centenary celebrations, lecture series by eminent persons is being organised. Topics relating to the priority R&D areas of the Department are identified and eminent persons who have contributed significantly in these areas are invited to deliver these eminent lectures. Following are the lectures delivered at our Centre.

"The Exciting and rewarding world of Chemistry and Chemical Engineering" by Prof. M.M. Sharma, Emertius Professor and former Director, University Institute of Chemical Technology, Mumbai on August 4, 2009.

"Plutonium: The promise, peril, puzzle" by Prof. Hecker, Director Emeritus, Los Alamos National Laboratory, USA on September 24, 2009.

"Closing the fuel cycle for a sustainable future nuclear energy" by Prof. Dr. Thomas Fanghanel, Director, Institute for Transuranium Elements, Joint Research Centre, European Commission on September 28, 2009.

"Next Generation Nuclear Reactors" by Dr. Jacques Bouchard, Special Advisor to Chairman, CEA and Chermain, GIF, CEA on September 28, 2009.

"Probing the Limits of Quantum Physics by Means of Nanotechnology" - by Prof. Herbert Dieter Gleiter, Director, Institute of Nanotechnology, Research Centre, Karlsruhe & Professor, German Academy of Sciences, Leopoldina, Germany on December 16, 2009.

"Nuclear Power: A Global View" by Dr. Yury Sokolov, Deputy Director General, IAEA on October 3, 2009.

SPECIAL LECTURES & IGC COLLOQUIA

"The Global financial and economic scenario & India" by Dr. V.B. Athreya, M.S. Swaminathan Research Foundation, organised in association with Tamilnadu Science Forum on January 6, 2009.

Vikram Sarabhai Memorial Lecture - "Tailored Thin Films and Nanomaterials" by Prof. K.L. Chopra, Former Director IIT Kharagpur & President, Society for Scientific Values on March 2, 2009.

"Challenges of modelling coastal atmospheric condition with particular reference to transport and dispersion of pollutants" by Prof. Sethuraman, Professor and State Climatologist Emeritus Department of Marine, Earth and Atmospheric Sciences, North Carolina State University, USA, on March 3, 2009.

"Science and Technology: Ethical Issues" by Prof. K.L. Chopra, Former Director, IIT Kharagpur & President, Society for Scientific Values, organised by Association of Atomic Research Centre Officers on March 4, 2009.

"Being a Woman in Today's World" by Dr. Geetha Arjun, E.V. Kalyani Medical Centre, Chennai, organised by Indian Women Scientist Association as part of *Woman's day Celebrations* on March 6, 2009.

"Thorium Breeders- The Future Reactors" by Dr. V. Jagannathan, BARC, Mumbai, on April 2, 2009.

"Molten Salt Reactor: An Introduction" - Seaborg Memorial Lecture - by Dr. D.D. Sood, BARC, Mumbai, organised by Chemistry Group, IGCAR on October 15, 2009.

"Strength and Creep of Nanocrystals" by Prof. Atul Chouksi, IISc, Bengaluru, Dr. Placid Rodriguez Memorial Lecture, organised by Indian Institute of Metals (Kalpakkam and Chennai Chapters) on November 29, 2009.

"Current Status of Prototype Fast Breeder Reactor" by Shri Prabhat Kumar, PD, BHAVINI, organised by IIM, Kalpakkam Chapter on December 15,2009.

SEMINARS, WORKSHOPS AND MEETINGS

1. Hindi Workshop on "Noting Drafting & Translation", organised by Hindi Cell, IGCAR on January 28, 2009.

2. Hindi Workshop on "Improving Writing Skills in Hindi" organised by Hindi Cell, IGCAR on June 3, 2009.

3. National Seminar on "Solvent Extraction in Nuclear Engineering" organised by IGCAR and the Kalpakkam Chapter of the Indian Institute of Chemical Engineers, June 23-24, 2009.

4. DAE-BRNS Theme Meeting on "Materials for Fast Breeder and Fusion Reactor Applications" organised by Indian Institute of Metals, Kalpakkam Chapter and IGCAR on June 26,2009.

5. Annual Quality Circle Meeting (QCAM 2009), July 23-24, 2009.

6. Specialists Meeting on Advances in Scientific Database in India (SMASD) organised by IGCAR and Indian National Science Academy, August 10-11, 2009.

7. National Seminar on "Development of Atomic Energy in India" organised by Hindi Cell, IGCAR, September 4, 2009.

8. "Hindi Fortnight 2009" organised by Hindi Cell, IGCAR September 14-25, 2009.

9. "Fourth National Symposium on Frontiers of Engineering (NatFOE4)" organised by IGCAR & Indian National Academy of Engineering, September 16, 2009.

10. Theme Meeting on "Structure and Thermodynamics of Emerging Materials 2009 (STEM 2009)", September 24-25, 2009.

11. "Workshop on Nuclear Power Plant Life Management (WoN-PLiM 2009)" organised by IGCAR, Board of Research in Nuclear Sciences and Atomic Energy Regulatory Board, October 6-9, 2009.

12. International Conference on "Sol-Gel Processes for Advanced Ceramics (SGPAC -09)", October 11-14, 2009.

13. INSA Theme Meeting on "Materials Science Challenges for Strategic Sectors", October 20-21, 2009.

14. One Day Training Programme on "Use of Unicode fonts in Hindi" organised by Hindi Cell, IGCAR November 24, 2009.

15. Annual Convention of Indian National Academy of Engineering 2009, December 17-18, 2009.

16. Seventh National Conference on "Recent Advances in Information Science and Technology (READIT-09)" organised by IGCAR in association with Kalpakkam Chapter of Madras Library Association, December 28-30, 2009.

Nurturing Activities for students/employees

1. "Summer Training Programme in Physics and Chemistry(STIPAC-2009)" a six weeks Training programme for final year M.Sc., (Physics/Chemistry) students from May 25, 2009 to July 3, 2009.

2. Awareness program for school children about solar eclipse organised by AARCO, July 21, 2009.

3. Prof. Brahm Prakash Memorial Materials Quiz 2009 organised by IIM, Kalpakkam Chapter, September 18-19, 2009.

News and Events

Graduation Function of 3rd batch
of BARC Training School at IGCAR

Prof. S.K. Joshi, JNCASR Vikram Sarabhai Professor, National Physical Laboratory, New Delhi addressing the Trainee Scientific Officers

The 3rd batch of forty three Trainee Scientific Officers from the BARC Training School at IGCAR have successfully completed their training and were graduated in a special ceremony held on September 1, 2009 at the Sarabhai Auditorium, Homi Bhabha Building, IGCAR. Distinguished Academician, Prof. S.K. Joshi, JNCASR Vikram Sarabhai Professor, National Physical Laboratory, New Delhi was the Chief Guest. Dr. M. Sai Baba, Head, BARC Training School at IGCAR welcomed the gathering. Dr. Baldev Raj, Distinguished Scientist and Director, IGCAR addressed the gathering. Prof. S.K. Joshi gave away the prestigious 'Homi Bhabha Prize' comprising of a medallion and books worth Rs.5000 to the meritorious toppers from all the disciplines. He also gave away the course completion certificates to all the passing out graduates. A few of the passing out Trainee Scientific officers, gave feedback on the academic programme and their stay during the training. A souvenir featuring reminiscences of the training programme at IGCAR was released by Prof. S.K. Joshi and Dr. Baldev Raj received the first copy. Prof. S.K. Joshi gave a very inspiring and enlightening lecture to the gathering. Dr. Vidya Sundararajan, S&HRPS proposed the vote of thanks.

3rd Batch Graduates of BARC Training School at IGCAR with the Chief Guest, Director, IGCAR, Senior colleagues of the Centre and members of S&HRPS

Eminent Visitors To IGCAR

Dr. M.R. Srinivasan, former Chairman, AEC and Member, AEC visited the Centre during January 23-24, 2009. He was presented with the status report on PFBR, roadmap and directions for future FBRs, metallic fuel development and Fast Reactor Fuel Cycle Facility by senior colleagues of the Centre. He visited laboratories in Fast Reactor Technology Group, Corrosion Loops and Hot Cells in Metallurgy and Materials Group and Structural Mechanics Laboratory of Reactor Engineering Group, Facilities in Safety Group and the construction site of PFBR. Dr. M.R. Srinivasan highlighted the advantages of going nuclear in tiding over the energy crisis without disturbing the environment in his address to the Trainee Scientific Officers and Research Scholars of the Centre. The talk was followed by interactive session, where he clarified the doubts raised by the student community. He has also addressed a joint convention of students from all the schools at Kalpakkam Township.

Dr. M.R. Srinivasan, former Chairman, AEC and Member, AEC with Dr. Baldev Raj, Director, IGCAR along with the Trainee Scientfic Officers and Research Scholars of the Centre

A team from IAEA led by Dr. C.Ganguly, Head, Nuclear Fuel Cycle and Materials Section, IAEA along with Ms.Kristie Hasnen, Multimedia Producer and Mr. Petr Pavlicek, Cameraman accompanied by the colleagues from DAE visited the FBTR, MAPS and the construction site of PFBR during February 13-14, 2009.

The IAEA team during the visit to the Centre along with Dr. Baldev Raj, Director, IGCAR and other senior colleagues

Dr. Casimir Pierre Zaleski, Scientist, CGEMP, University of Paris Dauphine, France and Mrs. Ann Downing Maclachlan Zaleski visited the Centre during February 27-28, 2009. They visited the Fast Breeder Test Reactor, laboratories in Fast Reactor Technology Group, Structural Mechanics Laboratory and the construction site of PFBR at BHAVINI.

Dr. Casimir Pierre Zaleski and Mrs.Ann Downing Maclachlan Zaleski in conversation with Dr. Baldev Raj, Director, IGCAR

Prof. K.L. Chopra, Former Director, IIT-Kharagpur and Honorary Professor, IIT-Delhi with Trainee Scientific Officers, Research Scholars and colleagues of the Centre

Prof. K.L. Chopra, former Director, IIT-Kharagpur and Honorary Professor, IIT-Delhi visited the Centre during March 2-4, 2009. He delivered the "5th Vikram Sarabhai Memorial Lecture" on "Tailored thin films and nanomaterials". Prof.Chopra held discussions with Director and senior colleagues of the Centre and visited various laboratories in the Centre and the construction site of PFBR. The Trainee Scientific Officers and Research Scholars had an interaction session with Prof. Chopra at research scholar enclave in the township. Prof.Chopra also presented a popular lecture on "Ethics in Science" to audience at IGCAR.
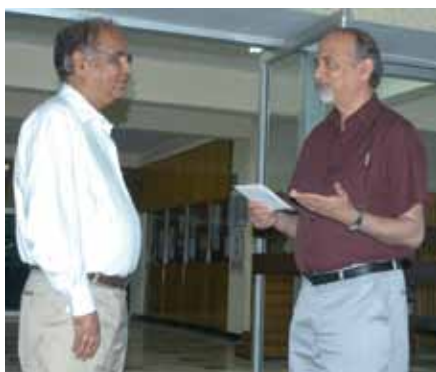
Shri D.P.Shrivastava, Ambassador of India to Czeck Republic in conversation with Dr. Baldev Raj, Director, IGCAR

Shri D. P. Shrivastava, *Ambassador of India to Czeck Republic*, visited the Centre on July 10, 2009. He met Dr.Baldev Raj, Director, IGCAR and other senior colleagues of the Centre and held discussions. He visited the FBTR and construction site of PFBR at BHAVINI.

Prof. Hecker, Director Emeritus, Los Alamos National Laboratory, USA with Dr. Baldev Raj, Director, IGCAR, Research Scholars and Trainee Scientfic Officers at IGCAR

Prof. Siegfried S. Hecker, *Director Emeritus, Los Alamos National Laboratory, USA* visited the Centre on September 24, 2009. He delivered a lecture on "Plutonium: The promise, peril and puzzle" as part of eminent lecture series. Prof. Hecker also visited the FBTR, Laboratories in Materials Science and Metallurgy & Materials Groups and also the construction site of PFBR at BHAVINI.

Prof. **M.M. Sharma,** *Emeritus Professor and former Director, University Institute of Chemical Technology, Mumbai* visited the Centre during August 3-4, 2009. He chaired the "Peer Review Committee of Chemical Sciences". Prof. M. M. Sharma delivered the lecture on "The exciting and rewarding world of Chemistry and Chemical Engineering" in the "Eminent Lecture Series" organized as part of commemorative celebrations of birth centenary of Dr. Homi Jehangir Bhabha. Prof. M. M. Sharma visited various laboratories of the Centre.

Prof. M. M. Sharma, Emeritus Professor and former Director, University Institute of Chemical Technology, Mumbai with Dr. Baldev Raj, Director, IGCAR along with other members of the "Peer Review Committee in Chemical Sciences" and senior colleagues of the Centre

Dr. **Mohammed El-Baradei,** *Director General, IAEA, Vienna* visited the Centre during September 27-28, 2009. He met Dr. Baldev Raj, Director, IGCAR and other senior colleagues. He visited the FBTR, Hot cells and laboratories in the Non-Destructive Evaluation Division, construction site of PFBR at BHAVINI, Nuclear Desalination Development Plant and Safety Research Institute of AERB. He was accompanied by Shri Sourabh Kumar, Indian Ambassador to IAEA, during his visits.

Dr. Mohammed El-Baradei, Director General, IAEA with Dr. Baldev Raj, Director, IGCAR

Prof.Thomas Fanghanel, Director, Institute for Transuranium Elements, Joint Research Centre, European Commission along with his colleague Dr. Frank Wastin during the visit to the Chemistry Group

Prof. **Thomas Fanghanel,** *Director, Institute for Transuranium Elements, Joint Research Centre, European Commission* visited the Centre during September 27-28, 2009. During his visit, he was taken around the FBTR, laboratories in the Non-Destructive Evaluation Division, Materials Science Group and Chemistry Group. He also visited the construction site of PFBR. Prof. Fanghanel delivered a Lecture on "Closing the Fuel Cycle for a Sustainable Future Nuclear Energy" as part of "Eminent Lecture Series".

Dr.**Jacques Bouchard,** *Special Advisor to Chairman, CEA and Chairman, GIF, CEA* visited the Centre during September 27-28, 2009. During his visit, he was taken around the FBTR, laboratories in the Non-Destructive Evaluation Division, Fast Reactor Technology Group, Safety Group and Structural Mechanics Laboratory. He also visited the construction site of PFBR. Dr. Bouchard delivered a lecture on the topic "Nuclear Energy and Sustainable Development" as part of the "Eminent Lecture Series".

Dr. Jacques Bouchard, Special Advisor to Chairman, CEA and Chairman, GIF,CEA during visit to Structural Mechanics Laboratory along with his colleague Dr. Sunil Felix and other senior colleagues of the Centre

Dr. Yury Sokolov, Deputy Director General, IAEA with Dr. Baldev Raj, Director, IGCAR

Dr.Yury Sokolov, Deputy Director General, IAEA visited the Centre on October 3, 2009. After a meeting with senior colleagues of the Centre, Dr. Sokolov visited the Fast Breeder Test Reactor, laboratories in Non-Destructive Evaluation Division and Hot Cells and the construction site of PFBR. Dr. Sokolov addressed and interacted with the Training School Officers and Research Scholars in the Centre.

A team of sitting members from the Legislative Assembly of Meghalaya, visited the Centre during October 28-29, 2009. The team visited Fast Breeder Test Reactor, Hot Cells and laboratories in Non-Destructive Evaluation Division and Safety Group. They also visited construction site of PFBR, Madras Atomic Power Station and Nuclear Desalination Development Plant.

Members from the Legislative Assembly of Meghalaya with Dr. P. Swaminathan, Director, EIG and other colleagues of the Centre

Dr. Baldev Raj, Director, IGCAR and senior colleagues of the Centre with the "People to People, Citizen Ambassador Programs" delegation

A delegation from "People to People, Citizen Ambassador Programs", USA led by Dr. Alan Edward Waltar visited the Centre during November 8-9, 2009. The delegation visited the Fast Breeder Test Reactor, Hot Cells and Laboratories in Non-Destructive Evaluation Division, Safety Group, Fast Reactor Technology Group and the construction site of PFBR.

Prof. **Herbert Dieter Gleiter**, Director, Institute of Nanotechnology, Research Center Karlsruhe and Professor, German Academy of Sciences visited the Centre on December 16, 2009. Prof. Gleiter visited the Fast Breeder Test Reactor, laboratories in the Metallurgy and Materials Group, Materials Science Group and the construction site of PFBR. Prof. Gleiter also delivered a lecture in the Homi Bhabha Eminent Lecture Series.

Prof. Herbert Dieter Gleiter, Director, Institute of Nanotechnology, Research Centre, Karlsruhe and Professor, German Academy of Sciences with Dr. Baldev Raj, Director, IGCAR and other senior colleagues of the Centre

5th CEA-IGCAR Annual Seminar on Liquid Metal Cooled Fast Reactor Safety

March 10-13, 2009

Under the continuing Indo-French Collaborative activities, 5th CEA-IGCAR Annual Seminar meeting on Fast Reactor Safety was organised by IGCAR during March 10-13, 2009. Nine French and twenty eight Indian delegates (from IGCAR, BHAVINI & AERB) participated in the seminar. While inaugurating the seminar, Dr. Baldev Raj, Director, IGCAR stressed the need for maintaining high levels of standards towards ensuring reactor

Dr. Baldev Raj, Director IGCAR and CEA delegates during the annual CEA-IGCAR Seminar

safety and commended the collaborative agreement that has laid foundation for sharing of rich technical information on reactor safety on a continuing basis. A total of about twenty presentations were made under topics on reactor operation, in-service inspection, Phenix end of life tests, PFBR commissioning program, monitoring of loose parts in the reactor, active versus passive decay heat removal systems, fuel safety etc. A detailed review of the status of collaborative works in the domains of sodium chemistry, hydrogen sensors, experimental and numerical simulation of sodium aerosol distribution, sodium leak detection, tritium behaviour in sodium, sodium water reaction, corium coolant interaction etc. was carried out. Further, the areas for future collaborative works such as IGCAR participation in the Phenix end of life tests, development of high temperature sensors for in-service inspection, evolving robust fuel safety criteria for MOX and carbide fuels, structural integrity assessment etc. were identified.

IAEA Consultancy Meetings

May 25-29, 2009

Two IAEA Consultancy meetings were held at IGCAR, Kalpakkam during May 25-29, 2009. One meeting chaired by Shri H.S. Kamath, Director, Nuclear Fuels Group, BARC, reviewed the document on "Status and trends of uranium plutonium mixed oxide, carbide, nitride and metallic fuels for sodium

cooled fast reactors - fabrication, properties and irradiation behaviour". The other one chaired by Dr. P.R. Vasudeva Rao, Director, Chemistry, Metallurgy and Materials Group, IGCAR reviewed the document on "Back end of the Fast Reactor Fuel Cycle: Status and Perspectives". Dr. H.P. Nawada,

Section Officer, Nuclear Fuel Cycle Section, IAEA was the Scientific Secretary for the two meetings. The participants of the meetings included Dr. Michel Masson, CEA, France, Dr. Mikhail Kormilitsyn, RIAR, Russia and Dr. Tomozo Koyama, JAEA, Japan (experts for the document on back end fuel cycle) and Dr. Ho Jin Ryu, Korea (expert for the document on nuclear fuel fabrication), besides many specialists in these areas from BARC and IGCAR. The review and finalisation of the documents in the meetings involved intense discussions on the current status of the developments in these areas. The meetings provided a valuable platform for the scientists of the

Shri S.C. Chetal Director, REG, Dr. P.R. Vasudeva Rao, Director, CG and Dr. P. Chellapandi, Director, SG with other participants at the IAEA Consultancy meeting

department to exchange their views with international experts in addition to the contribution to the document.

DAE-BRNS Theme Meeting on
Materials for Fast Breeder and Fusion Reactor Applications

June 26, 2009

Dr. Baldev Raj, Director, IGCAR with other dignitaries during the inauguration of the Theme meeting

As part of the birth centenary celebrations of Dr. Homi Bhabha, father of India's nuclear power programme, a one day Theme Meeting on "Materials for Fast Breeder and Fusion Reactor Applications" was organised jointly by IGCAR, Indian Institute Metals - Kalpakkam Chapter, and Board of Research in Nuclear Sciences on June 26, 2009 at the Convention Centre, Anupuram. Dr. Baldev Raj, Director, IGCAR inaugurated the theme meeting and emphasised the importance of synergy among various institutions in the country in the fission and fusion reactor research programs. Dr. P. R. Vasudeva Rao, Director, Chemistry, Metallurgy and Materials Group spoke about the genesis of the theme meeting. The key note lecture on "Development, Characterisation and Performance of Sodium Cooled Fast Breeder Reactor

and Fusion Reactor Materials" was delivered by Dr. K. Bhanu Sankara Rao, Associate Director, MDCG and Head, Mechanical Metallurgy Division. The theme meeting was conducted in three technical sessions devoted to Design, selection and production of Materials for FBRs, Mechanical Behaviour of Structural Materials and Materials for Fusion Reactor Systems.

About 150 delegates participated in the technical deliberations. Leading experts from IGCAR, MIDHANI, Nuclear Fuel Complex, International Advanced Research Centre for Powder Metallurgy and New Materials, Defense Metallurgical Research Laboratory, Institute for Plasma Research and BARC delivered invited talks.

Workshop on Nuclear Power Plant Life Management (WoN-PLiM 2009)

October 6-9, 2009

Dr. Philip Tipping, Nuclear Energy and Materials Consultant, Swiss Federal Nuclear Safety Inspectorate (HSK), Switzerland addressing the delegates during inaugural function of WoN-PLiM 2009

Commemorating the birth centenary of Dr. Homi Jehangir Bhabha, a Workshop on Nuclear Power Plant Life Management (WoN-PLiM) was organized jointly by IGCAR, BRNS and AERB during October 6-9, 2009 at IGCAR under the Chairmanship of Dr. Baldev Raj, Director, IGCAR. Dr. T. Jayakumar, Director, Metallurgy and Materials Group, gave the welcome address, Shri S.C. Chetal, Distinguished Scientist and Director, Reactor Engineering Group, IGCAR presided over the inaugural function and Dr. Philip Tipping, Nuclear Energy and Materials Consultant, Swiss Federal Nuclear Safety Inspectorate, Switzerland gave the inaugural address, during which he lauded the pioneering and visionary contributions of Dr. Homi Bhabha and the lead role being played by India in the area of sodium cooled fast reactors.

The workshop was attended by about one hundred and eighty five scientists and engineers from various units of DAE, IIT Madras, SERC, DMRL, NTPC, L&T and Walchand Nagar Industries. In the workshop, sixteen eminent experts from various units of DAE and Dr. Philip Tipping, delivered invited lectures covering various Power Plant Life Management aspects of FBRs, PHWRs and BWRs including ageing management, life extension, risk analysis, safety upgradation, mitigation strategies, in-service inspection, regulatory guidelines and public acceptance.

Technical visits to FBTR, MAPS and BHAVINI were organised for the delegates and a panel discussion was conducted on October 9, 2009. During the feedback session, delegates appreciated the technical program and requested holding exclusive workshops for life extension of electronic instruments and concrete structures.

International Conference on Sol-gel Processes for Advanced Ceramics (SGPAC-2009)

October 11-14, 2009

An International Conference on Sol-gel Processes for Advanced Ceramics (SGPAC-2009) was jointly organised by IGCAR and BARC during October 11-14, 2009 at the Convention Centre, Anupuram. It was supported by the Board of Research in Nuclear Sciences, Materials Research Society of India (Kalpakkam Chapter) and the Indian Ceramic Society (Tamil Nadu Chapter). Dr. Baldev Raj, Director, IGCAR welcomed the delegates and made introductory remarks about the theme of the conference. The conference was inaugurated by Dr. Anil Kakodkar, Chairman, AEC and Secretary, DAE, Government of India. In his inaugural address, he highlighted the versatility of the sol-gel processes

Dr. Anil Kakodkar, Chairman, AEC, Dr. Baldev Raj,Director, IGCAR, Dr. Srikumar Banerjee, Director, BARC, Dr. P. R. Vasudeva Rao, Director CG, with other dignitaries during the inauguration of the conference

for the fabrication of a variety of advanced ceramics including nuclear fuels. Dr. Srikumar Banerjee, Director, BARC compared and contrasted the sol-gel processes and the powder metallurgical processes in his special address. Dr. G. Sundararajan, Director, International Advanced Research Centre for Powder Metallurgy and New Materials (ARCI), Hyderabad gave the key note address on the demonstration of the sol-gel coating technology for commercial applications.

About one hundred and fifty delegates comprising of plenary and invited speakers, participants from overseas, students and research scholars participated in this conference. In all, sixty eight contributed papers were presented in the oral as well as poster

sessions. These papers covered the application of sol-gel processes for the fabrication of a variety of materials such as nuclear and industrial ceramics, thin films, coatings, glasses and glass fibres, bioceramics, aerogels and porous ceramics, ceramic fibres etc. A technical exhibition was also organized as part of this conference in which ARCI, Hyderabad and Central Glass and Ceramic Institute, Kolkata had put up informative stalls on their products in the area of sol-gel. This conference facilitated good interaction among the young researchers and eminent scientists in the area of sol-gel science and technology. In order to motivate young research scholars prizes were awarded to the best poster and oral presentations made by student participants.

7th National Conference on
Recent Advances in Information Science and Technology
(READIT-2009)

December 29-30, 2009

The 7th biennial national conference on "Recent Advances in Information Science and Technology (READIT 2009)" was organised jointly by Scientific Information Resource Division of IGCAR and Kalpakkam Chapter of Madras Library Association (MALA) on December 29-30, 2009 at the Sarabhai Auditorium, Kalpakkam with the theme of 'Knowledge Representation through Semantic Library'. Dr. Baldev Raj, Director, IGCAR in his presidential address emphasised the importance of semantics in information retrieval and need of Knowledge

Domains. Prof. D.K. Subramanian, Consulting Advisor to Tata Consultancy Services and former Dean & Professor Indian Institute of Science, Bengaluru delivered the inaugural address. Prof. D.K. Subramanian highlighted the semantic technologies for knowledge representation in his address. The conference had four major sessions on 'Semantic Technologies for Knowledge Representation', 'Digital Library Infrastructure and Information Retrieval', 'Open Source Solutions and Federated Search' and 'Knowledge Management Practices in Library &

Dr. Baldev Raj, Director, IGCAR delivering the presidential address at the READIT conference, Prof. D.K. Subramanian, consultant advisor to Tata Consultancy Services and former Dean & Professor Indian Institute of Science, Dr. P. Swaminathan, Organising Committee, READIT.

Information Centers'. About two hundred delegates including research scholars and students of information science, Library & IT professionals participated in the technical deliberations. The conference included invited talks from eminent persons from academic institutions, industries and R&D organisations. The conference had one session exclusively for research scholars and students. There was also a separate poster session for the contributed papers.

An exhibition was organised as part of the conference in which latest IT gadgets, standards and books were displayed. This conference facilitated good interaction among the young researchers, professionals and eminent speakers in the area of information science. During the valedictory function, Dr. M. Sai Baba, Head, SIRD & Convenor, READIT 2009 summed up the overall deliberations of the conference. Dr. J.K. Suresh, Associate Vice President and Chief Knowledge Manager, INFOSYS gave the Keynote Address followed by Valedictory Address by Shri. S.C. Chetal, Director, Reactor Engineering Group, IGCAR. A Pre-Conference tutorial on Digital Repositories Creation and Preservation Management was also arranged on December 28, 2009 as part of READIT 2009.

Industrial Safety Activities

❑ Environmental & Industrial Safety Section provides training to various employees and contract personnel regularly.

❑ As per AERB stipulation 100% contract workers & 20% employees are trained every year.

❑ First aid training is given every year to 10% of employees.

❑ Fire squad members (50%) and 20% of employees are trained every year in fire fighting techniques.

First Aid Training in Progress

❑ Height pass test is conducted for contract workers and eligible workers are given height pass certificate to work at height above 3.5 meters.

❑ Procurement, installation & maintenance of portable fire extinguishers are carried out in IGCAR and Townships as per AERB guidelines.

❑ Testing of pressure vessels and material handling equipments are carried out periodically as per AERB regulations. Various safety and environment related reports are sent to AERB as mentioned above.

❑ Safety promotional activities like quiz, essay, slogan and cartoon competition are held every year to promote safety culture and prizes are

Physical Tests for Height Pass

awarded. Also National Safety Day, Fire Safety Week, Environment Day and Road Safety Week are celebrated every year to improve safety awareness.

Fire Fighting Demonstration

Prize Distribution Ceremony

Activities of Quality Circle

Quality Circle (QC) is a human building concept which is being practiced in industry by the collective participation of grass root level work force to improve the individual as well as the organisation. In IGCAR, Quality Circles Annual Meet which is one of the main activities of Quality Circle was conducted in July 2009. An inspiring Keynote address was delivered by Dr. N. Ravichandran, CEO, Lucas TVS, Chennai. 250 members from 27 Quality Circles, representing various groups of IGCAR, MAPS, GSO and Schools from Kalpakkam & nearby villages, participated and presented their Quality Circle

case-studies in three different categories viz. Mechanical & Manufacturing, Plant Operation & Services and School activities. Three rolling trophies were instituted for these three categories. 'MOON' Quality Circle won Dr. Placid Rodriguez rolling trophy in Mechanical and Manufacturing category, 'EXCEL' Quality Circle won Shri M.K. Ramamurthy rolling trophy in Operation & Services category and 'CONCILIUM' Quality Circle won Dr. Radhakrishnan rolling trophy in school activities category. Eminent judges from Quality Circle Forum of India, Chennai Chapter assessed the Quality Circle case studies

and adjudged twelve Quality Circle presentations as "Par Excellence", ten Quality Circles as "Excellence" and five Quality Circles as "Distinguished". Knowledge gained by different Quality Circles by participating in QCAM will help in spreading Quality Circle movements in DAE units and schools at Kalpakkam.

Shri. C.V. Gowri Sankar from QCFI Chennai Chapter delivered a technical talk which benefited members of Quality Circles. Fifty Quality Circle members from DAE units and schools visited M/s. Ashok Leyland Ltd, Chennai to interact with few of their top teams to enhance Quality Circle skills.

Quality Circles Awards

Four Quality Circles from IGCAR have secured prizes for their case studies in Chennai Chapter Quality Circles Convention (CCQCC-2009, Tamil Nadu State Convention) held at Tiruchirapalli during September 5-6, 2009. The MOON Quality Circles team of Fast Reactor Technology Group has secured Par Excellence (First), the STAR Quality Circles team of Engineering Service Group has secured Excellence (Second), the EXCEL Quality Circle team of Fast Reactor Technology Group and IRIS Quality Circle team of Metallurgy and Materials Group has secured Distinguished (Third) awards.

Excel Group receiving award

Concilium Group receiving award

Moon Group receiving award

Release of Hindi Glossary

November 6, 2009

The Department of Atomic Energy has made significant progress in various facets of Nuclear Science and Engineering. As the achievements in peaceful uses of atomic energy relate to the common man and it is imperative that these are communicated to the masses. This must be done in Hindi and other regional languages which would require translating the text from English to Hindi and subsequently to other regional languages. For facilitating the translation, a need was felt for a glossary that would provide Hindi equivalent of English scientific and technical terms used in nuclear industry. The glossary must have the approval of competent body and should be regarded as a source of reference for the whole of nuclear industry. With this in view, a committee was constituted by Dr. Baldev Raj, Director, IGCAR, with members from IGCAR and BARC Facilities at Kalpakkam, with the responsibility to prepare a suitable English-Hindi glossary, containing terms related to various aspects of nuclear industry. The committee under the chairmanship of Shri G. Vaidyanathan, Director, FRTG, started functioning in collaboration with experts from Commission of Scientific and Technical Terminology (CSTT), Ministry of Human Resource Development, Government of India. The committee decided to compile words from all DAE units and NPCIL and provide their appropriate Hindi equivalents for

Shri A. P. Joshi, Additional Secretary, Department of Atomic Energy releasing the compilation of "Hindi Glossary", Dr. R.K. Bhandari, Director, VECC, Smt. Revathi Iyer, JC(I&M), DAE, Shri G. Vaidyanathan, Chairman of the committee and other colleagues at the function.

inclusion into the glossary. Meetings were held at Hyderabad, Kolkata and Mumbai, where words from different units were discussed at length. Finally a glossary with 8500 words was compiled in March, 2009 and the printing was completed by October 2009. The glossary was released by Shri A.P. Joshi, Additional Secretary DAE, in the presence of Smt. Revathi Iyer, Joint Secretary (I&M), DAE during the 12th All India Atomic Energy Official Language conference held at VECC, Kolkata. The glossary was received well and there was lot of appreciation for the efforts taken to prepare it. The next attempt is to bring out a Tamil glossary of nuclear terms.

IGCAR – Technology Transfer Cell

A Technology Transfer Cell is set up at IGCAR during the year 2009 for liaisoning with scientists and engineers of the Centre to promote technology transfer in the form of patents, technical know-how, consultancy, and interact with industries to facilitate such transfer of technology. The mandate of the IGCAR-TTC is: (i) to work out modalities for technology transfer (ii) to liaise between the scientists/engineers of IGCAR, who are the investors, and the user industries (iii) to organize industry-inventor meets, visits etc. (iv) to prepare technology transfer documents and expedite the transfer of technology and (v) to pursue any other aspect related to technology transfer. The cell has already established the modalities for technology transfer, liaising with the inventors and the user industries, organising industry-inventor meets, and preparing technology transfer documents. Currently technology transfer of a few selected technologies are in progress. The Cell is headed by Dr. U. Kamachi Mudali, Head, CSTS-RPM & RRDD.

IGC COUNCIL

Chairman

Dr. Baldev Raj, B.E, Ph.D, D.Sc.(hc), Distinguished Scientist & Director, Indira Gandhi Centre for Atomic Research is a Member, German National Academy of Sciences, International Nuclear Energy Academy; Fellow, Third World Academy of Sciences, Fellow of all Engineering and Science Academies in India. His specialisations include testing & evaluation using nondestructive methodologies, materials characterisation, materials development, performance assessment and technology management, science and technology of fast reactors and associated fuel cycle. He has more than 750 publications in leading referred journals and books. He has co-authored 12 books and co-edited 32 books and special journal volumes, 5 Indian Standards and 18 patents to his credit. He is on the editorial boards of national and international journals. He is Editor-in-Chief of two series of books: one related to NDE Science & Technology and another related to Metallurgy & Materials. He is the past-President of International Committee on NDT. He is Vice President, International Institute of Welding (2009-2010), Academia NDT International (2009-2011), Indian National Academy of Engineering (2009-2010), Materials Research Society of India (2009-2011); Board of Director, Bharatiya Nabhikiya Vidyut Nigam Ltd. He is member of Standing Advisory Group on Nuclear Energy in IAEA and Chairman, Research Advisory Council of NTPC; Member, Scientific Advisory Council to Prime Minister and Scientific Advisory Committee to Cabinet. He has won may awards and honours, notable among them being Life Time Achievement Award of Indian Society for Non-Destructive Testing (2004), Indian Welding Society (2004), Indian Institute of Welding; Jaeger Lecture Award of International Institute of Welding (2004), International Researcher Award of International Committee on NDT (2000-2004), Indian Nuclear Society Award (2004), National Metallurgist Award (2007); Padma Shri from Government of India; Distinguished Alumni Award (2007) of Indian Institute of Science; Pandit Jawaharlal Nehru National Award from the Department of Sciene & Technology of Government of Madhya Pradesh (2007); Prof. Jai Krishna Memorial Award of Indian National Academy of Engineering (2008); Distinguished Materials Scientist Award of MRSI (2009); FICCI Annual Award for outstanding research in Materials Science (2007-08), etc. He is member, Global Energy International Prize Committee (Russia); National Nanotechnology Advisory Board of South Africa; Chairman of India-Brazil-South Africa initiative on Nano Science & Technology. His interest includes technology management, heritage, philosophy, religion and education.

Members

Dr. P. Chellapandi, Outstanding Scientist and Director, Safety Group & Associate Director of Nuclear Engineering Group. He is from the 22nd batch of BARC Training School with first rank. He joined IGCAR in 1979 and since then, he is working for the design and development of 500 MWe PFBR, over a wide spectrum of design, viz., conceptualisation, development of sophisticated computer codes, detailed analysis, design validation, preparation of preliminary safety analysis reports, execution of R&D activities involving national academic institutions and R&D establishments in the country. He got his B.E (Hons) in Mechanical Engineering with first rank from Madras University in 1978, and M.Tech in Engineering Mechanics (Gold Medalist with CGPA 10) and Ph.D in Applied Mechanics from IIT Madras. He is a senior professor of Homi Bhabha National Institute. He has played a key role to establish a state-of art structural mechanics laboratory at IGCAR, for successful erection of safety vessel in June 2008 and for getting the safety clearance recently from Project Design Safety Committee. He is also the convener of Task-force which is co-ordinating the manufacture and erection of reactor assembly components for PFBR. He has provided significant design support for FBTR, high temperature design of reduction retort for titanium sponge plant for DMRL, Hyderabad and thermo-mechanical analysis of scramjet engine to DRDL, Hyderabad. He has guided 50 Post Graduate students and published about 420 papers in journals, national and international conferences. He is a Fellow of Indian National Academy of Engineering. He has received the Homi Bhabha Science and Technology Award for the year 1997, Indian Nuclear Society Award and National Design Award in Mechanical Engineering in 2006, DAE Group achievement award for Design of PFBR Main Vessel and Safety Vessel, 2006, DAE Group Achievement Award for Seismic Design and Qualification of PFBR Components,2007 for his outstanding contributions in the design of Fast Breeder Reactor Components, Agni Award for Excellence in Self-reliance from DRDO, 2007 and DAE Group Achievement Award for Design and Manufacture of Grid Plate of PFBR (2008).

Shri S.C. Chetal graduated in Mechanical Engineering from Delhi College of Engineering in 1970. After graduating from the 14th Batch of BARC Training School, he joined IGCAR in 1971. Since then, he has been engaged in the field of fast reactor engineering. He has made contributions towards design of FBTR sodium systems and components. At present, he is Distinguished Scientist & Director, Reactor Engineering Group, IGCAR. He has made contributions towards the material selection, manufacturing technology, R&D, design and construction of 500 MWe Prototype Fast Breeder Reactor. He is member of many professional institutions and fellow of Indian National Academy of Engineering. He is a recipient of Indian Nuclear Society INS Award 2003 for contributions towards nuclear related high technology, National Design Award-2007 by Institution of Engineers, 2003 VASVIK Award, Agni Award for Excellence in Self-reliance by DRDO for titanium sponge production, and Certification of Appreciation by IAEA towards fast reactor technology. His interests include pressure vessel and materials technology. He has to his credit 350 publications in Journals/Symposium/ Conferences. He is on the Board of BHAVINI.

Dr. T. Jayakumar, B.Tech.(Metallurgy, REC Warangal), M.S (Metallurgy, IIT Madras), Ph.D (Engineering, University of Saarland, Germany) is currently Outstanding Scientist & Director, Metallurgy and Materials Group at IGCAR. Since 1978, he has been engaged in the field of Non-destructive Evaluation. Over the years he has carried out and steered innovative research and development programmes in the areas of Non-Destructive Evaluation, Failure Analysis and Structural integrity of Nuclear Components specifically for the Fast Breeder Reactor components. He is a Fellow of the Indian National Academy of Engineering. He has been a recipient of several awards such as National NDT Award from ISNT, Metallurgist of the Year award from IIM, Homi Bhabha Science and Technology Award from DAE. He has co-authored 3 books, co-edited 3 books and has published over 250 papers in International Journals. He also has 6 patents to his credit.

Shri R.N. Jayaraj, presently the Chief Executive of Nuclear Fuel Complex (NFC), Hyderabad, is a Mechanical Engineer from Osmania University, Hyderabad. Shri Jayaraj, after obtaining the Bachelors Degree in Mechanical Engineering in the year 1973, joined the 17th batch of BARC Training School, Mumbai, India for one-year orientation course in Nuclear Engineering. At BARC, he has carried out development and manufacturing of metallic fuels for thermal research reactors. Shri Jayaraj joined NFC in 1970s and was responsible for establishing a facility for the fabrication of core sub-assemblies for the Fast Breeder Test Reactor (FBTR). After successful completion of the first core requirement, he was assigned the responsibility of fabricating fuels for all the Power Reactors in India. Shri Jayaraj has played a pioneering role in standardising the manufacturing processes for the fuel bundles required for 540 MWe Pressurised Heavy Water Reactors (PHWRs). Presently he is engaged in the expansion activities of fuel fabrication capacities to meet the enhanced fuel demands. Shri Jayaraj has received many prestigious awards including the Indian Nuclear Society (INS) Award and The Indian Institute of Metals (IIM) SMS Demag Excellence Award-2009 (Gold Medal). He was also conferred with the Honorary Fellowship of Indian Institute of Chemical Engineers. Shri Jayaraj, besides being a Member of IGC Council, is on the Board of Directors of Uranium Corporation of India Limited (UCIL) and Indian Rare Earths Limited (IREL). He is also the Council Member of Indian Institute of Metals (IIM), Kolkata and the Chairman of Indian Nuclear Society, Hyderabad Chapter.

Shri H.S. Kamath, B.E (Metallurgy), is a Distinguished Scientist and Director of the Nuclear Fuels Group in BARC. He has been associated with the development of plutonium bearing nuclear fuels for the past thirty five years, which started with the fabrication of fuel for 'PURNIMA' in 1970-1972. His main area of work is in the development of uranium-plutonium mixed oxide (MOX) fuels for nuclear power programme. He has made important contributions in this field, both in laboratory scale as well as industrial scale activities. His most important contribution has been the setting up of the industrial scale MOX fuel fabrication plant at Tarapur. Shri Kamath is the recipient of Indian Nuclear Society Award for the year 2003 in recognition of his outstanding contributions in the field of nuclear fuel fabrication. Shri H.S. Kamath is the recipient of DAE Lifetime Achievement Award for the year 2007.

Prof. P.K. Kaw, Ph.D. (Physics) from IIT Delhi, is the Director of Institute for Plasma Research, Gandhinagar since 1986. The Institute has pioneered plasma physics research in India which includes design, development and fabrication of two tokamaks, ADITYA and SST1, research work on a large number of fundamental plasma physics experiments and work on industrial applications of plasma physics. ADITYA was the first tokamak to discover intermittency in edge and SOL turbulence. The Institute also spearheaded India's case for participation in ITER and is now the nodal domestic agency for ITER. Prof. Kaw's personal research work in this period includes physics of intermittency, drift waves and anomalous transport, MARFES, solitons, laser fusion, anomalous stopping effects, dusty plasmas, non-neutral plasmas, quark gluon plasmas, etc. Earlier he had held positions like Princeton University Plasma Physics Laboratory Research Staff and Professor at Physical Research Laboratory, Ahmedabad before taking over as Director, Plasma Physics Program in 1982. He played a key role in initiating tokamak physics program in India. He has more than 305 research papers to his credit in international journals. He has several honours to his credit and he delivered important lectures: Artsimovitch Memorial lecture at the IAEA Fusion Energy Conference in 1992, Invited talk on International Energy Research at the APS Centennial celebrations (1999) in Atlanta, Georgia and a presentation on the International impact of USDOE Fusion Theory Program to the NSF-NRC Panel Chaired by C F Kennel, San Diego are just a few of them to name. Prof. Kaw was also the Chairman of the International Fusion Research Council (IFRC) of IAEA from 2000 to 2007 and was the Chairman of the Science & Technology Advisory Committee [STAC] of the ITER Governing Council till December 2009. He was awarded the TWAS Prize in Physics during 2008, by the TWAS Council of the Academy of Sciences for the developing world.

Shri H.S. Kushwaha, B.Sc., M.Tech.(IIT, Kanpur), is presently the Director of Health, Safety and Environment Group at BARC. He has made significant and important contributions in the design and analysis of nuclear structures, components and piping of Indian Pressurised Heavy Water Reactors (PHWR). He has done pioneering work in the area of seismic design and analysis of 500 MWe PHWR at Tarapur, Maharashtra. He has developed several finite element computer programmes in the field of structural mechanics, heat transfer and fluid mechanics. He has developed an improved finite element method using up-winding schemes to solve three dimensional advection-diffusion equation. He is an active member of Project Design Safety Committee of PHWRs/ FBR, Civil Engineering Safety Committee and Safety Review Committee for Operating Plants (SARCOP) constituted by AERB, Mumbai. He has published around 400 papers/reports in national and international journals.

Shri Y.C. Manjunatha, Director, Engineering Services Group of Indira Gandhi Centre for Atomic Research, Kalpakkam, is a M.Tech. in Electrical Engineering from IIT, Madras and graduated from the 16th batch of BARC Training School. He steers one of the largest multidisciplinary groups in the Centre which focuses on providing reliable and robust services through cutting edge technologies and methodologies. The Group comprises of AC&VSD, CWD, CED, ESD & QAD and infrastructural divisions of GSO. Some of his major contributions are development and sustenance of infrastructural works of IGCAR & GSO involving civil, electrical, air conditioning and ventilation, communication, workshop and QA activities. He has published more than twelve papers. He has nurtured and mentored the quality circle activities of the Group. He has a significant contribution in making the project site and townships more green and presentable. Introduction of a systematic domestic solid waste management system at GSO is being appreciated by all. The present focus is on establishment of 2 MGD desalination plant, water treatment plants and provision of common services features to FRFCF. He is a fellow of Institution of Engineers, patron of ISHRAE and Chairman of Kalpakkam Chapter of Indian Society of Non-Destructive Testing.

Shri S.D. Misra, B.E (Electrical & Mechanical Engineering) is presently the Director of Nuclear Recycle Group at BARC. He is from 13th Batch of BARC Training School and has been involved in the Back End activities of Nuclear Fuel Cycle. He was a member of the team that pioneered the setting up of the first Vitrification Plant in the country. Shri Misra was responsible for the design and construction of vitrification plants at Trombay & Kalpakkam. He was also instrumental in solving all the problems faced in the first resin fixation facility at Narora Atomic Power Project and made it operational. Shri Misra has participated in a number of symposia and seminars on

radioactive waste management and has also worked as an expert on various technical committees of IAEA. Presently he is a Member of International Radioactive Waste Technical Committee (WATEC) of IAEA. He has also served as Director, Purchase & Stores, DPS. In this capacity, he has successfully overcome the problems of technology control regime and made available some of the critical stores for the programmes of the department. Presently, as Director, Nuclear Recycle Group, he is holding the responsibility of setting up and operation of Reprocessing and Waste Management Plants at various sites in the country.

Dr. Prasenjit Mukherjee, IAS was born on 27th June 1957 and had his early education in Orissa. He passed his B.A. Honors in English in 1974, securing the first position in first class with distinction in other subjects. He was awarded the University Gold Medal by the Utkal University for securing the first position in M.A. English in 1976. From 1977 to 1980 he served as a lecturer in Berhampur University, Orissa. He appeared for the Civil Services Examination and was selected to the Indian Audit & Accounts Service in 1980. In 1991, he went on deputation to Government of India in the Ministry of Commerce where he worked as Director (Finance & West Europe). Under the Colombo Plan, he was selected and deputed to the University of Manchester Institute of Science & Technology (UMIST) in U.K. in 1995 from where he successfully completed his M.Sc. degree in Project Management. On reversion to the department, he served as Accountant General (Audit) II, Lucknow, U.P., from November 1996 to June 2000, and as Accountant General (A& E), Karnataka, Bangalore from July 2000 to December 2004. In December 2004, he went on deputation to the Department of Space as Joint Secretary (Finance) and in April 2008, he joined the Department of Atomic Energy as Joint Secretary (R&D). Recently, Dr. Mukherjee was awarded the Ph.D. degree from the National Law School of India University at Bangalore on the subject of disinvestment in India.

Shri R. Natarajan, a Chemical Engineer from Annamalai University, joined the Department of Atomic Energy in 1975. He is presently the Director of Reprocessing Group in IGCAR. Under his leadership, the CORAL facility, for establishing the process technology for the reprocessing of fast reactor fuels, was designed, erected and commissioned. He led the team which has successfully completed the reprocessing of fast reactor spent fuel, with a burn-up of as high as 155 GWd/t with plutonium rich fuels, for the first time in the world. As Director of Reprocessing Group, he is responsible for the R&D activities of fast reactor fuel reprocessing and setting up of demonstration as well as the commercial PFBR fuel reprocessing plants. His specialisation is in the design process flow sheets and plant design. He has also experience in the design and operation of Thorium-Uranium cycles. He has participated in the irradiated thorium fuel reprocessing campaigns at the Reprocessing Development Laboratory and the ^{233}U recovered is used as fuel for the reactor KAMINI. He has interests in solvent extraction process modeling, extraction equipment design, design of feed clarification systems of high active solutions, acid recovery systems, system designs of radioactive offgas circuits and ventilation design of radiochemical plants. He has over ninety five technical presentations and publications to his credit. He has won prestigious NOCIL Award for Excellence in Design and Development of Process Plant and Equipment for the year 2005 for his contribution in the development of fast reactor fuel reprocessing. He is also the recipient of Indian Nuclear Society's INS award for the year 2006 for his contributions in Nuclear Fuel Cycle technologies.

Shri A.L.N. Rao, B.E. (Electrical), is presently the Chairman & Chief Executive of the Heavy Water Board. He is from the 15th batch of BARC Training School. He was awarded Junior License Certificate in 1974 and took independent charge of the unit consisting of reactor, turbine, generator and associated utilities and control systems of TAPS. He has participated in the first refuelling operations which consisted of transferring the irradiated fuel bundles from the reactor core to fuel storage pool and loading the fresh fuel bundles from storage pool into the reactor under 60 feet of water. He had also replaced the core components which was a challenging task. In the year 1978, he obtained Senior License Certificate and took independent charge of the complete plant in shifts. After moving to Heavy Water Board in 1984, he closely followed up the project activities of the Captive Power Plant of Heavy Water Plant (Manuguru) and in the year 1987 he took over as Operation Manager of Captive Power Plant. He assumed charge as General Manager of the Heavy Water Plant (Manuguru), which is the largest heavy water producing plant in India, in the year 1998. He became Associate Director (Projects/Energy & Services) in the year 2003 at the Central Office and took charge as Director (Energy & Services/Operation) in the year 2004. In 2005 he was designated as Executive Director (Projects/Energy & Services). During this period,

he formed Energy Cells at every plant with common monitoring at corporate office. The Specific Energy Consumption had come down to 32 GJ/kg of Heavy Water produced during this period. He discharged the duties as the Secretary of the Heavy Water Board. He coordinated all the activities related to export of Heavy Water to South Korea and the Republic of China. As Management Representative for Quality Management Systems as per ISO 9001, he followed up all the activities and obtained ISO 9001 Certificate for Board Office.

Dr. R.K. Sinha, B.E (Mechanical Engineering), is presently a Distinguished Scientist, Director of Reactor Design and Development Group, and Director of Design Manufacturing and Automation Group at BARC. He is a nationally and internationally recognised expert in the area of nuclear reactor technology. He has handled several major assignments relating to the Indian research and power reactors. In particular, he has specialised in design, development and safety related activities relating to coolant channels of heavy water reactors. He is currently guiding the design and development of the innovative Advanced Heavy Water Reactor and Compact High Temperature Reactor. Dr. Sinha has received several awards and honours including the Homi Bhabha Science and Technology Award, VASVIK Award, Indian Nuclear Society Award and DAE Special Contributions Award. He is a Fellow of the Indian National Academy of Engineering.

Shri G. Srinivasan is a mechanical engineer from the 18th batch of BARC Training School. He joined FBTR project as a designer in 1975, and participated in the design, fabrication and installation of Reactor Assembly Components. He moved over to O&M in 1983. After holding the positions of Senior Engineer (Planning) & Senior Engineer (Technical), he took over as Technical Services Superintendent and later as AD (O&M). He is Director, ROMG since Sep. 2008.

Dr. P. Swaminathan, graduated with honours degree in Electronics & Communication Engineering from REC, Tiruchirapalli in 1971. He is the Gold medalist of University of Madras. After undergoing one year course in Nuclear Science & Engineering from BARC Training School, he joined IGCAR in 1972. He further underwent one year training course in main frame computer system from International Honeywell Bull Training Institute, Paris. Dr. P Swaminathan is the main architect for the design, development, installation and commissioning of Fault Tolerant Safety Critical Real Time Computer System for FBTR and library INFO service committee. As Director of Electronics & Instrumentation Group, he is actively engaged in the development of Safety Instrumentation, Pulsating sensors, Distributed Digital Control System, Full scope Training Simulator and Knowledge Management System for Fast Breeder Reactor Programe. Dr. P Swaminathan is a Fellow of Institution of Engineers. He also holds master degree in Management Science and doctorate degree in electronics engineering. He has brought out Indian standards for the usage of computers in nuclear installations. He has over 50 publications in international journals/seminars. Also as Chairman, Hospital Management Committee, he ensures smooth functioning of the Health Care System and flow of campus wide networked library & scientific information.

Shri Umesh Chandra is Senior Executive Director (Safety and Knowledge Management) in NPCIL. His areas of responsibilities include Reactor Safety & Analysis of Design, Health, Safety & Environment of nuclear power plants in operation and construction, Software Quality Assurance, Training Simulators, Knowledge Management, IT infrastructure and Communications. He has been responsible for establishing R&D infrastructure and activities in NPCIL, including setting up an R&D Centre at Tarapur and a computer based C&I lab at NPCIL HQ. He has been responsible for design of Control and Instrumentation of 540 MWe PHWRs at Tarapur. Earlier at BARC, he has been a developer of computer based control and monitoring systems of several nuclear power plants. He has also been responsible for establishment of a group engaged in Independent Verification and Validation of Digital Systems in NPCIL. He has contributed in preparation of safety guides of AERB for safety systems and computer based I&C systems and also in safety reviews of projects. Shri Umesh Chandra is a Distinguished Scientist and a graduate of IIT, Kanpur.

Shri G. Vaidyanathan, graduated in Engineering from Delhi University in 1971 and joined IGCAR in 1972 after completion of one year orientation course in BARC Training School. Later he acquired a Post Graduate Degree in Operation Management. Presently he is an Outstanding Scientist and Director of Fast Reactor Technology Group. Since 1972, he has been actively involved in the field of fast reactor design, thermal hydraulic analysis and experiments. He has made significant contributions to numerical simulation of heat transfer and fluid flow processes in sodium cooled fast reactors. He has meticulously planned and carried out R&D for the thermal hydraulics of Fast Reactors. He has also contributed significantly as member of the IGCAR safety committee. He was instrumental in setting up the Steam Generator Test Facility at IGCAR. He has to his credit about 185 publications in journals/conferences and has co-authored one book.

Dr. P.R. Vasudeva Rao, is a Distinguished Scientist and presently Director of Chemistry Group in IGCAR. He obtained his Doctorate degree in Inorganic Chemistry from Bombay University in 1979. He has played an active role in shaping the Radiochemistry Programme of IGCAR to its current status. His research interests cover a wide range of areas such as development of alternate extractants and resins for actinide recovery solvent extraction, third phase formation, thermodynamics, applications of photochemistry in actinide separations, development of pyrochemical and other non-aqueous processes for recovery of actinides and rare earths, thermochemical studies on nuclear materials, fuel behaviour in reactors, burn-up measurements and non-destructive assay. He has published more than 150 papers in reputed international journals apart from guiding several research scholars for their doctorate degrees. He is a life member of Indian Nuclear Society, Materials Research Society of India, Society for Advancement of Electrochemical Science and Technology, and Indian Association of Nuclear Chemists and Allied Scientists (IANCAS). He has been awarded the MRSI Medal in 1998 and the INS award for the year 2007. He is also a Fellow of Tamil Nadu Academy of Sciences. He is a member of the International Advisory Board of the Journal of Nuclear Materials.

Dr. V. Venugopal, M.Sc.,Ph.D, is presently an Outstanding Scientist and the Director of Radiochemistry and Isotope Group at BARC, Mumbai, and Officer-in-charge, Nuclear Material Accounting and Control (NUMAC) cell of DAE. He is currently a member of Standing Advisory Group for Safeguard Implementation (SAGSI) to advice Director General IAEA on Safeguards Matters. He is a specialist in the field of thermal/ thermodynamics of plutonium based fuels at high temperature, chemical quality control of fuel, X-ray and solid state chemistry and oversees Radioisotope and Radiation Technology Programs at BARC. He is the Chairman of Radiation Technology and Applications Committee (RTA C) of BRNS and a member of BRIT board. He is a member of safety committees such as OPSRC and CFSRC under BSC at BARC. He is a Senior Professor of Homi Bhabha National Institute (HBNI). He is the convenor of chemistry discipline in HBNI. He has to his credit more than 190 publications in international journals. Widely acclaimed as an expert in the area of thermodynamics, Dr. Venugopal is the President of Indian Thermal Analysis Society (ITAS), President of Indian Association of Nuclear Chemists and allied Scientists (IANCAS) and Vice President INS. He is also a member of several professional bodies NAARRI, ISAS, ISEAS, ISMAS, MRSI and Hindi Vigyan Parishad. He has received many awards including the Netzsch-ITAS award in 2001, ISCAS silver medal in 2002 and MRSI medal for 2003-04, INS award for 2005 and Special contribution award of DAE in 2006.

Dr. C.S. Sundar, obtained his Masters degree in Physics from the University of Delhi in 1972, and a Ph.D in Physics from the University of Madras in 1983. He heads the Materials Science Group at IGCAR with a comprehensive research programme on basic research in materials science. Dr. Sundar's research contributions, spanning over three decades, has been on the investigation of structure, defects and phase transitions in novel materials using the techniques of positron annihilation and infrared spectroscopy, and has over 100 journal publications. He is a recipient of the Materials Research Society of India Medal, 1994 and the MRSI-ICSC superconductivity and Materials Research Annual Prize 2007. He is a Fellow of the Indian Academy of Sciences, Bangalore and the National Academy of Sciences, Allahabad. Dr. Sundar is a member of the DST-Programme Advisory Committee on Condensed Matter Physics and Materials Science and the Nano Science Advisory Group of Department of Science and Technology. He   is on the Editorial Board of PRAMANA & Solid State Communications.

Members of IGCSC and Activities of Various Groups

Chairman
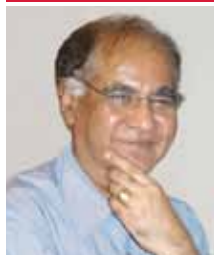
Dr. Baldev Raj
Director, IGCAR

Chemistry Group

Dr. P.R. Vasudeva Rao	Dr. V. Ganesan	Dr. T. Gnanasekaran	Shri G. Ravishankar	Dr. T.G. Srinivasan
Director	*Head, MCD*	*Head, LM&SCD*	*Head, CFD*	*Head, FChD*

The Chemistry Group is responsible for carrying out R&D to provide inputs with respect to all the chemistry aspects of the fast reactor and its fuel cycle. Besides the R&D activities, the Chemistry Group also provides extensive analytical support using a wide range of analytical techniques to all the programmes at Kalpakkam. The areas of R&D in Chemistry Group include sodium chemistry, chemistry of un-irradiated as well as irradiated fuel materials, development of fuel cycle, high temperature chemistry, analytical chemistry, spectroscopy and boron chemistry. Chemistry Group also has been developing instrumentation and facilities in support of the R&D programme. Development of sensors for PFBR and sensors for environmental applications, cover gas purification system for PFBR, development of radionuclide traps for PFBR, development of cleaning and decontamination techniques for fast reactor components, development of Laser Induced Breakdown Spectroscopy and X-ray absorption based techniques for on-line monitoring of plutonium streams in reprocessing plants, development of technology for production of plutonium rich fuels and minor actinide containing fuels through sol-gel route and development of sodium bonding for metallic fuels are some of the R&D programmes on the anvil. Recent achievements include successful testing of the electrochemical hydrogen sensor in PHENIX reactor in France, trial fabrication of fuel pins containing uranium dioxide microspheres, production of enriched elemental boron, mixer settler demonstration of partitioning of minor actinides and lanthanides from fuel solution in hot cells, demonstration of sodium bonding of U-Zr slug with SS316 pin and lab scale separation of ^{89}Sr from yttrium irradiated in FBTR.

Electronics and Instrumentation Group

The Electronics and Instrumentation Group is actively engaged in the development of Strategic Safety Instrumentation Systems for Fast Breeder Reactor and Fuel Reprocessing Programme such as Real Time Computer Systems, Safety Logic Systems, Expert systems, Distributed Digital Control Systems etc. Unique Instrumentation systems such as Electromagnetic Time Domain Survey System is also being developed to detect deeply buried uranium ore. Highly reliable instrumentation systems are being developed using modern VLSI design tools, thermal design tools, EMI/EMC design tools etc. Application software packages are being developed using powerful CASE TOOL. The development process is ISO certified. A Full scope Replica Type Training Simulator is being developed for training the operators of Prototype Fast Breeder Reactor. Walk-through of different areas of the reactor is being developed using PDMS package. State of the art visualisation center with stereoscopic projection is set up. Intranet based Knowledge Management

| Dr. P. Swaminathan
Director | Shri S. Ilango Sambasivan
Head, EID | Shri N. Murali
Head, RTSD | Dr. M. Sai Baba
Head, SIRD | Shri S.A.V. Satya Murty
Head, CD | Dr. A. Vijaya
Head, MD |

System is being managed. Simplicity in instrumentation is being realised through the innovative programme on creation of pulsating sensors for diverse parameters, enabling development of completely indigenous plant monitoring and surveillance systems, rapid analytical and diagnostic tools. Security electronics systems are constantly being updated for Kalpakkam site. Biometric hand geometry based attendance system is commissioned and is operating satisfactorily. The group has Scientific Information Resource Division which is in pursuance of its objective of providing efficient and effective information service to the Scientists, Engineers, TSOs and Research Scholars at Kalpakkam Campus. The group is also responsible to ensure satisfactory health services to the residents of Kalpakkam and Anupuram Townships.

Engineering Services Group

Engineering Services Group is responsible for providing quality services pertaining to Civil Engineering, Electrical Engineering, Voice Communication Systems, Air-conditioning & Ventilation Systems, Material Handling Equipments, Central Workshop activities, Quality Control & Quality Assurance and Testing. The group also coordinates the telecommunication requirements of the Centre. The group has a mandate to establish additional infrastructure requirements so as to meet Design, R&D and operational objectives of IGCAR. The group has expert teams with capability to design, engineer and execute systems under their jurisdiction. Electricity, water, quality-air and other services are being extended to other units of DAE located at Kalpakkam. The nature of work involves interaction with several State Government and Central Government Organisations.

| Shri Y.C. Manjunatha
Director | Shri K. Manoharan
Deputy Director, GSO | Shri A. Jyothish Kumar
Head, ESD | Shri A.S.L.K. Rao
Head, ACVSD & CWD |

| Shri C. Sivathanu Pillai
Head, CED | Dr. B. Venkatraman
Head, QAD | Shri N.Vijayan Varier
Head, TC&QCS |

Fast Reactor Technology Group

The Fast Reactor Technology Group is actively involved in development and testing of scaled models, prototype components for PFBR, sodium pumps and instrumentation and process development for boron enrichment and separation technologies. The group has sodium and water test facilities, 5.5 MWt steam generator test facility and boron enrichment plant. FRTG carries out heat and mass transfer studies in water loops, liquid sodium

Shri G. Vaidyanathan	Shri P. Kalyanasundaram	Dr. C. Anand Babu	Shri B. Krishnakumar	Shri K.K. Rajan
Director	*Associate Director, FRTG*	*Head, ST&THD*	*Head, C&IDD*	*Head, SFD*

and cover gas and development of sodium components like cold trap, sodium level and flow sensors and leak detectors. FRTG also carries out testing of control rod mechanisms, inflatable seals and full scale fuel handling machines in air and sodium. Further studies are carried out for pressure drop and cavitation in fuel and other subassemblies and reactor assembly flow patterns. The steam generator test facility is used for carrying out detailed temperature measurements, study of transient response and thermo hydraulic instability of sodium heated once-through steam generator. The group is also responsible for vibration testing of steam generator, intermediate heat exchanger, rotating machinery etc. In short, the group is working on all engineering aspects of FBRs.

Metallurgy and Materials Group

Dr. T. Jayakumar	Shri K.V. Kasiviswanathan	Dr. A.K. Bhaduri	Dr. R.K. Dayal
Director , MMG & Head, NDED	*Associate Director, GRIP*	*Head, MTD*	*Head, CSTD*

Shri Jojo Joseph	Dr. M.D. Mathew	Dr. S. Venugopal	Dr. M. Vijayalakshmi
Head, PIED	*Head, MMD*	*Head, RIRD*	*Head, PMD*

Metallurgy and Materials Group pursues a wide range of Research Programmes of the Centre that encompass both basic and applied aspects of the structural materials development for Fast Breeder Reactors and associated fuel cycle facilities. The key areas of research and development have been broadly classified and addressed in the dedicated administrative Divisions, include : 1. Materials Design and Manufacturing Technology, 2. Materials Mechanics and Properties, 3. Physical Metallurgy and Characterisation, 4. Non-destructive Evaluation and Inservice Inspection, 5. Irradiation Experiments and Post-Irradiation Examination, 6. Robotics, Innovative design, Engineering and Synthesis and 7. Corrosion Science and Technology. The current activities of importance being pursued are: development of special materials like Oxide Dispersion Strengthened (ODS) Ferritic Steels and Reduced Activation Ferritic-Martensitic (RAFM) Steels, development of welding consumables, optimisation of thermo mechanical treatments and other fabrication processes, characterisation of microstructures and mechanical properties and their interrelationship, modeling of microstructural stability and phase evolution, corrosion and bio-fouling studies, development and application of specialised NDE techniques and advanced mechanical property measurements like impression creep testing, irradiation experiments and development of technologies for robotics and remote handling. The group also has several novel technology development missions for FBRs such as the development of hard facing procedures for critical components, studies on leak detection in sodium circuits using Raman distributed optical fibre sensor and ferrofluid based seals for sodium pump applications.

Materials Science Group

| **Dr. C.S. Sundar** | **Dr. A.K. Arora** | **Dr. A.K. Tyagi** | **Shri M.C. Valsakumar** |
| *Director* | *Head, CMPD* | *Head, SND* | *Head, MPD* |

The Materials Science Group, comprising of three Divisions, has the mandate of pursuing high quality basic research on topical problems in Materials Science, to work towards ion beam and computer simulation of radiation damage and to pursue research on innovative sensors accruing from basic research in superconductivity and nanomaterials. The Condensed Matter Physics Division focuses on the investigation of physical properties of novel materials under temperature, pressure and magnetic fields. Active research programs on Raman spectroscopy studies of vibrational properties, Dynamic light scattering and Confocal Microscopy studies of soft condensed matter, Laser heated diamond anvil cell facility for synthesis and study of materials under high pressure and high temperature and investigation of material properties at low temperatures under high magnetic fields and pressures are being pursued. The indigenously built SQUID sensors and control electronics have been translated into SQUID based measuring systems such as a high field magnetometer, a SQUID based set-up for Non-Destructive Evaluation (NDE), and SQUID based Magnetoencephalography (MEG). The activities of Materials Physics Division pertain to studies on Ion beam simulation of radiation damage using a 1.7 MV tandem accelerator; in depth studies on defects using Positron Annihilation Spectroscopy and computer simulation of material properties. The Surface and Nanoscience Division focuses on studies on thin films using a variety of techniques such as Secondary Ion Mass Spectrometry and Scanning Probe Microscopy. Studies on controlled growth of nanometric multi-layer films for increased hardness, and exploration of nanomaterials, micro-machined cantilevers and MEMS as sensors are being actively pursued.

Reactor Engineering Group

| **Shri S.C. Chetal** | **Dr. P. Chellapandi** | **Shri V. Balasubramaniyan** | **Shri K. Madhusoodanan** | **Dr. P. Mohanakrishnan** |
| *Director* | *Associate Director, NEG* | *Head, HTSD* | *Head, PPCD* | *Head, RPD* |

| **Shri P. Puthiyavinayagam** | **Shri S. Raghupathy** | **Shri P. Selvaraj** | **Shri C. Sivathanu Pillai** |
| *Head, RCD* | *Head, CH&MD* | *Head, MHD* | *Head, CED* |

Reactor Engineering Group (REG) is responsible for the design of fast reactors. It has carried out the design of 500 MWe Prototype Fast Breeder Reactor (PFBR). REG is responsible for getting the regulatory clearance for PFBR from AERB. R&D co-ordination towards FBRs and execution of R&D for structural mechanics is also the responsibility of the group. Along with BHAVINI, REG engineers are responsible for getting the NSSS components

of PFBR manufactured by the Indian industries. REG provides the design support to FBTR. REG is presently engaged in design of the future 500 MWe FBRs to provide enhanced safety and improved economics. This includes safety criteria, innovative design futures, manufacturing technology programme and R&D needs. REG has acquired expertise in design of fast reactors and design of components for elevated temperature applications. As a spin off, mechanical design expertise is being provided to a number of organisations for non-reactor activities.

Reactor Operations and Maintenance Group

| **Shri G. Srinivasan** | **Dr. V. Ramanathan** | **Shri B. Ananthapadmanaban** | **Shri K.V. Suresh Kumar** | **Miss S. Usha** | **Shri P.R. Swaminathan** |
| Director | Associate Director, O&M | Head, RMD | Head, ROD | Head, TSD | Head, PPD |

ROMG is responsible for safe operation of Fast Breeder Test Reactor (FBTR) and KAMINI reactor within the limits given in technical specification documents. The group also takes part in the operational safety review of PFBR project documents. The Training Section of the group, besides training O&M staff of FBTR and KAMINI, is also responsible for training the O&M staff of PFBR and future FBRs. Progressive modifications in FBTR to increase its availability and for gaining newer experience in operation, utilising the reactor for irradiation of advanced fuels and materials for fast reactors and conducting safety related experiments form a major part of ROMG's activities.

Reprocessing Group

| **Shri R. Natarajan** | **Dr. U. Kamachi Mudali** | **Shri P. Ramkumar** | **Shri A. Ravishankar** | **Shri V. Sundararaman** | **Shri M. Venkataraman** |
| Director | Head, RRDD | Head, RPSD | Head, RPDD | Head, FRPD | Head, RPOD |

The success of Indian Fast Breeder Reactor (FBR) programme depends on the closure of fuel cycle within a short period. The Reprocessing Group (RpG) of IGCAR is responsible for the development of fast reactor fuel reprocessing technology as well as design, construction and operation of the reprocessing plants. Various R&D activities are being carried in the Reprocessing Development Laboratory (RDL). Extensive, engineering scale testing of equipment and systems are carried out before installation in hot cells. Chopper, dissolver, feed clarification equipment, centrifugal extractors and different types of pulse columns are few of the important equipment being developed at RDL. Apart from equipment development, research is undertaken for understanding and solving various process and chemistry problems of fast reactor fuel reprocessing such as, process flowsheet studies to improve the plant performance for higher recoveries and reduced waste generation, mathematical modeling of solvent extraction of the complex U-Pu system, solvent management, development of online monitoring of Pu for process control, liquid flow metering in high radioactive fields etc. In one of the hot cell facilities at RDL, ^{233}U was recovered from irradiated thorium rods using THOREX process which is used as fuel in KAMINI reactor and in FBTR (as PFBR test fuel). The other hot cell facility, called CORAL (COmpact facility for Reprocessing Advanced fuels in Lead cells) commissioned in 2003, is being deployed as a versatile test bed for validating the process flow sheet and scaling up of equipment designs for fast reactor fuel reprocessing, by processing the FBTR spent fuel. This experimental facility has been used for

reprocessing several batches of mixed carbide fuels irradiated in FBTR with 25, 50, 100 and 155 GWd/t burn ups. This has provided valuable experience to the design of Demonstration Fast Reactor Fuel Reprocessing Plant (DFRP) in which all the types of FBTR fuels, namely the mixed carbide and oxide of different compositions, will be reprocessed on a regular basis. DFRP is designed to reprocess PFBR fuel subassemblies also for demonstrating the reprocessing of irradiated PFBR oxide fuels. In addition to these activities, RpG is also carrying out the design of the reprocessing plant, FRP, for reprocessing spent fuels of PFBR on commercial basis.

Safety Group

Dr. P. Chellapandi	Shri N. Kasinathan	Dr. B. Venkatraman
Director	*Head, SED*	*Head, RSD*

Safety Group consists of Safety Engineering Division, Radiological Safety Division and Environmental & Industrial Safety Section. Safety Engineering Division is engaged in the simulated experimental studies and development of computer codes for severe accident analysis specific to Fast Breeder Reactor situations. This includes investigation of core disruptive accident scenarios, sodium fire, molten fuel coolant interaction, core catcher, post accident heat removal capabilities and fire hazard analysis. Radiological Safety Division is mainly responsible for the research and development activities in radiation safety. The division provides health physics services for all the radioactive facilities in IGCAR. Studies on criticality safety, radiological safety, shield design, bio-dosimetry, concrete ageing, environmental impact, atmospheric dispersion, aerosol transport, meteorological measurement and development of radiation detectors, pulsed neutron generator for actinide assay and decision support system for radiological emergencies are some of the key areas of research being carried out presently. Environmental & Industrial Safety Section provides industrial safety services to all the facilities at IGCAR. The section also carries out R&D in the domain of biodiversity, biofouling, sediment characterisation, Phytoplankton (plants) and Zooplankton (animals) studies. The group organises public awareness programs on radiation safety and nuclear energy. It also carries out training and awareness programs on industrial, radiation and fire safety to occupational workers.

Fast Reactor Fuel Cycle Facility

Shri P.V. Kumar
Project Director

Work on design of the Fast Reactor Fuel Cycle Facility (FRFCF) to close the fuel cycle of Prototype Fast Breeder Reactor (PFBR) is in progress. This work is being piloted by IGCAR with technical support from BARC and NFC. Revised financial sanction for the preparatory project for development of site infrastructure and engineering of FRFCF has been obtained and the work is in progress. Approval of AERB for the site has been obtained. Technical investigations of the site like geotechnical, hydro-geological studies and estimation of design basis flood level have been completed. Basic infrastructure like approach roads, construction power supply system, and storage/construction office space is being created at the site to reduce the lead time required to commence the construction work once the FRFCF project is sanctioned. Review of the preliminary safety analysis report by Project Design Safety Committee for FRFCF and specialist working groups is in progress. The detailed project report and detailed design are planned to be prepared with assistance from consultants. Process of appointment of consultants is in progress. Detailed project report for FRFCF is planned to be submitted for financial sanction during the year 2009-10.

Planning Division

Shri A.S.L.K. Rao
Head, PD

Planning Division is responsible for budget monitoring and control of capital projects of the Centre under R&D, I&M and Power Sectors. Being the nodal agency it has to closely coordinate between Project Coordinators, Accounts, Purchase and Stores for meeting the financial milestones. In addition, it interacts regularly with DAE for the matters related to approvals, financial sanctions, clarifications, reports and also provide inputs to DAE for queries raised in Parliament, Planning Commission, Finance Ministry and Department of Science and Technology etc. It also coordinates with BARC, NFC, RRCAT and VECC for obtaining their support for the capital projects executed by them for the Centre. In order to ease the work functions in Administration and Accounts wings, several online services were made available in the intranet for use by the officials of the Centre. With a view to implementing integrated approach towards office automation of financial, purchase, stores and administration and accounts activities, a work flow automation system has been designed and action for the procurement and installation of the system is in progress.

Strategic and Human Resources Planning Section

Dr. M. Sai Baba
Head, S & HRPS

The section has the mandate of planning for the Strategic and Human Resource needs of the Centre which involve: Planning and running the training school programs at Training School; Collaborative projects with various R&D organisations and academic institutes; Compilation of technical reports on important activities of the Centre; interacting and coordinating with national and international delegations; Assessing and projecting the human resource needs of the Centre for effective deployment and utilisation; Interacting with the research scholars at the Centre; Planning and organising meetings related to human resource and personality development.

Madras Regional Purchase Unit

Shri K. Balachander
Regional Director, MRPU

Material Management activities for IGCAR and General Services Organisation are taken care by Madras Regional Purchase Unit which comes under Directorate of Purchase & Stores of Department of Atomic Energy. Procurement and payment to suppliers are carried out at Chennai and inventory and accounting are carried out by Central Stores at Kalpakkam. Total expenditure for purchase of material and equipment in the calendar year 2009 has crossed 150 crores.Some of the major equipment for which orders have been placed are Welded Grid Plate, Secondary Ion Mass Spectrometer, Transmission Electron Microscope and Distribution Transformers. Timely action taken by MRPU has resulted in excellent compliance of expenditure budget targets.

Administration and Accounts

Shri V. Dayalan
Chief Administrative Officer

Shri C.G.S. NAIR
Joint Controller (Finance & Accounts)

Shri R.G. Raghavan
AO(R&SR), Secretary, IGCSC

LIST OF IMPORTANT ABBREVIATIONS

AERB	Atomic Energy Regulatory Board
BARC	Bhabha Atomic Research Centre
BARCF	BARC Facilities
BHAVINI	Bharatiya Nabhikiya Vidyut Nigam Limited
CDPS	Central Data Processing System
CERMON	Continuous Environmental Radiation Monitoring Network
CG	Chemistry Group
CMPD	Condensed Matter Physics Division
CORAL	COmpact facility for Reprocessing Advanced fuels in Lead cell
CSTD	Corrosion Science and Technology Division
CWD	Central Workshop Division
EID	Electronics and Instrumentation Division
EIG	Electronics and Instrumentation Group
ESG	Engineering Services Group
FBR	Fast Breeder Reactor
FBTR	Fast Breeder Test Reactor
FChD	Fuel Chemistry Division
FRFCF	Fast Reactor Fuel Cycle Facility
FRTG	Fast Reactor Technology Group
IAEA	International Atomic Energy Agency
IIT	Indian Institute of Technology
IMSc	Institute of Mathematical Sciences
LMFBR	Liquid Metal Cooled Fast Breeder Reactor
MAPS	Madras Atomic Power Station
MCD	Materials Chemistry Division
MD	Medical Division
MMD	Mechanical Metallurgy Division
MMG	Metallurgy and Materials Group
MPD	Metal Physics Division
MSG	Materials Science Group
MTD	Materials Technology Division
NFC	Nuclear Fuel Complex
NICB	Nuclear Island Connected Buildings
NPC	Nuclear Power Corporation
NSSS	Nuclear Steam Supply System
PFBR	Prototype Fast Breeder Reactor
PHWR	Pressurised Heavy Water Reactor
PMD	Physical Metallurgy Division
REG	Reactor Engineering Group
ROMG	Reactor Operation and Maintenance Group
RPD	Reactor Physics Division
RpG	Reprocessing Group
RRDD	Reprocessing Research and Development Division
RSD	Radiological Safety Division
SED	Safety Engineering Division
SG	Safety Group
SGTF	Steam Generator Test Facility
SIRD	Scientific Information and Resources Division
SND	Surface & Nanoscience Division
SRI	Safety Research Institute
SOWART	Sodium Water Reaction Test facility

INDIRA GANDHI CENTRE FOR ATOMIC RESEARCH

DIRECTOR, IGCAR
Dr. BALDEV RAJ

IGC COUNCIL

IGC SCIENTIFIC COMMITTEE [IGCSC]

DIRECTOR'S ADVISORY COMMITTEE [DAC]

DIVISIONS & HEADS

CHEMICAL FACILITIES
Shri G. RAVISHANKAR

FUEL CHEMISTRY
Dr. T.G. SRINIVASAN

LIQUID METALS & STRUCTURAL CHEMISTRY
Dr. T. GNANASEKARAN

MATERIALS CHEMISTRY
Dr. V. GANESAN

POST IRRADIATION EXAMINATION
Shri JOJO JOSEPH

REMOTE HANDLING, IRRADIATION EXPERIMENTS & ROBOTICS
Dr. S. VENUGOPAL

CORROSION SCIENCE & TECHNOLOGY
Dr. R.K. DAYAL

MATERIALS TECHNOLOGY
Dr. A.K. BHADURI

MECHANICAL METALLURGY
Dr. M.D. MATHEW

NON-DESTRUCTIVE EVALUATION
Dr. T. JAYAKUMAR

PHYSICAL METALLURGY
Dr. M. VIJAYALAKSHMI

CONDENSED MATTER PHYSICS
Dr. A.K. ARORA

MATERIALS PHYSICS
Shri M.C. VALSAKUMAR

SURFACE & NANOMATERIALS
Dr. A.K. TYAGI

COMPUTER
Shri S.A.V. SATYA MURTY

ELECTRONICS & INSTRUMENT.
Shri S. ILANGO SAMBASIVAN

MEDICAL
Dr. A. VIJAYA

REAL TIME SYSTEMS
Shri N. MURALI

SCIENTIFIC INFO.RESOURCE
Dr. M. SAI BABA

A/C & VENTILATION SYSTEM
Shri A.S.L.K. RAO
ACE (MECHANICAL)

CENTRAL WORKSHOP
Shri A.S.L.K. RAO
ACE (MECHANICAL)

CIVIL ENGINEERING
Shri C. SIVATHANU PILLAI
ACE (CIVIL)

ELECTRICAL SERVICES
Shri A. JYOTHISH KUMAR

QUALITY ASSURANCE
Dr. B. VENKATRAMAN

ADMINISTRATIVE OFFICER(R&SR)
Shri R.G. RAGHAVAN

ADMINISTRATIVE OFFICER (P)
Smt. B. INDIRA

Groups (center column)

CHEMISTRY GROUP
DIRECTOR
Dr. P.R. VASUDEVA RAO

REMOTE HANDLING, ROBOTICS, IRRADIATION EXPERIMENTS & PIE GROUP
ASSOCIATE DIRECTOR
Shri K.V. KASIVISWANATHAN

METALLURGY & MATERIALS GROUP
DIRECTOR
Dr. T. JAYAKUMAR

MATERIALS SCIENCE GROUP
DIRECTOR
Dr. C.S. SUNDAR

ELECTRONICS & INSTRUMENTATION GROUP
DIRECTOR
Dr. P. SWAMINATHAN

ENGINEERING SERVICES GROUP
DIRECTOR
Shri Y.C. MANJUNATHA
CHIEF ENGINEER

TECH.COORDINATION AND QUALITY CONTROL SECTION
Shri N. VIJAYAN VARIER *

*STATIONED AT MUMBAI

REACTOR OPERATIONS & MAINTENANCE GROUP
DIRECTOR
Shri G. SRINIVASAN

OPERATION & MAINTENANCE
ASSOCIATE DIRECTOR
Dr. V. RAMANATHAN

FAST REACTOR TECHNOLOGY GROUP
DIRECTOR
Shri G. VAIDYANATHAN

FAST REACTOR TECHNOLOGY GROUP
ASSOCIATE DIRECTOR
Shri P. KALYANASUNDARAM

FAST REACTOR FUEL CYCLE FACILITY PROJECT
PROJECT DIRECTOR
Shri P.V. KUMAR

REACTOR ENGINEERING GROUP
DIRECTOR
Shri S.C.CHETAL

NUCLEAR ENGINEERING GROUP
ASSOCIATE DIRECTOR
Dr. P. CHELLAPANDI

REPROCESSING GROUP
DIRECTOR
Shri R. NATARAJAN

PLANNING DIVISION
Shri A.S.L.K. RAO

SAFETY GROUP
DIRECTOR
Dr. P. CHELLAPANDI

STRATEGIC & HR PLANNING SECTION / TRAINING SCHOOL
Dr. M. SAI BABA

DIVISIONS & HEADS (right column)

PROJECTS PLANNING
Shri P.R. SWAMINATHAN

TECHNICAL SERVICES
Miss S. USHA

REACTOR OPERATION
Shri K.V. SURESH KUMAR
REACTOR SUPERINTENDENT

REACTOR MAINTENANCE
Shri B. ANANTHAPADMANABAN

COMPONENTS & INSTRUMENT. DEVELOPMENT
Shri B. KRISHNAKUMAR

SEPARATION TECHNOLOGY & THERMAL HYDRAULICS
Dr. C. ANAND BABU

SODIUM FACILITIES
Shri K.K. RAJAN

CIVIL ENGINEERING
Shri C. SIVATHANU PILLAI
(FBR Related Works)

HEAT TRANSPORT SYSTEMS
Shri V. BALASUBRAMANIYAN

POWER PLANT CONTROL
Shri K. MADHUSOODANAN

REACTOR PHYSICS
Dr. P. MOHANA KRISHNAN

COMPONENTS HANDLING & MECHANISM
Shri S. RAGHUPATHY

MECHANICS & HYDRAULICS
Shri P. SELVARAJ

REACTOR COMPONENTS
Shri P. PUTHIYAVINAYAGAM

FUEL REPROCESSING PROCESS
Shri V. SUNDARA RAMAN

REPROCESSING PLANT OPERATIONS
Shri M. VENKATARAMAN

REPROCESSING RES. & DEV.
Dr. U. KAMACHI MUDALI

REPROCESSING PROJECTS & SERVICES
Shri P. RAMKUMAR

REPROCESSING PLANT DESIGN
Shri A. RAVISANKAR

RADIOLOGICAL SAFETY
Dr. B. VENKATRAMAN

SAFETY ENGINEERING
Shri N. KASINATHAN

Administration (bottom)

CHIEF ADMINISTRATIVE OFFICER
Shri V. DAYALAN

JOINT CONTROLLER (FINANCE & ACCOUNTS)
Shri C.G.S. NAIR

DEPUTY CONTROLLER OF ACCOUNTS
Shri R. SATHYAMURTHY

ACCOUNTS OFFICER
Shri P.N. MADHAVAN

Fast Breeder Reactors
Towards Energy
Security for the Nation